



TECHNISCHE  
UNIVERSITÄT  
WIEN

DISSERTATION

*Mechanisms of electrochemical oxygen exchange  
on mixed conducting model electrodes in H<sub>2</sub>-H<sub>2</sub>O  
atmosphere*

Ausgeführt zur Erlangung des akademischen Grades eines Doktors der  
Naturwissenschaften unter der Leitung von

Univ.-Prof. Dipl.-Phys. Dr. Jürgen Fleig

E164

Institut für Chemische Technologien und Analytik,

Fachbereich Elektrochemie,

der Technischen Universität Wien

Fakultät für Chemie

von

Dipl. Ing. Andreas Nennung

Matrikelnummer 9371261

Kolonitzplatz 8/16-17

A-1030 Wien

Wien, am 27.04.2016



# Abstract

Solid oxide cells are on the verge of commercialization, but still much research is attributed to optimizing long term stability, for example by decreasing the operating temperature significantly below 800°C. For this goal, new electrode materials with high activity for oxygen exchange at intermediate temperatures are searched for. Mixed ionic and electronic conductors (MIECs) are a promising class of electrode materials, because all species (oxygen ions, electrons and atmospheric oxygen) necessary for electrochemical oxygen exchange are accessible on the entire surface area. While already much research effort was dedicated to the investigation of mixed conducting oxygen electrodes, fundamental investigations of the fuel side electrodes are rather scarce and only ceria-based materials have been studied on a detailed mechanistic level.

In this thesis, mixed conducting perovskite-type electrode materials are in the focus of research. The main goal was the development of methods and models to characterize mixed conducting acceptor doped perovskite-type materials in  $H_2+H_2O$  atmospheres. Electrochemical impedance spectroscopy (EIS) was used to quantify the area-specific resistance of the surface reaction, as well as electronic and ionic conductivity of mixed conductors. Additional analytic methods, such as ambient pressure X-ray photoelectron spectroscopy (AP-XPS) and  $^{18}O$  isotope exchange with subsequent depth profiling were employed to gain a better insight into the mechanisms of electrochemical oxygen exchange at the surface.

For the impedance measurements, thin film model electrodes were deposited on YSZ substrates. As an experimental challenge, the electronic conductivity of acceptor-doped oxides in  $H_2+H_2O$  atmosphere is typically rather low, resulting in a complex interplay of electrochemical reactions and in-plane charge transport, which complicates the interpretation of impedance spectra. Therefore, a novel electrode design was developed, consisting of a mixed conducting thin film and metallic current collectors. Two interdigitating metallic current collectors are placed in a microelectrode, which allows in-plane measurements between the current collectors as well as electrochemical measurements versus a large counter electrode. Equivalent circuit models for quantifying the spectra of both measurement modes were developed and applied to simultaneously fit both spectra, using the same parameter set. In this manner, electronic conductivity as well as the area-specific resistance of the surface reaction and the chemical capacitance can be determined on a single microelectrode. This method together with in-plane measurements on microelectrodes on MgO substrates was employed to investigate the effect of the Fe

content in  $\text{SrTi}_{1-x}\text{Fe}_x\text{O}_{3-\delta}$  on the electronic and ionic conductivity as well as the area specific resistance of the surface oxygen exchange reaction.

The derived equivalent circuit models predict that the electrochemically active zone in weakly electron conducting materials is restricted to the vicinity of the current collectors.  $^{18}\text{O}$  Isotope exchange experiments were performed to map this zone on mixed conducting  $\text{SrTi}_{1-x}\text{Fe}_x\text{O}_{3-\delta}$  and  $\text{Ge}_{0.8}\text{Gd}_{0.2}\text{O}_{1.9-\delta}$  thin films with polarized current collectors in reducing  $\text{H}_2^{18}\text{O} + \text{H}_2$  atmosphere. Subsequent investigation of the  $^{18}\text{O}$  distribution revealed the electrochemically active areas where the  $^{18}\text{O}$  content depended on the polarization.

Further insight into the mechanisms of oxygen exchange was gained by simultaneously acquiring the electrical ( $k^a$ ) and tracer ( $k^*$ ) exchange coefficient of oxygen in three different atmospheres: dry  $^{18}\text{O}_2$ ,  $\text{H}_2^{18}\text{O} + ^{16}\text{O}_2$  and  $\text{H}_2^{18}\text{O} + \text{H}_2$ . While good agreement of both coefficients is found in dry  $^{18}\text{O}_2$ , the tracer exchange coefficient is more than two orders of magnitude higher than the electrical one in humidified atmospheres. This huge difference can be explained by a fast equilibrium rate of water adsorption on surface oxygen vacancies and subsequent dissociation into two surface hydroxyl groups (and the reverse desorption of water), which enables  $^{18}\text{O}$  isotope exchange without an electron transfer. These results are highly important in oxidizing conditions, as they highlight how easily the electrochemical oxygen exchange activity can be over-estimated even when only traces of water are present in the atmosphere. In reducing conditions, the very high tracer exchange coefficient rules out the dissociation or desorption of  $\text{H}_2\text{O}$  to be rate limiting in the surface reaction.

Additional information on the surface chemistry in operating conditions was gained by ambient pressure XPS investigation of model cells with a thin film working electrodes of  $\text{La}_{0.6}\text{Sr}_{0.4}\text{CoO}_{3-\delta}$  (LSC),  $\text{La}_{0.6}\text{Sr}_{0.4}\text{FeO}_{3-\delta}$  (LSF) or  $\text{SrTi}_{0.7}\text{Fe}_{0.3}\text{O}_{3-\delta}$  (STF). This enabled very surface-sensitive chemical analysis near to technological operating conditions. The cells were investigated during well-defined electrochemical polarization in oxidizing ( $\text{O}_2$ ) and in reducing ( $\text{H}_2+\text{H}_2\text{O}$ ) atmospheres. In oxidizing atmosphere all materials exhibit additional surface species of strontium and oxygen. Switching between oxidizing and reducing atmospheres as well as electrochemical polarization caused reversible shifts in the measured binding energy. These shifts can be correlated to a Fermi level shift due to variations in the chemical potential of oxygen. Changes of oxidation states were detected on Fe, which appears as  $\text{Fe}^{\text{III}}$  in oxidizing atmosphere and as mixed  $\text{Fe}^{\text{II/III}}$  in  $\text{H}_2+\text{H}_2\text{O}$ . Cathodic polarization in reducing atmosphere leads to the evolution of  $\text{Fe}^0$  particles that can be reversibly oxidized and reduced by very small applied potentials. The current-voltage characteristics are very steep when metallic Fe is present and rather shallow without the presence of metallic Fe, which indicates a high catalytic activity of the formed Fe particles. The evolution of metallic Fe could be reproduced in a lab-based UHV XPS analyzer, which proves that the electrode bulk oxygen partial pressure is more decisive than the atmospheric conditions.

# Kurzfassung

Festoxidbrennstoffzellen sind eine vielversprechende Technologie der Stromerzeugung und auf dem Weg zur kommerziellen Produktion. Trotzdem ist noch viel Forschungsarbeit zur Verbesserung der Langzeitstabilität, zum Beispiel durch Reduktion der Betriebstemperatur weit unter 800°C, notwendig. Für dieses Ziel werden neue Elektrodenmaterialien mit hoher Sauerstoffaustauschrate gesucht. Gemischte Elektronen- und Ionenleiter sind eine vielversprechende Klasse von Materialien für diesen Zweck, da die Sauerstoffaustauschreaktion auf der gesamten Elektrodenoberfläche stattfinden kann. Gemischte Leiter werden derzeit vorrangig als Sauerstoffelektroden untersucht, während mechanistische Studien gemischter Leiter für brennstoffseitige Elektroden derzeit fast ausschließlich für Ceroxid-basierte Materialien verfügbar sind.

Die elektrochemischen Eigenschaften von gemischt leitenden Materialien mit Perowskit-Struktur sind der Fokus dieser Dissertation. Ein Hauptziel ist die Entwicklung von Methoden und Modellen, um gemischt leitende Materialien in H<sub>2</sub>+H<sub>2</sub>O Atmosphäre zu untersuchen. Mit Elektrochemischer Impedanzspektroskopie wurde die elektronische und ionische Leitfähigkeit, sowie der flächenbezogene Widerstand der elektrochemischen Sauerstoffaustauschreaktion gemischter Leiter bestimmt. Mit in-operando Photoelektronen Spektroskopie und <sup>18</sup>O Isotopenaustausch Experimente wurde die Sauerstoffaustauschreaktion weiter untersucht.

Die Impedanzmessungen wurden an Dünnschichtelektroden auf Yttrium-stabilisierten Zirkonoxidsubstraten durchgeführt. Die vergleichsweise geringe elektronische Leitfähigkeit gemischter Leiter wie SrTi<sub>1-x</sub>Fe<sub>x</sub>O<sub>3-δ</sub> und La<sub>0,6</sub>Sr<sub>0,4</sub>FeO<sub>3-δ</sub> in H<sub>2</sub>+H<sub>2</sub>O Atmosphäre stellte eine experimentelle Herausforderung dar, welche durch das Hinzufügen metallischer Stromsammler gelöst werden konnte. Ein neues Design von Mikroelektroden wurde entwickelt, bei welchem jede Elektrode zwei ineinandergreifende Stromsammler enthält. Diese Geometrie ermöglicht „*in-plane*“ Kontaktierung, bei welcher die Impedanz zwischen den Stromsammlern innerhalb einer Elektrode gemessen wird, und „*elektrochemische*“ Kontaktierung, bei welcher die Mikroelektrode gegen eine makroskopische Gegenelektrode kontaktiert wird. Für beide Kontaktmodi wurden Ersatzschaltbilder entwickelt, welche gleichzeitig mit nur einem Parameterset gefittet werden. Durch diese Methode können elektronische und ionische Leitfähigkeit, sowie der flächenbezogene Widerstand der Sauerstoffaustauschreaktion an nur einer Mikroelektrode bestimmt werden. Diese Methode wurde zusammen mit „*in-plane*“ Messungen an Mikroelektroden auf isolierenden MgO Substraten zur Untersuchung des

Einfluss der Eisendotierung in  $\text{SrTi}_x\text{Fe}_{1-x}\text{O}_{3-\delta}$  Dünnschichten auf die elektronische und ionische Leitfähigkeit, sowie den Widerstand der Sauerstoffaustauschreaktion eingesetzt.

Laut dem Ersatzschaltbild für gemischte Leiter mit geringer elektronischer Leitfähigkeit ist nur ein kleiner Bereich in der Nähe der Stromsammler elektrochemisch aktiv. Bei Isotopenaustausch-experimenten in  $\text{H}_2^{18}\text{O} + \text{H}_2$  Atmosphäre an Dünnschichten aus  $\text{SrTi}_{1-x}\text{Fe}_x\text{O}_{3-\delta}$  und  $\text{Ge}_{0.8}\text{Gd}_{0.2}\text{O}_{1.9-\delta}$  mit elektrisch polarisierten Stromsammlern konnte der Einfluss der Polarisation auf die  $^{18}\text{O}$  Verteilung abgebildet werden.

Weitere Einsicht in den Mechanismus der Sauerstoffaustauschreaktion konnte durch gleichzeitige Bestimmung des elektrischen ( $k^q$ ) und des Isotopenaustauschkoeffizienten ( $k^*$ ) von Sauerstoff gewonnen werden. Dafür wurde Impedanzspektroskopie während Isotopenaustauschexperimenten in drei verschiedenen Atmosphären durchgeführt:  $^{18}\text{O}_2$  (trocken),  $\text{H}_2^{18}\text{O} + ^{16}\text{O}_2$  und  $\text{H}_2^{18}\text{O} + \text{H}_2$ . Der Vergleich beider Koeffizienten zeigt gute Übereinstimmung in trockener  $^{18}\text{O}_2$  Atmosphäre und stark beschleunigten Isotopenaustausch ( $k^* > 100 k^q$ ) in feuchter oxidierender und reduzierender Atmosphäre. Der beschleunigte Isotopenaustausch kann durch eine sehr hohe Gleichgewichtsrate von Wasseradsorption an Sauerstoffdefektstellen und Dissoziation in zwei oberflächliche OH Gruppen erklärt werden. Bei dieser Reaktion findet kein Elektronentransfer statt, womit sie  $k^*$  um Größenordnungen beschleunigen kann, ohne sich auf  $k^q$  auszuwirken. Die Ergebnisse warnen vor einer Überschätzung der elektrochemischen Sauerstoffaustauschaktivität wenn nur Spuren von Wasser bei  $^{18}\text{O}_2$  Austauschexperimenten vorhanden sind.

Zusätzliche Informationen über die Oberflächenchemie konnte durch in-operando Photoelektronenspektroskopie an elektrochemischen Modellzellen mit  $\text{La}_{0.6}\text{Sr}_{0.4}\text{CoO}_{3-\delta}$  (LSC),  $\text{La}_{0.6}\text{Sr}_{0.4}\text{FeO}_{3-\delta}$  (LSF) oder  $\text{SrTi}_{0.7}\text{Fe}_{0.3}\text{O}_{3-\delta}$  (STF) Dünnschichtelektroden gewonnen werden. Die Oberflächenchemie wurde während definierter elektrochemischer Polarisation der Elektroden in oxidierender ( $\text{O}_2$ ) und reduzierender ( $\text{H}_2 + \text{H}_2\text{O}$ ) Atmosphäre untersucht. Ändern des Sauerstoffpartialdruckes in den Elektroden durch Wechsel der Atmosphäre sowie durch elektrochemische Polarisation verursachten reversible Änderungen der Bindungsenergie aller beobachteten Peaks. Diese Änderungen konnten auf eine Verschiebung der Fermienergie in Abhängigkeit vom Sauerstoffpartialdruck zurückgeführt werden. Der Oxidationszustand von oberflächennahem Eisen hängt vom Sauerstoffpartialdruck in der Elektrode ab. In oxidierender Atmosphäre ist Eisen hauptsächlich als  $\text{Fe}^{3+}$  vorhanden, während in reduzierender Atmosphäre  $\text{Fe}^{2+}$  und  $\text{Fe}^{3+}$  koexistieren. Kathodische Polarisation in reduzierender Atmosphäre führt sogar zur reversiblen Bildung von metallischem Eisen. Dieses bildet Nanopartikel an der Oberfläche, welche die Aktivität für  $\text{H}_2\text{O}$  Elektrolyse stark verbessern. Die Bildung von  $\text{Fe}^0$  Nanopartikeln konnte auch in einem labor-basierten UHV Spektrometer nachgewiesen werden, was nahelegt, dass der Sauerstoffpartialdruck in der Elektrode entscheidender ist als die Atmosphäre.

# INHALTSVERZEICHNIS

<b>Abstract</b> .....	<b>iii</b>
<b>Kurzfassung</b> .....	<b>v</b>
<b>1 Introduction</b> .....	<b>5</b>
<b>2 Defect models of the investigated materials</b> .....	<b>11</b>
2.1 Defects in p-doped oxides and their equilibria .....	11
2.2 Chemical capacitance .....	13
2.3 Calculated defect diagrams of $\text{La}_{0.6}\text{Sr}_{0.4}\text{FeO}_{3-\delta}$ , $\text{SrTi}_{0.7}\text{Fe}_{0.3}\text{O}_{3-\delta}$ and $\text{La}_{0.8}\text{Sr}_{0.2}\text{CrO}_{3-\delta}$ .....	14
2.3.1 $\text{La}_{0.6}\text{Sr}_{0.4}\text{FeO}_{3-\delta}$ .....	14
2.3.2 $\text{SrTi}_{0.7}\text{Fe}_{0.3}\text{O}_{3-\delta}$ .....	15
2.3.3 $\text{La}_{0.8}\text{Sr}_{0.2}\text{CrO}_{3-\delta}$ .....	16
<b>3 A novel impedance spectroscopic method for investigation of weakly electron conductive electrode materials</b> .....	<b>17</b>
3.1 Introduction.....	17
3.2 Experimental details and measurement modes .....	18
3.2.1 <i>Sample preparation and electrode design</i> .....	18
3.2.2 <i>Contacting modes and impedance measurements</i> .....	20
3.3 Equivalent circuit models for thin film electrodes with current collectors .....	21
3.3.1 <i>Transmission line circuit model for transport losses in thin film electrodes</i> .....	21
3.3.2 <i>Application of the generalized transmission line circuit to MIEC electrodes with interdigitating current collectors</i> .....	25
3.4 Experimental results and discussion.....	31
3.4.1 <i>Frequency dependence of the electrode polarization</i> .....	32
3.4.2 <i>Geometry variations</i> .....	33
3.4.3 <i>Temperature dependence</i> .....	36
3.4.4 <i>Possibilities and restrictions</i> .....	37
3.5 Conclusions .....	38
3.6 Mathematical derivation of the equivalent circuit.....	39
3.6.1 <i>Polarization of a mixed conducting electrode without transport losses</i> .....	39
3.6.2 <i>Relation between polarization potential and current</i> .....	39
3.6.3 <i>Impedance of the generalized transmission lines</i> .....	41
3.6.4 <i>Symmetric terminal polarization</i> .....	42
3.6.5 <i>Asymmetric terminal polarization</i> .....	43
3.6.6 <i>Infinite length boundary conditions</i> .....	43

3.6.7 Analytic functions for electrochemical and in-plane impedance.....	44
<b>4 The electrochemical properties of Sr(Ti,Fe)O<sub>3-δ</sub> for solid oxide fuel cell anodes...</b>	<b>47</b>
4.1 Introduction.....	47
4.2 Experimental.....	48
4.3 Results and Discussion.....	50
4.3.1 In-plane conductivity of STF.....	50
4.3.2 Electrochemical activity.....	54
4.4 Conclusions.....	59
<b>5 Mapping electrochemically driven gas exchange of mixed conducting SrTi<sub>0.7</sub>Fe<sub>0.3</sub>O<sub>3-δ</sub> and Ce<sub>0.8</sub>Gd<sub>0.2</sub>O<sub>2-δ</sub> thin films by <sup>18</sup>O tracer incorporation under reducing atmosphere.....</b>	<b>61</b>
5.1 Introduction.....	61
5.2 Experimental.....	61
5.2.1 Sample preparation.....	61
5.2.2 Electrode design.....	62
5.3 Results and discussion.....	63
5.3.1 Thermal diffusion profiles.....	63
5.3.2 Effect of cathodic bias.....	65
5.3.3 Effect of polarity and electrode placement.....	67
5.4 Conclusions.....	69
<b>6 Water-induced decoupling of tracer and electrochemical oxygen exchange kinetics on mixed conducting SOFC electrodes.....</b>	<b>71</b>
6.1 Introduction.....	71
6.2 Experimental.....	73
6.3 Results and discussion.....	74
6.3.1 Effect of humidity on $k^a$ .....	74
6.3.2 Correlation of $k^*$ and $k^a$ in dry and humid conditions.....	75
6.4 Conclusions.....	79
<b>7 Ambient pressure XPS study of mixed conducting perovskite-type SOFC cathode and anode materials under well-defined electrochemical polarization.....</b>	<b>81</b>
7.1 Introduction.....	81
7.2 Experimental.....	82
7.2.1 Sample design and preparation.....	82
7.2.2 Near ambient pressure XPS and impedance measurements.....	84
7.3 Results and discussion.....	87
7.3.1 Bulk and surface states.....	87
7.3.2 Electronic conduction mechanism and valence band structure.....	89

7.3.3 Differences between oxidizing and reducing atmosphere .....	91
7.3.4 XPS under electrochemical polarization.....	95
7.3.5 Oxygen partial pressure ( $pO_2^{eff}$ ) dependent chemical capacitance as an indicator for the defect chemical regime.....	102
7.4 Conclusions .....	104
<b>8 XPS investigation of polarized SOFC anodes at operation temperature in UHV... 105</b>	
8.1 Introduction.....	105
8.2 Experimental .....	106
8.2.1 Adaption of the 1" type sample holder for steady state high temperature experiments.....	106
8.2.2 Fabrication of a model cell for UHV based experiments.....	108
8.2.3 Deposition of the working electrode and current collector.....	108
8.2.4 Pre-reduction procedure.....	109
8.2.5 Measurements inside the UHV chamber.....	110
8.3 Results and discussion.....	111
8.3.1 Evolution of metallic Fe from LSF and STF.....	111
8.3.2 Evolution of metallic Ni from $La_{0.7}Sr_{0.2}Cr_{0.9}Ni_{0.1}O_{3-\delta}$ .....	113
8.3.3 Near-surface oxidation states of Cr .....	114
8.3.4 Binding energies .....	115
8.4 Conclusions .....	118
<b>9 The electrolyte spreading resistance of microelectrodes - more than a resistive offset .....</b>	<b>119</b>
9.1 Introduction.....	119
9.2 Numerical model.....	120
9.3 Effect of finite substrate dimensions.....	121
9.4 Electrolyte resistance of surface and TPB active electrodes .....	122
9.5 Effects of non-ideal counter electrodes.....	124
9.6 Conclusions .....	127
<b>Summary .....</b>	<b>129</b>
<b>References .....</b>	<b>133</b>
<b>List of Abbreviations and Acronyms .....</b>	<b>141</b>
<b>List of Figures .....</b>	<b>143</b>
<b>List of Tables.....</b>	<b>150</b>
<b>Acknowledgements .....</b>	<b>151</b>



# 1 Introduction

Solid oxide cells (SOCs) can transform chemically bound energy from a fuel into electrical power and vice versa. When those devices are operated as solid oxide fuel cells (SOFCs), they are very versatile power generation systems, due to their fuel flexibility<sup>1-2</sup> and excellent scalability<sup>3</sup>. In electrolysis operation, as solid oxide electrolysis cells (SOECs), typically water is split into H<sub>2</sub> and O<sub>2</sub><sup>4</sup>, but CO<sub>2</sub> electrolysis<sup>5</sup> or CO<sub>2</sub>-H<sub>2</sub>O co-electrolysis is investigated as well<sup>6</sup>. Due to the increase in entropy during the water splitting reaction, meaning that  $\Delta_R G < \Delta_R H$ , high-temperature electrolysis is theoretically<sup>7</sup> and even practically<sup>4</sup> possible with an electrical efficiency >100%, meaning that the cell takes up heat from the surrounding during the electrolysis operation. Much research effort is nowadays attributed to the investigation of oxygen exchange reactions and optimization of kinetics and durability of electrodes, especially on the oxygen side. Mixed ionic and electronic conductors are a promising class of materials to replace the triple-phase boundary active (La,Sr)MnO<sub>3- $\delta$</sub> -Zr<sub>1-x</sub>Y<sub>x</sub>O<sub>2-x/2</sub> (LSM-YSZ, oxygen electrode) and Ni-Zr<sub>1-x</sub>Y<sub>x</sub>O<sub>2-x/2</sub> (Ni-YSZ, fuel electrode) composites that are usually employed in currently commercially available SOFCs<sup>8</sup>. On such mixed conducting materials the electrochemical exchange of oxygen (oxygen reduction or fuel oxidation) is possible on the entire electrode surface, in contrast to only electron conducting electrodes, which are active along the atmosphere-electrode-electrolyte triple phase boundary, see Figure 1. The larger electrochemically active area thus results in possibly improved reaction rates. Mixed conductors are therefore widely studied for oxygen electrodes<sup>3, 9-10</sup>, and partly reveal impressive advantages in terms of polarization resistance.

Mixed conductors are also promising alternatives for fuel side electrodes, where currently triple phase boundary active Ni-YSZ cermets are employed. These Ni-YSZ electrodes typically exhibit acceptably low polarization resistance, but suffer from weaknesses such as sulphur poisoning<sup>11</sup>, carbon deposition during operation in hydrocarbon fuels<sup>12</sup> and structural instability in oxidizing atmosphere due to Ni oxidation. Compared to oxygen electrodes, the development and mechanistic understanding of mixed conducting fuel side electrodes is still lagging behind. In particular, ceria-based and perovskite-type materials have been studied so far. Largely porous electrodes were used, which allow only limited insight into materials parameters and rate-limiting processes. Low polarization resistance (comparable to Ni-YSZ cermets, but not lower) and high stability during redox cycling was

e.g. found on porous  $(\text{La,Sr})\text{FeO}_{3-\delta}$ <sup>13</sup>  $(\text{La,Sr})(\text{Cr,Fe})\text{O}_{3-\delta}$ <sup>14</sup> or  $(\text{La,Sr})(\text{Cr,Mn})\text{O}_{3-\delta}$ <sup>15-18</sup>. The latter also shows significant activity in methane<sup>19-20</sup>. Furthermore, metal-free anodes may be less prone to some problems of Ni-YSZ cermets, such as sulphur-poisoning and redox cycling stability<sup>3,21</sup>.

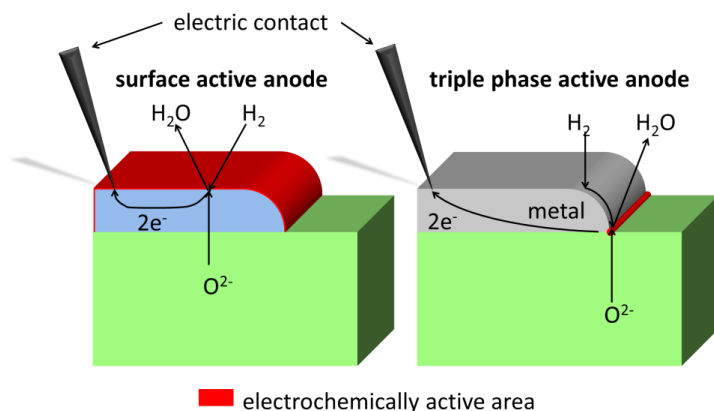


Figure 1. Sketch of the electrochemically active zones on mixed conducting (left) and metallic (right) SOFC anodes.

Detailed mechanistic investigations of charge transport processes and the oxygen exchange reaction at the surface of oxide electrodes are scarce for reducing conditions. So far, thorough studies on geometrically well-defined thin film electrodes have been mostly performed on ceria-based materials<sup>22-26</sup>, and only very recently, first mechanistic studies of perovskite-type materials, e.g.  $\text{La}_{0.6}\text{Sr}_{0.4}\text{FeO}_{3-\delta}$ <sup>27</sup> have become available.

For fundamental investigations of the oxygen exchange reaction at the electrode surface, thin film model electrodes are proven to be a very useful tool<sup>28-32</sup>. For example, the well-defined geometry allows the quantitative comparison of the oxygen exchange activity of various mixed conducting materials<sup>30, 33-34</sup>. Due to the well-defined geometry and known surface area, surface and triple phase boundary activity can be distinguished, e.g. by geometry variations of  $(\text{La,Sr})\text{MnO}_{3-\delta}$ <sup>35</sup>, or Pt<sup>36-37</sup> thin film microelectrodes. On  $(\text{La,Sr})\text{MnO}_{3-\delta}$  even the individual roles of grain and grain boundaries in the oxygen exchange can be differentiated<sup>38</sup>. Another advantage of model electrodes is the facile usage of a counter electrode with much lower polarization resistance. When microelectrodes are investigated, typically a much larger counter electrode of the same material is used, and in case of extended thin film electrodes, a porous counter electrode with much larger effective surface area can be implemented.

Although the usage of thin film model electrodes is widespread for oxygen electrodes, studies of perovskite-type thin film electrodes in  $\text{H}_2+\text{H}_2\text{O}$  atmospheres are very scarce and only Ref.<sup>27</sup> is available so far. Therefore, also the methods and models by which potential mixed conducting fuel side electrode materials can be tested are only partly

developed and optimized and especially little is known about the mechanism and rate limiting step of water splitting or hydrogen oxidation reaction at the surface. Better insight into the fundamental processes occurring on mixed conducting fuel side electrodes is therefore of high relevance for a more targeted minimization of overpotential losses in solid oxide cells by material and geometry optimization.

The goal of this thesis is to gain an improved fundamental understanding of the electrochemical properties and possible mechanisms of oxygen exchange on reduction-stable perovskite-type materials in reducing  $H_2+H_2O$  atmospheres. Different acceptor-doped perovskite-type electrode materials were investigated:

- $SrTi_{0.7}Fe_{0.3}O_{3-\delta}$  (STF73) and  $SrTi_{0.3}Fe_{0.7}O_{3-\delta}$  (STF37)
- $La_{0.6}Sr_{0.4}FeO_{3-\delta}$  (LSF64)
- $Ce_{0.8}Gd_{0.2}O_{1.9-\delta}$  (GDC)
- (La,Sr)CrO<sub>3</sub>-based, A-deficient  $La_{0.7}Sr_{0.2}Cr_{0.9}Ni_{0.1}O_{3-\delta}$

All these materials are acceptor doped mixed ionic and electronic conductors in reducing atmospheres and are thermodynamically stable in 1:1  $H_2+H_2O$  atmosphere at temperatures of about 600°C.

The most widely employed characterization technique throughout this thesis is electrochemical impedance spectroscopy (EIS). However, a meaningful interpretation of impedance spectra, even of thin film model electrodes is challenging in  $H_2+H_2O$ , due to the limited electronic conductivity of acceptor-doped perovskites in reducing atmospheres. Application of micro-structured thin film current collectors embedded between thin film electrode and electrolyte reduces the impact of the electronic sheet resistance on the polarization resistance of the electrodes. Nevertheless, in-plane charge transport may have a significant impact on the polarization resistance, which is discussed in detail in **chapter 3**. A novel microelectrode design with two interdigitating current collectors on each microelectrode is introduced. Equivalent circuit models based on the rate laws of charge transport and electrochemical reactions in linear irreversible thermodynamics are derived for this electrode design and fitted to measured impedance spectra as a proof-of-concept of the method.

In **chapter 4** the methods derived in chapter 3 are used to thoroughly investigate the electrochemical properties of  $Sr(Ti,Fe)O_{3-\delta}$  thin film model electrodes, containing 30 and 70 mol% Fe. Bulk and surface properties are correlated with defect chemical models and factors that influence water splitting/hydrogen oxidation activity are discussed.

The circuit model and electrochemical measurements predict an electrochemically active zone in the vicinity of a current collector. In this zone the MIEC is polarized and electrochemically driven oxygen exchange is possible.

This electrochemically active zone is visualized in **chapter 5**. Tracer exchange in reducing  $\text{H}_2+\text{H}_2^{18}\text{O}$  atmosphere was performed on STF and GDC thin films on YSZ, which contained polarized current collectors. Subsequent imaging of the tracer distribution by secondary ion mass spectroscopy (SIMS) qualitatively confirmed the circuit model and increased or decreased  $^{18}\text{O}$  fraction could be visualized in the vicinity of cathodically and anodically polarized current collectors, respectively. However, the observed tracer exchange in equilibrium was much faster compared to expectations from the electrochemical surface ASR. Also the response of the tracer incorporation rate to polarization was much weaker than expected from typical kinetic models that suggest an exponential dependence of reaction rates to electrochemical polarization.

Systematic investigations of these unexpected results were then performed in the study described in **chapter 6**. The electrical ( $k^q$ ) and the tracer ( $k^*$ ) exchange coefficients of oxygen on MIEC surfaces were determined and compared by simultaneous impedance spectroscopy and tracer exchange with subsequent SIMS analysis. These experiments were performed in dry  $^{18}\text{O}_2$ ,  $^{16}\text{O}_2$  humidified with  $\text{H}_2^{18}\text{O}$ , and reducing  $\text{H}_2+\text{H}_2^{18}\text{O}$ . In humid oxidizing and humid reducing atmospheres, very high tracer exchange coefficients were observed and explained by an additional reaction pathway for tracer exchange via the dissociation of water. This tracer exchange mechanism does not contribute to the electrochemical activity and can explain the huge difference between the two measured coefficients.

Additional information on possible mechanisms of oxygen exchange was gained in synchrotron based XPS measurements (**chapter 7**). Model cells with thin film working electrodes that exhibit surface-limited kinetics were investigated by near-ambient pressure XPS and impedance spectroscopy. Working electrode materials were  $\text{La}_{0.6}\text{Sr}_{0.4}\text{CoO}_{3-\delta}$ , (LSC)  $\text{La}_{0.6}\text{Sr}_{0.4}\text{FeO}_{3-\delta}$ , (LSF) and  $\text{SrTi}_{0.7}\text{Fe}_{0.3}\text{O}_{3-\delta}$  (STF). Chemically distinct surface species of Sr and O were found on all materials in oxidizing atmosphere (0.5 mbar  $\text{O}_2$ ), indicating that the surface termination is not a perovskite bulk-plane. The binding energy of all fixed valent element's peaks shifted as a function of the effective  $\text{pO}_2$ , due to a Fermi level shift. In reducing  $\text{H}_2+\text{H}_2\text{O}$  atmosphere, Fe can be observed in oxidation states +3, +2 and 0, depending on the electrochemical polarization. The evolving  $\text{Fe}^0$  phase, which forms highly dispersed particles, strongly increases the electrochemical activity.

In **chapter 8** the phenomenon of metal exsolution from perovskite B-site cations was further investigated using a lab-based XPS analyser on heated and electrochemically

polarized model cells with a thin film working electrode. Cells with  $\text{La}_{0.6}\text{Sr}_{0.4}\text{FeO}_{3-\delta}$ ,  $\text{SrTi}_{0.3}\text{Fe}_{0.7}\text{FeO}_{3-\delta}$  and  $\text{La}_{0.7}\text{Sr}_{0.2}\text{Cr}_{0.9}\text{Ni}_{0.1}\text{O}_{3-\delta}$  working electrode were examined. The evolution of a secondary metallic phase in reducing conditions was proved for all investigated materials by XPS and SEM investigations.

In **chapter 9**, a numerical study of microelectrode impedance spectra is presented, focusing on the spreading resistance<sup>28</sup> in the electrolyte. It is shown that the electrolyte spreading resistance of a microelectrode not only depends on the dimensions of the electrolyte, but also on the applied frequency and the electrochemical properties of working and counter electrodes. This frequency dependent current density distribution in the electrolyte causes additional features in the impedance spectra that are especially pronounced when a counter electrode with low chemical capacitance, such as a porous metal electrode, is used on the bottom of the substrate.



## 2 Defect models of the investigated materials

### 2.1 Defects in p-doped oxides and their equilibria

In this thesis, the electrochemical properties of several reduction stable oxides were investigated in reducing conditions. The defect chemical models of these materials are, however, rather similar. Here, a short general introduction is given, using Kröger-Vink notation. The electrochemical properties of acceptor doped SOFC electrode materials are largely determined by the acceptor dopant (A) and the transition metal (TM) present in the cationic lattice. Written in Kröger-Vink notation, these defects are

- Acceptor dopant:  $A'$
- Transition metal (in various oxidation states):  $TM, TM^\times, TM', TM''$
- Oxygen vacancies:  $V_O^{\ddot{}}$

The defect charge of the transition metal is always with respect to the lattice position. E.g.  $Fe^{3+}$  is uncharged in III-III perovskites e.g.  $(La,Sr)FeO_{3-\delta}$  and has negative charge in II-IV perovskites, e.g.  $Sr(Ti,Fe)O_{3-\delta}$ . Accordingly,  $Sr(Ti,Fe)O_{3-\delta}$  is strictly speaking not acceptor doped by a fixed valent dopant, but rather doped with a transition metal that acts as an acceptor in its preferred oxidation state  $Fe^{3+}$ . Some perovskite-type oxides (e.g. undoped or donor-doped  $SrTiO_3$ <sup>39-40</sup> without TM, or  $(La,Sr)CoO_{3-\delta}$ <sup>41</sup>), have highly mobile, delocalized electronic defects, with a metal-like resistance-temperature relation. In such cases a model using delocalized electrons  $e'$  and holes  $h'$  in analogy to semiconductors is appropriate.

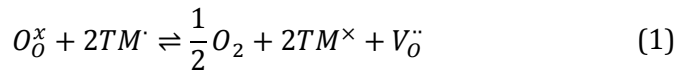
However, our results and recent thermogravimetric measurements<sup>42</sup> suggest that in the materials investigated in this thesis interpretation of electronic defects in terms of localized point defects is physically more correct. Therefore, in the defect model presented throughout this thesis, electronic defects are localized and attributed to different oxidation states of the transition metal.

In oxides containing iron or cerium, electronic defects, especially in reducing atmosphere, tend to be localized e.g. as reduced  $Fe^{2+}$  (see section 7.3.4 and <sup>43</sup>) or  $Ce^{3+}$  ions<sup>22</sup>. The mobility of these electronic defects is rather low and thermally activated. Still, the most appropriate model describing the localised electronic defects is in many cases an open debate. For example, the assumption of an  $Fe^{4+}$  ion is likely a severe simplification. Recent X-ray absorption studies on acceptor doped  $LaFeO_3$ -based materials<sup>44-45</sup> highlighted the redox-activity of oxygen anions, and therefore consider the entire  $TMO_6$  octahedron as the

redox active element. These considerations do not affect the defect chemical calculations, because  $TM'$  or  $(TMO_6)'$  may be treated identically in the equations of the defect equilibria.

In the investigated temperature range used in this thesis (typ. 400-800°C) electronic defects and the oxygen content equilibrate fast with the surrounding atmosphere, leading to two defect equilibria that are important in the entire partial pressure range relevant for SOFC operation:

- The oxygen release reaction



$$K_{red} = \frac{\sqrt{pO_2} [TM^\times]^2 [V_O^{\cdot\cdot}]}{[O_O^x] [TM']^2} \quad (2)$$

- The disproportionation of the transition metal



$$K_i = \frac{[TM'] [TM'']}{[TM^\times]^2} \quad (4)$$

Following conservation laws additionally apply:

- Conservation of TM content

$$[TM'] + [TM^\times] + [TM''] + [TM'''] = [TM]_{tot} \quad (5)$$

- Conservation of oxygen lattice sites

$$[V_O^{\cdot\cdot}] + [O_O^x] = 3c_{lattice} \quad (6)$$

where  $c_{lattice}$  is the concentration of  $ABO_3$  formula units.

- Charge neutrality

$$2[V_O^{\cdot\cdot}] + [TM'] = 2[TM''] + [TM''] + [A'] \quad (7)$$

The two equilibrium constants  $K_{red}$  and  $K_i$  have to be gained from oxygen nonstoichiometry measurements, for example by thermogravimetry and coulometric titration, and fitting of the oxygen nonstoichiometry to the measured data. The other parameters (TM content, acceptor content and volume density of  $ABO_3$  unit cells) are known from the material's composition.

## 2.2 Chemical capacitance

The equivalent circuit models of mixed conducting electrodes typically contain a parallel connection of a resistor ( $R_{\text{surface}}$ ) and a capacitor or constant phase element ( $Q_{\text{chem}}$ ) that model the electrode arc. The impedance function of a constant phase element reads

$$Z_{CPE} = \frac{1}{T(i\omega)^p}. \quad (8)$$

Also when a constant phase element is used for fitting, a chemical capacitance can be estimated, using the relation<sup>46</sup>

$$C_{\text{chem}} = (R_{\text{surface}}^{1-p} T_{\text{chem}})^{\frac{1}{p}}. \quad (9)$$

The chemical capacitance of a mixed conducting SOFC electrode is – in analogy to an electrostatic capacitance – the derivative of electronic charge in the working electrode ( $Q_{\text{electron}}^{WE}$ ) by the “voltage drop” in the electrode, which is the electrode overpotential ( $\eta$ ) in electrodes with surface limited kinetics. In order to maintain electroneutrality, this charge is compensated by a change in the oxygen ion content. It can therefore be seen as a measure for the ease of changing the oxygen ion content under the investigated conditions.

$$C_{\text{chem}} = \frac{dQ_{\text{electron}}^{WE}}{d\eta} = -\frac{dQ_{\text{ion}}^{WE}}{d\eta} = -V c_{\text{lattice}} z e \frac{d(3-\delta)}{d\eta}. \quad (10)$$

$V$  is the sample volume,  $c_{\text{lattice}}$  is the volume density of  $ABO_3$  unit cells,  $z$  is the charge number of the mobile ion (-2 for oxygen),  $\eta$  the overpotential of the electrode and  $\delta$  the oxygen vacancy concentration per formula unit, e.g.  $\text{La}_{0.6}\text{Sr}_{0.4}\text{FeO}_{3-\delta}$ .

For surface limited electrode kinetics the overpotential can be used to calculate the change of the chemical potential of oxygen ( $\Delta\mu_O = z\eta$ ), or oxygen partial pressure in the electrode bulk ( $pO_2$ ), using Nernst’s equation

$$\ln\left(\frac{p_{O_2}}{p_{O_2}^{\text{atm}}}\right) = \frac{\eta * 4e}{k_b T} \quad (11)$$

where  $p_{O_2}^{\text{atm}}$  is the atmospheric oxygen partial pressure. Consequently, also the chemical capacitance can be written as function of the oxygen partial pressure. Using the simplifications  $d(3-\delta) = -d\delta$  and  $d \ln\left(\frac{p_{O_2}}{p_{O_2}^{\text{atm}}}\right) = d \ln(pO_2)$  equations (10) and (11) can be combined to

$$C_{\text{chem}} = V c_{\text{lattice}} 4e^2 * \frac{-d\delta}{d\mu_O} = V c_{\text{lattice}} * \frac{8e^2}{k_b T} \frac{-d\delta}{d \ln(pO_2)}. \quad (12)$$

So far, equation (12) is not based on a specific defect model. However, the magnitude and  $pO_2$  dependence of the chemical capacitance can be used as a fingerprint of the defect chemical regime of an oxide and in some cases also the amount of certain defects can be determined or estimated.

In a mixed conducting oxide, the chemical potential of oxygen is given via the chemical potentials of oxygen ions and electrons.

$$\mu_O = \mu_{ion} - 2\mu_{eon} \quad (13)$$

Using equation (13) and the charge neutrality ( $dc_{eon} = 2d\delta, dc_{ion} = -d\delta$ ), the chemical capacitance can be written as

$$C_{chem} = Vc_{lattice} 4e^2 * \left( 4 \frac{d\mu_{eon}}{dc_{eon}} + \frac{d\mu_{ion}}{dc_{ion}} \right)^{-1}. \quad (14)$$

Here, the concentrations of electrons (eon) and ions (ion) are given per unit cell. The concentration dependence of the chemical potential can then be calculated, assuming non-interacting point defects, e.g.  $\frac{d\mu}{dc} = k_b T \frac{1}{c}$ . This simplifies equation (14) to

$$C_{chem} = \frac{Vc_{lattice} 4e^2}{k_b T} * \left( \frac{4}{c_{eon}} + \frac{1}{c_{ion}} \right)^{-1}. \quad (15)$$

## 2.3 Calculated defect diagrams of $La_{0.6}Sr_{0.4}FeO_{3-\delta}$ , $SrTi_{0.7}Fe_{0.3}O_{3-\delta}$ and $La_{0.8}Sr_{0.2}CrO_{3-\delta}$

The defect chemical model presented above can describe the oxygen non-stoichiometry of a variety of acceptor-doped oxides, which is exemplified on the materials that were investigated within this thesis.

### 2.3.1 $La_{0.6}Sr_{0.4}FeO_{3-\delta}$

For LSF64, an acceptor concentration [A'] of 40%, and a TM (Fe) content of 1 per unit cell describes the material's stoichiometry. Since LSF is formally a III-III perovskite, the non-defect oxidation state of Fe is  $Fe^{3+} = Fe_{Fe}^{\times}$ . In Ref.<sup>47</sup> the oxygen nonstoichiometry of LSF64 was measured and fitted to this model, and following values were obtained for  $K_{red}$  and  $K_i$  at 615°C:

$$\Delta G_{red}^0 = 0.48 \text{ eV}, K_{red} = 1.18 * 10^{-3} \quad (16)$$

$$\Delta G_i^0 = 1.17 \text{ eV}, K_i = 2.36 * 10^{-7} \quad (17)$$

With these values, the defect diagram in Figure 2 was calculated.

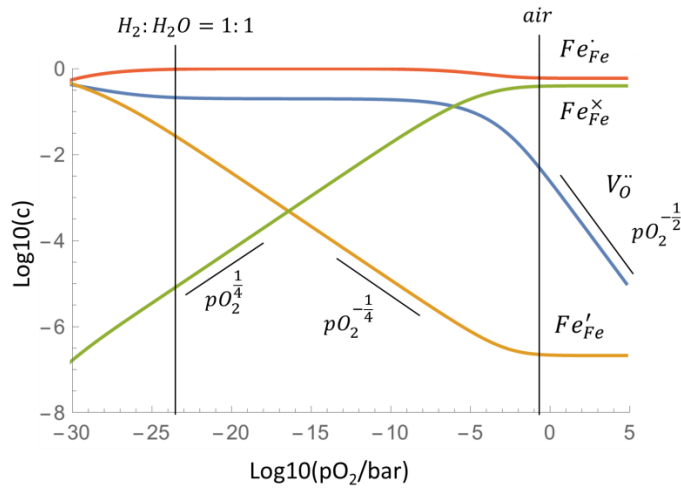


Figure 2. Computed defect diagram of LSF64 at 615°C, using oxygen nonstoichiometry data from Ref.<sup>47</sup> and the defect model from section 2.1. Defect concentrations are normalized to the number of  $ABO_3$  formula units.

### 2.3.2 $SrTi_{0.7}Fe_{0.3}O_{3-\delta}$

The defect model of STF is similar to that of LSF, with the major difference that STF is a nominal II-IV perovskite. Therefore  $Fe^{4+} = Fe_{Ti}^{\times}$ . Strictly speaking STF is not acceptor doped, but  $Fe^{3+} = Fe_{Ti}'$  acts like an acceptor. The defect charges of Fe are shifted relative to LSF, so  $TM'$  and  $TM^{\times}$  have to be changed to  $TM^{\times}$  and  $TM'$ , respectively in reactions (1) and (3) to correspond to equal Fe oxidation states in LSF and STF. Oxygen nonstoichiometry data from Ref.<sup>42</sup>, was used to calculate following equilibrium constants:

$$\Delta G_{red}^0 = 0.25 \text{ eV}, K_{red} = 0.04 \quad (18)$$

$$\Delta G_i^0 = 1.38 \text{ eV}, K_i = 1.52 * 10^{-8} \quad (19)$$

With these data, the defect diagram in Figure 3 was calculated.

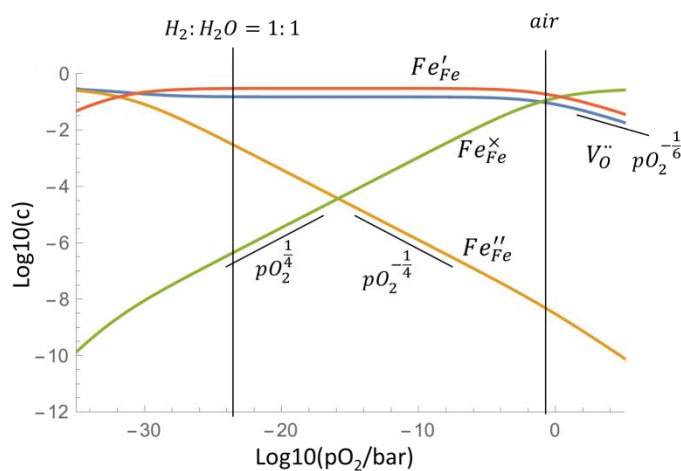


Figure 3. Computed defect diagram of STF73 at 615°C, using oxygen nonstoichiometry data from Ref.<sup>42</sup> and the defect model from section 2.1. Defect concentrations are normalized to the number of  $ABO_3$  formula units.

### 2.3.3 La<sub>0.8</sub>Sr<sub>0.2</sub>CrO<sub>3-δ</sub>

(La,Sr)CrO<sub>3-δ</sub> based perovskites have a defect model that is very similar to that of LSF. However, the reduction enthalpy is significantly higher, which implies that the transition from mainly electronic compensation of the acceptor charge to mainly ionic charge compensation occurs only in very reducing conditions. Because of this high reduction enthalpy (La,Sr)CrO<sub>3-δ</sub> is also stable in very reducing conditions, where LSF already decomposes<sup>47</sup>. Also reduced Cr<sup>2+</sup> is not present, even in very reducing conditions, which simplifies the defect chemical equations by removing the TM disproportionation reaction (equation (3)) from the defect equilibria. Oxygen vacancies are hardly present in oxidizing conditions, while in reducing H<sub>2</sub>+H<sub>2</sub>O atmospheres a significant amount of oxygen vacancies is expected from thermogravimetric data<sup>48</sup>, which is sufficient for enabling surface active thin film electrodes. For this material oxygen nonstoichiometry data is only available from high temperature data ( $\geq 1000^\circ\text{C}$ )<sup>49</sup>, and the assumed value of  $\Delta G_{red}^0 = 2.02 \text{ eV}$ ,  $K_i = 3.16 \cdot 10^{-12}$  at 615°C was extrapolated. Therefore, the exact values on the pO<sub>2</sub> axis in the calculated defect diagram in Figure 4 may be inaccurate, but give a good qualitative picture.

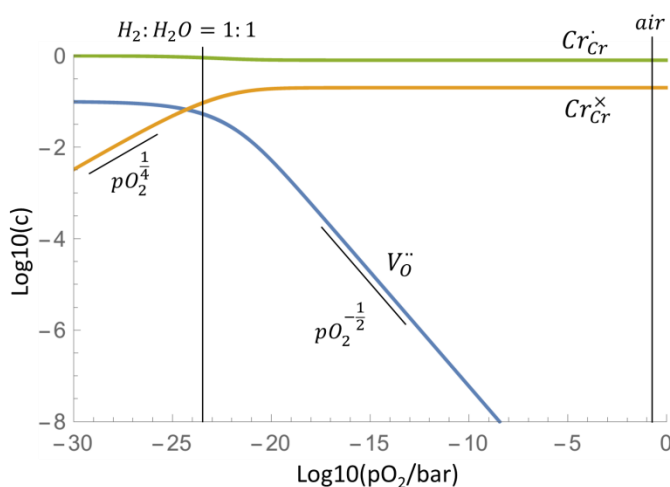


Figure 4. Computed defect diagram of La<sub>0.8</sub>Sr<sub>0.2</sub>CrO<sub>3-δ</sub> at 615°C, using defect chemical data from Ref.<sup>49</sup>, extrapolated from 1000°C to 615°C and the defect chemical model from section 2.1. Defect concentrations are normalized to the number of ABO<sub>3</sub> formula units.

When Ni is co-doped at the perovskite B-site, an element easily reducible to the metallic state is introduced into a perovskite with very high thermo-chemical stability, and reasonable electron and ion conductivity in reducing conditions. It was already shown that this class of materials can form morphologically stable nano-sized Ni exsolutions<sup>50-51</sup>.

# 3 A novel impedance spectroscopic method for investigation of weakly electron conductive electrode materials

*This chapter contains in large part material published in the journal "Physical Chemistry and Chemical Physics" <sup>52</sup>*

## 3.1 Introduction

Thin film model electrodes offer well-defined geometry and surface area, simple charge transport paths and good geometrical reproducibility, making them a very useful design for the investigation of fundamental reaction mechanisms. This was extensively shown for cathode materials <sup>28-32</sup>, but mechanistic electrochemical<sup>24</sup> and near-ambient pressure XPS<sup>22,26,53</sup> studies on mixed conducting thin film anodes are only available for ceria-based materials. When acceptor-doped mixed conductors are used as SOFC anodes rather than cathodes, not only the surface reaction changes, but also some crucial bulk parameters such as electronic and ionic conductivity may change by orders of magnitude. Owing to the low chemical potential of oxygen in H<sub>2</sub> - H<sub>2</sub>O atmospheres, especially the electronic p-type conductivity significantly decreases. Accordingly, not only the surface reaction and ionic charge transport, but also electronic conduction may be rate limiting in reducing atmosphere. This further complicates the interpretation of conventional impedance studies on such anodes, even for thin film electrodes.

For example, moderate electronic conductivity (in the order of 1 S/cm) may lead to medium-frequency features in the impedance spectra for electrodes without additional current collectors <sup>54</sup>, whereas in the case of much lower electronic conductivity a current collector is mandatory<sup>27</sup>. In Ref. <sup>24</sup>, the electronic and ionic in-plane conductivities of ceria films were measured by a method which requires the film to be an excellent ionic conductor and to exhibit an electrolytic conductivity domain. The relevance of electronic and ionic charge transport in MIEC electrodes was also confirmed by numerical simulations<sup>55-56</sup>. However, for impedance spectroscopic analysis of other mixed conducting thin film anodes a novel approach is required which not only considers resistive contributions from the surface reaction but also all charge transport processes in the electrode bulk.

In this chapter an experimental approach for such measurements is introduced. Two interdigitating metallic current collectors are placed in one thin film microelectrode. This allows an “in-plane” impedance measurement between these two current collectors as well as an electrochemical measurement versus an extended counter-electrode. In this manner we obtain two complementary impedance spectra on one and the same electrode. For both measurement modes, equivalent circuit models are developed. Those can be used for simultaneous fitting of both acquired spectra with the same parameter set. By this technique, electronic and ionic conductivity as well as the area specific resistance of the surface reaction and the chemical capacitance can be quantified on a single microelectrode.

This novel method is demonstrated to be applicable to  $\text{SrTi}_{0.7}\text{Fe}_{0.3}\text{O}_{3-\delta}$  electrodes in  $\text{H}_2$  -  $\text{H}_2\text{O}$  atmosphere.

## 3.2 Experimental details and measurement modes

### 3.2.1 Sample preparation and electrode design

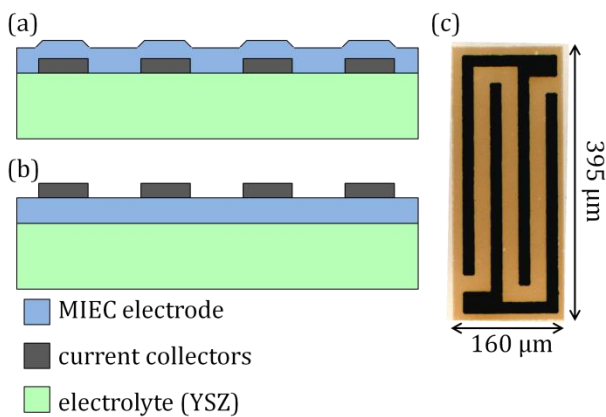


Figure 5. Sketched cross-section of a microelectrode with (a) embedded current collectors, or (b) current collectors on top of the MIEC film. (c): optical micrograph of a produced electrode in transmitted light mode.

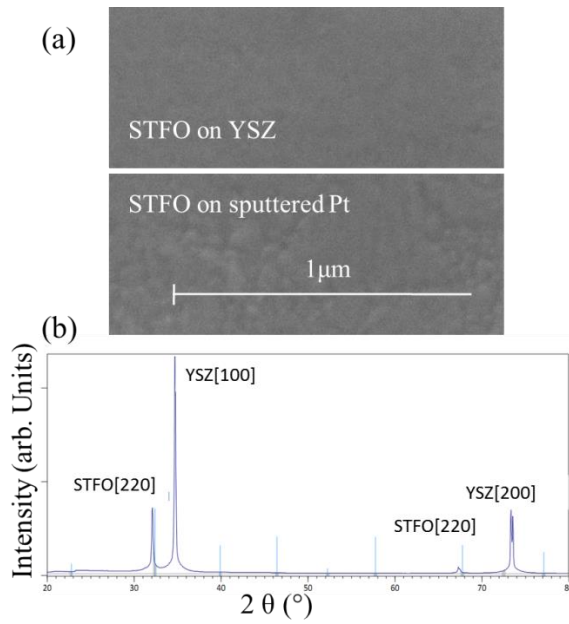


Figure 6. (a) SEM image of a 300 nm thick STFO film on YSZ and sputtered Pt. (b) Diffraction pattern of the thin film.

Pulsed laser deposition (PLD) was used to produce dense thin films of  $\text{SrTi}_{0.7}\text{Fe}_{0.3}\text{O}_{3-\delta}$  (STF73) with a thickness ranging from 103 to 310 nm on single-crystalline yttria-stabilized zirconia (YSZ) with 9.5 mol %  $\text{Y}_2\text{O}_3$ . The YSZ substrates had a size of  $10 \times 10 \times 0.5 \text{ mm}^3$  and [100] surface orientation. Thin films were deposited at a substrate temperature of  $610 \pm 10^\circ\text{C}$  in 0.02 mbar oxygen. The deposition time was varied between 16.6 minutes (3000 pulses) and 50 minutes (9000 pulses) with the laser operating at a pulse energy of 400 mJ (at the laser) and a repetition rate of 3 Hz. Prior to the STFO deposition, a microstructured platinum thin film was employed as an electronic current collector (Figure 5a). For comparison, Pt current collectors were also deposited on top of the STFO layer (Figure 5b). The platinum layer (roughly 100 nm thickness) was sputter deposited and microstructured by photolithography and ion beam etching. To increase the adhesion of the Pt films, 5 nm of titanium were employed as adhesion layer. SEM images indicated dense and flat films for STFO grown on YSZ and on platinum (see Figure 6).  $\theta$ - $2\theta$  diffraction patterns measured on a Bruker D8 GADDS indicate single phase, [110] oriented thin films grown on YSZ (see Figure 6b). Other orientations were not observed. Breaking edge images of the film indicate a thickness of  $310 \pm 10 \text{ nm}$  for the film deposited with 9000 pulses (0.034 nm per pulse). After deposition of the STFO films and current collectors, rectangular microelectrodes with a size of  $160 \times 395 \mu\text{m}^2$  were produced by means of photolithography and ion beam etching.

### 3.2.2 Contacting modes and impedance measurements

No. of metal fingers	Finger distance ( $2l$ ) ( $\mu\text{m}$ )	Finger width ( $2b$ ) ( $\mu\text{m}$ )	Meander length ( $\mu\text{m}$ )	Effective circumference ( $\mu\text{m}$ )	MIEC dimensions ( $\mu\text{m}^2$ )
4	5	15	2625	1090	$160 \times 395$
6	11.7	15	1840	1052	$160 \times 395$
8	25	15	1160	985	$160 \times 395$

Table 1. Dimensions of the electrodes and current collectors. The meander length and effective circumference are according to Figure 7a.

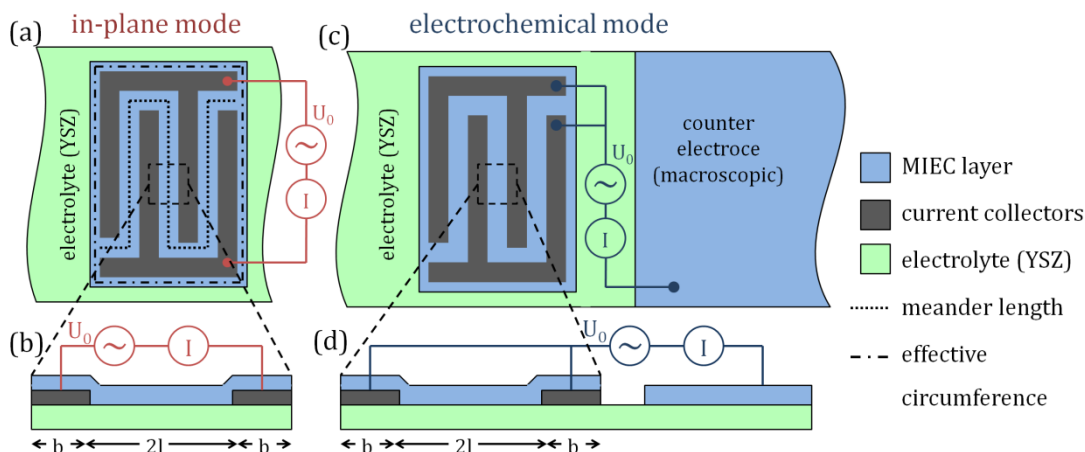


Figure 7. Top view (a, c) and cross-section (b, d) of the two measurement modes. In the in-plane mode (a, b) the voltage is applied between the two metal finger structures. In the electrochemical mode (c, d), both current collectors are treated as one electrical terminal and measured against a macroscopic counter-electrode.

The geometry of the electrode and current collectors is sketched in Figure 7. Three different geometries for the current collectors with varying finger distance were used on the same substrate and the exact measures are given in Table 1

The two current collectors in each microelectrode reduce the impact of the electronic sheet resistance. Nevertheless, the resistances caused by charge transport processes may still be relevant compared to the resistance of the surface reaction (depending on the exact geometry, temperature and atmospheric conditions). In order to separate resistive contributions of transport processes from those of the surface reaction, each microelectrode contains two interdigitating Pt current collectors. By two different contact configurations two measurement modes can be realized. This is sketched in Figure 7 in top view and cross section. In the in-plane measurement (Figure 7a,b), the impedance is measured between the two metal finger structures. In the electrochemical mode (Figure 7c,d) both current collectors are electrically treated as one terminal. The impedance is then measured against the macroscopic counter electrode of the same material, also containing a Pt current collector. This is the measurement mode which is usually applied for electrochemical characterization of microelectrodes. Owing to the much larger counter

electrode, the impedance in the electrochemical mode is almost entirely determined by the microelectrode and the electrolyte <sup>28</sup>.

These two measurement modes on one and the same electrode are the basis of the present study. In the following we derive equivalent circuits describing the corresponding impedance measurements and explain why fitting of both modes enables the simultaneous determination of all relevant resistive and capacitive materials parameters of the system, i.e. ionic conductivity, electronic conductivity, area-specific resistance of the surface reaction and interfacial resistance as well as the chemical capacitance.

The STFO electrodes were investigated with this novel technique in  $H_2 - H_2O$  atmosphere and consistency of the analysis was confirmed by geometry. Piezoelectric high-precision actuators (Newport Agilis) were employed to contact the current collectors in the electrodes via gold-plated steel tips with a tip radius of 1-3  $\mu m$ . Details on the measurement stage are given in Ref.<sup>57</sup>. The impedance spectra were acquired using a Novocontrol Alpha-A High Performance Frequency Analyser, equipped with a Novocontrol POT/GAL 30 V/2 A interface, in the frequency range of 0.01 Hz to 1 MHz at AC an amplitude of 10 mV RMS. The measurements were carried out at temperatures between 490 and 800°C in an atmosphere of 2.5 %  $H_2$  and about 2.5 %  $H_2O$  vapor in argon as carrier gas.

### 3.3 Equivalent circuit models for thin film electrodes with current collectors

#### 3.3.1 Transmission line circuit model for transport losses in thin film electrodes

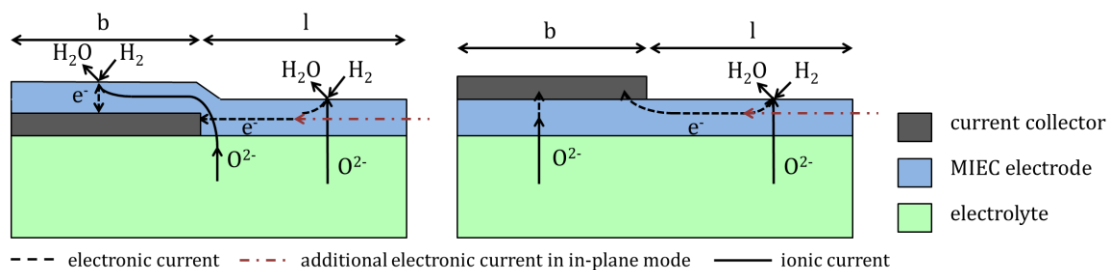


Figure 8. Processes relevant for the impedance of a MIEC anode with metal fingers below the anode (left) and on top (right). Arrows indicate anodic current, although impedance spectroscopy probes both directions.

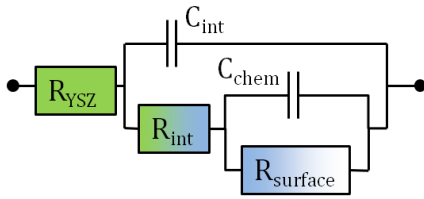


Figure 9 Equivalent circuit for MIEC electrodes with high electronic and ionic conductivity, according to ref.<sup>58</sup>.

For a meaningful interpretation of the impedance measurements in both measurement modes, a thorough discussion of the polarization and charge transport processes within mixed conducting thin film electrodes with current collectors is required. In Figure 8, the possible reaction paths for anodic current flow are sketched. In  $H_2 - H_2O$  atmosphere, the main resistive contributions are typically the hydrogen oxidation on the surface of the MIEC layer as well as electronic and ionic in-plane charge transport within the thin film. Additionally, also a spreading resistance in the electrolyte and an ionic interface resistance at the electrolyte-MIEC interface have to be considered; these turned out to be comparatively small in the case of STFO.

As a starting point, the impedance response of MIEC electrodes with very high electronic and ionic conductivity and rate limiting surface kinetics will be discussed. For such electrodes, all ionic and electronic in-plane and across-plane charge transport processes are without resistance. According to Refs.<sup>30, 58</sup> the equivalent circuit consists of a resistive offset caused by the electrolyte ( $R_{YSZ}$ ) and an electrode part containing the resistance related to the surface reaction ( $R_{surface}$ ) in parallel with the chemical capacitance of the MIEC bulk ( $C_{chem}$ ). If the ionic transport across the electrode-YSZ interface causes an additional resistive contribution, an interfacial resistance and capacitance ( $R_{int}$  and  $C_{int}$ ) have to be added, as depicted in Figure 9. Also in cases where in-plane charge transport losses become relevant, this circuit will play a central role.

As a next step we consider a thin film electrode with moderate or low electronic and ionic conductivity. It was shown by Jamnik and Maier that for one-dimensional systems the impedance of the MIEC bulk is described by a transmission line circuit<sup>58</sup>.

In our case, one-dimensionality is not given since in-plane as well as across-plane currents are important. However, still the concept of a transmission line, reflecting the electrochemical potentials and the transport of electrons and oxygen ions, is applicable. This is shown in the following.

The geometry of our thin film electrodes (Figure 7) is characterized by a very large ratio between film thickness (100-300 nm) and lateral finger distance or width (5-25  $\mu m$ ), i.e. an aspect ratio in the order of 1:100. Moreover, the MIEC film is either in electric contact

with an excellent electron conductor (current collector) or a fast ion conductor (YSZ). The combination of these two facts allows us to define a “fast” and a “slow” carrier. Those are not distinguished by their specific conductivities in the MIEC. Rather, the “fast” carrier can easily move either in the current collector (electrons) or in the electrolyte (ions) and therefore its electrochemical potential is laterally homogeneous in the “fast” phase. Hence, only across-plane transport of this “fast” carrier has to be considered in the MIEC. On the other hand, for the “slow” carrier in-plane distances are much larger than across-plane distances and therefore only in-plane variations of its electrochemical potential in the MIEC are relevant.

Owing to this lateral variation, the driving force for oxygen exchange (and stoichiometric polarization) becomes inhomogeneous along the electrode. This can be quantified by a local “polarization potential” ( $\eta^*$ ), which reflects the driving force of across-plane currents of “fast” carriers and the surface reaction. The dimension of  $\eta^*$  is Volt, although it cannot be related to an electrostatic potential step. In the simplest case of lossless lateral current within the electrode it is position independent and equals the applied voltage, see appendix (A1).

For in-plane transport losses (of the “slow” carrier), but lossless across-plane charge transport of the “fast” carrier (in the MIEC and across interfaces), the polarization potential is simply the local driving force of the surface reaction. It correlates with the change of the local chemical potential of oxygen in the electrode  $\Delta\mu_O^{ode}$  due to an applied bias via

$$\eta^* = \frac{\Delta\mu_O^{ode}}{2F} = \frac{\Delta\tilde{\mu}_{ion}^{ode} - 2\Delta\tilde{\mu}_{eon}^{ode}}{2F} . \quad (20)$$

The symbols  $\tilde{\mu}_{ion}^{ode}$  and  $\tilde{\mu}_{eon}^{ode}$  denote electrochemical potentials of oxygen ions and electrons in the MIEC, respectively;  $\Delta$  indicates the difference to the equilibrium value without applied bias. Therefore  $\Delta\mu_O^{ode}$  is also the difference in the chemical potential of oxygen between the atmosphere and the polarized electrode. It varies in-plane in a polarized MIEC electrode.

When across-plane charge transport losses of the “fast” carrier within the MIEC or across an interface are relevant, the polarization potential has to be defined in a more general manner. For the MIEC layer on top of the electrolyte and thus ions being “fast” carriers it is given by

$$\eta^{* \text{ yte}} = \frac{\Delta\tilde{\mu}_{ion}^{\text{yte}} - 2\Delta\tilde{\mu}_{eon}^{ode}}{2F} . \quad (21)$$

In contrast to equation (20), the electrochemical potential of oxygen ions is now located in the electrolyte and  $\eta^{*yte}$  formally reflects the overall driving force of the reaction  $\text{H}_2\text{O} + 2 e_{ode}^- \rightarrow \text{H}_2 + \text{O}_{yte}^{2-}$ . It corresponds to the sum of kinetic losses of the surface reaction, the according across-plane ionic current within the MIEC and the ion transfer at the MIEC-electrolyte interface.

For a MIEC on top of the current collector, electrons are the “fast” and ions the “slow” carrier. The polarization potential can then be defined as

$$\eta^{*metal} = \frac{\Delta\tilde{\mu}_{ion}^{ode} - 2\Delta\tilde{\mu}_{eon}^{metal}}{2F} . \quad (22)$$

Here, the electrochemical potential of electrons is located in the metal. Therefore,  $\eta^{*metal}$  corresponds to the overall driving force of both, surface reaction and electronic across-plane current within the MIEC (and if relevant across a Schottky barrier at the MIEC-current collector interface). Therefore it is the driving force of the reaction  $\text{H}_2\text{O} + 2 e_{metal}^- \rightarrow \text{H}_2 + \text{O}_{ode}^{2-}$ . For an electrode geometry consisting of long and thin metal fingers, the local polarization potential only depends on the distance from the metal fingers.

In the following, it is explained on an argumentative level that the one-dimensional generalized transmission line circuits given in Figure 10 can describe such a system. In appendix A2 and A3 the impedance functions of these circuits are derived from the rate laws of charge transport and reactions for mixed conducting thin films. However, the following equivalent circuits are graphical and more intuitive representations of these equations.

In-plane transport of the “slow” charge carrier can be quantified by the sheet resistance elements ( $R_{eon}$  or  $R_{ion}$ ). The “fast” charge carrier moves either in a good electronic or a good ionic conductor and therefore has laterally homogeneous electrochemical potential in the “fast” phase, irrespective of its conductivity in the MIEC. This is treated by a short circuit in its transport rail of the equivalent circuit. The element  $Y_{ap}$  describes the (area-specific) across-plane admittance and is related to surface reaction and transport of the “fast” carrier.  $Y_{ap}$  also includes charging and discharging of the chemical capacitance as well as possible interfacial resistances. More specific circuits for this element will be introduced later. Defining this element as an admittance allows a mathematically consistent discretization into small (or infinitesimal) elements. In Figure 10 the resulting circuits for a MIEC on the electrolyte (Figure 10a) and on the current collector (Figure 10b) are shown. Also a symbolic representation of the transmission lines (r.h.s.) is given,

which will be used in the following. The l.h.s. terms in Figure 10 emphasize that the driving forces for the in-plane and across-plane currents are determined by the electrochemical potentials of ions and electrons as given in equation (21) and (22).

The impedance of such a transmission line depends on the left- and right-hand side termination. When a thin film MIEC electrode with current collectors is described by such a circuit, the edges of the metal fingers are appropriate locations of the terminals. For negligible losses in the electrolyte and counter electrode, the polarization potential at these points equals the applied voltage, which is either  $+U_0$  or  $-U_0$ , depending on the finger and measurement mode.

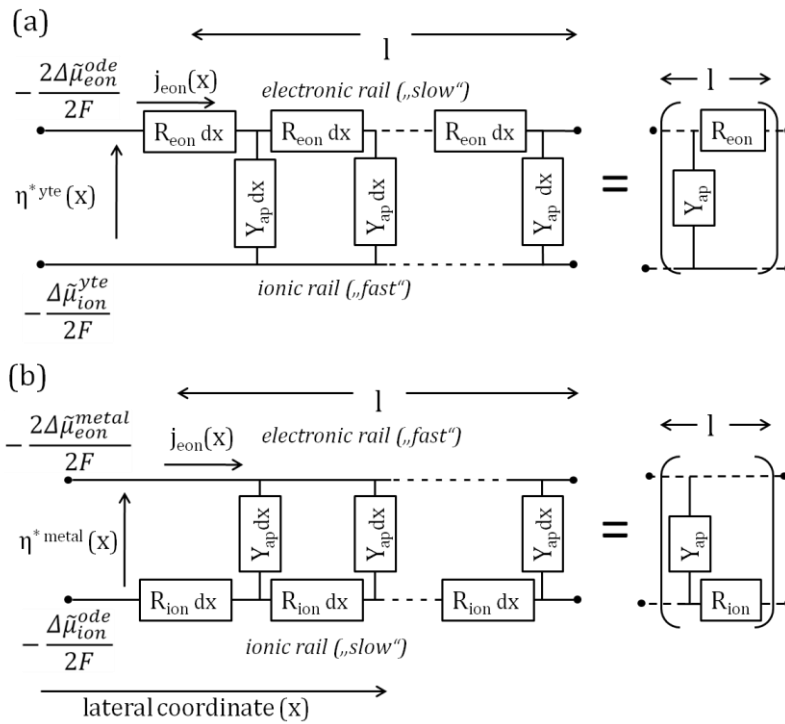


Figure 10. Generalized transmission line circuit describing a MIEC thin film on an electrolyte (a). Generalized transmission line circuit describing a MIEC film on an electronic conductor (e.g. current collector) (b)

### 3.3.2 Application of the generalized transmission line circuit to MIEC electrodes with interdigitating current collectors

In this section, we specify the equivalent circuits for the MIEC electrodes used in this study. Those electrodes consist of two regions with different electrochemical properties: The region of the current collectors and the free MIEC area (electrode grown on YSZ without current collectors). The circuit of the free MIEC area does not depend on the location of the current collectors (above or beneath the MIEC layer), whereas this location does play an important role in the region of the current collectors. The circuits are very similar for electrochemical and in-plane measurement and differ only at the terminal

parts. Still, the impedance spectra for both modes are very different. Across-plane charge transport of electrons is assumed to be lossless in all cases.

### 3.3.2.1 Free MIEC area

A mixed conducting thin film on an ionic conductor can be modeled by the transmission line circuit displayed in Figure 10a. The element  $R_{\text{eon}}$  represents the electronic sheet resistance ( $R_{\text{eon}} = \rho_{\text{eon}}/d$ ) with  $\rho_{\text{eon}}$  and  $d$  being the electronic resistivity and film thickness, respectively. The across-plane admittance (element  $Y_{\text{ap}}$  of the circuit) reflects ionic across-plane charge transport resistances and oxygen exchange via the surface reaction and the chemical capacitance. In our STFO electrodes, ionic across-plane charge transport within the MIEC is almost lossless, while a small resistance at the STFO-YSZ interface could be observed. Consequently, the element  $Y_{\text{ap}}$  can be specified by the simplified equivalent circuit in Figure 9 (without YSZ resistance). The terminals of the transmission line are at the edges of the metal fingers, see Figure 11a. At the edges of the metal fingers the electrochemical potential of electrons is defined by the current collector, and the electrochemical potential of oxygen ions remains at its equilibrium value when neglecting the electrolyte resistance. Consequently, in the electrochemical measurement mode (Figure 7a,b), the polarization potential of the left and right hand side terminal is the applied voltage  $+U_0$ , see appendix A1. The electrolyte resistance will be introduced later as a terminal part. In the in-plane mode (Figure 7c,d), the left and right-hand side terminals are oppositely polarized with  $+U_0$  and  $-U_0$ , respectively. This situation is sketched in Figure 11a. These conditions can also be described by simpler circuits that use only one voltage source: The electrochemical mode is equal to an open end terminal in the center of the transmission line (Figure 11b), and the in-plane mode corresponds to a short circuit in the center of the transmission line (Figure 11c). This equivalence becomes clear when calculating the in-plane distribution of the polarization potential for both measurement modes, which is plotted in Figure 12. The calculation also includes the transmission line above the current collectors. In the electrochemical mode, the gradient of  $\eta^*$  is zero in the center between the metal fingers (equal to an open end boundary). In the in-plane mode,  $\eta^*$  is zero in the center (equal to a short circuit). The corresponding equations are derived in the appendix (A.3.2, A.3.3). In the following circuits, the representation involving only one voltage source will be used, meaning that only half of the metal finger distance ( $l$ ) is considered in the circuit. The resulting transmission line for the free surface area is part of the final circuits in Figure 13.

### 3.3.2.2 Region beneath the current collector

One possible realization of the electrode has metallic current collectors on top of the MIEC film (sketched in Figure 8, r.h.s.). Beneath the metal, the MIEC is conductively connected with the electrolyte and with an electronic conductor, therefore both charge carriers can be treated as “fast” carriers. Accordingly, relevant ionic as well as electronic charge transport within the MIEC layer only occurs across-plane, so only the ionic STFO-YSZ interface resistance has to be considered for charge transport. The surface reaction, on the other hand, is blocked by the dense platinum layer. Consequently, a well suited model for this region is the simplified equivalent circuit in Figure 9 (without YSZ resistance) with  $R_{\text{surface}} \rightarrow \infty$ . The resulting circuit is the l.h.s. part of the circuits in Figure 13.

### 3.3.2.3 Region above the current collector

The MIEC region above the current collector exhibits a homogeneous electrochemical potential of electrons and can be modeled by the transmission line circuit in Figure 10b.  $R_{\text{ion}}$  stands for the ionic sheet resistance ( $R_{\text{ion}} = \rho_{\text{ion}}/d$ ), with  $\rho_{\text{ion}}$  being the ionic resistivity of the film on top of the current collector. The across-plane admittance  $Y_{\text{ap}}$  can be described by a parallel connection of the chemical capacitance  $C_{\text{chem}}$  and surface resistance  $R_{\text{surface}}$ , provided an electronic interface resistance between MIEC and current collector is negligible. Due to the different microstructure of the MIEC on YSZ and metal, also  $R_{\text{surface}}$  and  $C_{\text{chem}}$  might be different on these two substrates. In the case of our STFO electrodes, strong differences could be excluded by geometry variations, see section 3.4.2. Therefore, these parameters are set to be equal on for the MIEC on YSZ and on the current collector. Also for this transmission-line circuit, potentials at the terminals have to be defined. At the edges of the metal fingers oxygen ions are exchanged between MIEC and electrolyte. Here, the ionic MIEC-electrolyte interface resistance has to be considered as a terminal part of the transmission line. If this interface resistance is small compared to the total resistance, the terminal can be approximated by  $R_{\text{int}2} = \sqrt{R_{\text{int}} R_{\text{ion}}}$  (see appendix 3.6.6). Also a capacitance at the current-collector|YSZ interface is likely to be relevant<sup>59</sup>, this is represented by the  $C_{\text{Pt}}$  element which is placed in parallel to the transmission line. The resulting circuit is the left-hand side transmission line in Figure 13. Owing to symmetry reasons, the polarization potential at the two edges of a metal finger is equal. Equivalent to this symmetrical terminal polarization, the transmission line can also be terminated with an open end in the center of the metal finger. This termination is appropriate for both modes. Accordingly, only half of the metal finger width ( $b$ ) is considered in the equivalent circuit.

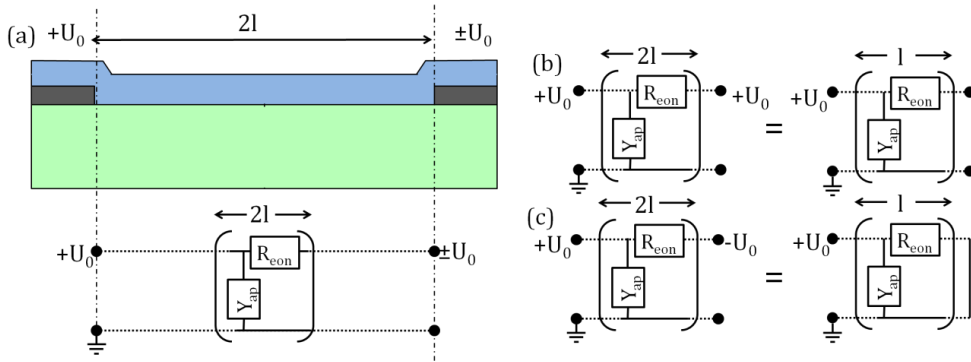


Figure 11. Terminals of the transmission line circuit which are set to the metal finger edges (a). For the electrochemical measurement mode (b), two circuits with different given boundary conditions result in the same impedance function. The same is true for the in-plane measurement mode (c).

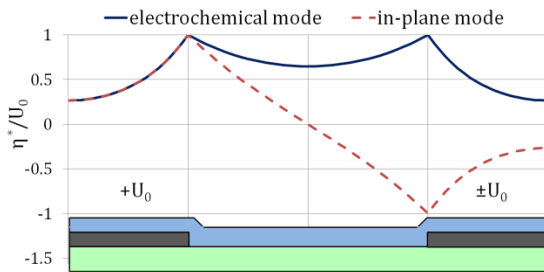


Figure 12. Calculated normalized polarization potential ( $\eta^*/U_0$ ) in the DC case for in-plane and electrochemical measurement modes.

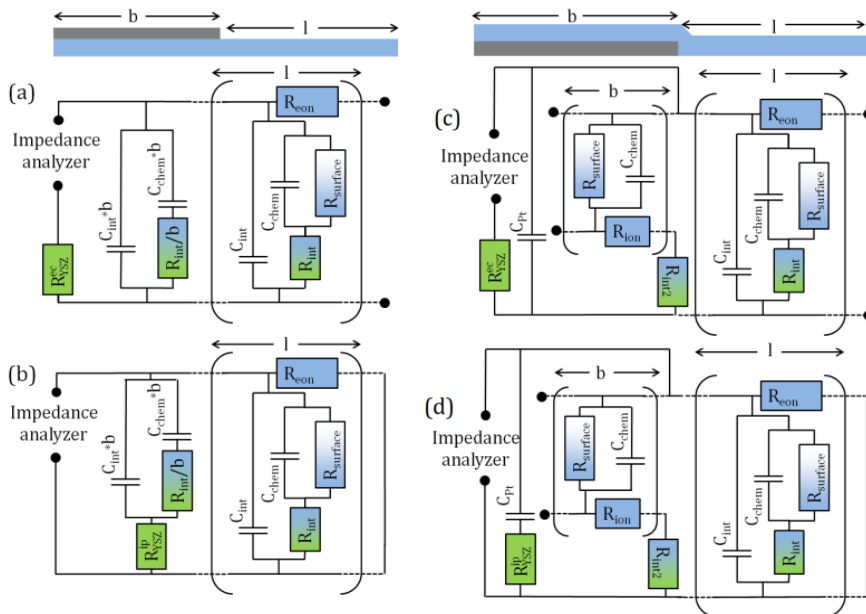


Figure 13. (a-b) Full equivalent circuits for electrodes with current collectors deposited on top of the current collectors: (a) electrochemical mode, (b) in-plane mode. (c-d) Full equivalent circuits for electrodes with embedded current collectors, also in (c) electrochemical and (d) in-plane mode. The elements  $R_{int}$ ,  $C_{int}$ ,  $C_{chem}$  and  $R_{surface}$  reflect area-specific resistances and capacitances,  $R_{eon}$  and  $R_{ion}$  are electronic and ionic sheet resistance, respectively.

### 3.3.2.4 Electrolyte resistance

Owing to the different current paths, the magnitude of the electrolyte resistance is very different in the electrochemical and in-plane mode and is treated differently in in-plane and electrochemical measurement mode. In the electrochemical mode, the entire measured current has to pass the electrolyte. Therefore, the electrolyte causes a simple resistive offset in this case (the element  $R_{YSZ}^{ec}$  in the final circuit - Figure 13a and c). In the DC-case of the in-plane mode, a pure electronic current path is possible with the electrolyte not playing any role. In the high frequency regime, however, ionic current in the electrolyte between two adjacent metal fingers may become relevant for the impedance. This ionic current is capacitively coupled to the current collecting fingers. An exact description would require numerical methods. For the absolute resistive contribution of the electrolyte being small compared to the in-plane DC resistance, which is the case for anodes with moderate or low electronic conductivity, an approximation can be made: The electrolyte resistance is placed in series to the capacitively coupled current path between the metal fingers (the element  $R_{YSZ}^{ip}$  in the final circuit - Figure 13b and d) – so it causes a resistive offset in the high-frequency regime and plays no role in the DC-case. If the electronic sheet resistance is very high (exceeding the condition in equation (24)), there will also be a DC ionic in-plane current in the electrolyte. However, in this case, the DC resistance of the in-plane mode will be orders of magnitude larger than the electrolyte resistance. The final equivalent circuits for in-plane and electrochemical modes differ in only two points: The right-hand side boundary of the free electrode transmission line is either an open end or a short circuit and the electrolyte resistance is treated differently. The according analytic impedance functions are given in the appendix (3.6.7).

### 3.3.2.5 Fitting routine

Given the rather complex circuits, concerns regarding overparametrisation may arise. This may indeed be a problem when only one measurement mode is used for fitting of experimental results. However, the derived equivalent circuits are valid for in-plane and electrochemical measurement on one and the same electrode and therefore include identical materials parameters. Both acquired impedance spectra can thus be simultaneously fitted with a single parameter set by minimizing the sum of squared relative errors for both spectra. Such a simultaneous fit of two different measurements strongly increases the significance of the fitting parameters in terms of accuracy and mechanistic interpretation, compared to the fitting of only one spectrum. This dual fit is key for being able to accurately deduce all relevant resistive and capacitive parameters which contribute to the electrode impedance. In-plane electronic and ionic charge transport affect the spectra of the electrochemical mode in a very similar manner, but

have very different consequences in the in-plane mode. Before running the fitting routine, the measured impedance spectra have to be corrected for the electrode geometry. For the electrochemical mode, the spectra are normalized to the total circumference of both metal fingers. In the in-plane mode, the impedance is normalized to the meander length between the fingers. At the borders of the mixed conducting electrode, the in-plane current density is zero, irrespective of the used measurement mode. This condition is equivalent to the electrochemical measurement mode. Accordingly, also the in-plane measurement includes a (small) contribution which corresponds to the circuit of the electrochemical measurement mode, caused by the open end boundary condition at the MIEC border. Since this contribution is proportional to the effective circumference of the MIEC layer, an according proportion of the current measured in the electrochemical mode has to be subtracted from the in-plane measurement. This is done even though the effect is rather small. After normalization to the metal finger circumference, the impedance has the unit of  $\Omega\text{cm}$ , such as the circuit model. The fitting parameters reflect area-specific capacitances and resistances for across-plane current ( $R_{\text{surface}}$ ,  $R_{\text{int}}$ ,  $C_{\text{chem}}$ ,  $C_{\text{Pt}}$ ,  $C_{\text{int}}$ ) and the electronic and ionic sheet resistance for the in-plane current ( $R_{\text{eon}}$  and  $R_{\text{ion}}$ ). Only the electrolyte resistances of both modes are not corrected for geometry. However, after a calibration (comparison with circular electrodes), they can be used to determine the ionic conductivity of the substrate. From a known conductivity-temperature relationship the electrode temperature can then be calculated <sup>36</sup>.

### 3.3.2.6 Simulated spectra for current collector above and beneath the electrode

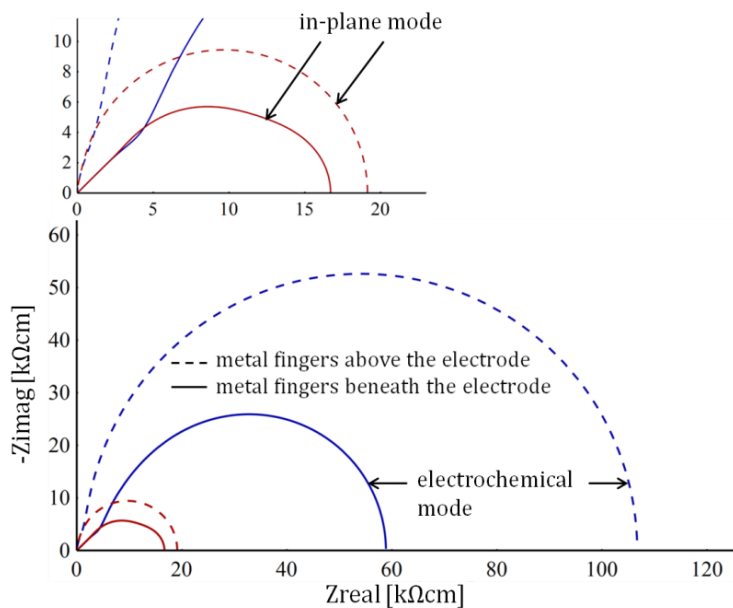


Figure 14. Simulated spectra for current collectors on top (dashed lines) and beneath the electrode (solid lines). The inset shows a magnification of the in-plane spectra.

The shape and size of impedance spectra is typically very different for in-plane and electrochemical mode and also strongly depends on the placement of the current collector and of course on the corresponding materials parameters. Examples of simulated spectra are shown in Figure 14. Typical values obtained in section 3.4 have been chosen for the main resistive, capacitive and geometric parameters (surface area-specific resistance (ASR):  $100 \text{ } \Omega\text{cm}^2$ , electronic resistivity:  $200 \text{ } \Omega\text{cm}$ , ionic resistivity:  $2000 \text{ } \Omega\text{cm}$ , chemical capacitance:  $5 \text{ mFcm}^{-2}$ , film thickness:  $100 \text{ nm}$ , metal finger width and distance:  $20 \text{ } \mu\text{m}$ ). Electrolyte as well as interfacial resistances and capacitances were set to 0 since they deliver only minor contributions to the impedance spectra considered in this study. The most obvious difference caused by the placement of the metal layer is a smaller DC resistance when the current collectors are beneath the electrode, which is caused by a larger area exposed to the atmosphere. Also these spectra exhibit more features. This was also experimentally confirmed (not shown) and indicates that this configuration is advantageous when aiming at the determination of all relevant electrochemical properties. For electrodes with metal fingers on top, the large chemical capacitance of the part covered by the current collectors is measured in parallel to the transmission line circuit of the free surface region. This parallel circuit disguises the Warburg-like impedance that is typically observed for transmission lines in the high-frequency range. Furthermore, the ionic conductivity is not relevant in the corresponding circuit model and thus not available. Also, the platinum current collectors may be catalytically active when placed on top of the MIEC, which might further complicate the analysis. In the experiments shown in the following, only electrodes deposited above the metal fingers have therefore been used. According to the circuit model, the electronic conductivity is measured in-plane above the YSZ substrate, while the ionic conductivity is measured in-plane above the current collector.

### 3.4 Experimental results and discussion

The suggested method for investigating mixed conducting electrodes in reducing atmosphere was applied to  $\text{SrTi}_{0.7}\text{Fe}_{0.3}\text{O}_{3-\delta}$  electrodes deposited on top of platinum current collectors (cf. section 3.2.2). In the following, we first show measured impedance spectra and discuss the origin of the different features. Then, the consistency of the new method is demonstrated by variations of the electrode geometry. Finally, information on the temperature dependence of the materials parameters is given.

### 3.4.1 Frequency dependence of the electrode polarization

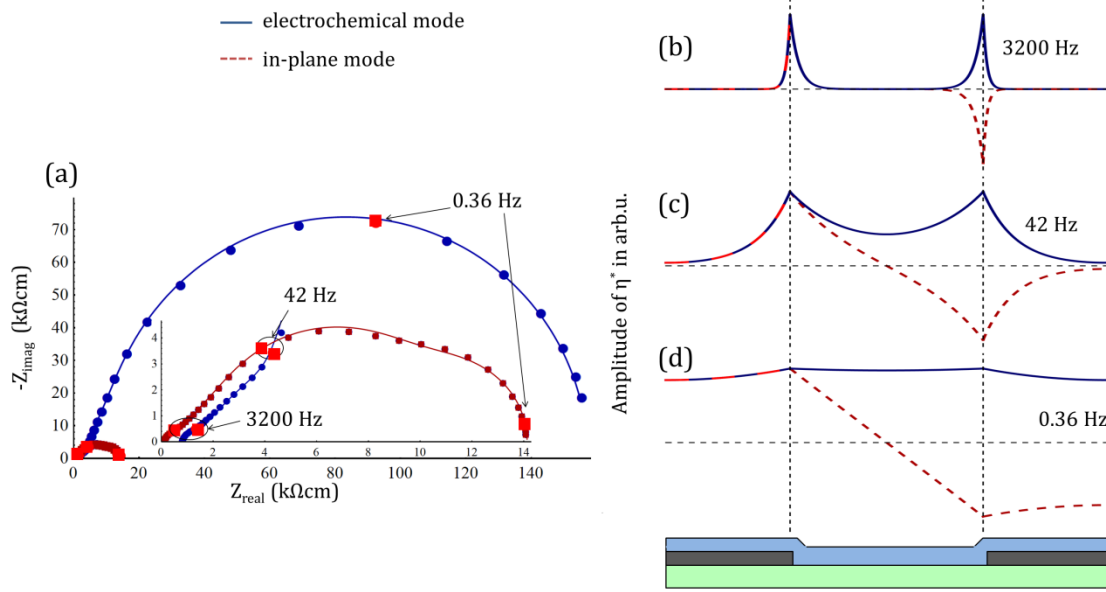


Figure 15. (a) Measured (symbols) and fitted (lines) impedance spectra of an electrode with 103 nm thickness and 11.6 mm finger distance at 660°C. (b–d) The calculated lateral distribution of the polarization potential is plotted for three different frequencies.

Figure 15a displays the in-plane and electrochemical impedance spectra after normalization, measured at 660°C with 11.7 μm finger distance and a STFO film thickness of 103 nm. Both spectra reveal several impedance features, partly semicircle-like and partly with 45° slopes in the Nyquist plot. The circuits derived in section 3.3 were used to simultaneously fit both spectra.

Nine parameters are considered in the equivalent circuits ( $R_{\text{surface}}$ ,  $R_{\text{int}}$ ,  $C_{\text{chem}}$ ,  $C_{\text{Pt}}$ ,  $C_{\text{int}}$ ,  $R_{\text{eon}}$ ,  $R_{\text{ion}}$ ,  $R_{\text{YSZ}}^{\text{ec}}$  and  $R_{\text{YSZ}}^{\text{ip}}$ ). In order to increase the numerical stability of the fitting routine, the electrolyte resistances ( $R_{\text{YSZ}}^{\text{ec}}$ ,  $R_{\text{YSZ}}^{\text{ip}}$ ) were determined from the resistive offset in the high-frequency region of the two measurement modes and set as fixed values during the fitting routine. Also the capacitance of the Pt-Ti-YSZ ( $C_{\text{Pt}}$ ) interface was found to be too large for a reliable determination of the STFO-YSZ interface capacitance, cf.  $C_{\text{int}}$  could therefore not be fitted and was fixed to 0 in the fitting routine. Hence, only six independent parameters were used to fit both spectra. ( $R_{\text{surface}}$ ,  $R_{\text{int}}$ ,  $C_{\text{chem}}$ ,  $C_{\text{Pt}}$ ,  $R_{\text{eon}}$ ,  $R_{\text{ion}}$ ).

The Nyquist plots in Figure 15a also show fit lines that demonstrate the accurate fit. In order to understand the mechanisms causing the shape of both spectra, the fit parameters and the circuit models were used to calculate the amplitude of the local polarization potential as a function of position and frequency. From this, an important conclusion can be drawn: The fraction of the electrode area which is polarized strongly depends on the frequency, as sketched in Figure 15b-d. This is understandable on a qualitative level: At

high frequencies (e.g. measurement at 3200 Hz, Figure 15b), oxygen exchange in the film is possible via charging and discharging of the chemical capacitance. Compared to this process, electronic and ionic in-plane charge transport exhibits comparatively high resistance. This results in a short attenuation length of the polarization potential. The impedance response of electrochemical and in-plane measurement in this frequency range is very similar (except for the electrolyte offset) and is mainly determined by the chemical capacitance and the electronic conductivity. At lower frequencies, the impedance of the chemical capacitance increases and the attenuation length becomes larger. For attenuation lengths comparable to or larger than the finger distance, the spectra of the two measurement modes become very different (below 42 Hz in Figure 15). The slightly asymmetric shape of the low-frequency semicircle in the electrochemical mode as well as the small low-frequency semicircle in the in-plane measurement (between 42 and 0.36 Hz) are related to the resistance of the in-plane current of oxygen ions on top of the current collectors.

For near-DC conditions oxygen exchange in the MIEC occurs primarily via the surface reaction, which is rate-limiting for the STFO electrodes used in this study. Therefore the polarization is nearly homogeneous along the electrode in the electrochemical mode. Accordingly, the main contribution to the DC-resistance of the electrochemical measurement is the surface reaction. For in-plane measurements, the polarization potential varies linearly and the DC-resistance is mainly given by the electronic sheet resistance. However, for a large distance between the current collector fingers or very low electronic conductivity, the attenuation length of the electrode polarization may be similar to or smaller than the finger distance in near-DC conditions. In this case, both spectra become very similar in shape and size (after normalization) and electron transport as well as oxygen exchange contribute to both spectra in the same way. This was also confirmed experimentally at lower temperature (not shown).

### **3.4.2 Geometry variations**

The derived equivalent circuits are applicable to electrodes of different thickness and metal finger distance. The size and shape of the spectra changes with geometry, but the deduced materials parameters should stay the same. In order to prove this, a sample with a 103 nm thick STFO film was prepared. Three different electrode geometries were realized on this sample: The width of the metal fingers was kept constant at 15  $\mu\text{m}$  and the metal finger distance was varied between 5, 11.6 and 25  $\mu\text{m}$ . Figure 16a depicts typical impedance spectra including the fit for these three metal finger distances. The quality of the fits is very good, given that there are only six independent parameters for the fit of two impedance spectra. The parameters determined for different geometries at a constant

temperature of 660°C are summarized in Figure 16b. Three different electrodes were measured and averaged for each finger distance.

Although some parameters (surface ASR and ionic resistivity) exhibit substantial scatter even for nominally identical electrodes and thus partly large error bars, the fitted materials parameters are independent of the exact electrode geometry. The accurate fit of the measurements, combined with the independence of the fitting parameters on the metal finger distance strongly suggests the validity of the model and the appropriateness of the method. Also the error of the fitting routine for one electrode is smaller than the corresponding standard deviation found for different microelectrodes, on one sample.

The measurements were repeated for a three times thicker film (310 nm) and they confirmed the consistency in terms of finger distance variation. The results of both film thicknesses are summarized in Table 2, averaged over all finger distances.

Many parameters (chemical capacitance, electronic resistivity and area-specific resistance (ASR) of the ionic interface) only slightly depend on the film thickness, however, some parameters show significant trends. The capacitance of the Pt-Ti-YSZ interface is considerably smaller for the 310 nm film. Moreover, the surface ASR is larger for the 103 nm film, but even nominally identical thin films exhibited similar scatter for this parameter. The (in-plane) ionic resistivity of the 310 nm film is significantly smaller. Electronic and ionic conductivity of the thicker film are in reasonable agreement with values measured on sintered pellets of similarly doped  $(\text{Sr}_{1-x}\text{Fe}_x)\text{TiO}_3$  <sup>60-61</sup>. Further investigations are required to understand the reasons behind the different ionic resistivity of the two films. For example, a thickness dependent microstructure might be the origin of the higher lateral ionic resistivity of the thinner film. In-plane tracer diffusion experiments could reveal further information on ionic transport properties but those are far from trivial to perform on thin films <sup>62-64</sup>. Moreover, four-point conductivity measurements <sup>65</sup> would be helpful as cross-check experiments but those require deposition of the films on an insulating substrate, which might affect the results. However, variation of the current collector geometry on the same thin film revealed consistent results in all fitting parameters.

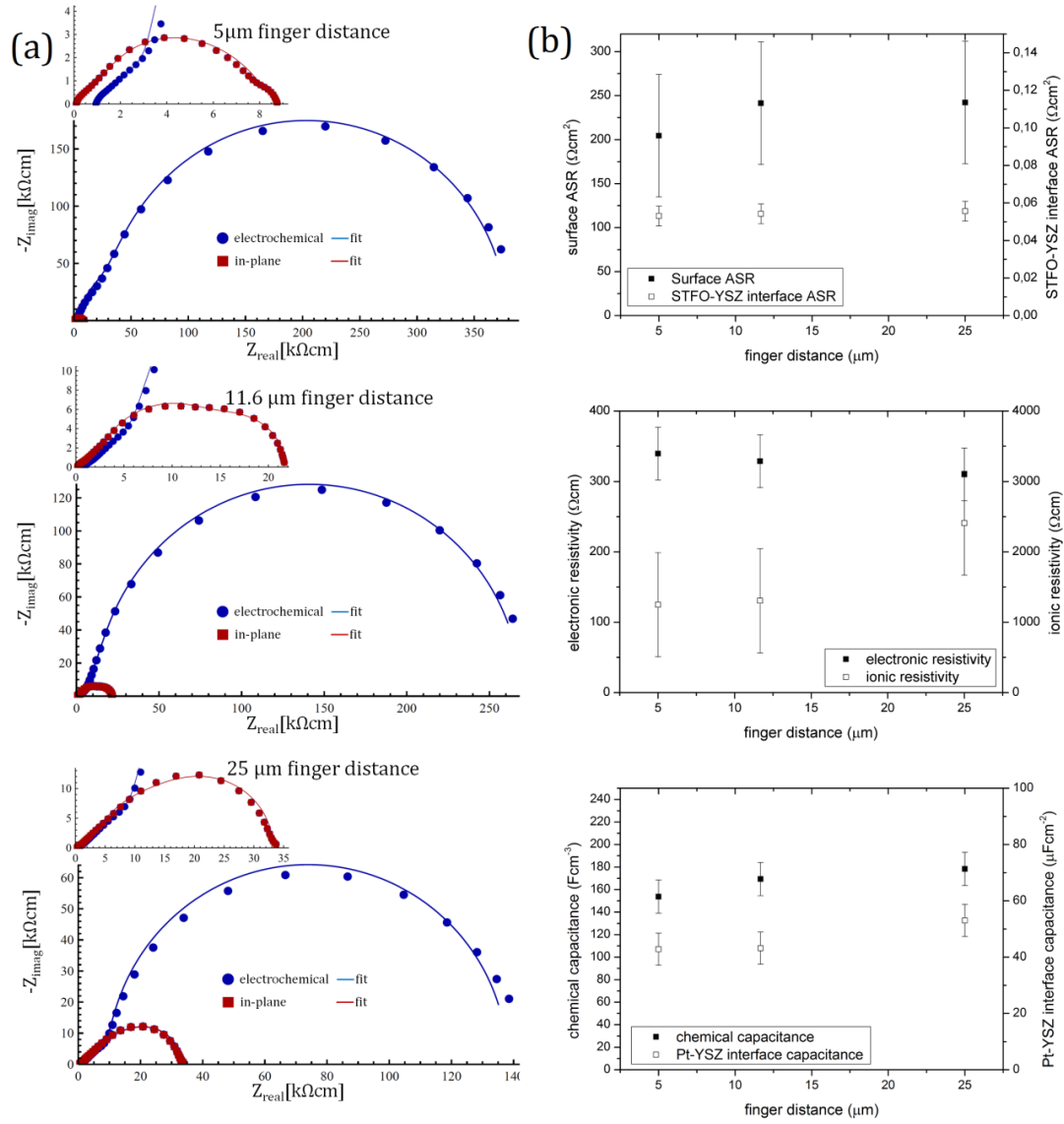


Figure 16. (a): Impedance spectra (symbols) including fit (lines) for a 103 nm thick STFO microelectrode with different finger distances at 660°C. The insets show magnifications emphasising the in-plane measurements. (b): Materials parameters of different electrodes at 660°C with a film thickness of 103 nm, deduced by fitting of the impedance spectra. The parameters are independent of the metal finger distance (ASR = area specific resistance).

Electrode property	103 nm film	310 nm film
Chemical capacitance ( $\text{Fcm}^{-3}$ )	$167 \pm 13$	$160 \pm 16$
Surface ASR ( $\Omega\text{cm}^2$ )	$229 \pm 62$	$137 \pm 42$
STFO-YSZ interface ASR ( $\Omega\text{cm}^2$ )	$0.054 \pm 0.005$	$0.055 \pm 0.007$
Pt-Ti-YSZ interface capacitance ( $\mu\text{Fcm}^{-2}$ )	$46 \pm 5$	$25 \pm 3$
Ionic resistivity ( $\Omega\text{cm}$ )	$1650 \pm 656$	$395 \pm 105$
Electronic resistivity	$326 \pm 33$	$291 \pm 70$

Table 2. Mean values of the fitting parameters and their standard deviation for two different thin film samples at 660°C.

### 3.4.3 Temperature dependence

All relevant resistive materials parameters of STFO anodes are thermally activated. The determination of these activation energies provides valuable information for both application and mechanistic interpretation. Even though it is not the scope of this chapter to perform a detailed study of these temperature dependences and their defect chemical interpretation, first results can be given and some activation energies can be estimated.

The activation energies of the different resistive parameters are listed in Table 3. Constant activation energy in the investigated temperature range can be observed for electronic and ionic resistivity. Interestingly, electronic and ionic resistivity differ by less than one order of magnitude. Chemical capacitance and interfacial capacitance (not shown) are also temperature-dependent, but not Arrhenius-type thermally activated. The increase of the chemical capacitance with increasing temperature probably reflects the increasing concentration of electronic and / or ionic defects. The surface reaction exhibits a rather low activation energy at low temperatures (<610°C), which increases strongly at elevated temperature. Such a result might be explained by two parallel reaction paths. However, also time-dependent changes of  $R_{\text{surface}}$  were observed (activation with increasing temperature and degradation when again decreasing the temperature). The Arrhenius plot therefore reflects both, temperature and time-dependent changes of the surface kinetics. Further investigations on this phenomenon are necessary for a detailed understanding.

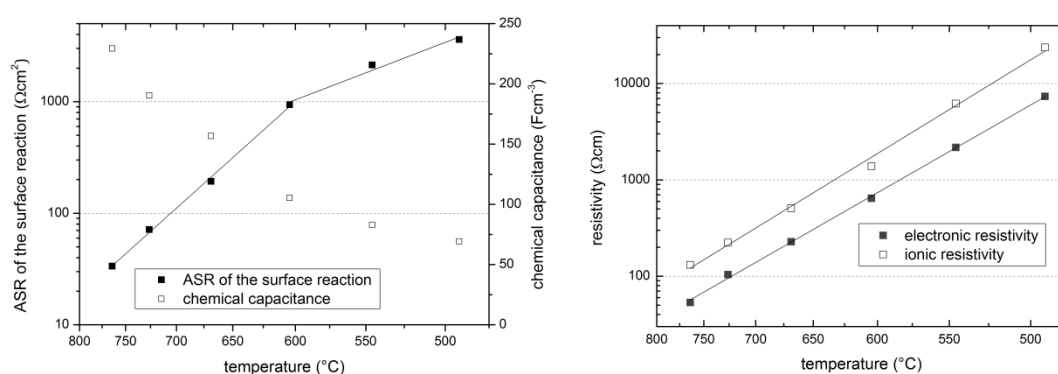


Figure 17. Arrhenius plot of the relevant resistive parameters and plot of the chemical capacitance between 490 and 760°C.

Resistive property	Activation energy
Electronic resistivity	$1.2 \pm 0.1$ eV
Ionic resistivity	$1.3 \pm 0.1$ eV
Surface ASR, $T < 610^\circ\text{C}$	$0.7 \pm 0.2$ eV
Surface ASR, $T > 610^\circ\text{C}$	$1.6 \pm 0.2$ eV
Ionic interface ASR	$1.2 \pm 0.2$ eV

Table 3. Activation energies of the resistive parameters, 310 nm film

### 3.4.4 Possibilities and restrictions

The novel method introduced in this chapter is expected to be applicable to a wide variety of mixed conductors, especially for materials with high electronic sheet resistance. However, if certain parameters are either very large or very small, the impedance response of the electrodes becomes insensitive to them. The most important value in this respect is the characteristic attenuation length of the polarization potential ( $l_a$ ) in the DC-case, which is related to the resistances of in-plane current and the surface reaction. It is given by

$$l_a = \sqrt{\frac{R_{surface}}{R_{sheet}}}, \quad (23)$$

with  $R_{sheet}$  being the ionic ( $R_{ion}$ ) or electronic ( $R_{eon}$ ) sheet resistance. If this length is much smaller than half of the metal finger distance, the center between the metal fingers is unpolarized in both measurement modes. Then the (geometry-corrected) impedance spectra for electrochemical and in-plane measurement become very similar and the fitting error strongly increases. For a reliable quantification of the ionic resistivity, the attenuation length above the metal fingers has to be larger than half of the metal finger width. For a typical thin film electrode with fine structured current collectors (thickness: 200nm, finger width and distance: 5 $\mu$ m), this leads to an upper limit of both electronic and ionic resistivity:

$$\rho[\Omega cm] < 320 cm^{-1} * R_{surface}[\Omega cm^2]. \quad (24)$$

For the electronic resistivity, there are also lower boundaries: if the DC resistance of the in-plane measurement is comparable or smaller than the corresponding electrolyte resistance, there exists no analytical model for the impedance response of the in-plane measurement. In this case, only its DC-value can be used to determine the electronic resistivity, but a simultaneous fit of two spectra is no longer possible. If the electronic conductivity is very high, which is the case for many mixed conducting cathodes in air ( $\gg 1$  S/cm), the resistance of the current collectors or a possible Schottky barrier between MIEC and metal (which was neglected so far) may become similar or even larger than the sheet resistance. In such a case, a large separation of the current collectors or a 4-point measurement that eliminates possible contact resistances (e.g. Van der Pauw method <sup>65</sup>) is required for the determination of the electronic sheet resistance. Accordingly, our novel approach is not considered to be a replacement of established methods, but rather a helpful complementary tool to investigate mixed conductors with properties typically occurring in reducing atmosphere.

### 3.5 Conclusions

Many mixed conducting oxide materials exhibit low electronic conductivity when placed in reducing atmosphere. Therefore, electronic and ionic charge transport as well as the electrochemical surface reaction can cause significant resistive contributions that lead to complex impedance spectra even for geometrically simple thin film electrodes. We developed a novel design of thin film microelectrodes with two interdigitating current collectors per electrode. This configuration enables two different measurement modes on one and the same microelectrode: an in-plane mode where the voltage is applied between both current collectors on one electrode and a conventional electrochemical measurement versus a macroscopic counter-electrode. An appropriate impedance model was developed for both measurement modes, based on two transmission lines representing a mixed conducting thin film either in contact with the current collector or the electrolyte. Both acquired impedance spectra can be simultaneously fitted to these equivalent circuits using a single parameter set. Hence, all relevant resistive and capacitive contributions can be quantified and a possible overparametrization of the model is avoided. A more detailed analysis showed that the polarization potential, which is related to the local chemical potential of oxygen, varies laterally in the mixed conductor. This variation strongly depends on the measurement mode as well as the frequency. This method was successfully employed to  $\text{SrTi}_{0.7}\text{Fe}_{0.3}\text{O}_{3-\delta}$  anodes, where electronic and ionic conductivity, ASR of the surface reaction, chemical capacitance and the resistance of the electrode-electrolyte interface could be determined on a single thin film electrode with comparatively small experimental effort. However, it was also shown that this approach is only applicable for a limited parameter range in terms of ionic and electronic conductivity. Acceptor-doped mixed conductors in reducing atmosphere are often within this parameter range and our method is expected to be particularly helpful for analyzing such materials.

## 3.6 Mathematical derivation of the equivalent circuit

### 3.6.1 Polarization of a mixed conducting electrode without transport losses

As a starting point, the polarization of a mixed conducting microelectrode (working electrode) with rate limiting surface kinetics and negligible losses in the electrolyte is briefly discussed. When neglecting resistive losses in the electrolyte and counter-electrode, the electrochemical potential of oxygen ions ( $\tilde{\mu}_{ion}$ ) remains unchanged in working electrode, counter electrode and electrolyte, ( $\Delta\tilde{\mu}_{ion} = 0$ ). The electrochemical potential of electrons in the working electrode is defined by the voltage applied to the current collector ( $\Delta\tilde{\mu}_{eon}^{ode} = -FU_0$ ). Consequently, the chemical potential of oxygen in the electrode ( $\Delta\mu_O^{ode}$ ) given by

$$\Delta\mu_O^{ode} = \Delta\tilde{\mu}_{ion}^{ode} - 2\Delta\tilde{\mu}_{eon}^{ode} = 2FU_0 . \quad (25)$$

Therefore the polarization potential  $\eta^*$  (equation (20)) equals the applied voltage  $U_0$ .

### 3.6.2 Relation between polarization potential and current

When charge transport losses in a thin film MIEC play a significant role, the polarization potential ( $\eta^*$ ) also varies in-plane. For a thin film MIEC on either an electronic or an ionic conductor, a direct relation between in-plane currents and polarization potential can be established. The electric current density  $j_k$  of a charge carrier  $k$  with charge number  $z_k$  is proportional to the gradient of its electrochemical potential and conductivity  $\sigma_k$ . For gradients only along the in-plane coordinate of a MIEC film, this can be expressed by

$$j_k = -\frac{d\tilde{\mu}_k}{dx} \frac{1}{z_k F \rho_k} . \quad (26)$$

(i) For a MIEC on an ionic conductor, the polarization potential was defined as (see equation (20))

$$\eta^{*yte} = \frac{\Delta\tilde{\mu}_{ion}^{yte} - 2\Delta\tilde{\mu}_{eon}^{ode}}{2F} . \quad (27)$$

The electrochemical potential of ions in the electrolyte is assumed to be laterally homogeneous due to its high ionic conductivity and much larger thickness compared to the MIEC film. Differentiating equation (27) with respect to the spatial coordinate ( $x$ ) and combining it with equation (26), one obtains

$$\frac{d}{dx} \eta^{*yte}(x) = \frac{d}{dx} \frac{-\tilde{\mu}_{eon}^{ode}(x)}{F} \quad (28)$$

$$\frac{d}{dx} \eta^{*yte}(x) = -j_{eon} \rho_{eon} . \quad (29)$$

Only the current density integrated along the film thickness ( $d$ ) is measurable and can be related to the electronic sheet resistance ( $R_{eon}$ ). When assuming homogeneous electronic conductivity within the entire film, equation (29) transfers to

$$\frac{d}{dx} \eta^{*yte}(x) = -I_{eon} R_{eon} \quad (30)$$

with

$$R_{eon} = \frac{\rho_{eon}}{d} \quad (31)$$

And the current per electrode length

$$I_{eon} = d j_{eon} . \quad (32)$$

**(ii)** For a MIEC film on an electronic conductor, the polarization potential was defined as (see equation (21)):

$$\eta^{*metal} = \frac{\Delta \tilde{\mu}_{ion}^{ode} - 2 \Delta \tilde{\mu}_{eon}^{metal}}{2F} . \quad (33)$$

This expression can be differentiated with respect to the spatial coordinate and combined with equation (26):

$$\frac{d}{dx} \eta^{*metal}(x) = \frac{d}{dx} \frac{\tilde{\mu}_{ion}^{ode}(x)}{2F} \quad (34)$$

$$\frac{d}{dx} \eta^{*metal}(x) = j_{ion} \rho_{ion} \quad (35)$$

Analogous to the case discussed above, we obtain

$$\frac{d}{dx} \eta^{*metal}(x) = I_{ion} R_{ion} , \quad (36)$$

$$R_{ion} = \frac{\rho_{ion}}{d} , \quad (37)$$

$$I_{ion} = j_{ion} d . \quad (38)$$

$R_{ion}$  is the ionic sheet resistance. The different signs in equation (30) and (36) indicate that electronic current (in technical direction) is directed towards lower polarization potential, while ionic current is directed towards higher polarization potential. This result may seem confusing, but the polarization potential does not reflect an electrostatic potential. Rather it can be related to the chemical potential of oxygen and different flux directions are well known from chemical diffusion (see Ref<sup>66</sup> and section 3.6.3).

### 3.6.3 Impedance of the generalized transmission lines

The generalized transmission line circuits in Figure 10 are applicable to thin films in which transport losses occur in only one spatial direction, and the electrochemical potential of the “fast” charge carrier is homogeneous in its fast phase. This is the case for our electrodes with a thin film MIEC being deposited either on an ionic or an electronic conductor. In impedance measurements, the current at the terminals of the electronic rail is measured. For a MIEC on the current collector it is therefore appropriate to consider the electronic current in the current collector rather than the ionic current in the MIEC. The electronic current is exactly opposite to the ionic one ( $I_{eon}(x) = -I_{ion}(x)$ ), as visible in the circuit model in Figure 11b,c). Hence, a single equation can describe charge transport in both situations, MIEC on the current collector and MIEC on the electrolyte. It reads

$$\frac{d}{dx} \eta^* = -R_{sheet} I_{eon}(x) \quad (39)$$

and represents equation (30) and (36). The sheet resistance  $R_{sheet}$  is either electronic (for MIEC on electrolyte) or ionic (for MIEC on metal). Apart from its influence on in-plane charge transport, the polarization potential is also the driving force of across-plane currents and the surface reaction. The relation between polarization potential, in-plane currents and across-plane currents can be quantified by a one dimensional continuity equation

$$\frac{d}{dx} I_{eon} = -Y_{ap} \eta^*(x) . \quad (40)$$

The source term  $Y_{ap} \eta^*$  describes the local across-plane current density of the polarization-driven electrochemical reactions (e.g. surface reaction and charging of the chemical capacitance). The across-plane admittance  $Y_{ap}$  is here treated on a black-box level, it is adopted to certain situations in sections 3.3.2.1 and 3.3.2.3. Equations (39) and (40) result from the laws of charge transport and reactions that are driven by the local polarization potential, without the use of an equivalent circuit. The generalized transmission line circuit is therefore a graphical representation of these processes that can be described by equivalent equations.

The two equations describing the generalized transmission line can be combined by differentiating equation (39) and we obtain

$$\frac{d^2}{dx^2} \eta^*(x) = -R_{sheet} \frac{d}{dx} I_{eon}(x) = R_{sheet} Y_{ap} \eta^*(x) . \quad (41)$$

With an exponential ansatz, the general solution can be found.

$$\eta^*(x) = A e^{\gamma x} + B e^{-\gamma x} \quad (42)$$

$$I_{eon}(x) = -\frac{A\gamma e^{\gamma x} - B\gamma e^{-\gamma x}}{R_{sheet}} \quad (43)$$

$$\gamma = \sqrt{R_{sheet}Y_{ap}} \quad (44)$$

The parameters A and B are determined by the polarization potentials of the left and right hand side terminal, which depend on the measurement mode. For our electrode design, the edges of the metal fingers are the boundaries of the transmission line. At these points, lateral electronic or ionic charge transport within the electrode is not required and the polarization potential for both transmission lines can be calculated as

$$\eta^* = U_0 - \eta_{terminal} \quad (45)$$

$\eta_{terminal}$  reflects the overpotential in the terminal parts caused by the circuit elements  $R_{int2}$  and  $R_{VSZ}$  in Figure 13. Without loss of generality,  $\eta_{terminal} = 0$  can be assumed in the following calculation of the transmission line impedance.

### 3.6.4 Symmetric terminal polarization

Symmetric terminal polarization means equal polarization potential on the left and right hand side of a generalized transmission line. This is the case for the free MIEC area in the electrochemical measurement mode. Also electrodes deposited on top of the metal fingers exhibit symmetrical terminal polarization for the MIEC above the current collector. For a transmission line with a length of  $2l$  and  $x=0$  in the center between the terminals these conditions read:

$$\eta^*(-l) = U_0, \quad \eta^*(l) = U_0 \quad (46)$$

With these boundary conditions, equation (42) can be solved as

$$\eta^*(x) = U_0 * \frac{\cosh(\gamma x)}{\cosh(\gamma l)} \quad (47)$$

And the resulting in-plane current is given by

$$I_{eon}(x) = \frac{U_0}{R_{sheet}} * \frac{\sinh(\gamma x)}{\cosh(\gamma l)} \quad (48)$$

Equation (48) exhibits zero in-plane current in the center ( $I_{eon}(0) = 0$ ). Therefore an open end terminal in the center of the transmission line is equal to symmetric boundary conditions, which is depicted in Figure 11b.

In impedance spectroscopic measurements, the spatial distribution of current and potential remains on a black box level. Only the length-specific total impedance ( $Z$ ) can be measured at the terminals. In the symmetrical case this is given by

$$Z_{sym} = \frac{\eta^*(-l)}{I(-l)} = \frac{R_{sheet}}{\gamma} \coth(\gamma l) . \quad (49)$$

### 3.6.5 Asymmetric terminal polarization

Asymmetric terminal polarization means opposite polarization of the left and right hand side terminals. This is found for the free surface area in the in-plane measurement mode and can be represented by

$$\eta^*(-l) = U_0 , \quad \eta^*(l) = -U_0 . \quad (50)$$

Under these boundary conditions, the solution of equation (42) is given by

$$\eta^*(x) = U_0 * \frac{\sinh(\gamma x)}{\sinh(\gamma l)} . \quad (51)$$

In analogy to section 3.6.4, the measurable length-specific impedance in the asymmetric case is given by

$$Z_{asym} = \frac{\eta^*(-l)}{I(-l)} = \frac{R_{sheet}}{\gamma} \tanh(\gamma l) . \quad (52)$$

Equation (51) exhibits zero polarization potential in the center ( $\eta^*(0)=0$ ), which is equal to a short-circuit terminal in the center, as depicted in Figure 11c.

### 3.6.6 Infinite length boundary conditions

The characteristic attenuation length of  $\eta^*$  in a transmission line is  $\text{real}(\gamma^{-1})$ . Hence,  $\text{real}(\gamma l)$  is the ratio between the lateral feature size of an electrode and the charge carrier diffusion length. When the attenuation length is much smaller than the lateral feature size ( $\text{real}(\gamma l) \gg 1$ ), the impedance functions for symmetric and asymmetric boundary conditions converge against the solution for an infinitely long transmission line. An example is the Gerischer impedance. We then obtain

$$\tanh(\gamma l) \approx \coth(\gamma l) \approx 1 \quad | \quad \text{real}(\gamma l) \gg 1 . \quad (53)$$

With this approximation, equations (49) and (52) lead to

$$Z_{inf} = \sqrt{\frac{R_{sheet}}{Y_{ap}}} . \quad (54)$$

This situation can be found in the high-frequency region of the impedance spectra of typical mixed conducting anodes (see section 3.4.1). In the DC-case, infinite length boundary

conditions occur in the case of very large separation of the metal fingers as well as for very low electronic conductivity.

The same approximation is also applicable to a special part of our system: When the electrode is deposited above the current collectors, the oxygen ions flowing in the region above the current collectors still have to pass the electrode-electrolyte interface, as sketched in Figure 8, left. This interfacial resistance has to be treated as a terminal part, which can be approximated by a transmission line consisting of the ionic sheet resistance  $R_{ion}$  and the MIEC-electrolyte interface resistance  $R_{int}$ . For typical parameters (small ionic interface resistance and moderate ion conduction) the attenuation length in this transmission line is small and infinite length boundary conditions are applicable. According to equation (52), this can be expressed as

$$R_{int2} = \sqrt{R_{ion}R_{int}} . \quad (55)$$

$R_{int}$  is the area specific ionic resistance of the MIEC/electrolyte interface,  $R_{ion}$  is the ionic sheet resistance and  $R_{int2}$  is the terminal resistance of the left hand side transmission line depicted in Figure 13.

### 3.6.7 Analytic functions for electrochemical and in-plane impedance

The circuits derived in section 3.3.2 can finally be expressed by analytical impedance functions, which were used for fitting and are given here. For a parallel circuit, the following abbreviation will be used:  $Z1||Z2 = Z1 Z2/(Z1 + Z2)$ . The symbols have the meanings of the equivalent circuit elements in Figure 13,  $\omega$  is the angular frequency,  $b$  and  $l$  are half of the metal finger width and half of the metal finger distance, respectively.

#### MIEC above the current collector

The according circuits are depicted in Figure 13.  $Z_{free}$  and  $Z_{metal}$  are the inverse of the area specific across-plane admittance ( $Y_{ap}^{-1}$ ) for the free MIEC area and above the current collector, respectively. The impedance of the electrochemical mode ( $Z_{ec}$ ) is given by

$$Z_{ec} = R_{YSZ}^{ec} + \frac{1}{i\omega C_{Pt} * b} \parallel \left( \sqrt{R_{eon} Z_{free}} * \coth \left( \sqrt{\frac{R_{eon}}{Z_{free}}} * l \right) \parallel \left( \sqrt{R_{ion} Z_{metal}} * \coth \left( \sqrt{\frac{R_{ion}}{Z_{metal}}} * b \right) + \sqrt{R_{int}R_{ion}} \right) \right) \quad (56)$$

with

$$Z_{free} = \frac{1}{i\omega C_{int}} \parallel \left( R_{int} + \left( R_{surface} \parallel \frac{1}{i\omega C_{chem}} \right) \right) \quad (57)$$

and

$$Z_{metal} = R_{surface} \parallel \frac{1}{i\omega C_{chem}}. \quad (58)$$

The impedance of the in-plane ( $Z_{ip}$ ) mode differs only in the treatment of the electrolyte resistance and in the boundary conditions for the free MIEC area (asymmetric boundary conditions lead to a hyperbolic tangent function in the corresponding transmission line impedance). Equation (59) is corrected, as the coth and tanh functions were switched in the original publication<sup>52</sup>.

$$Z_{ip} = \left( R_{YSZ}^{ip} + \frac{1}{i\omega C_{pt} * b} \right) \parallel \left( \sqrt{R_{eon} Z_{free}} * \tanh \left( \sqrt{\frac{R_{eon}}{Z_{free}}} * l \right) \parallel \left( \sqrt{R_{ion} Z_{metal}} * \coth \left( \sqrt{\frac{R_{ion}}{Z_{metal}}} * b \right) + \sqrt{R_{int} R_{ion}} \right) \right). \quad (59)$$

### MIEC beneath current collectors

The impedance of the circuit in Figure 13 in the electrochemical mode ( $Z_{ec}$ ) is given by

$$Z_{ec} = R_{YSZ}^{ec} + \sqrt{R_{eon} Z_{free}} * \coth \left( \sqrt{\frac{R_{eon}}{Z_{free}}} * l \right) \parallel \frac{1}{b} * \left( \frac{1}{i\omega C_{int}} \parallel \left( R_{int} + \frac{1}{i\omega C_{chem}} \right) \right). \quad (60)$$

$Z_{free}$  is in accordance with equation (57). Also here, the impedance of the in-plane mode ( $Z_{ip}$ ) differs only in the treatment of the electrolyte resistance and in the boundary conditions of the free MIEC area, which is expressed by

$$Z_{ip} = \sqrt{R_{eon} Z_{free}} * \tanh \left( \sqrt{\frac{R_{eon}}{Z_{free}}} * l \right) \parallel \left( R_{YSZ}^{ip} + \frac{1}{b} * \left( \frac{1}{i\omega C_{int}} \parallel \left( R_{int} + \frac{1}{i\omega C_{chem}} \right) \right) \right). \quad (61)$$



## 4 The electrochemical properties of $\text{Sr}(\text{Ti},\text{Fe})\text{O}_{3-\delta}$ for solid oxide fuel cell anodes

### 4.1 Introduction

Reduction stable mixed conductors may be applicable in SOFC anodes. Several mixed conductors, such as acceptor doped  $(\text{La},\text{Sr})(\text{Cr},\text{Mn})\text{O}_3$ <sup>15-18</sup>, donor-doped  $\text{SrTiO}_3$ <sup>12, 67</sup> and recently  $\text{Sr}(\text{Ti},\text{Fe})\text{O}_{3-\delta}\text{-Ce}_{0.9}\text{Gd}_{0.1}\text{O}_{2-\delta}$  (STF-GDC) composites<sup>13</sup> were investigated in form of porous SOFC anodes. For STF-GDC composites, the anode polarization resistance was  $<0.2 \Omega\text{cm}^2$  at  $800^\circ\text{C}$ , and the polarization resistance decreased with higher Fe content. The extraction of materials parameters such as electronic and ionic conductivity from porous electrodes is, however, not straightforward. Thin film model electrodes allow better insight into fundamental processes, but such studies of the polarization mechanisms in reducing atmospheres are still largely missing on most mixed conducting SOFC anode materials, except for (Gd or Sm) doped ceria<sup>23-24, 26, 53, 68-69</sup>.

In chapter 3 a special electrode geometry was developed for separating the different resistive effects in weakly electron conducting electrode materials and this technique was first applied to  $\text{SrTi}_{0.7}\text{Fe}_{0.3}\text{O}_{3-\delta}$  thin film electrodes<sup>52</sup>.

This chapter focusses on the electrochemical properties of model thin film electrodes of  $\text{Sr}(\text{Ti},\text{Fe})\text{O}_{3-\delta}$  (STF) with 30 and 70 mol% Fe doping. STF is a well suited model material, because its conductivity and performance as a SOFC cathode material<sup>60-61, 70-74</sup> is well characterized, and higher Fe content increases both oxygen exchange activity and conductivity in air. Electrochemical impedance spectroscopy was used to quantify the oxygen exchange activity, as well as electronic and ionic conductivity of the STF thin film electrodes. Lithographically patterned Pt current collectors were applied on top or beneath the STF thin film to compensate the comparatively low electronic conductivity in reducing conditions<sup>52, 60</sup>. The new electrode design presented in chapter 3 with two interdigitating current collectors on each electrode allows measurements which are optimized for determining the ionic and electronic conductivity and oxygen exchange resistance.

## 4.2 Experimental

Thin film electrodes of  $\text{SrTi}_{0.3}\text{Fe}_{0.7}\text{O}_{3-\delta}$  (STF37) and  $\text{SrTi}_{0.7}\text{Fe}_{0.3}\text{O}_{3-\delta}$  (STF73) were prepared by pulsed laser deposition (PLD), using a KrF excimer laser (Lambda COMPexPro 201F, 248 nm wavelength). Deposition was performed at 650°C substrate temperature with the laser operating at 400 mJ, 5 Hz for 30 minutes, resulting in a final film thickness of approx. 120 nm for STF37 and 170 nm for STF73. Either [100] oriented 9.5 mol%  $\text{Y}_2\text{O}_3$  doped Zirconia (YSZ) single crystals or [100] oriented MgO single crystals were used as substrates. The target powders were prepared via solid state reaction of appropriately weighed  $\text{SrCO}_3$ ,  $\text{Fe}_2\text{O}_3$  and  $\text{TiO}_2$  powders and sintering in air at 1400°C.

For a better electrical contact micro-patterned current collectors, consisting of 75 nm sputtered Pt and ~5 nm Ti adhesion layer, were either deposited on top of the STF film or embedded between substrate and STF, and structured using photolithography. The various resulting sample geometries are summarized in Figure 18.

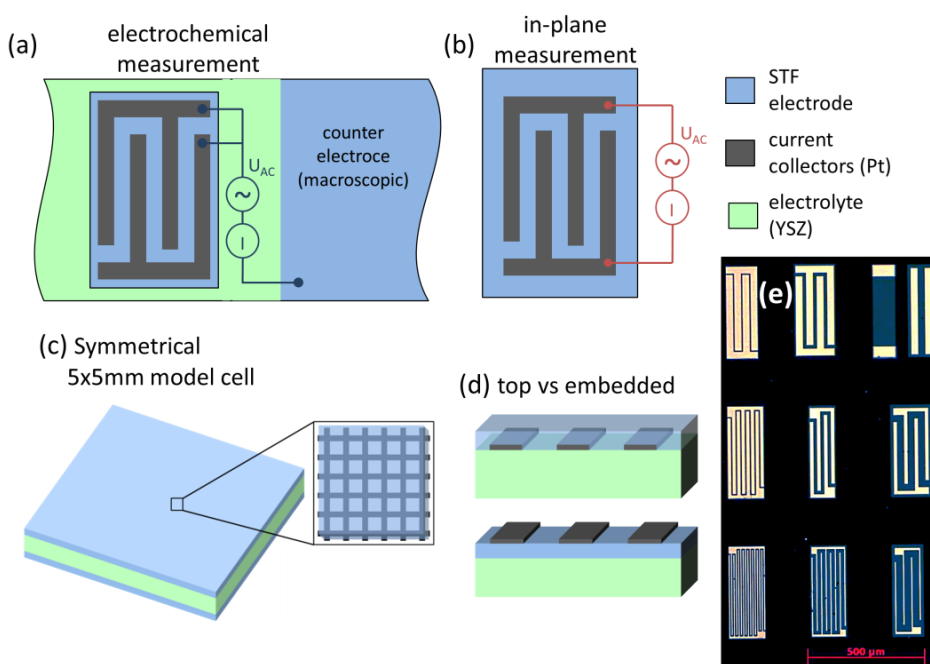


Figure 18. Types of investigated samples: (a) Microelectrode with current collectors on YSZ in electrochemical contacting mode. (b) Continuous STF thin film with embedded current collectors on MgO for in-plane conductivity measurements. (c) Symmetrical 5x5mm cell used for temperature-dependent measurements. (d) Sketch thin films with top and embedded current collectors. (f) Micrograph of microelectrodes with the 9 investigated current collector geometries.

### **Samples with microelectrodes**

Samples with microelectrodes were fabricated by application of the patterned current collector and deposition of the STF thin film on  $10 \times 10 \times 0.5$  mm<sup>3</sup> YSZ substrates. Subsequently, rectangular microelectrodes and macroscopic counter electrodes were prepared by photolithography and argon ion beam etching. Each microelectrode contains two current collectors, as shown in Figure 18a. In the electrochemical mode the entire microelectrode is polarized against the larger counter electrode. Equivalent circuit models for these measurement modes were derived in section 3. The width and distance between the current collecting fingers were both varied between 5, 15 and 30  $\mu$ m, resulting in a total of 9 different current collector geometries that are shown in Figure 18e. Microelectrodes of all 9 geometries were investigated in an asymmetrically heated, gas tight micro-contact measurement chamber and contacted with gold-plated steel tips, using piezoelectric manipulators. A ceramic heating stage (Linkam TMS 1000) was used to heat the samples up to  $\sim 650^\circ\text{C}$  in humidified Ar-H<sub>2</sub> (Alphagaz Arcal 10), containing 25 mbar H<sub>2</sub> and ca. 18 mbar H<sub>2</sub>O. Furthermore, such samples were characterized in a tube furnace setup with precisely controlled, homogeneous temperature<sup>57</sup> in varying H<sub>2</sub>:H<sub>2</sub>O mixing ratio.

### **STF thin films on MgO substrates**

STF thin films on MgO substrates were used for in-plane conductivity measurements and fabricated similar to the samples with microelectrodes, only structuring of the STF layer was omitted, because the current is anyway restricted to the region between the current collecting fingers, see Figure 18b. These samples were characterized by impedance spectroscopy in a tube furnace setup at  $650^\circ\text{C}$  under varying H<sub>2</sub>:H<sub>2</sub>O mixing ratio.

### **Symmetrical samples with 'macroscopic' electrodes**

Symmetrical samples with 'macroscopic' electrodes were prepared by symmetrical deposition of STF electrodes with embedded current collectors on YSZ substrates, as sketched in Figure 18c. Sample dimensions were  $5 \times 5 \times 0.5$  mm<sup>3</sup> and the current collector was structured as a fine structured grid (4  $\mu$ m stripes, 11  $\mu$ m holes). The symmetrical model cells were characterized by impedance spectroscopy in a homogeneously heated tube furnace setup in a temperature range of  $350$ - $800^\circ\text{C}$ , again using humidified Ar-H<sub>2</sub> mixture. All impedance measurements were performed with a Novocontrol Alpha-A impedance analyzer at 10 mV RMS.

## 4.3 Results and Discussion

### 4.3.1 In-plane conductivity of STF

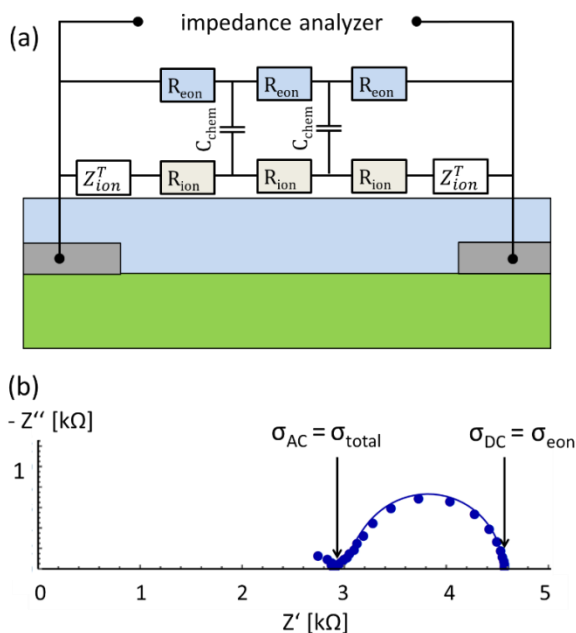


Figure 19. (a) Equivalent circuit used to fit the in-plane measurements on MgO substrates. (b) Impedance spectrum (circles) and fit (solid line) of an in-plane measurement of STF37 at 650°C.

The electronic and ionic in-plane conductivity of STF37 and STF73 thin films on insulating magnesia substrates was measured by impedance spectroscopy, using interdigitating embedded current collectors, as sketched in Figure 18b. The impedance spectra were measured at 650°C in different H<sub>2</sub>:H<sub>2</sub>O mixtures. A typical spectrum recorded on STF 37 is shown in Figure 19 (circles). It consists of the onset of a distorted high frequency arc, which is caused by the geometric capacitance (not considered in the fit), and a well separated low frequency feature. The latter deviates from an ideal semicircle, partly resembling a 45° Warburg type impedance, indicative for a diffusive process.

Additional variation of the finger distance (between 5 and 30 μm) revealed a linear increase of the measured resistances with finger distance, showing that in-plane conduction is predominant and surface exchange processes have a negligible impact. In such a case, the high frequency axis intercept should correspond to the total conductivity, while the low frequency limit resistance only reflects the electronic conductivity, due to the ion blocking electrodes. This very simple first analysis, also sketched in Figure 19b yields essentially the same conductivity values as fitting to the impedance model discussed in the following.

An equivalent circuit model for an STF film on an insulating substrate is shown in Figure 19a, and it includes a transmission line with an ionic (ion) and an electronic (eon) rail,

which are coupled via chemical capacitors. This circuit model including analytical impedance functions was derived in Ref <sup>69</sup>, with electronic and ionic terminal impedances still to be specified. In our case the high electronic conductivity of the current collector allows to treat the electronic terminal as a short circuit. Oxygen ions, on the other hand, cannot be exchanged at the current collector interface. The typical treatment of an (ion) blocking electrode would be a capacitor in the ionic rail. However, in our specific case the current collectors are parallel to the thin film plane. Hence also in-plane migration of oxygen ions on top of the current collector may take place and this was considered by an open Warburg impedance as terminating element. After normalization to sheet resistances, its impedance is

$$Z_{ion}^T = R_{ion} * \frac{\coth\left(\frac{w_{finger}}{2} \sqrt{i\omega C_{chem} R_{ion}}\right)}{\sqrt{i\omega C_{chem} R_{ion}}}. \quad (62)$$

$R_{ion}$  is the ionic sheet resistance (resistivity divided by film thickness),  $C_{chem}$  the area-specific chemical capacitance and  $w_{finger}$  is the width of the current collecting finger.

Although the circuit model looks rather complex, only three fit parameters are used (ionic and electronic conductivity, and chemical capacitance), if the in-plane ionic conductivity and chemical capacitance of the thin film is assumed independent of the substrate (current collector or MgO).

These in-plane conductivity measurements were carried out in different H<sub>2</sub>:H<sub>2</sub>O mixing ratios at 650°C, corresponding to a pO<sub>2</sub> range of about 10<sup>-25</sup> to 10<sup>-21</sup> bar, and fitted to the equivalent circuit model discussed above. Simple reading of AC and DC resistances, indicated in Figure 19b yielded the same conductivities, but no capacitance values.

The results are discussed in terms of following point defect model for STF: Electronic and ionic conductivity, as well as chemical capacitance are governed by the concentrations and mobilities of oxygen vacancies ( $V_O^{\bullet\bullet}$ ) and electronic defects, which correspond to different oxidation states of Fe: Fe<sup>2+</sup>( $Fe_{Ti}''$ ), Fe<sup>3+</sup>( $Fe_{Ti}'$ ) and formally also Fe<sup>4+</sup>( $Fe_{Ti}^{\times}$ ). The results presented here, as well as XPS<sup>43</sup> and thermogravimetric measurements<sup>42</sup> support the model of non-interacting, localized point defects. In the low pO<sub>2</sub> regime, Fe in STF is mainly present as Fe<sup>3+</sup>, and the defect charge is largely compensated by oxygen vacancies, making them the majority charge carrier,  $[V_O^{\bullet\bullet}] \approx 0.5[Fe_{Ti}']$ , see also section 2.3.2.

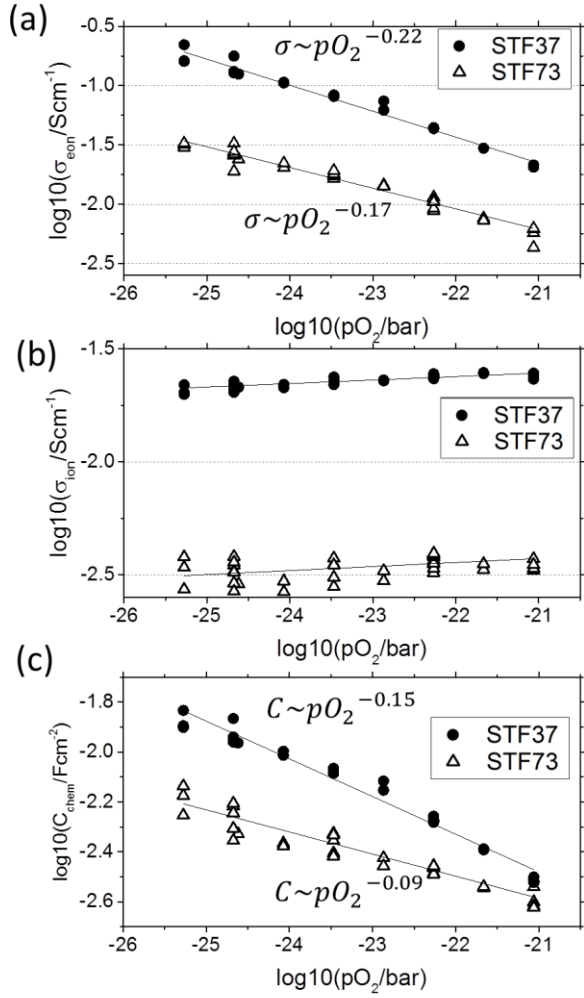


Figure 20. Electronic conductivity (a), ionic conductivity (b) and chemical capacitance (c) of STF37 and STF73 at 650°C in varying H<sub>2</sub>:H<sub>2</sub>O mixing ratio, plotted as a function of pO<sub>2</sub>.

In this defect regime ( $\log([V_O^{\bullet\bullet}]) \approx const$  and  $\log([Fe_{Ti}'] ) \approx const$ ), the concentration of 'electrons' ( $Fe_{Ti}''$ ) as the minority charge carrier with a concentration in the order of few % of  $[Fe_{total}]$ <sup>42-43</sup> should have a simple dependence on pO<sub>2</sub>

$$[Fe_{Ti}''] \sim pO_2^{-\frac{1}{4}}. \quad (63)$$

Most likely, a  $Fe_{Ti}''$  polaron hopping mechanism causes the moderate electronic conductivity ( $\sigma_{eon}$ ), which is then proportional to the  $Fe_{Ti}''$  concentration and hence to pO<sub>2</sub><sup>0.25</sup>. Moreover, the chemical capacitance per cm<sup>3</sup> is expected to be proportional to  $[Fe_{Ti}'']$  via the relation<sup>75</sup>

$$C_{chem} = \frac{e^2}{k_b T} [Fe_{Ti}''], \quad (64)$$

where e is the elementary charge and k<sub>b</sub> the Boltzmann constant, see also section 2.2.

The atmospheric oxygen partial pressure ( $pO_2$ ) can be varied via variation of the H<sub>2</sub>:H<sub>2</sub>O mixing ratio, and calculated by the mass action law

$$H_2 + \frac{1}{2}O_2 \rightleftharpoons H_2O, \quad pO_2 = \left(\frac{p_{H_2O}}{p_{H_2}}\right)^2 e^{-\frac{\Delta_r G^0}{k_b T}}. \quad (65)$$

Here,  $\Delta_r G^0$  is the Gibbs free enthalpy of hydrogen oxidation at standard pressure<sup>76</sup>. Furthermore, the effective  $pO_2$  in the electrode bulk can be varied by application of overpotential, according to Nernst's equation

$$pO_2^{eff} = pO_2 e^{-\frac{4e\eta}{k_b T}}, \quad (66)$$

where  $\eta$  is the overpotential of the electrode, calculated from the applied potential by subtracting resistive losses within the electrolyte and the counter electrode.

In line with the defect chemical model, the ionic conductivity plotted in Figure 20b is (within the experimental error) independent of the  $pO_2$ , and for STF37 it even exceeds the conductivity of single crystalline YSZ (0.022 vs 0.009 Scm<sup>-1</sup> at 650°C). When comparing STF37 and STF73, higher Fe content increases the ionic conductivity by almost one order of magnitude, and thus stronger than the oxygen vacancy concentration (factor 2.33). This suggests that oxygen vacancies become more mobile with higher Fe doping. Most likely, the migration barriers of a vacancy jump are different for different nearest neighbour cation configurations and therefore it is not surprising that the vacancy mobility also depends on the Fe dopant concentration. Still, an increase of oxygen vacancy mobility with dopant concentration is rather uncommon in ion conductors; e.g. in zirconia or ceria the vacancy mobility decreases with increasing acceptor concentration<sup>77-78</sup>.

Figure 20a shows that the electronic conductivity is  $pO_2$  dependent and higher for STF37. The slopes are flatter than expected from the point defect model  $\sigma_{eon} \sim pO_2^{-0.22}$  is found for STF37 and  $\sigma_{eon} \sim pO_2^{-0.17}$  for STF73. The total conductivity (including the slightly flatter slopes) of the measurements presented here also matches the (total) conductivity vs.  $pO_2$  curves of sintered STF<sup>60</sup> pellets with similar Fe content, when the slightly different temperature (750 vs 650°C) is accounted for.

Also the chemical capacitance (Figure 20c) qualitatively follows the defect chemical model, but the slopes of  $C_{chem} \sim pO_2^{-0.15}$  for STF37 and  $C_{chem} \sim pO_2^{-0.09}$  for STF73 are significantly flatter than expected from an idealized point defect model in equation (64) and again the deviation is larger for STF73. These partly severe deviations from the idealized point defect model may be related interfacial contributions or defect-defect interactions.

### 4.3.2 Electrochemical activity

#### Effect of the current collector placement

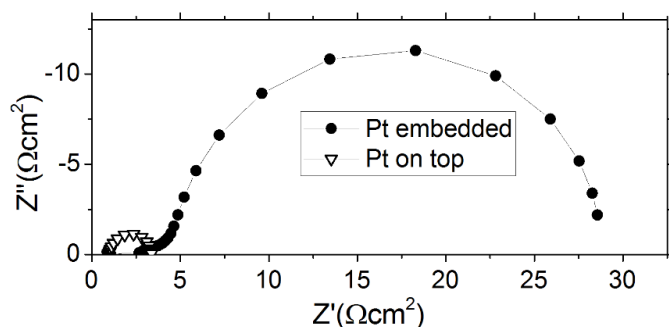


Figure 21. Impedance spectra of STF37 microelectrodes measured in the electrochemical mode with current collectors embedded and on top at 650°C, normalized to the atmosphere exposed STF surface area.

The area-specific resistance of the surface reaction was investigated on STF37 microelectrodes with current collector either on top or beneath the STF thin film, as sketched in Figure 18a and Figure 18d. Exemplary electrochemical impedance spectra of STF37 are given in Figure 21. Circuit models elaborated in Ref.<sup>52</sup> for different current collector positions may explain the slightly different shape of the two impedance spectra due to different ion conduction paths. The following measurements, however, show that also the mechanism of oxygen exchange depends on the placement of the current collector.

When the current collector is placed on top of the electrodes, a part of the STF film is covered by Pt. Mapping of  $^{18}\text{O}$  exchange on similar electrodes revealed that the Pt film is not permeable for oxygen and therefore reduces the electrochemically active area of the STF electrode<sup>79</sup>. This causes the difference in the high frequency axis offset of the normalized spectra in Figure 21. At the triple phase boundary, however, the oxygen exchange is catalysed by platinum<sup>37,78</sup>, causing the much smaller electrode arc with Pt on top. The contributions of the STF surface and the triple phase boundary can be separated by variation of the current collector geometry. The area-specific resistances of the electrodes were determined by fitting the low frequency part of the impedance spectra with a parallel resistor and constant phase element and normalizing the resistance to the atmosphere-exposed STF area. This simplified model yielded the same ASR values as fitting the measurements with the entire, mechanistically correct circuit model from Ref.<sup>52</sup>, which also takes the additional in-plane measurement into account.

When plotting the inverse of this resistance against the triple phase boundary density of the electrode, the contributions from different reaction paths (STF surface vs three phase boundary) can be separated by a simple linear regression, as given in Figure 22. The effect of the triple phase boundary density on the electrochemical activity of the surface is very



## Temperature dependence of oxygen exchange kinetics

The temperature dependence of the area-specific resistance on the surface reaction was investigated in more detail using symmetrical model cells with “macroscopic”  $5 \times 5 \text{ mm}^2$  model electrodes, as sketched Figure 18c. A triple-phase boundary-free, embedded current collector grid with small feature size ( $11 \times 11 \text{ }\mu\text{m}^2$  holes and  $4 \text{ }\mu\text{m}$  stripes) was used to ensure homogeneous polarization of the entire STF film and negligible in-plane charge transport resistances due to the small in-plane length scales. Hence, the diameter of the electrode arc is a measure for the ASR, as seen in Figure 23a. Experiments were performed in 25 mbar  $\text{H}_2 + 25 \text{ mbar H}_2\text{O}$  as a function of temperature. At  $800^\circ\text{C}$  the ASR of STF37 is roughly half of STF73, see Figure 23a. The better performance for higher Fe content is in line with studies using STF as a cathode material<sup>70</sup> and studies using porous STF-GDC composite anodes<sup>13</sup>. Activation energies extracted from the Arrhenius plots in Figure 23b are below 1 eV in both cases (0.82 eV on STF73 and 0.92 eV on STF37). Such values are in the range of other mixed conducting hydrogen electrode materials, such as ceria<sup>81-82</sup>, but they are very low, compared to the  $\sim 2 \text{ eV}$  of the  $\text{O}_2$  reduction reaction on STF<sup>70</sup>. This significant difference highlights the mechanistic difference between oxidizing and reducing oxygen exchange.

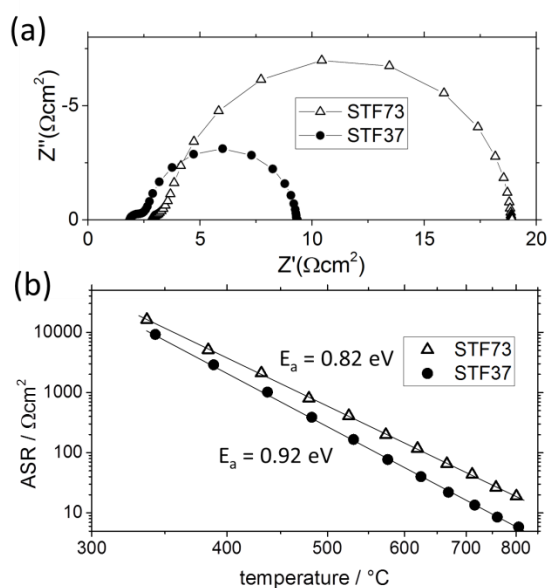


Figure 23. (a) Impedance spectra of macroscopic symmetrical cells with STF37 and STF73 electrodes (b) Arrhenius plot of the area specific resistance of the electrodes $^\circ\text{C}$ .

## Evolution of Fe<sup>0</sup> particles

In a previous ambient-pressure XPS study, the evolution of Fe<sup>0</sup> on the surface of STF73 was observed during cathodic polarization in 1:1 H<sub>2</sub>:H<sub>2</sub>O atmosphere<sup>43</sup>. This Fe<sup>0</sup> evolution was accompanied by strongly increased water splitting kinetics. The enhancement of SOFC anode performance by exsolution of easily reducible transition metals was also demonstrated on various (La,Sr)TiO<sub>3</sub> based materials<sup>51, 67, 83</sup>, (La,Sr)FeO<sub>3-δ</sub><sup>84</sup> and rare earth vanadates<sup>85</sup>.

In this study extent and electrochemical implications of Fe exsolution from STF were further investigated. STF thin films on YSZ were reduced at 650°C or 800°C for 5 hours in 25 mbar H<sub>2</sub> + 0.6 mbar H<sub>2</sub>O, which is sufficiently reducing for metallic Fe to be stable over Fe oxide<sup>76</sup>. As shown SEM images in Figure 24, metallic particles can be clearly observed on STF37 after reduction at 650°C. At 800°C, these particles are much larger and even volume decomposition is conceivable, considering the roughening of the remaining STF37 surface. STF73, on the other hand, appears more stable, and Fe exsolution was not observed. The electrochemical effect of the Fe<sup>0</sup> particles was investigated by impedance spectroscopy on STF37 microelectrodes performed in electrochemical mode. The oxygen partial pressure at 650°C was varied between 10<sup>-21</sup> and 10<sup>-26</sup> bar by changing the mixing ratio of H<sub>2</sub>:H<sub>2</sub>O and a constant total pressure (pH<sub>2</sub> + pH<sub>2</sub>O = 50 mbar). The ASR and chemical capacitance extracted during three atmospheric cycles are shown in Figure 25a.

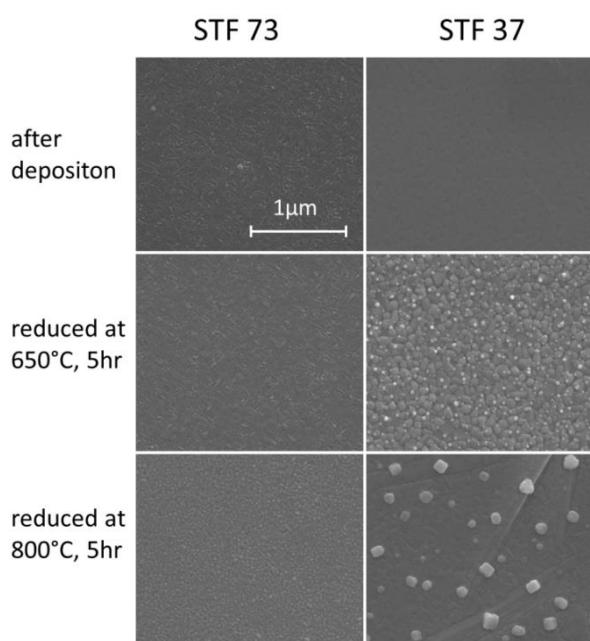


Figure 24. SEM images of STF37 and STF73 before and after reduction at 650°C and 800°C for 5h in 25mbar H<sub>2</sub>+0.8mbar H<sub>2</sub>O.

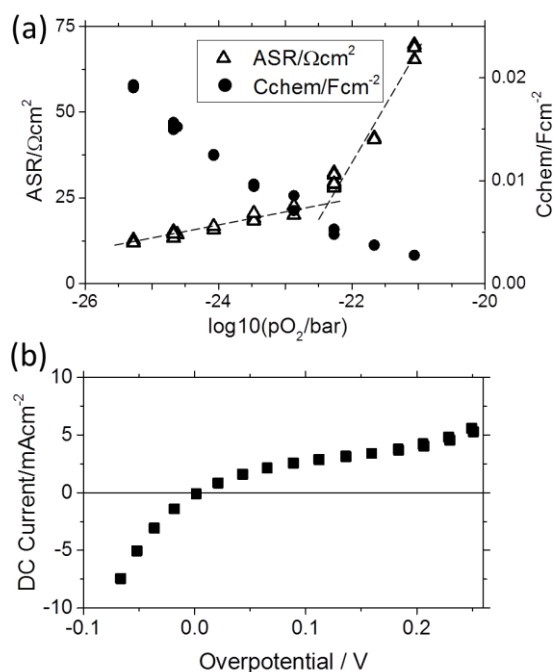


Figure 25. Area specific resistance and chemical capacitance as function of  $\text{pO}_2$  (a) and DC characteristics (b) of STF37 at  $650^\circ\text{C}$ .

Also here, higher electrochemical activity was observed in hydrogen-rich conditions, which favour  $\text{Fe}^0$  exsolution. The good reproducibility of the electrical measurements, however, suggests that no bulk decomposition takes place under these conditions. Such pronounced resistance variation was absent on STF73 (not shown). This is in line with the SEM image in Figure 24, which do not show any evidence for  $\text{Fe}^0$  particles.

The catalytic effect of  $\text{Fe}^0$  can also explain the untypical current-voltage characteristics in hydrogen-rich conditions, depicted in Figure 25b. Two DC sweeps were recorded at  $650^\circ\text{C}$  in a  $\text{H}_2:\text{H}_2\text{O}$  mixture of 12:1. The curve becomes rather steep for cathodic overpotential and shallow under anodic overpotential. This curve cannot be fitted by the sum of two exponential curves, as one might expect from Butler-Volmer type kinetics. In line with an ambient-pressure XPS study<sup>43</sup> and SEM imaging in Figure 24, metallic Fe nanoparticles are expected at open circuit potential and cathodic polarization, which increases the water splitting capability. During anodic polarization, these particles become oxidized (Possibly Fe even diffuses back into the perovskite lattice) and the U-I characteristics becomes shallow.

The high reproducibility of the ASR and chemical capacitance values during  $\text{pO}_2$  or bias cycles at  $650^\circ\text{C}$  and the absence of any hysteresis suggest that  $\text{Fe}^0$  precipitates mainly in near-surface regions while bulk decomposition does not take place. However, at  $800^\circ\text{C}$  conductivity and ASR measurements become irreproducible in hydrogen rich conditions (not shown) and in line with SEM measurements (Figure 24) bulk decomposition of the

STF is considered to be plausible. This supposed decomposition of STF37 at 800°C is at first sight in contrast to results on STF-GDC composite anodes, which were tested in 0.97:0.03 bar H<sub>2</sub>:H<sub>2</sub>O at 800°C<sup>13</sup>. There, however, the electrodes were tested in an electrochemical cell operating at 0.7 V and thus during anodic polarization of the anode, which increases the chemical potential of oxygen in the anode bulk ( $pO_2^{eff}$ ) compared to the atmosphere and stabilizes the perovskite phase.

Overall, these results indicate that the evolution of metallic Fe from STF can strongly increase the electrode kinetics, but only occurs under conditions that are very close to bulk decomposition of the perovskite.

## 4.4 Conclusions

The electrochemical properties of Sr(Ti,Fe)O<sub>3-δ</sub> thin film electrodes with 30 and 70 mol% Fe were investigated in reducing H<sub>2</sub>+H<sub>2</sub>O atmosphere at 650°C. In reducing atmosphere, the partial reduction of Fe<sup>3+</sup> to Fe<sup>2+</sup> leads to a polaron-type electronic conductivity in the order of 10<sup>-2</sup>-10<sup>-1</sup> S/cm, with higher values in more reducing conditions and for STF37. The ionic conductivities of 0.022 S/cm for STF37 and 0.0035 S/cm for STF73 at 650°C are independent of oxygen partial pressure, which is in line with the almost pO<sub>2</sub> independent oxygen vacancy concentration and STF37 is thus better ion conductive than yttria stabilised zirconia. Higher Fe concentration also decreases the area-specific resistance of the surface reaction.

In measurements of the electrochemical surface activity of STF the rather low electronic conductivity could be compensated by application of additional patterned thin film Pt current collectors beneath the STF thin films. Current collectors on top of the STF thin film strongly decrease the polarization resistance due to the additional triple-phase boundary activity, which is far beyond that of Ni-YSZ.

In hydrogen-rich atmospheres or during cathodic polarization the very low chemical potential of oxygen promotes the formation of catalytically active Fe<sup>0</sup> particles on the surface of STF37, which decreases the ASR of the electrode. In water-rich atmosphere these particles are oxidized and the ASR increases<sup>43,84</sup>. Hence, two kinetic regimes with different reaction mechanisms can be switched by slight variation of the electrode overpotential, or gas composition. At 650°C bulk-related properties such as chemical capacitance and conductivity remain unaffected by the evolution of Fe<sup>0</sup>, indicating that only a very small fraction of the bulk iron becomes metallic, while at 800°C decomposition of STF37 might take place in hydrogen rich conditions.



## 5 Mapping electrochemically driven gas exchange of mixed conducting $\text{SrTi}_{0.7}\text{Fe}_{0.3}\text{O}_{3-\delta}$ and $\text{Ce}_{0.8}\text{Gd}_{0.2}\text{O}_{2-\delta}$ thin films by $^{18}\text{O}$ tracer incorporation under reducing atmosphere

*This chapter contains in large part material published in the journal "Solid State Ionics" <sup>81</sup>*

### 5.1 Introduction

It has been demonstrated that isotope exchange, followed by SIMS analysis, is a very powerful method to monitor the surface reaction kinetics and the bulk diffusion of oxygen <sup>37, 86-87</sup>. Moreover the high lateral and depth resolution of SIMS allows visualization of electrochemically active regions of the electrodes. This has already been shown for cathode materials<sup>87-88</sup>, while in reducing atmosphere voltage driven  $^{18}\text{O}$  tracer exchange studies are rarely employed.

In this chapter, the distribution of  $^{18}\text{O}$  in thin films of  $\text{SrTi}_{0.7}\text{Fe}_{0.3}\text{O}_{3-\delta}$  (STFO) and  $\text{Ce}_{0.8}\text{Gd}_{0.2}\text{O}_{2-\delta}$  (GDC) on yttria stabilized zirconia (YSZ) substrates is investigated after tracer exchange in  $\text{H}_2+\text{H}_2^{18}\text{O}$  atmosphere during electrochemical polarization. It has already been shown in chapter 3 that the electrochemically active zone is restricted to the vicinity of a current collector. By comparison of the tracer distribution after thermally driven oxygen exchange and after experiments with cathodic and anodic bias, the width of the electrochemically active region and the factors governing the oxygen exchange could be visualized.

### 5.2 Experimental

#### 5.2.1 Sample preparation

The GDC target ( $\text{Ce}_{0.8}\text{Gd}_{0.2}\text{O}_{2-\delta}$ ) for pulsed laser deposition was prepared from powder (Treibacher AG, Austria) by isostatical pressing and subsequent sintering at 1550°C for five hours. The STFO ( $\text{SrTi}_{0.7}\text{Fe}_{0.3}\text{O}_{3-\delta}$ ) powder was prepared by solid state reaction from  $\text{SrCO}_3$  (99.99% pure, Sigma-Aldrich),  $\text{TiO}_2$  (99.99% pure, Sigma Aldrich), and  $\text{Fe}_2\text{O}_3$  (99.98 % pure, Sigma Aldrich). The educts were thoroughly mixed, calcined at 800°C, ground, again calcined at 1000°C, and – after a further grinding step – isostatically pressed and sintered at 1250°C. The phase purity of both targets was confirmed by X-ray diffraction. STFO and GDC thin films were deposited on (100)-oriented yttria stabilized

zirconia single crystals (YSZ, 9.5 mol%  $\text{Y}_2\text{O}_3$  in  $\text{ZrO}_2$ , supplier: CrysTec, Germany) by pulsed laser deposition (PLD) using a KrF excimer-laser (Lambda COMPexPro 201F, 248 nm wavelength). The deposition of 200 nm thin films was carried out in  $4 \times 10^{-2}$  mbar of pure oxygen with a pulse repetition rate of 5 Hz and a nominal pulse energy of 400 mJ. The substrate temperature during the deposition was controlled by a pyrometer (Heitronics, Germany) and was 650°C.

### 5.2.2 Electrode design

Despite acceptor doping  $\text{SrTi}_{0.7}\text{Fe}_{0.3}\text{O}_{3-\delta}$  (STFO) and  $\text{Ce}_{0.8}\text{Gd}_{0.2}\text{O}_{2-\delta}$  (GDC) are even weak n-type conductors in reducing atmosphere at the  $^{18}\text{O}$  exchange temperature<sup>61,69</sup>. Due to the much lower electronic conductivity compared to oxidizing conditions, the electrochemically active region is expected to be limited to a small area around the electric contact. In order to investigate the width of this active region, rectangular ( $160 \mu\text{m} \times 400 \mu\text{m}$ ) noble metal current collectors were sputter deposited (MCS 020, BAL-TEC AG, Germany) in two steps: on top of the YSZ substrate (prior to MIEC deposition) and on top of the deposited MIEC layer. The sample design is sketched in Figure 26a; bottom and top current collectors and one large counter-electrode were placed on one and the same sample. The bottom current collectors (5 nm Ti / 100 nm Pt) were structured from a thin film by ion beam etching, the top electrodes (5 nm Cr / 100 nm Au) were produced by a lift-off method. For the buried current collectors platinum was chosen, since it is sufficiently stable during subsequent PLD deposition of the oxide. For the top electrodes Au was used owing to its poor catalytic activity to avoid three phase boundary activity. For the sake of clarity, the electrode region with contacting noble metal collectors are named as electrodes with top current collectors (ET) and electrodes with bottom current collectors (EB), and abbreviations ET and EB are used throughout the text.

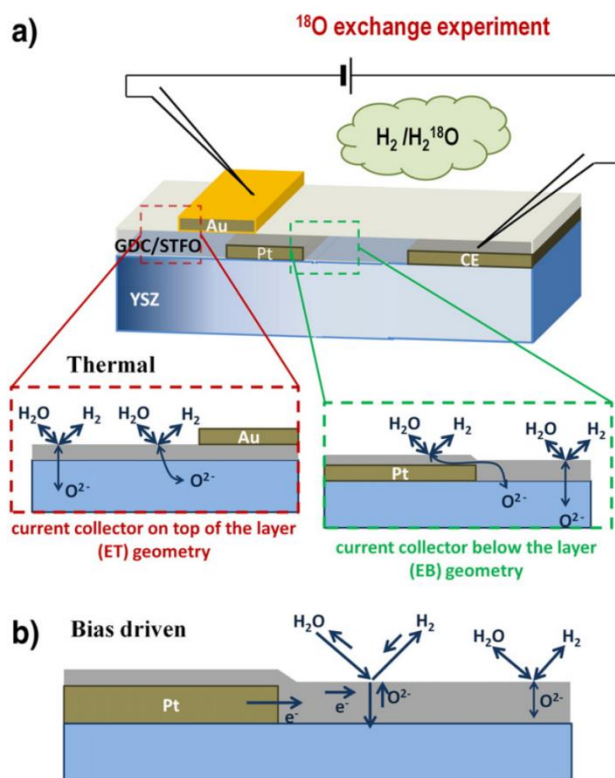


Figure 26. (a) Noble metal electrodes, which provide an electrical contact and block oxygen diffusion, were prepared below (EB geometry) and on top (ET geometry) of the GDC or STFO layer. The oxygen diffusion pathways under equilibrium conditions are sketched for ET and EB current collectors. Working and counter electrodes were contacted and polarized in the tracer exchange chamber. b) Increased oxygen incorporation rate caused by cathodic bias near an EB current collector; in some distance from the current collector edge only thermally driven tracer exchange remains due to limited electronic conductivity within the MIEC thin film.

## 5.3 Results and discussion

### 5.3.1 Thermal diffusion profiles

Distribution images of  $^{18}\text{O}$  as well as lateral profiles of the  $^{18}\text{O}$  fraction obtained under equilibrium conditions (EB geometry) are depicted in Figure 27 and Figure 28 for STFO and GDC, respectively (in the lateral profiles the zero-bias curves are given in red color). The zero-bias profiles of both materials exhibit laterally almost constant tracer fractions for the free MIEC part and an increase to a higher value close to the EB current collector edge. The high tracer content above the EB current collectors can be explained by the oxide ion blocking character of the Pt layer, which impedes the diffusion of  $^{18}\text{O}^{2-}$  ions into the YSZ electrolyte. Therefore, the tracer is simply piled up above Pt, leading to the high tracer fraction observed. Strongly different surface exchange coefficients  $k^*$  caused by different microstructures of the MIEC parts on Pt and YSZ can be ruled out by previous electrochemical experiments<sup>24, 52, 81</sup>. It should further be noted, that the depth profiles reveal constant tracer fraction within the MIEC film, thus indicating surface kinetics to be

almost exclusively rate limiting for the thermal exchange of oxygen in both materials (cf. Figure 28b for GDC; the small concentration step at the MIEC/YSZ interface indicates an additional small resistance).

Interestingly, for both MIEC materials the zero-bias lateral tracer distribution exhibits a certain slope rather than an ideal step close to the edge of the EB current collectors. This lateral profile can be explained by in-plane diffusion of oxygen in the MIEC film from the region with high tracer fraction (above Pt) to the MIEC on YSZ and then into the electrolyte – see Figure 26a, EB. Hence, the width of this slope should correlate with the diffusion length of oxygen ions. By comparison of Figure 27b and Figure 28c it becomes obvious that the thermal profile of STFO is steeper than that of the GDC film, which is expected due to the higher ionic conductivity in GDC ( $\sigma_{\text{GDC}} = 3.3 \times 10^{-4} \text{ S} \cdot \text{cm}^{-1}$ <sup>68</sup>,  $\sigma_{\text{STFO}} = 5.5 \times 10^{-6} \text{ S} \cdot \text{cm}^{-1}$  (see section 3.4) at 410°C).

While the results appear reasonable on a qualitative scale, the amount of incorporated tracer corresponds to a  $k^*$  value of roughly  $2 \cdot 10^{-8}$  to  $10^{-7}$  cm/s for STFO and  $5 \cdot 10^{-8}$  to  $2 \cdot 10^{-7}$  cm/s for GDC. The large estimation errors result in from uncertainty regarding the gas-phase tracer fraction and different results when either the tracer fraction above the YSZ or above the current collector is evaluated. Using the relation

$$k^* = \frac{k_B T}{z^2 e^2 ASR c_O} \quad (68)$$

an area specific resistance (ASR) of roughly 9-90  $\Omega\text{cm}^2$  can be estimated. This calculated ASR is roughly 1-2 orders of magnitude lower than the values obtained by electrochemical impedance spectroscopy<sup>52,81</sup>. The correlation of  $k^*$  and ASR is more closely investigated in the next chapter, where different mechanisms for electrical and tracer oxygen exchange explain the large observed differences in exchange coefficients.

### 5.3.2 Effect of cathodic bias

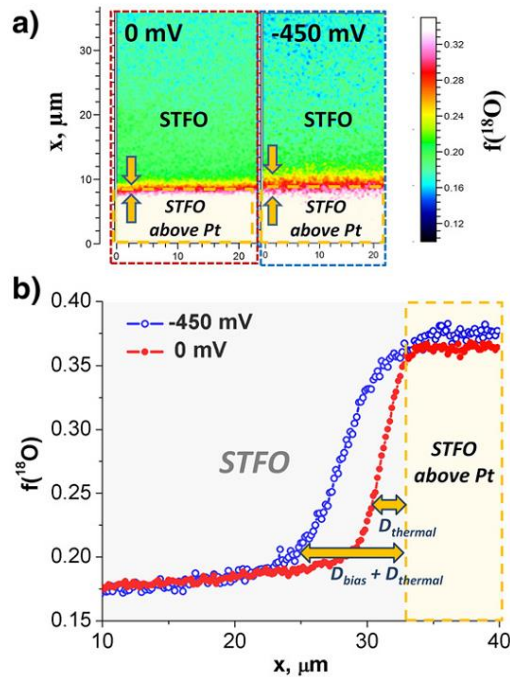


Figure 27. Isotope distribution images measured by ToF-SIMS and (b) lateral tracer fraction profiles of an STFO thin film near to the edge of an electrode with EB geometry for thermally and bias driven  $^{18}\text{O}$  incorporation.

The incorporation of  $^{18}\text{O}$  into the region close to the EB current collector changes upon polarization (see Figure 27 and Figure 28). Close to the current collector, tracer incorporation is enhanced with cathodic bias and the increase of the tracer fraction in the active zone is partly (or even mostly) due to the (electro-) chemically driven current. At a sufficient distance from the electrode, however, the surface exchange rate of  $^{18}\text{O}$  again approaches its equilibrium value. This can be easily understood by the following consideration: On the one hand, the cathodic voltage causes an increased  $^{18}\text{O}$  incorporation rate into the MIEC. On the other hand, the electronic sheet resistance in the MIEC becomes more important for longer distances from the current collector and hence causes a decay of the voltage driven  $^{18}\text{O}$  incorporation rate (this is sketched in Figure 26b).

Also on top of the Pt current collector, the tracer fraction was found to be virtually unaffected by the applied bias (the slight differences in the tracer fraction on top of the Pt electrodes can probably be attributed to a small inhomogeneity of the surface exchange coefficient e.g. due to a slight temperature inhomogeneity). This is due to the fact that oxygen ions incorporated above the current collector need to diffuse from the reaction site, which is remote from the current collector edges, into the electrolyte. Because of the high in-plane transport resistance of the oxygen ions<sup>52</sup>, the MIEC above the current collector remains unpolarized and the tracer fraction is independent of the applied bias.

Accordingly, this region is not electrochemically active despite having the highest tracer fraction.

GDC exhibits a larger active zone than STFO upon cathodic bias, which is most probably caused by its higher electronic conductivity -  $2 \pm 0.5 \times 10^{-4} \text{ S} \cdot \text{cm}^{-1}$  for GDC <sup>68</sup> and  $1.5 \pm 0.5 \times 10^{-5} \text{ S} \cdot \text{cm}^{-1}$  for STFO <sup>52</sup> at 410°C without bias. At higher cathodic bias (-500 mV) the electrochemically active zone of GDC becomes very broad, see Figure 28d. (The lower isotope fraction measured in the larger measurement area of  $150 \mu\text{m} \times 150 \mu\text{m}$  – shown in Figure 28c, d – might be caused by longer measurement time together with flooding by Ar gas. Since Ar contains some oxygen residuals this could lead to certain <sup>16</sup>O coverage on the surface.)

Within the investigated  $p(\text{O}_2)$  range ( $8.4 \times 10^{-33}$  mbar without polarization and  $10^{-40}$ - $10^{-46}$  mbar at -500 mV, 410°C) the well investigated defect model of GDC implies a large, nearly constant number of oxygen vacancies but an electron concentration and thus electronic conductivity proportional to  $p(\text{O}_2)^{-1/4}$  <sup>68</sup>. According to Nernst's equation, a cathodic bias is equivalent to a decrease in oxygen partial pressure and therefore leads to enhanced electronic conductivity in the polarized region, which strongly increases the extent of the electrochemically active zone. Thus the lateral broadening for increasing voltage can be explained by a polarization driven increase in electronic conductivity. Similar results were obtained for Pt electrodes on YSZ, where a broadening of the active zone for a very high cathodic bias was shown in oxygen atmosphere <sup>89</sup>. In the cited study, YSZ was transferred into a mixed conductor in the close vicinity of a Pt electrode by applying strong cathodic polarizations and an oxygen incorporation mechanism including lateral electron transport in the mixed conducting YSZ (similar to the situation on GDC here) could be verified by electrochemical and tracer based methods.

For an in-depth understanding of the exact mechanism on the GDC anodes in the present study an exact quantification of the oxygen chemical potential is necessary, which, however, is rather non-trivial. First, we do not know the exact ohmic polarization of the electrolyte. Due to frequency-dependent current paths, the high-frequency intercept in impedance spectra does not represent the electrolyte resistance in dc conditions. Second, the decay of this non-equilibrium chemical potential is non-linear and complicated to calculate.

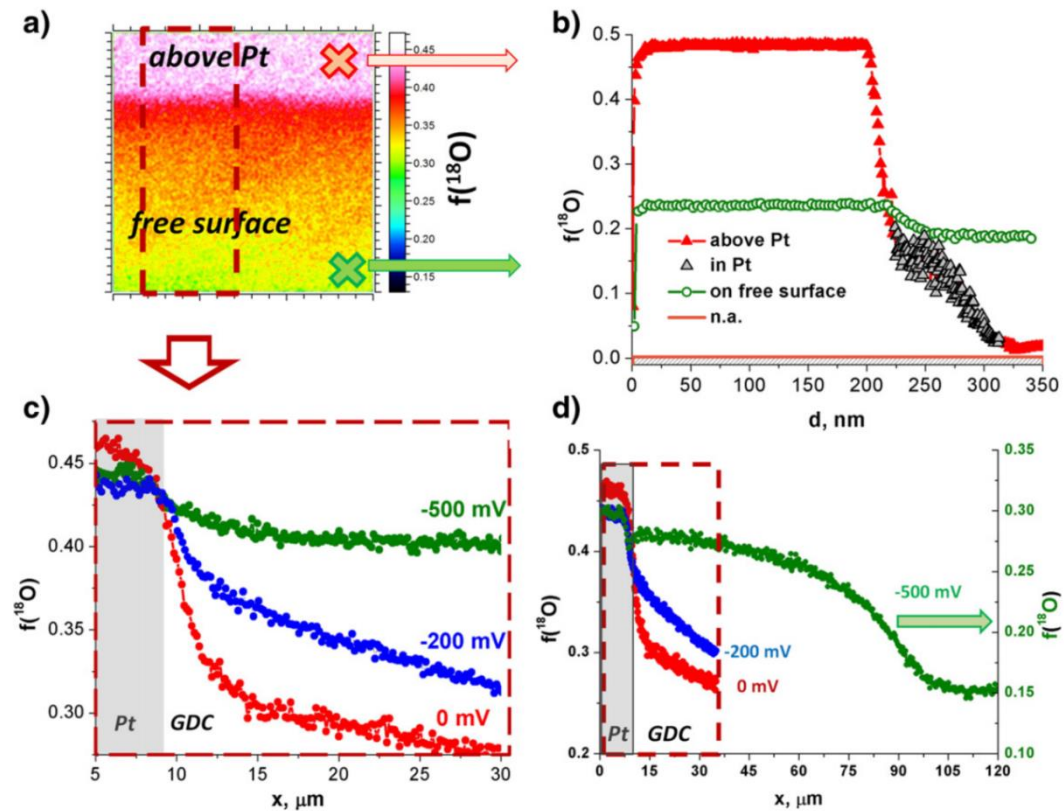


Figure 28. Isotope distribution image with lateral tracer fraction profiles in a GDC thin film near to an EB current collector and the corresponding profiles for three different bias values (c and d). Cathodic bias (-200 mV: blue curve; -500 mV: green curve) locally increases the electronic conductivity and thus the width of the electrochemically active zone. (b) The depth profiles of isotope concentration were checked in the MIEC film on top of the EB current collector (red triangles) and on top of YSZ (green circles).

### 5.3.3 Effect of polarity and electrode placement

Enhanced incorporation of  $^{18}\text{O}$  tracer upon application of cathodic bias could be successfully demonstrated and visualized. Under anodic bias, oxygen release (formation of  $\text{H}_2\text{O}$ ) is promoted and the oxygen incorporation from the tracer gas is reduced in the electrochemically active region. This leads to reduced tracer fraction near the current collector edges, while locations far from the current collector edges exhibit tracer concentrations corresponding to the equilibrium exchange rate. Figure 29 compares the tracer profiles for +500 mV and -500 mV in the ET and EB geometries for STFO. As it was discussed before, the EB geometry leads to an increased isotope concentration on the EB current collector, irrespective of the polarization (Figure 29a). (The somewhat different isotope concentrations on the current collector are most probably again due to Ar flooding during SIMS measurements and the different analysis area as already discussed above; -500 mV was analyzed in  $150\ \mu\text{m} \times 150\ \mu\text{m}$  area and +500 mV in  $50\ \mu\text{m} \times 50\ \mu\text{m}$  area.)

However, comparing the lateral isotope distribution close to the current collector edge clearly indicates reduced  $^{18}\text{O}$  incorporation with anodic bias (Figure 29a EB geometry).

For the SIMS measurements with ET geometry the gold current collector was chemically removed after  $^{18}\text{O}$  exchange. As one can see from Figure 29b, the lateral isotope concentration beneath the ET current collector decays virtually to the natural abundance value. The decay length reflects the in-plane thermal diffusion from the free surface of the MIEC to the MIEC part which is below the gold layer. Next to the MIEC/current collector edge a cathodic polarization again causes an enhanced  $^{18}\text{O}$  fraction in a certain width. Under anodic polarization, slightly less  $^{18}\text{O}$  incorporation is found near the ET current collector. This effect appears less pronounced than in the EB geometry case, due to the impact of the ET current collector discussed above.

Also here, the correlation with electrochemical measurements is only correct on a qualitative level. Overpotentials of +300 mV and -300 mV (the overpotential is significantly smaller than the applied voltage) correspond to a relative  $p\text{O}_2$  change (in the electrode) of 18 orders of magnitude, still the rate of oxygen incorporation only changes by roughly 30%. This very surprising result is clarified in the next chapter and attributed to the fact that the tracer oxygen exchange is not directly driven electrically, but rather the equilibrium rate changes slightly with bias.

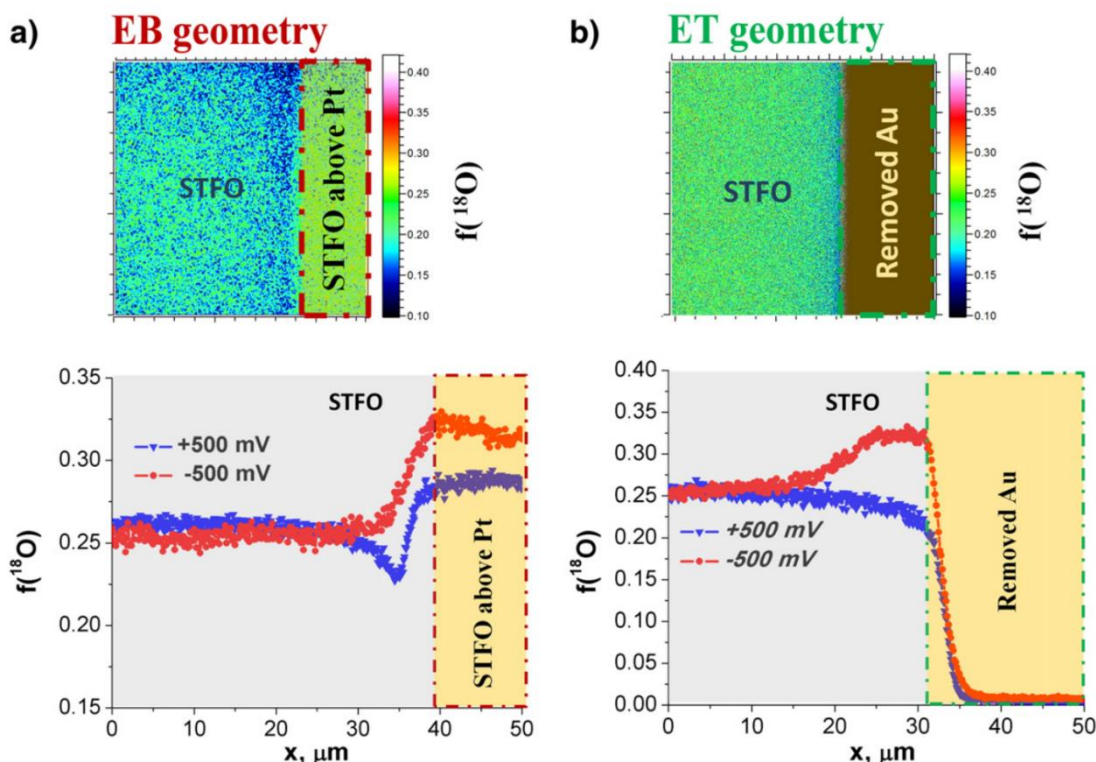


Figure 29. Isotope distribution images and lateral tracer fraction profiles of cathodically (-500 mV) and anodically (+500 mV) polarized noble metal electrodes with (a) EB and (b) ET geometry on the STFO layer.

## 5.4 Conclusions

Thin MIEC layers of GDC and STFO on single-crystalline YSZ substrates were exposed to  $H_2/H_2^{18}O$  atmosphere for thermally and electrochemically driven tracer exchange experiments. Rectangular noble metal thin film current collectors were deposited on top and beneath the MIEC layer and used for polarization. The lateral distribution of the tracer revealed several interesting features:

**(i)** In case of thermal tracer exchange, an enhanced tracer fraction is found on top of the metallic current collector due to its ionically blocking nature. At the edges of the current collector, the concentration of  $^{18}O$  decreases with a finite step width that is correlated with in-plane diffusion of oxygen ions.

**(ii)** Due to the low electronic conductivity of STFO and GDC, the MIEC area that is influenced by an applied bias is restricted to a region close to the current collector. The width of this active region depends on the bias. It amounts to only 10-15  $\mu m$  for STFO but more than 100  $\mu m$  for GDC at a cathodic bias of -500mV.

**(iii)** Not only enhanced tracer incorporation due to cathodic bias but also reduced incorporation due to anodic bias could be experimentally resolved in the active region.

**(iv)** The total amount of oxygen incorporated is roughly 1-2 orders of magnitude larger than what was expected from electrochemical measurements. Also the relative changes of tracer oxygen incorporation rate are only in the order of 30% when comparing high anodic with high cathodic bias. These very unexpected results are attributed to different mechanisms for electrical oxygen exchange and tracer oxygen exchange in humid atmosphere. This is investigated in detail in the following chapter.



## 6 Water-induced decoupling of tracer and electrochemical oxygen exchange kinetics on mixed conducting SOFC electrodes

*This chapter contains in large part material submitted to "Journal of Physical Chemistry Letters" <sup>90</sup>*

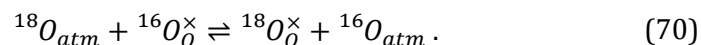
### 6.1 Introduction

The oxygen exchange coefficient of such MIEC electrodes is proportional to the achievable current density and thus the potential performance of SOFC electrode materials. It is often measured via electrochemical impedance spectroscopy (EIS)<sup>33-34, 69-70</sup>, as area specific resistance (ASR) of the surface reaction. An electrical exchange coefficient ( $k^q$ ) can be calculated via the relation<sup>66,91</sup>

$$k^q = \frac{k_b T}{(ze)^2 c_o ASR}. \quad (69)$$

Symbol  $c_o$  denotes the oxygen ion concentration,  $z$  is the charge number (-2 for oxygen ions) and  $k_b$ ,  $T$ ,  $e$  are Boltzmann's constant, temperature and elementary charge, respectively.

Another common method for analyzing oxygen exchange kinetics of MIECs is <sup>18</sup>O isotope exchange and depth profiling (IEDP), yielding a tracer exchange coefficient ( $k^*$ ). In a tracer exchange experiment, the net flux of oxygen is zero and <sup>16</sup>O and <sup>18</sup>O atoms swap their positions between oxide ( $O_o^\times$ ) and atmosphere ( $O_{atm}$ ).  $c_o \cdot k^*$  is therefore the equilibrium rate (in oxygen atoms/cm<sup>2</sup>s) of the reaction



This reaction may be mechanistically different from that of electrical measurements, where a net flux of oxygen ions and therefore charge transfer is required for a measurable electric current. Generally  $c_o \cdot k^q$  is the equilibrium rate (in oxygen atoms/cm<sup>2</sup>s) of the electrical oxygen exchange reaction



Only if the two reaction steps of <sup>18</sup>O incorporation and <sup>16</sup>O release in reaction (2) are locally unrelated and are mediated by an electron transfer, i.e. reduction and oxidation

steps as in reaction (71), the tracer exchange mechanism is equal to the electrical exchange reaction (71). Then the parameters  $k^*$  and  $k^q$  are identical (or at least similar since a small difference due to correlation effects as for diffusion coefficients may still remain)<sup>91</sup>.

Although strongly different  $k^*$  and  $k^q$  values are in principle possible, their equality is assumed in most cases<sup>33, 92</sup> and the conceptual differences of electrical and isotope exchange measurements are hardly mentioned. Also only very few studies compare the two coefficients obtained upon identical conditions. Despite some difficulties in detailed analysis of the tracer profiles, similar values of  $k^*$  and  $k^q$  were found for  $\text{La}_{0.6}\text{Sr}_{0.4}\text{CoO}_{3-\delta}$  at 400°C<sup>93</sup> in dry  $\text{O}_2$ , indicating that the rate limiting step is identical in both types of experiments. Some studies showed strongly increased tracer exchange in humidified ( $\text{H}_2^{18}\text{O}$ ) atmosphere, e.g. on  $\text{La}_2\text{Mo}_2\text{O}_9$ <sup>94-95</sup>,  $(\text{Ce,Gd})\text{O}_{2-\delta}$  and  $(\text{Zr,Y})\text{O}_{2-\delta}$ <sup>96</sup>. In Refs.<sup>97-98</sup> strongly increased tracer exchange kinetics and slightly faster electrochemical kinetics on Pt-YSZ electrodes were attributed to fast water dissociation on the oxide surface. Also, significant  $^{18}\text{O}$  exchange with water at temperatures around 350°C on  $(\text{La,Sr})\text{MnO}_{3-\delta}$  (LSM) and 250°C on  $(\text{La,Sr})(\text{Co,Fe})\text{O}_{3-\delta}$  (LSCF) was reported and related to dissociation of water<sup>99-100</sup>. In a recent oxygen exchange kinetics study on LSM and LSCF materials<sup>100</sup> it was shown that water exchange has a lower exchange activation energy and is faster than oxygen exchange, although it was not highlighted in the chapter. From ambient pressure XPS measurements<sup>23</sup> on  $(\text{Ce,Sm})\text{O}_{2-\delta}$  in  $\text{H}_2+\text{H}_2\text{O}$  atmosphere, fast water dissociation on surface oxygen vacancies is assumed as well. However, these studies only rely on indirect observations, because the individual rates of electrically driven oxygen exchange and water dissociation on the surface were not quantified and correlated for identical conditions.

In the experiments presented in this chapter,  $k^*$  and  $k^q$  are simultaneously determined for different mixed conducting oxides by impedance spectroscopy during isotope exchange in various  $^{18}\text{O}$  containing atmospheres. Hence, quantitative comparison of the two types of oxygen exchange coefficients became possible. Partly very severe differences with  $k^* > 100k^q$  are found, particularly in humid atmosphere, and a mechanistic explanation is provided.

## 6.2 Experimental

### Target preparation

The  $\text{SrTi}_{0.7}\text{Fe}_{0.3}\text{O}_{3-\delta}$  (STF) target for pulsed laser deposition was prepared by solid state reaction from  $\text{SrCO}_3$ ,  $\text{TiO}_2$ , and  $\text{Fe}_2\text{O}_3$ . The powders were calcined at  $1100^\circ\text{C}$ , 12 hours, and sintered at  $1400^\circ\text{C}$ , 5 hours. The  $\text{La}_{0.6}\text{Sr}_{0.4}\text{FeO}_{3-\delta}$  (LSF) target was prepared from commercially available powder (Sigma Aldrich). The LSF and STF powders were pressed into pellets using a cold isostatic press and sintered at  $1250^\circ\text{C}$  for 5 h. The phase purity of both targets was confirmed by X-ray diffraction.

### Electrode preparation

Prior to deposition of the electrodes a thin film Pt mesh ( $25 \times 25 \mu\text{m}^2$  mesh holes with  $5 \mu\text{m}$  wide bars) was prepared on the [100]-oriented, single crystalline substrates (YSZ, 9.5 mol %  $\text{Y}_2\text{O}_3$  in  $\text{ZrO}_2$ , supplier: CrysTec, Germany). Subsequently STF or LSF thin films were deposited by pulsed laser deposition (PLD), using a KrF excimer-laser (Lambda COMPexPro 201F, 248 nm wavelength). The deposition of thin films was carried out at  $650^\circ\text{C}$  with a pulse repetition rate of 5 Hz and a pulse energy of 400 mJ in  $4 \cdot 10^{-2}$  and  $2 \cdot 10^{-2}$  mbar of oxygen for LSF and STF, respectively. Deposition times of 30/20 minutes for LSF and STF led to the film thicknesses indicated in Figure 31 and Figure 32. The thin films investigated in reducing atmosphere were patterned to microelectrodes with a diameter of  $300 \mu\text{m}$  by photolithography and argon ion beam etching. In oxidizing atmosphere, however, the lithography process strongly increased the electrochemical ASR, and therefore lithography after electrode deposition was avoided. Instead, a kinetically fast, porous LSF counter electrode was used on the bottom of the substrate as sketched in Figure 31a. The fast counter electrode kinetics was proved in section 7.

### Isotope exchange experiments

The samples were heated to  $396\text{-}418^\circ\text{C}$  in various  $^{18}\text{O}$  containing atmospheres. Impedance spectra were acquired with a Novocontrol Alpha analyser, equipped with a Novocontrol Pot/Gal interface. After isotope exchange for 10-20 minutes the samples were quenched with a rate of  $\sim 150^\circ\text{C}/\text{min}$ . Four different atmospheres were used during isotope exchange:

- 200 mbar  $^{18}\text{O}_2$ , dried via a zeolite filter (dry oxidizing)
- bottled  $^{18}\text{O}_2$  without drying step (usual oxidizing)
- 200 mbar  $^{16}\text{O}_2$  humidified with  $\text{H}_2^{18}\text{O}$  (humid oxidizing)
- 25 mbar  $\text{H}_2$  in Ar, humidified with  $\text{H}_2^{18}\text{O}$  (humid reducing).

Water vapor pressures in humid gases were 15-25 mbar

## Isotope depth profiling

The resulting  $^{18}\text{O}$  isotope exchange depth profiles were subsequently measured by means of time-of-flight secondary ion mass spectrometry (ToF-SIMS), using a ToF-SIMS 5 (ION-TOF GmbH, Germany). Collimated burst alignment (CBA) mode<sup>101</sup> was used, which allows more accurate determination of the  $^{18}\text{O}$  content in oxides.  $\text{Bi}_3^{++}$  primary ions were used (25 kV). Negative secondary ions were analysed. For the sputtering of material 1 kV  $\text{Ce}^+$  ions were used with a sputter crater of  $500\ \mu\text{m} \times 500\ \mu\text{m}$ . The charging of the surface was compensated with an electron flood gun. For integration of depth profiles, the MIEC area on top of the (ion blocking) current collector was excluded. The isotope fraction was obtained by normalizing integrated intensities of  $^{18}\text{O}$  and  $^{16}\text{O}$ :

$$f(^{18}\text{O}) = \frac{I(^{18}\text{O})}{I(^{16}\text{O}) + I(^{18}\text{O})} \quad (72)$$

## 6.3 Results and discussion

### 6.3.1 Effect of humidity on $k^q$

While most of the later result focus on the effect of water on  $k^*$ , the effect of humidity on  $k^q$  is interesting as well. It can, however, not be clearly resolved by acquisition of  $k^*$  and  $k^q$  on different samples, because  $k^q$  may vary by a factor of  $\sim 2$  simply because of sample deviation. Switching between oxidizing and reducing atmospheres using the same sample could, however, prove that humidity significantly decreases  $k^q$ , by a factor of  $\sim 2$ . It will be shown in the following that this effect is small compared to the influence of humidity on  $k^*$ . A mechanistic explanation of this effect is not the scope of this chapter and theories were derived in Refs. <sup>96-99</sup>

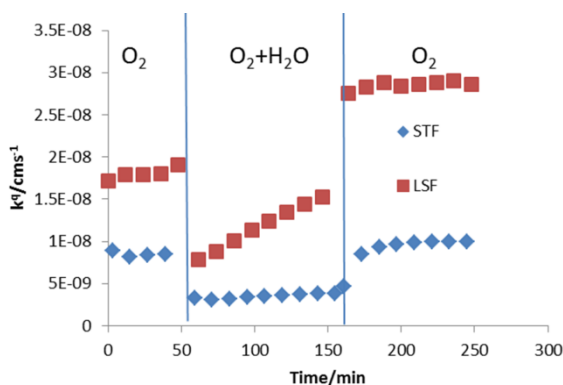
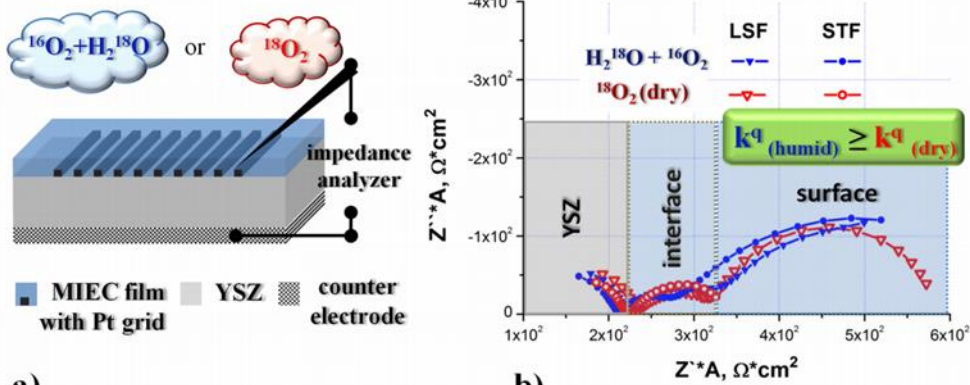


Figure 30.  $k^q$  as a function of time while switching between dry and humid oxidizing atmospheres at  $420^\circ\text{C}$ .

### 6.3.2 Correlation of $k^*$ and $k^q$ in dry and humid conditions

#### Impedance measurements



#### Isotope exchange depth profiles

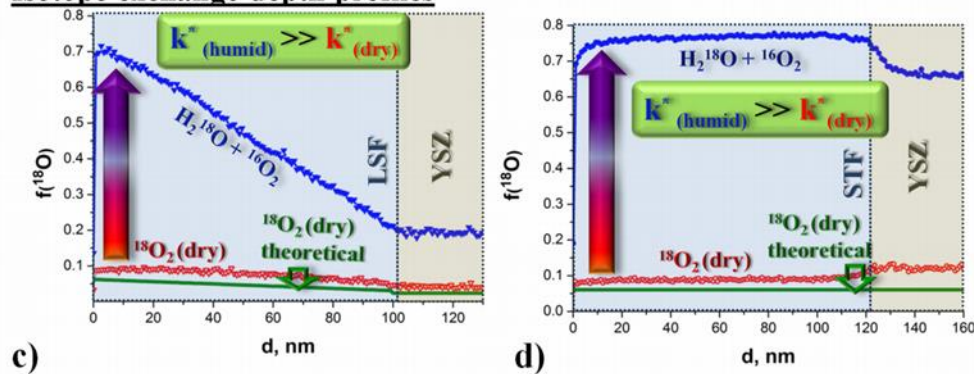


Figure 31. a) Sketch of sample geometry and tracer exchange routine during EIS. For measurements in reducing atmosphere the MIEC films were micropatterned to circular microelectrodes. b) Impedance measurements on  $\text{La}_{0.6}\text{Sr}_{0.4}\text{FeO}_{3-\delta}$  (LSF) and  $\text{SrTi}_{0.3}\text{Fe}_{0.7}\text{O}_{3-\delta}$  (STF) thin film electrodes during tracer exchange in dry and humid oxidizing atmosphere at  $418^\circ\text{C}$ , normalized to the active electrode area. c) and d)  $^{18}\text{O}$  tracer depth profiles in LSF and STF measured after the exchange, including a simulation assuming  $k^* = k^q_{\text{dry}}(^{18}\text{O}_2(\text{dry}) \text{ theoretical})$ .

#### HUMID-REDUCING ATMOSPHERE ( $\text{H}_2\ ^{18}\text{O} + \text{H}_2$ )

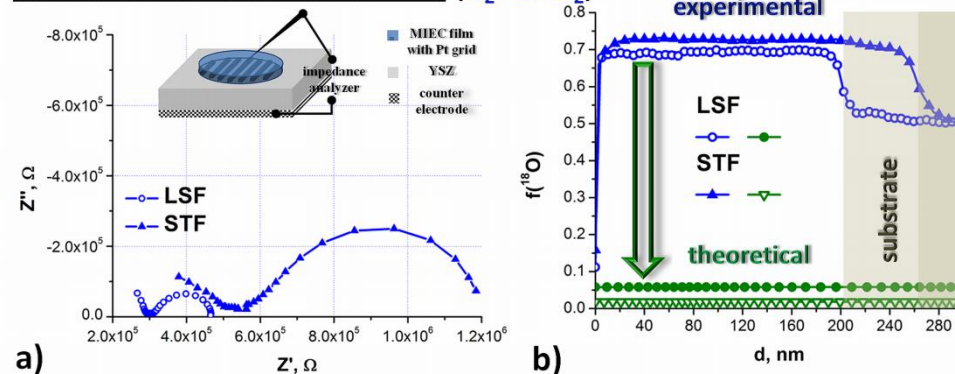


Figure 32. a) Impedance measurements on LSF and STF thin films microelectrodes during isotope exchange in humid reducing atmosphere at  $396^\circ\text{C}$ . b) Measured  $^{18}\text{O}$  depth profiles, including a simulation assuming  $k^* = k^q$  (theoretical).

material	dry oxidizing	usual oxidizing	humid oxidizing	humid reducing
LSF	$k^* = 1.3 \cdot 10^{-8} \text{ cms}^{-1}$	$k^* = 1.5 \cdot 10^{-8} \text{ cms}^{-1}$	$k^* = 1.5 \cdot 10^{-6} \text{ cms}^{-1}$	$k^* = 2.5 \cdot 10^{-6} \text{ cms}^{-1}$
	$k^q = 7.5 \cdot 10^{-9} \text{ cms}^{-1}$	$k^q = 3.1 \cdot 10^{-9} \text{ cms}^{-1}$	$k^q = 9.0 \cdot 10^{-9} \text{ cms}^{-1}$	$k^q = 1.8 \cdot 10^{-8} \text{ cms}^{-1}$
	<b><math>k^*/k^q = 1.7</math></b>	<b><math>k^*/k^q = 4.8</math></b>	<b><math>k^*/k^q = 166.7</math></b>	<b><math>k^*/k^q = 138.9</math></b>
STF	$k^* = 3.0 \cdot 10^{-8} \text{ cms}^{-1}$	$k^* = 3.5 \cdot 10^{-8} \text{ cms}^{-1}$	$k^* = 5.0 \cdot 10^{-6} \text{ cms}^{-1}$	$k^* = 4.3 \cdot 10^{-6} \text{ cms}^{-1}$
	$k^q = 1.9 \cdot 10^{-8} \text{ cms}^{-1}$	$k^q = 5.9 \cdot 10^{-9} \text{ cms}^{-1}$	$k^q = 5.0 \cdot 10^{-9} \text{ cms}^{-1}$	$k^q = 5.0 \cdot 10^{-9} \text{ cms}^{-1}$
	<b><math>k^*/k^q = 1.6</math></b>	<b><math>k^*/k^q = 5.9</math></b>	<b><math>k^*/k^q = 1000.0</math></b>	<b><math>k^*/k^q = 860.0</math></b>

Table 4. Summary of tracer ( $k^*$ ) and electrical ( $k^q$ ) exchange coefficients of  $\text{La}_{0.6}\text{Sr}_{0.4}\text{FeO}_{3-\delta}$  and  $\text{SrTi}_{0.3}\text{Fe}_{0.7}\text{O}_{3-\delta}$  in various atmospheres.

The acquired impedance spectra in Figure 31b show the onset of a high frequency arc caused by the electrolyte and a possible contact resistance. One or two arcs are found at intermediate and low frequencies; those are attributed to the electrode reactions. The smaller intermediate frequency arc is most probably caused by an interfacial ion diffusion barrier, but also the counter electrode may contribute<sup>27, 30, 33</sup>. In agreement with many earlier studies, the area-specific resistance of the surface reaction (ASR) was determined by fitting the low-frequency semicircle with a parallel resistor and a constant phase element; for normalization the electrochemically active electrode area was used. Electrical exchange coefficients ( $k^q$ ) were then calculated from equation (69) and all values are summarized in Table 4. Interestingly, in all atmospheres and for both materials the ASR is in the range of  $200 \text{ } \Omega \cdot \text{cm}^2$  ( $k^q \approx 8 \cdot 10^{-9} \text{ cm/s}$ ), and differences are far less than one order of magnitude.

In Figure 31c,d and Figure 32b, depth profiles of the  $^{18}\text{O}_2$  isotope fraction ( $f(^{18}\text{O})$ ) are shown for dry and humid oxidizing as well as humid reducing exchange conditions. All profiles were calculated from raw data by restricting the in-plane integration to MIEC regions without the ion blocking platinum current collector beneath. Most of the depth profiles are flat within the MIEC film and some exhibit a distinct step at the MIEC-electrolyte interface. Only for LSF in oxidizing conditions (Figure 31c) a clear slope can be observed, indicating low ionic conductivity. This is caused by the small amount of oxygen vacancies of LSF in oxidizing atmosphere, especially at lower temperatures ( $\delta \approx 0.0001$  at  $418^\circ\text{C}$ <sup>47</sup>). For STF in oxidizing and reducing conditions but also for LSF in reducing conditions the oxygen vacancy concentration and thus the ionic conductivity is rather high<sup>42, 47</sup>, thus explaining the flat profiles. In all humidified atmospheres, the tracer fraction is even close to the atmospheric value of 80%  $\text{H}_2^{18}\text{O}$  (see below).

These profiles were fitted using finite element simulations, considering isotope exchange ( $k^*$ ) and diffusion ( $D^*$ ) coefficients of the MIEC and an interfacial diffusion barrier at the MIEC|YSZ interface ( $D^*_{int}$ ). In the simulation  $D^*$  of YSZ was fixed to the value calculated from the measured ionic conductivity of YSZ using Nernst-Einstein's relation and a Haven

ratio of 0.65 i.e. to  $2 \cdot 10^{-7}$  cm<sup>2</sup>/s at 418°C and  $1 \cdot 10^{-9}$  cm<sup>2</sup>/s at 396°C. A reasonable  $D^*$  value of the MIEC was only found for LSF in oxidizing atmosphere and the following discussion is limited to  $k^*$  values. Atmospheric <sup>18</sup>O concentration of 97.1% (provided by the supplier) was assumed in dry oxidizing conditions, whereas a concentration of 80% H<sub>2</sub><sup>18</sup>O was estimated for humid conditions by evaluating the <sup>18</sup>O concentration found in the MIEC on top of the ion blocking Pt layer (not shown). The derived exchange coefficients are summarized in Table 4. Simulated profiles assuming  $k^* = k^q$  are also shown in Figure 31 and Figure 32.

Please note that the surface kinetics of thin film electrodes may vary from sample to sample and also due to degradation. Therefore the main information is revealed by the ratio of  $k^q/k^*$  obtained on one and the same sample at exactly the same time. The ratios in all four atmospheres are summarized in the bar graph of Figure 33. In dry oxidizing atmosphere, reasonable agreement of  $k^*$  and  $k^q$  is found. Accordingly, we conclude that <sup>18</sup>O<sub>2</sub> is exchanged via a redox reaction (reaction 1 in Figure 33) which corresponds to the electrochemical exchange measured in electrical experiments. The slightly higher  $k^*$  may have several reasons: For example, the ASR of the surface reaction may be overestimated since other processes (e.g. in-plane charge transport<sup>52</sup>) might increase the diameter of the electrode arc, leading to slightly underestimated  $k^q$  values. Moreover, the tremendous increase of  $k^*$  in humid atmospheres (see below) suggests that even traces of residual humidity may increase  $k^*$ . The increase of the  $k^q/k^*$  ratio found upon removal of the zeolite filter is an indication for this effect (see “usual oxidizing” column in Table 4).

In humidified oxidizing atmosphere, the electrode ASR slightly increases, which decreases  $k^q$ , while the tracer surface exchange coefficient  $k^*$  is two to three orders of magnitude larger than  $k^q$  for LSF and STF. Such a large difference requires different mechanisms of electrical and tracer oxygen exchange, in particular since H<sub>2</sub><sup>18</sup>O (which does not directly contribute to  $k^q$ ) is the only source of oxygen tracer. An isotope exchange mechanism that is not mediated by an electron transfer can increase  $k^*$ , but cannot contribute to  $k^q$ . Such a mechanism is the fast adsorption of water on a surface oxygen vacancy and the subsequent dissociation into two hydroxyl groups (reaction 2 in Figure 33). A fast rate of this process is also assumed on ceria surfaces in reducing conditions<sup>6</sup>. This reaction, together with the subsequent water desorption using a neighboring oxygen ion (reaction 3 in Figure 33), enables the exchange of <sup>18</sup>O without an electron transfer and the oxidation states of the contributing O and H atoms remain -2 and 1, respectively.

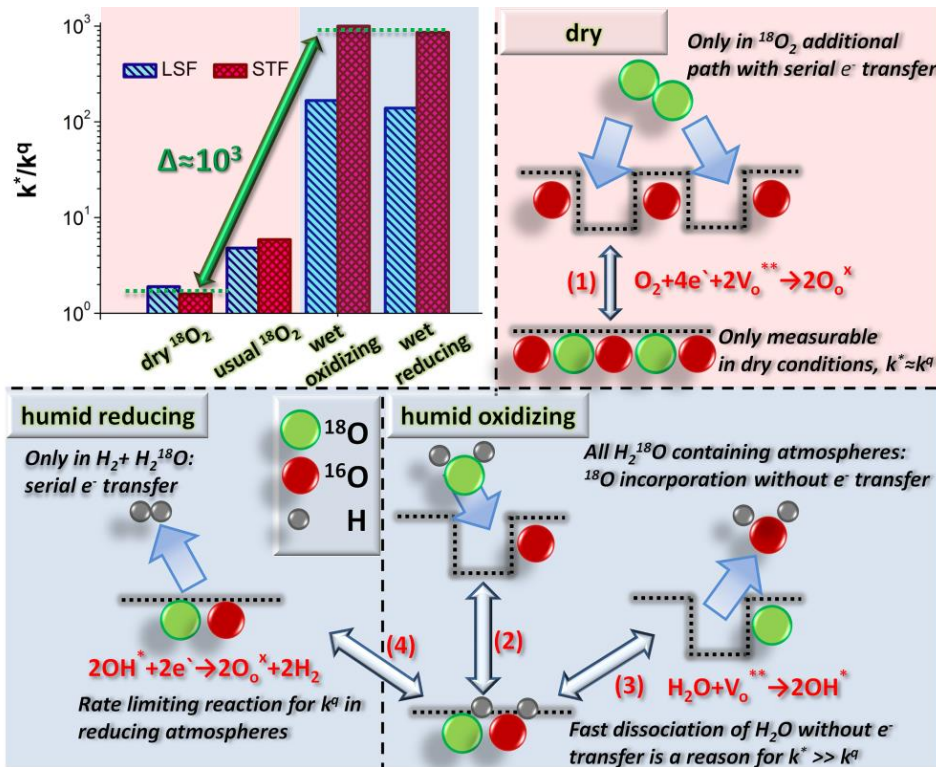


Figure 33. In order to highlight the difference between dry and humid atmospheres, the ratios of  $k^q/k^*$  from Table 1 are shown in the bar graph. The sketches show different oxygen incorporation mechanisms in  $^{18}\text{O}_2$  and  $\text{H}_2^{18}\text{O}$  atmospheres. Reaction (1) shows the  $^{18}\text{O}_2$  incorporation (only in dry atmosphere) into surface vacancies, requiring an electron transfer. Proposed mechanism of the  $\text{H}_2^{18}\text{O}$  tracer exchange reaction: (2) Tracer-marked water adsorbs on a surface vacancy and dissociates into two  $\text{OH}^-$  groups. The tracer marked  $^{18}\text{OH}^-$  can then be transformed to tracer  $^{18}\text{O}^{2-}$  via two parallel processes: (3) Fast desorption of water, using a neighbouring oxide ion. (4) Slow electron transfer to two surface hydroxyls and formation of  $\text{H}_2$ .

These results are of high relevance for tracer exchange experiments in  $\text{O}_2$  atmosphere as they highlight the importance of having absolutely water-free gas during an isotope exchange experiment. Even traces of humidity ( $\text{H}_2^{18}\text{O}$ ) can lead to accelerated tracer exchange that, however, does not imply increased performance as SOFC electrode. Such traces of  $\text{H}_2^{18}\text{O}$  may easily be present in bottled  $^{18}\text{O}_2$  gas since some residual  $\text{H}_2$  (25 ppm according to the manufacturer) is present in  $^{18}\text{O}_2$  isotope enriched oxygen bottles. Most probably the hydrogen is oxidized to  $\text{H}_2^{18}\text{O}$  at exchange temperatures. Also higher levels of  $\text{H}_2^{16}\text{O}$  (adsorbed on the chamber walls or going in via leakage) are very detrimental since this may remove  $^{18}\text{O}$  from the solid without electron transfer and thus may lower the measured  $k^*$  value.

In reducing conditions, the  $\text{H}_2 + \text{H}_2^{18}\text{O}$  atmosphere inevitably contains water, hence only one ratio of  $k^*/k^q$  is measurable. Similar to humid oxidizing atmosphere, this ratio is very large ( $>100$ ) and thus  $k^*$  is no measure for electrochemical exchange kinetics. However, due to the different electrochemical surface reaction in  $\text{H}_2/\text{H}_2\text{O}$ , the very fast tracer exchange still delivers valuable mechanistic information on the electrochemical processes.

If water dissociation (reaction 2, Figure 33) was rate limiting in the overall water splitting reaction ( $H_2O + V_O^{\cdot\cdot} + 2e' \rightarrow O_O^{\times} + H_2$ ), the  $H_2$  desorption reaction (reaction 4, Figure 33) would be faster than the desorption of  $H_2^{16}O$  (reaction 3, Figure 33), and the isotope exchange reaction would be mediated by an electron transfer. Consequently, an agreement of  $k^q$  and  $k^*$  would imply water dissociation to be rate limiting. Our experiments prove by a direct measurement of reaction rates rate limiting water dissociation is not the case and  $k^* > 100 k^q$ . Clearly, the rate of water dissociation and desorption is much faster than the hydrogen reduction and desorption, therefore either the charge transfer from a surface transition-metal to a surface hydroxyl or the formation of  $H_2$  from two hydroxyl groups is rate-limiting, as already assumed for ceria<sup>23</sup>. Methodologically, this means that it is impossible to obtain correct electrical exchange rates from measured  $k^*$  values in humid conditions, since moving to dry conditions is not possible with  $H_2^{18}O$  as the tracer source in reducing conditions.

The absolute  $k^*$  values in humid reducing and humid oxidizing conditions are very similar, which further indicates that tracer is exchanged via the same mechanism. Interestingly,  $k^q$  values found in oxidizing and reducing conditions are also very similar, in agreement with Ref.<sup>102</sup> despite their difference to  $k^*$ . This is still somewhat surprising, given the different surface reaction and defect concentrations within the electrode. A mechanistic discussion of this fact, however, is beyond the scope of this chapter.

## 6.4 Conclusions

Impedance spectroscopic measurements on LSF and STF model electrodes performed during  $^{18}O$  tracer exchange, which allowed simultaneous determination of electrical ( $k^q$ ) and the tracer ( $k^*$ ) exchange coefficients of oxygen. The experiments were performed in three different atmospheres: dry  $^{18}O_2$ ,  $^{16}O_2$  humidified with  $H_2^{18}O$ , and reducing  $H_2+H_2^{18}O$ .

In dry oxidizing atmosphere, reasonable agreement of  $k^*$  and  $k^q$  was found, indicating that  $^{18}O_2$  isotope exchange occurs via a redox reaction, which is mediated by a bulk electron transfer.

In humid oxidizing and humid reducing atmospheres, however, very high tracer exchange coefficients ( $k^* > 100 k^q$ ) were observed. This huge difference can only be explained by different mechanisms of electrical and tracer oxygen exchange. A fast equilibrium rate of water dissociation on a surface oxygen vacancy, forming two surface OH groups was suggested as the dominating tracer exchange mechanism. In this reaction, no electron transfer is required because the contributing O and H atoms remain in oxidation states -2 and +1, respectively. Such a reaction without an electron transfer cannot be driven

electrically, so it does not contribute to  $k^q$ , while increasing  $k^*$  by more than two orders of magnitude.

Due to this hydroxyl mediated mechanism it is crucial to avoid even traces of humidity when tracer exchange coefficients are related to the electrochemical activity of electrode materials. In the case of  $H_2+H_2O$  atmosphere these results prove that water dissociation and desorption is fast and that the electron transfer to a surface OH group or the subsequent evolution of  $H_2$  is rate limiting.

## 7 Ambient pressure XPS study of mixed conducting perovskite-type SOFC cathode and anode materials under well-defined electrochemical polarization

*This chapter contains in large part material published in "The Journal of Physical Chemistry C" <sup>43</sup>*

### 7.1 Introduction

While the bulk defect chemistry of many mixed conducting oxides is quite well understood, little is known about the actual surface chemistry and reaction mechanisms of oxygen exchange on polarized mixed conducting electrodes. Particularly for mixed conducting electrodes employed in solid oxide fuel/electrolysis cells (SOFC/SOEC), a more detailed knowledge of composition and chemistry of the surfaces is essential. This may help to develop more effective strategies for electrode optimization and to establish a firm model basis for an important type of electrode reactions in solid state electrochemistry.

In-situ techniques are of high relevance in addressing these topics, since measurements of many crucial surface properties such as transition metal oxidation states, adsorbate coverage and surface potentials are only meaningful under (or at least near to) working conditions.

In this respect near-ambient pressure X-ray photoelectron spectroscopy (NAP-XPS) has become an increasingly popular technique to observe the chemical changes of catalytically active oxide surfaces under realistic operating conditions<sup>22, 103-107</sup>. However, the interpretation of such measurements is often highly complex owing to several reasons. The chemical environment of surface ions is different from the bulk and therefore ions of an oxide may exhibit modified chemical surface states (e.g. different oxidation number or neighboring atoms). Still those do not necessarily contribute to the electrochemical surface reaction and have to be distinguished from reacting or catalyzing species. For a mechanistic interpretation of oxygen exchange kinetics also the effect of electrochemical polarization and atmosphere on the binding energy and concentration of surface species needs to be investigated. Such extensive studies were already performed on ceria-based mixed conducting anodes and  $\text{La}_{0.6}\text{Sr}_{0.4}\text{CoO}_{3-\delta}$  (LSC) cathodes<sup>22-23, 25-26, 108</sup>. Much less is

known about the surface chemistry of perovskite-type anodes and cathodes other than LSC and in-situ XPS studies are largely missing for this class of materials. Also the direct comparison of the surface chemistry of mixed conducting oxides in oxidizing and reducing atmospheres, relevant e.g. for symmetric SOFCs, has not been accomplished so far.

In this chapter, the surface chemistry of the three different mixed conducting perovskite-type electrode materials  $\text{La}_{0.6}\text{Sr}_{0.4}\text{CoO}_{3-\delta}$  (LSC),  $\text{La}_{0.6}\text{Sr}_{0.4}\text{FeO}_{3-\delta}$  (LSF) and  $\text{SrTi}_{0.7}\text{Fe}_{0.3}\text{O}_{3-\delta}$  (STF) is compared with and without well-defined electrochemical polarization. LSF and STF were studied in oxidizing and reducing conditions, LSC was only investigated in oxidizing atmosphere, due to its decomposition in  $\text{H}_2/\text{H}_2\text{O}$ . Given the significant differences between the materials and oxygen partial pressures, the focus of this study is to find surface species that are common for mixed conducting perovskites under in-situ conditions. However, it is not straightforward to interpret the origin and/or the nature of a detected surface species and its role in the oxygen exchange reaction. Therefore, also the response of surface species to electrochemical polarization was investigated and correlated to the electrochemical properties of the electrodes, as measured by simultaneous electrochemical impedance spectroscopy (EIS) during the XPS scans. Distinct surface states of strontium and oxygen were found on all three materials in oxidizing atmosphere. Moreover the different electronic conduction mechanisms (band-like in LSC and small polaron hopping in LSF and STF) were investigated and related to the differences in the valence band structure. Switching between oxidizing and reducing atmospheres as well as electrochemical polarization lead to a shift of the apparent binding energy, which can be explained by the correlation of Fermi level and the chemical potential of oxygen.

## 7.2 Experimental

### 7.2.1 Sample design and preparation

The samples with  $\text{La}_{0.6}\text{Sr}_{0.4}\text{FeO}_{3-\delta}$  (LSF) and  $\text{SrTi}_{0.7}\text{Fe}_{0.3}\text{O}_{3-\delta}$  (STF) thin film working electrodes and porous, kinetically fast counter electrodes were prepared as follows: In the first step, metallic, thin film current collectors were prepared on yttria-stabilized zirconia (single crystals  $5 \times 5 \times 0.5$  mm, (100)-oriented, 9.5 mol%  $\text{Y}_2\text{O}_3$ ; supplier: CrysTec, Germany). For this means, 5 nm Ti (BAL-TEC, Germany) and 100 nm Pt (99.95 % pure, OEGUSSA, Austria) were sputter deposited and micro-structured by subsequent photolithography and argon ion-beam etching. In the second step dense but polycrystalline films of LSF or STF were applied on top of the current collectors by pulsed laser deposition. This was done with a 248 nm Kr-F-excimer laser (Compex Pro 201F, Coherent Lambda, Germany) operating 5 Hz pulse rate and 400 mJ pulse energy.

The oxygen background pressure in the PLD chamber and the substrate temperature (measured by pyrometer, (Heitronics, Germany)) and deposition time for each material are given in Table 5.

<b>Material</b>	<b>temperature (°C)</b>	<b>pressure (mbar)</b>	<b>deposition time (min)</b>	<b>desired film thickness</b>
La <sub>0.6</sub> Sr <sub>0.4</sub> FeO <sub>3-δ</sub>	650	0.04	45	300 nm
La <sub>0.6</sub> Sr <sub>0.4</sub> CoO <sub>3-δ</sub>	650	0.04	30	300 nm
SrTi <sub>0.7</sub> Fe <sub>0.3</sub> O <sub>3-δ</sub>	620	0.02	30	300 nm

Table 5. Parameters for the thin film working electrode deposition via PLD.

The PLD targets were synthesized using different methods:

- LSF: commercial La<sub>0.6</sub>Sr<sub>0.4</sub>FeO<sub>3-δ</sub> powder (Sigma-Aldrich).
- STF: solid state reaction of properly weighed SrCO<sub>3</sub>, TiO<sub>2</sub> and Fe<sub>2</sub>O<sub>3</sub> powders.
- LSC: Pechini's method<sup>109</sup>.

All powders were isostatically pressed and sintered at 1200°C and phase purity of the targets was confirmed by powder XRD.

Porous, highly active counter electrodes were applied to the substrate prior to the working electrode by application of LSF paste (La<sub>0.6</sub>Sr<sub>0.4</sub>FeO<sub>3-δ</sub> powder, ethyl cellulose, and  $\alpha$ -Terpineol; all Sigma-Aldrich) and Pt paste (Gwent Electronics, UK), followed by drying and five hour annealing at 850°C in air. A sketch and a micrograph of such a sample with an oxide thin film electrode, containing finger-type current collectors, and a porous LSF-Pt counter electrode is depicted in Figure 34a-b. These samples were mounted between two platinum contacts in the chamber for near-ambient XPS measurements in the ISS beamline at the BESSY II synchrotron in Berlin (Figure 34c).

The sample with La<sub>0.6</sub>Sr<sub>0.4</sub>CoO<sub>3-δ</sub> (LSC) working electrode was prepared in a slightly different manner: Current collecting metal fingers were not required, due to the very high electronic conductivity of  $\sim 1000$  S/cm (see section 7.3.2). Instead, a Ti-Pt layer (5-100 nm) with a 3 mm circular hole was sputter deposited on top of the working electrode. The 3 mm hole was sufficiently small for homogeneous polarization. Moreover, the very high electrode activity of the LSC film required a different type of counter electrode: porous LSC thin films with a polarization resistance of 0.1-0.2  $\Omega\text{cm}^2$  at 600°C in air (at least one order of magnitude below the working electrode ASR)<sup>110</sup> were fabricated via PLD by decreasing the deposition temperature and increasing the chamber pressure to 450°C and 0.4 mbar, respectively.

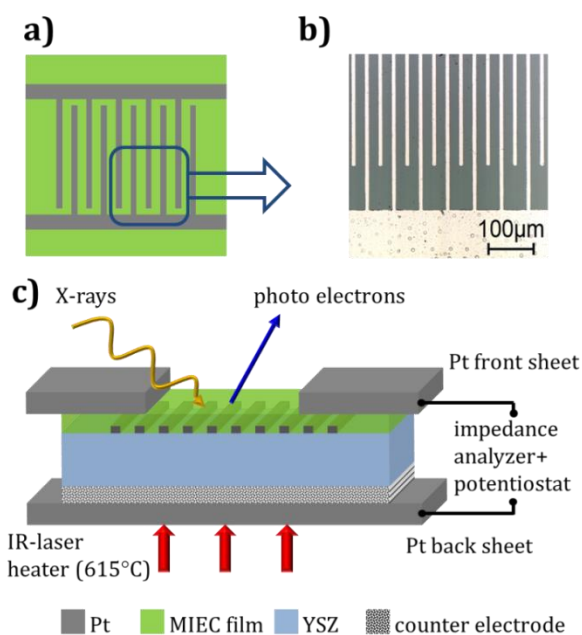


Figure 34. Sketch of the entire working electrode surface (a) and photograph of a part (b). The Pt current collectors (5 μm width, 25 μm distance) were placed beneath the LSF and STF layer to provide good electric contact. (c) Sketched cross section of the sample and mount in the ambient XPS chamber.

### 7.2.2 Near ambient pressure XPS and impedance measurements

The experiments were performed at the ISS beam line of the HZB/BESSY II synchrotron in Berlin with the near-ambient pressure high energy XPS setup (NAP-HE-XPS). In this setup XPS and XAS measurements can be performed at elevated pressures (up to 7 mbar) and X-ray energies from 80 to 2000 eV. The setup consists of a high pressure cell with an attached differentially pumped hemispherical analyzer (modified SPECS Phoibos 150) including a 2D delay line detector. For a detailed description of the setup see ref <sup>111</sup>. A sketch of the sample holder, which was used for in-situ XPS experiments under electrochemical polarization and simultaneous impedance measurements, is shown in Figure 1c. The thin film working electrode was connected to the positive pin of the impedance analyzer/potentiostat and the resulting energy shift of the XPS spectra due to the applied DC-voltage ( $U_{\text{set}}$ ) was subtracted. The porous counter electrode was connected to the grounded contact, which senses the current. This way, the photoemission current does not influence the electrochemical current measurement. Samples were heated via irradiation of the platinum back sheet by an infrared laser. The temperature was controlled by means of a pyrometer measuring the MIEC surface temperature, as well as by the conductivity of the YSZ electrolyte obtained from electrochemical impedance measurements. Both methods consistently yielded temperatures of  $615 \pm 15^\circ\text{C}$ . Measurements in oxidizing atmosphere were carried out in 0.5 mbar  $\text{O}_2$ , the reducing

atmosphere consisted of 0.25 mbar H<sub>2</sub> and 0.25 mbar H<sub>2</sub>O, leading to constant total pressure of 0.5 mbar.

Electrochemical impedance measurements with and without DC bias were carried out by an Alpha-A high performance frequency analyzer equipped with a POTGAL 30V 2A interface (both: Novocontrol, Germany). Impedance spectroscopy was typically performed in a frequency range between 10 mHz and 1 MHz and the AC root mean square voltage was limited to 5 mV to avoid XPS peak broadening. The electrochemically active areas of the electrodes depend on the material and atmospheres and two different situations can be distinguished: (i) In reducing atmosphere, the electronic conductivity of LSF and STF is low (around 0.01 Scm<sup>-1</sup> at 600°C<sup>27, 52</sup>). STF (as a thin film) is also a weak electron conductor in oxidizing atmosphere (around 0.1 Scm<sup>-1</sup>). Therefore, only the area on top of and between the current collecting fingers is electrochemically active (11 mm<sup>2</sup>), cf. Figure 34a. (ii) The electronic conductivity of LSF and LSC in oxidizing atmosphere is significantly higher (>20 Scm<sup>-1</sup>, see section 7.3.2), which is sufficient for homogeneous polarization of the entire free surface area, i.e. 5x5 mm<sup>2</sup> for LSF and a 3 mm diameter circle for LSC. The measured current and impedance values given in this chapter are normalized to these respective areas. Examples of impedance spectra for all three working electrode materials are shown in Figure 35. The main arc represents the electrochemical polarization resistance of the oxide electrode with LSC being most active. The high frequency intercept is caused by the electrolyte resistance. Here, differences are caused by the normalization to the different electrochemically active surface areas.

For electrochemical polarization, set voltages ( $U_{\text{set}}$ ) between +700 mV and -700 mV were applied to the working electrode. The individual cathodic and anodic set voltages were not applied in a linear sequence but rather alternately and partly repeatedly to check for the reversibility and reproducibility of the current-voltage characteristics and XPS features, i.e. to differentiate between reversible bias-induced changes and effects of beam damage or annealing time.

At each set voltage the collection of XPS and impedance data was started after a steady state DC current ( $I_{\text{DC}}$ ) was reached (typically after 2-5 minutes). The electrical measurements were carried out in 2-wire mode, due to the difficulties of the reference electrode placement on a solid electrolyte<sup>112</sup>. The area-specific resistance (ASR) of the porous LSF counter electrode was measured on symmetric samples within the in-situ chamber and found to be ~1.5 Ωcm<sup>2</sup> in 0.5 mbar O<sub>2</sub> and ~5-7 Ωcm<sup>2</sup> in 0.25 mbar H<sub>2</sub> + 0.25 mbar H<sub>2</sub>O at 615°C. This resistance can therefore safely be neglected compared to the working electrode resistance (50-1000 Ωcm<sup>2</sup> on LSF and STF depending on material, polarization and atmosphere). This is also the case for the samples with LSC working

electrode. The overpotential ( $\eta$ ) of the working electrode was therefore calculated according to

$$\eta = U_{set} - I_{DC} * R_{YSZ} . \quad (73)$$

The electrolyte resistance ( $R_{YSZ}$ ) could be easily determined by the high-frequency offset in the impedance spectra. Its value is slightly smaller than the fitting parameter  $R_{hf}$ , which is indicated in Figure 35. The appropriateness of the overpotential determination method was also confirmed by the XPS peak shift of non-redox active species under polarization (see section 7.3.4).

Surface sensitive photoelectron spectra were recorded with different photon energies, (252 eV for Sr 3d, 470 eV for Ti 2p, 650 eV for O 1s, 845 eV for Fe 2p and 975 eV for La 3d). These correspond to kinetic photoelectron energies between 110 and 130 eV, which lead to equal information depth (IMFP) of 0.5-0.57 nm, according to NIST standard reference database 71). For depth profiling, the photon energies were increased in 4 steps, resulting in to photoelectron energies up to 730 eV, and an information depth (IMFP) up to 1.5 nm. Due to the absence of a Fermi edge on the LSF and STF samples, binding energies were calculated using the nominal photon energy, which yields an uncertainty of  $\pm 0.1$  eV due to the monochromator mechanics. This uncertainty was confirmed by measurement on samples containing a Fermi edge feature.

The spectra were fitted with CasaXPS, using a Shirley background and mixed Gaussian-Lorentzian (GL30) peak shapes for the Sr and O components. The Sr 3d region was fitted using two doublets. The components of each doublet were restricted by equal FWHM, fixed doublet separation of 1.7 eV (spin orbit splitting)<sup>113</sup> and area ratio of 2:3. The O 1s region was fitted with 2 independent peaks on STF and 3 independent peaks on LSF and LSC.

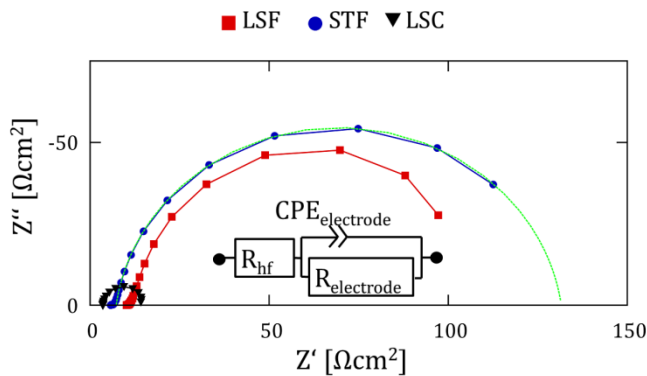


Figure 35. Impedance spectra of LSF (red squares), STF (blue circles) and LSC (black triangles) in 0.5 mbar  $O_2$  at  $615 \pm 15^\circ\text{C}$ . Fitting with a simplified impedance model (green line) enables a reasonable estimation of electrolyte losses and electrode polarization resistance.

## 7.3 Results and discussion

### 7.3.1 Bulk and surface states

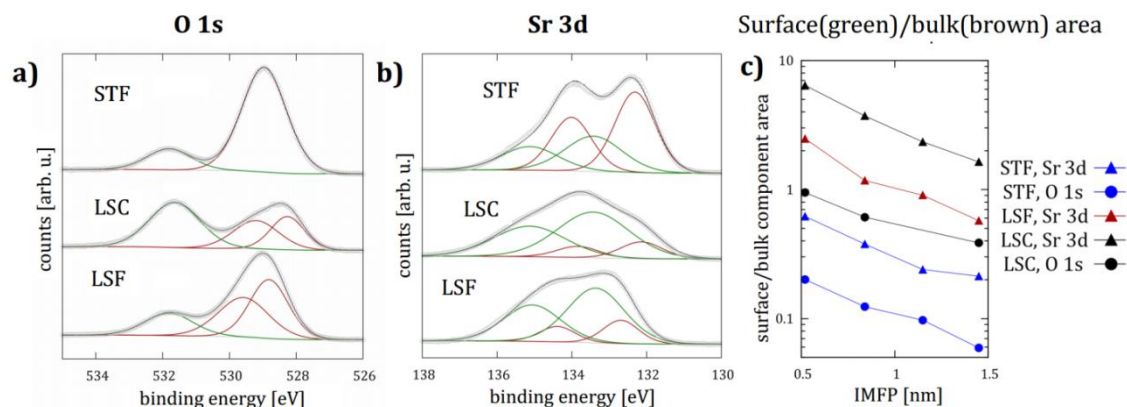


Figure 36. (a) O 1s and (b) Sr 3d spectra of STF, LSC and LSF in 0.5 mbar O<sub>2</sub>, 615°C, U<sub>set</sub> = 0 V. In addition to the fixed doublet separation of Sr 3d<sub>3/2</sub> and Sr 3d<sub>5/2</sub> states, two chemically different components (green and brown) can be fitted to the spectra of Sr and O. c) Plot of the area ratio of the high and low binding energy components as function of the analysis depth (IMFP) by photon energy variation shows strong surface enrichment of the high binding energy components. Both low binding energy O 1s components were summarized as “bulk” oxygen.

XPS spectra of strontium and oxygen obtained on unpolarized STF, LSC and LSF thin films in oxidizing atmosphere are shown in Figure 36a-b. In addition to the doublet splitting, two chemically different Sr species could be identified on all three materials with an energy separation of 0.8 eV on LSF, 1.1 eV on STF and 1.25 eV on LSC (see Figure 36b). In all materials, the area ratio of the high and low energy components strongly depends on the photoelectron inelastic mean free path (IMFP), see Figure 36c. The high binding energy component content is 2.5-4 times larger when comparing the smallest and largest IMFP. Hence, the high energy component can be attributed to a Sr surface species. In line with literature, this suggests a Sr rich surface termination<sup>108, 113</sup>. The O 1s region was fitted with three components on LSC and LSF, consisting of two weakly separated low-binding energy components and one high binding energy component (see Figure 36a). On STF, two well separated components were sufficient for a good fit. Again the IMFP dependence of the component area ratios (Figure 36c) indicates that the high binding energy component is a surface species both on LSF and LSC. Thus, both low binding energy components were summarized as bulk-related oxygen species. The low binding energy of the latter (peak maximum at 528.6-529.2 eV) is typical for perovskite-type oxides<sup>108</sup>. The surface component has a binding energy of 531.5-532 eV. Although small amounts of Si and P were detected, they cannot explain the high amount of surface oxygen. Additionally, impurities accumulated with time, while the surface component intensity decreased. On ceria surfaces in reducing conditions, the surface O1s component in this energy range was

discussed to be associated with surface hydroxyls<sup>23, 26</sup>. However, on perovskites surfaces in oxidizing conditions, adsorbed oxygen species<sup>108</sup> may as well play a role.

On the LSF surface, the surface oxygen component irreversibly disappeared during the first cathodic polarization of the thin film (see Figure 37). Simultaneously, the electrode resistance calculated from the impedance spectra decreased by a factor of 2.5.

The observed O 1s and Sr 3d peak shapes are in line with other ex-situ and also in-situ XPS studies on perovskite-type electrode materials<sup>108, 114-115</sup>. The results can thus be explained by an enrichment of SrO or Sr(OH)<sub>2</sub> on the sample surface. However, no correlation is found between the amount of surface oxygen and surface strontium when comparing the intensities of the three investigated materials. Also, beam damage (on LSC and STF) or cathodic polarization (on LSF) mostly influences the O 1s surface intensity, while the Sr 3d surface intensity remains almost constant. Possibly the Sr rich surface termination only causes a strongly separated O surface species in conjunction with hydroxylation, or originates from an entirely different surface species.

Core level spectra of La 3d (in LSF and LSC) and Ti 2p (in STF) in Figure 40 do not reveal any evidence for the existence of surface species, redox activity or other features typical for the perovskite-type environment.

### **Factors influencing the O1s surface intensity**

The intensity of the surface oxygen component on the LSC and STF samples slowly decreases with irradiation time. When the beam spot is moved to another sample position, the initial surface oxygen intensity is almost restored (Figure 37a-b). On these two materials, electrochemical polarization did not influence the surface oxygen intensity.

In contrast, on LSF the surface oxygen component irreversibly vanishes after an initial cathodic polarization.

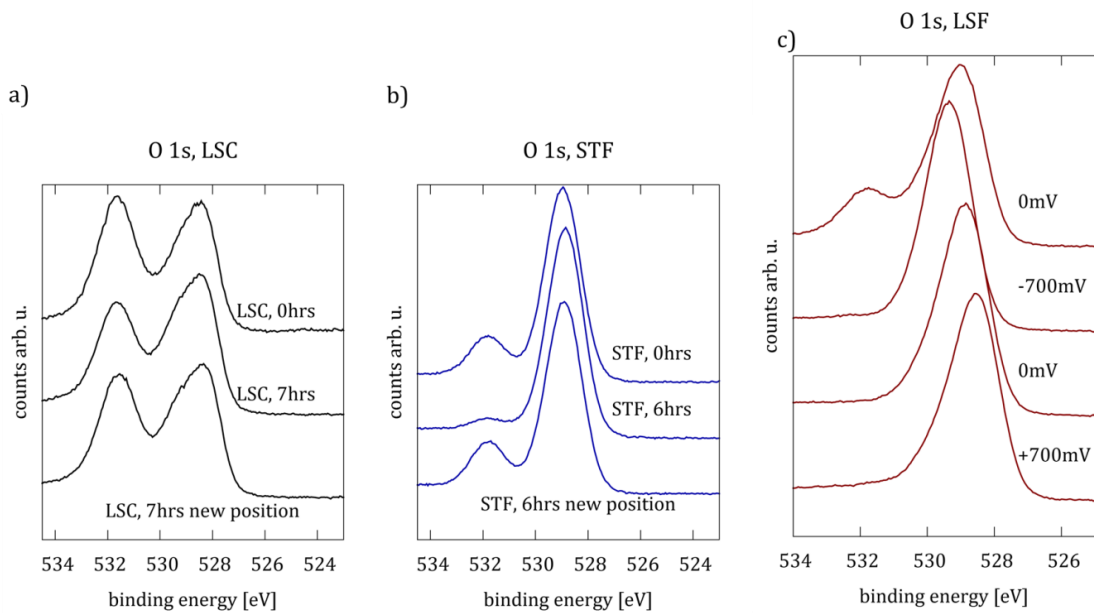


Figure 37. O 1s spectra of LSC (a) and STF (b) in 0.5 mbar O<sub>2</sub> as a function of beam irradiation time. After 6-7 hours of irradiation the high binding energy component – probably OH groups – has decreased in intensity. After moving to a new position, the previous intensity is almost restored. This effect is stronger on STF. (c) Subsequently recorded (top to bottom) XPS spectra of the O 1s region in LSF. The high binding energy (surface) component irreversibly disappears during an initial cathodic polarization, the effect of beam damage could therefore not be explicitly studied – the indicated potential is the set voltage, not  $\eta$ .

### 7.3.2 Electronic conduction mechanism and valence band structure

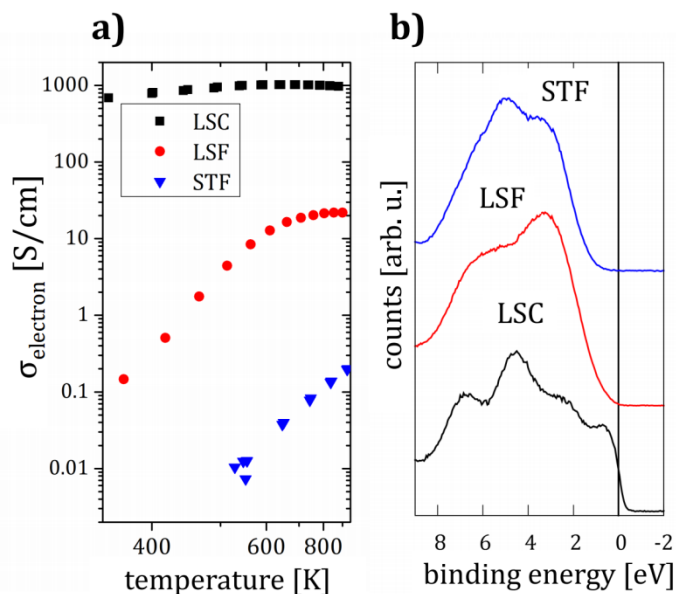


Figure 38. (a) Arrhenius plot of the electronic conductivity of LSC (black squares), LSF (red circles) and STF (blue triangles) thin films in air. (b) Valence band spectra at 615°C in 0.5 mbar O<sub>2</sub>. The conductivity of LSC is virtually temperature independent and a metal-like Fermi edge structure is visible in the valence band spectra. The conductivities of STF and LSF are thermally activated and their valence band structures are semiconductor-like.

The electronic conductivity of the materials was measured on thin films deposited on MgO [100] substrates by the van-der-Pauw method<sup>65</sup>. PLD parameters were equal to the samples investigated by XPS. The temperature dependence of the electronic conductivity and the valence band structure of LSC, LSF and STF are fundamentally different. In the case of LSC, the electronic conductivity is nearly independent of temperature and thermal activation is absent also at low temperature (Figure 38a). The absolute conductivity is only slightly lower when compared to bulk measurements ( $\sim 2000 \text{ Scm}^{-1}$  for bulk LSC at  $450^\circ\text{C}$ <sup>116</sup>). Also the valence band is only partly filled and the photoelectron spectra are cut off with a metal-like Fermi edge at 0 eV binding energy (Figure 38b). This is very different for LSF and STF, where the electronic conductivity is much lower and Arrhenius-type thermally activated, at least at lower temperatures, see Figure 38a. Also the valence band edge is clearly below the Fermi level. The temperature dependence of the conductivity of LSF and STF films are in qualitative agreement with literature bulk data. However, absolute values are 10 times lower and the thermal activation is more pronounced on the thin films<sup>74, 117</sup>. This may be due to different grain boundaries or strain effects in the PLD films.

The conductivity together with the XPS results suggest that in LSF and STF, the electronic defects are localized, which leads to a semiconductor-like behavior. A metallic electronic model appears more applicable for LSC, which is supported by thermogravimetric analysis of  $\text{La}_{0.6}\text{Sr}_{0.4}(\text{Co}_{1-x}\text{Fe}_x)\text{O}_{3-\delta}$  compounds<sup>118</sup>. There, thermogravimetric data is best fitted using a metallic electronic model for LSC and a semiconductor-like model with localized electronic defects fits the data for LSF and STF<sup>42</sup>.

### 7.3.3 Differences between oxidizing and reducing atmosphere

#### Binding energy and Fermi level

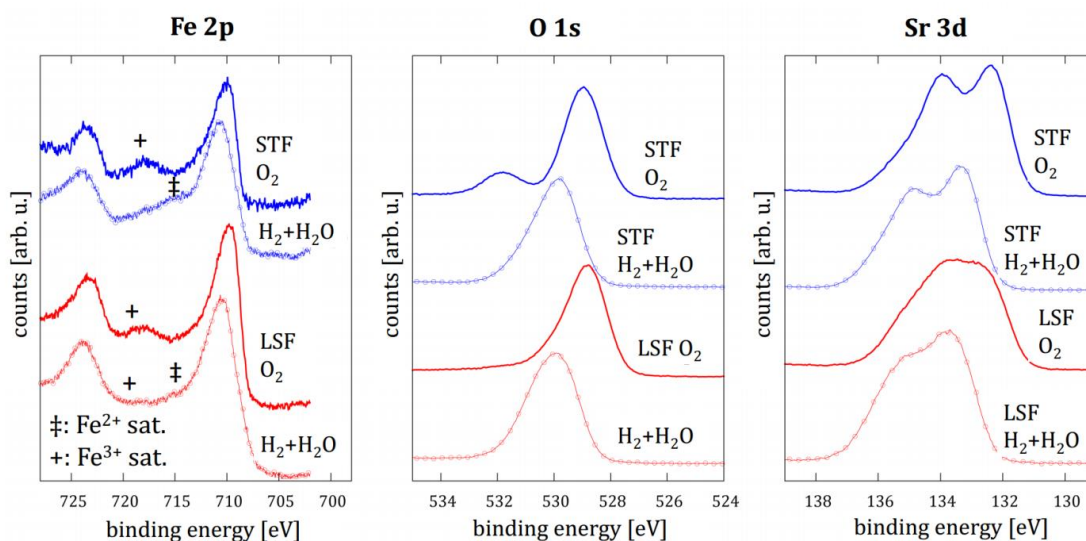


Figure 39. Fe 2p, O 1s and Sr 3d XPS spectra of STF (blue) and LSF (red) in O<sub>2</sub> (thick lines) and H<sub>2</sub>-H<sub>2</sub>O (thin lines + symbols) atmospheres: the binding energy of O and Sr increases by roughly 0.9 eV in reducing atmosphere, due to a Fermi level shift. The oxidation states of O and Sr remain unaffected. The well-separated oxygen component of STF at 532 eV disappears in reducing atmosphere. Satellite features in the Fe 2p spectra appear at 718 eV (indicating Fe<sup>3+</sup>) in oxidizing and 715+718 eV (indicating mixed Fe<sup>2+/3+</sup>) in reducing conditions. Intensities of the spectra were rescaled to compensate different gas-phase absorption and cation composition.

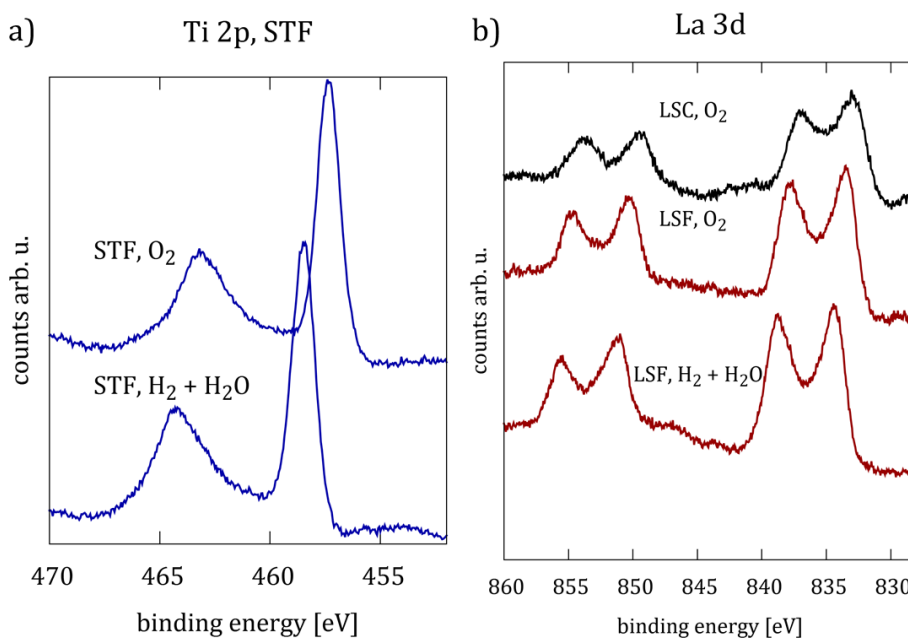


Figure 40 XPS spectra of the Ti 2p (a) and La 3d peaks (b). The Ti 2p<sub>1/2</sub> peak is strongly broadened, which is typical for this component. Also the La 3d region shows doublet splitting and in addition strong satellite features (at 838 and 856 eV). These are caused by a charge transfer to a neighbouring atom. When the atmosphere is changed from oxidizing to reducing, the binding energy increases by roughly 0.9V, due to a Fermi level shift.

XPS and impedance measurements were also performed in H<sub>2</sub>+H<sub>2</sub>O atmosphere and the effect of the different atmospheres is discussed in the following. Figure 39 shows peaks of Sr, O and Fe on LSF and STF in oxidizing and reducing atmospheres at 615°C in the unpolarized state.

Most obviously, the binding energy of all non-transition metal peaks in LSF and STF increases by about 0.8-1 eV in H<sub>2</sub>-H<sub>2</sub>O atmosphere. In order to understand the results, one has to keep in mind that the measured binding energy in XPS is always the energy difference between an occupied electronic level and the Fermi level of the sample. When the Fermi level of a material lies within the band gap (which is the case for LSF and STF at low pO<sub>2</sub>), small changes of the oxygen nonstoichiometry can cause a significant shift of the Fermi level, which influences the binding energy as sketched in Figure 41. Hence, any measured dependence of the binding energy on an experimental parameter may originate from a change of chemical bonding (e.g. oxidation state), or a change of the Fermi level. The relation of binding energies and atmosphere was already attributed to a Fermi level shift on doped ceria<sup>22</sup>. This interpretation is also valid on LSF and STF, which will be shown on a defect chemical basis.

The observed binding energy shift is - within experimental error - equal to the theoretical open circuit voltage of a hydrogen fuel cell operating with 0.5 mbar O<sub>2</sub> at the cathode and a 1:1 mixture of H<sub>2</sub> and H<sub>2</sub>O at the anode (0.89 V at 615°C, <sup>76</sup>). This voltage is related to the different chemical potentials of oxygen in the two atmospheres ( $\Delta\mu_0$ ) by

$$U_{cell} = \left| \frac{\Delta\mu_{O_2}}{4F} \right| \quad (74)$$

When oxygen is exchanged between atmosphere and oxide, the concentrations of oxygen vacancies and electrons change according to the oxygen exchange reaction



This reaction correlates the respective chemical potentials.

$$\frac{1}{2}\mu_{O_2} + \mu_{V_O^{\bullet\bullet}} + 2\mu_{e'} = 0 \quad (76)$$

Also the electron-hole generation



with its respective mass-action constant

$$K_i = c_{e'} c_{h'} \quad (78)$$

affects defect concentrations. The defect thermodynamics of STF and LSF (gained from electronic conductivity isotherms and thermogravimetric measurements<sup>42, 61, 118</sup>) can be described via diluted point defects with normalized concentrations. The chemical potential of each species (x) is then simply given by

$$\mu_x = \mu_x^0 + k_b T \ln c_x \quad (79)$$

Therefore, the chemical potential of ionic defects changes by variation of the oxide ion content  $c_O$  according to

$$\frac{d\mu_{V_O^{\cdot\cdot}}}{dc_O} = \frac{k_b T}{c_{V_O^{\cdot\cdot}}} \frac{dc_{V_O^{\cdot\cdot}}}{dc_O} = -\frac{k_b T}{c_{V_O^{\cdot\cdot}}} \quad (80)$$

For electrons, the situation is slightly more complicated since two types of defects are present. The charge neutrality couples the changes of ionic and electronic defects, e.g.  $d(c_{e'} - c_{h'}) = -2dc_O$ . Also the electron-hole equilibrium (equation (78)) has to be considered. Then we can write

$$-2 = \frac{d(c_{e'} - c_{h'})}{dc_O} = \frac{d\left(c_{e'} - \frac{K_i}{c_{e'}}\right)}{dc_O} = \left(1 + \frac{K_i}{(c_{e'})^2}\right) \frac{dc_{e'}}{dc_O} = \left(1 + \frac{c_{h'}}{c_{e'}}\right) \frac{dc_{e'}}{dc_O} \quad (81)$$

Using this relation, the change of the chemical potential of electrons reads

$$\frac{d\mu_{e'}}{dc_O} = \frac{k_b T}{c_{e'}} \frac{dc_{e'}}{dc_O} = \frac{k_b T}{c_{e'}} \left(-\frac{2}{1 + \frac{c_{h'}}{c_{e'}}}\right) = \frac{-2k_b T}{c_{e'} + c_{h'}} \quad (82)$$

For large parts of the oxygen partial pressure range between the used oxidizing and reducing conditions the concentration of oxygen vacancies is much larger than of electronic defects ( $c_{e'} + c_{h'} \ll c_{V_O^{\cdot\cdot}}$ ). Only above 0.1 mbar, oxygen vacancies may become the minority charge carriers in LSF bulk. Consequently, we see from comparing equations (80) and (82) that the change of the chemical potential of ionic defects is much smaller than for electronic ones

$$\frac{\partial \mu_{V_O^{\cdot\cdot}}}{\partial c_O} \ll \frac{\partial \mu_{e^-}}{\partial c_O} \quad (83)$$

Therefore (see equation (76)) we find

$$\Delta \mu_{O_2} \approx -4 \Delta \mu_{e'} \quad (84)$$

Since the electrochemical potential of electrons is proportional to the Fermi level, its change can be written as

$$\Delta\mu_{e'} = F\Delta E_f \quad (85)$$

In combination with equation (74), the Fermi level shift can now be calculated as

$$|\Delta E_f| \approx U_{cell} \quad (86)$$

Therefore, a binding energy shift of  $\sim 0.9$  eV can be explained by a shift of the Fermi level within the band gap. It does not indicate any chemical changes and the energy distance to the vacuum level remains constant – cf. Figure 41. Please note that such a change would not occur if oxygen vacancies were minority charge carriers also near the sample surface.

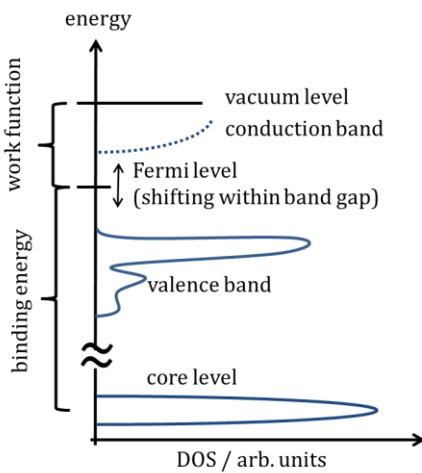


Figure 41. Changes of the defect chemistry under varying  $pO_2$  cause a shift of the Fermi level within the band gap. Accordingly the measured binding energy shifts – also for elements that do not undergo chemical changes.

### Chemical State Effects

In addition to the Fermi level shift, also the surface oxygen species (presumably OH) on STF vanishes in reducing atmosphere (on LSF this species already vanishes after an initial cathodic polarization) and the energy separation between surface and bulk Sr components becomes slightly smaller in reducing atmosphere, which explains the subtle change in the Sr peak shape in Figure 39. For LSF an unambiguous deconvolution of bulk and surface Sr is no longer possible in reducing atmosphere.

The peak shift of Fe (Figure 39) between the two atmospheres is much smaller than  $\Delta E_f$  ( $\sim 0.4$  eV vs 0.9 eV). Also the satellite features at 715 and 718 eV differ in oxidizing and reducing conditions. Comparison of this observation with literature data<sup>119</sup> on FeO, Fe<sub>3</sub>O<sub>4</sub> and Fe<sub>2</sub>O<sub>3</sub> samples indicates that Fe<sup>3+</sup> is dominant in oxidizing atmosphere and mixed Fe<sup>2+/3+</sup> states with similar amounts are formed under reducing conditions. Defect chemical bulk data for LSF in Ref.<sup>47</sup> predict a Fe<sup>2+</sup> fraction around 1.7%. Very similar values (1.5% for LSF and 2.5% for STF) were found when the Fe<sup>2+</sup> fraction is estimated from the chemical capacitance of the electrode semicircle, which is described in<sup>27</sup> and in the

supporting info. This is much less than estimated from the XPS results, which show comparable amounts of Fe<sup>2+</sup> and Fe<sup>3+</sup> on the sample surface. This indicates higher reducibility of surface cations, similar to ceria-based materials<sup>22</sup>. However, precise quantification of the relative amounts of Fe<sup>2+</sup> and Fe<sup>3+</sup> in reducing atmosphere is not straightforward, because the sample surface is possibly not entirely perovskite-terminated. A high temperature XRD study<sup>27</sup> of LSF powder of the same composition revealed the evolution of secondary phases near the surface in reducing conditions.

#### 7.3.4 XPS under electrochemical polarization

In addition to atmosphere variations also the effect of electrochemical polarization on the electrode surface chemistry was studied. The overpotential of the working electrode ( $\eta$ ) was calculated according to equation (73). Depending on the exact electrochemical properties of the electrode, the surface reaction as well as electronic or ionic charge transport may be rate-limiting. In oxidizing atmosphere several recent studies and own experiments showed that thin film electrode kinetics of LSC<sup>110</sup>, LSF<sup>27</sup> and STF<sup>70</sup> are limited by the electrochemical surface reaction when long distances from the current collectors are avoided. Previous electrochemical investigations in H<sub>2</sub>/H<sub>2</sub>O atmosphere<sup>27,52</sup> revealed that a current collector with small structures, allowing for short range charge transport through the electrode layer, is important to achieve homogeneous electrode polarization and surface limited electrode kinetics. According to these findings, the used current collectors beneath the electrode (5  $\mu\text{m}$  width, 25  $\mu\text{m}$  distance) are sufficiently fine for our LSF and STF films. In the case of surface reaction limited electrode kinetics, application of an overpotential ( $\eta$ ) changes the chemical potential of oxygen ( $\Delta\mu_{\text{O}_2}$ ) within the working electrode bulk homogeneously according to<sup>52</sup>

$$\Delta\mu_{\text{O}_2} = 4F\eta . \quad (87)$$

When oxygen vacancies are the majority charge carrier, the change in the chemical potential of oxygen changes the chemical potential of electrons (equation (84)) and therefore the Fermi level (equation (85)), which can be combined with equation (87) to

$$\Delta E_f = -\eta \quad (88)$$

In analogy to the observed binding energy shift between oxidizing and reducing atmospheres we therefore expect slopes of -1 eV/V when plotting the binding energy of non-redox-active elements as a function of the overpotential. This linear correlation was found in reducing atmosphere on ceria<sup>23</sup> and in oxidizing conditions on acceptor doped lanthanum ferrite based perovskites<sup>44</sup>.

## Polarization in oxidizing atmosphere

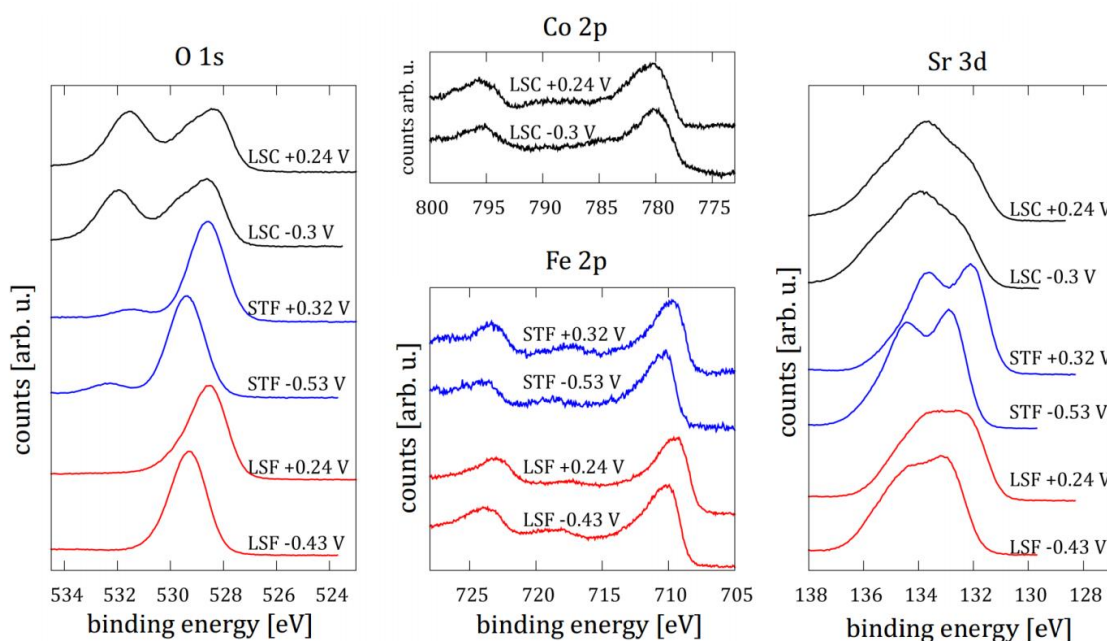


Figure 42. O 1s, Fe 2p, Co 2p and Sr 3d core level XPS spectra of LSC (black), STF (blue) and LSF (red) thin films under polarization (indicated voltage). No significant changes in surface and bulk states or transition metal satellite features are observed upon bias. Spectra were measured at photoelectron energies of 120-140 eV and scaled to compensate for different Sr and Fe contents.

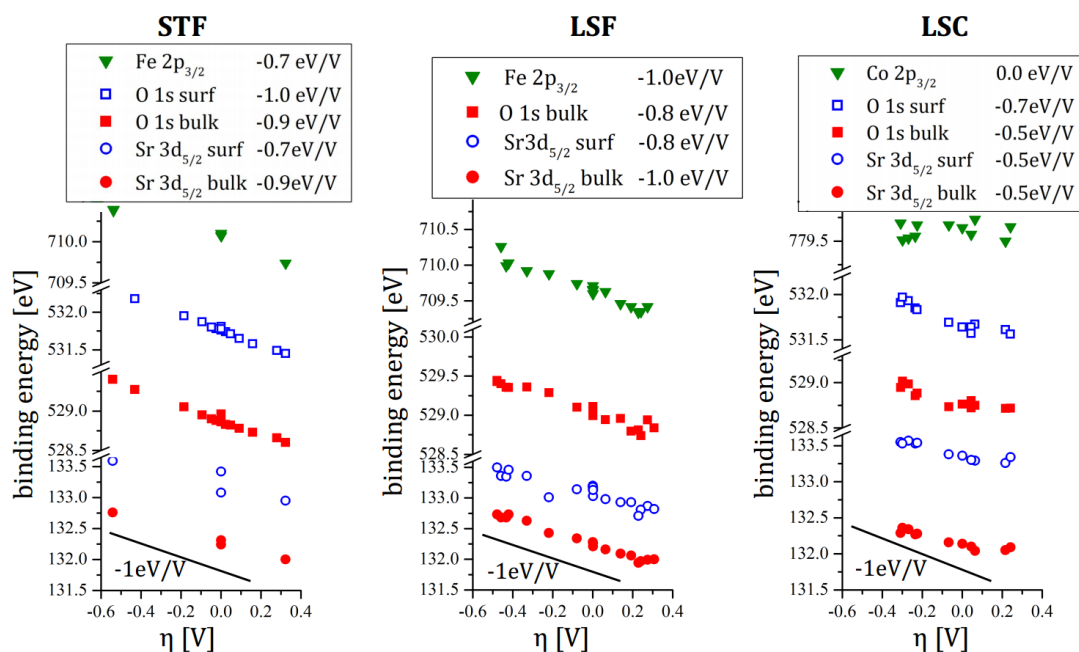


Figure 43. Peak positions as a function of overpotential in 0.5 mbar O<sub>2</sub>. On LSF and STF, all peaks shift with slopes of -0.7 to -1.0 eV/V, which is largely caused by a Fermi level shift. On LSC the slopes are significantly smaller (-0.5 to -0.7 eV/V) and the Co 2p peak does not shift at all. Most likely, the metallic electronic structure of LSC and the higher reducibility of Co ions cause the differences.

Examples of XPS spectra measured on LSC, STF and LSF during polarization in 0.5 mbar O<sub>2</sub> are shown in Figure 42. Except for the Co 2p peak all signals show significant energy shifts. The shifts were quantified and summarized in Figure 43. The valence band edge position is the zero crossing of a line fit at the turning point. All peak positions of LSF and STF shift with slopes close to the theoretical value of -1eV/V expected from the Fermi level shift (equation (88)). Slight deviations may have different reasons: data scattering and partly insufficient number of data points, a slight underestimation of the DC-case electrolyte resistance or resistance of the porous counter electrode. Changes in the surface potential step ( $\chi$ ) by surface dipoles may play a small role as well, see also below. Please note that the shift is due to the overpotential  $\eta$ , and the electrostatic effect of the working electrode potential ( $U_{\text{set}}$ ) is already subtracted. These results can also be seen as a validation of the method overpotential calculation<sup>23, 44</sup>. Moreover it supports our initial assumption of homogeneous electrode polarization and rate limiting surface kinetics. Also the effect of bias and atmosphere on the chemical capacitance of LSF fits well to literature data on bulk defect chemistry – for details see section 7.3.5.

The very weak effect of polarization on the chemical states of iron is particularly interesting. The defect chemical models of LSF and STF<sup>61, 118</sup> bulk in oxidizing atmosphere predict mixed Fe<sup>3+</sup>/Fe<sup>4+</sup> at anodic polarization (higher  $\mu_0$ ) and mostly Fe<sup>3+</sup> at cathodic polarization (lower  $\mu_0$ ). However, neither the binding energy nor the satellite structure of the Fe 2p peaks (Figure 42) indicate any chemical changes and only satellite features indicating Fe<sup>3+</sup> can be assigned at all bias values. The lack of spectroscopic evidence for Fe<sup>4+</sup> may have two reasons. Firstly, XPS is very surface sensitive with an information depth of  $\sim 1.5$  nm at the highest used photon energy. Given the trend that oxide surfaces are often easier reducible than the bulk, absence of Fe<sup>4+</sup> on the surface is not surprising. Additionally, recent studies highlight the degree of hybridization of the transition metal 3d and oxygen 2p orbitals in perovskites<sup>45</sup>. An X-ray absorption study on various acceptor doped lanthanum ferrite-based perovskites<sup>44</sup> also revealed changes in the occupancy of O 2p-like orbitals as function of overpotential. This study states that the electron hole is mainly located at O<sup>-</sup> anions instead of the Fe atom. Therefore an electron hole (i.e. a formal Fe<sup>4+</sup> ion) may only weakly differ from a Fe<sup>3+</sup> ion in the XPS spectra. When anodic bias is applied to the LSF electrode, bulk defect chemistry predicts that oxygen vacancies become minority charge carriers (equation (83) is not valid in this regime). The Fermi level should then be only weakly influenced by bias ( $\Delta E_f \ll \eta$ ). According to the defect chemistry of idealized LSF bulk the peak shift is expected to vanish for  $\eta > 0$ , which was not observed, see Figure 43; a possible surface space charge layer may play a role here.

The response of LSC to bias is somewhat different. The peaks shift significantly less with overpotential – slopes are between -0.3 to -0.7 eV/V for non-transition metals. The Co 2p peaks do not shift at all and the applied bias causes a very subtle change in the Co 2p satellite features between 785 and 790 eV, which can be used as an indication for the oxidation state. This is an indication for the redox activity of cobalt, but the effect is too weak for a quantitative analysis of oxidation states. The different response of LSC compared to STF and LSF is most probably related to its metal-like electronic structure and the resulting fundamentally different relation between oxygen nonstoichiometry, Fermi level and oxygen partial pressure<sup>118</sup>. However, a thorough discussion of the electronic defect structure of LSC is beyond the scope of this thesis.

In a theoretical model of electrochemically driven oxygen exchange at solid-gas interfaces a potential step ( $\chi$ ) between the electrode bulk and an oxygen adsorbate was considered<sup>120</sup>. According to this model, adsorbate concentration and the potential step should drastically change when the electrode is polarized and for a rate limiting charge transfer this would strongly affect the current-overpotential characteristics. A substantial change of adsorbate coverage and  $\chi$  with  $\eta$  should lead to significant deviations in the energy separation and amount of surface and bulk states with  $\eta$ .

However, in our study neither the intensities nor the energy separation of surface and bulk components change substantially upon polarization, as visible in Figure 42 and Figure 43. Small differences in the slopes in Figure 43 are still within statistical errors. Only the LSF surface oxygen component, irreversibly vanishes after an initial cathodic polarization. This suggests that the observed oxygen and strontium surface species are not directly involved in the surface reaction and that the reaction intermediates have a rather low surface coverage.

## Polarization in reducing atmosphere – Redox activity of iron

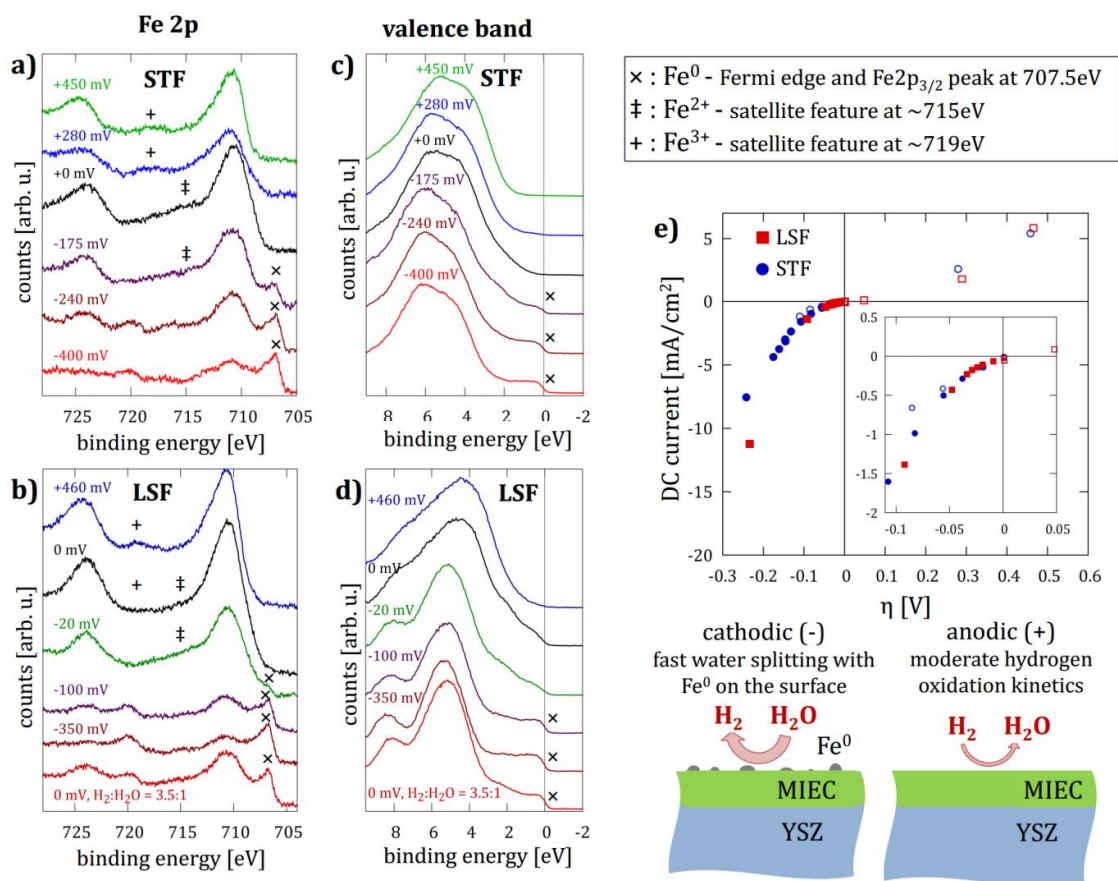


Figure 44. Valence band and Fe 2p XPS spectra of STF (a,c) and LSF (b,d) polarized by different overpotentials in  $\text{H}_2/\text{H}_2\text{O}$  atmosphere. Each spectrum is plotted with the same scale. Near-surface Fe gets gradually reduced from  $\text{Fe}^{3+}$  to  $\text{Fe}^{2+}$  with decreasing anodic bias. Upon cathodic polarization, an additional  $\text{Fe}^0$  species evolves, visible by the evolution of a Fermi edge feature in the valence band ( $\times$ ) and an additional Fe  $2p_{3/2}$  peak at 706.5 eV ( $\times$ ). Simultaneously, a strong decrease in the total Fe signal is observed. The applied overpotentials are indicated for each spectrum. e) DC-characteristics of LSF (red squares) and STF (blue circles). When  $\text{Fe}^0$  is present during cathodic polarization (filled symbols), the current increases strongly nonlinear already for very small bias (inset).

Also in reducing atmosphere, the relation of overpotential and binding energies gives slopes between -0.8 and -1 eV/V for all elements but iron (not shown). This suggests that these elements do not undergo valence changes upon polarization and that merely the Fermi level shift influences their binding energies. Iron, however, shows significant chemical changes: at open-circuit voltage, the satellite structure indicates mixed  $\text{Fe}^{2+}/\text{Fe}^{3+}$  valence near the surface. Anodic bias increases the amount of  $\text{Fe}^{3+}$  and for both LSF and STF no  $\text{Fe}^{2+}$  satellite features are present when  $\eta \geq +280$  mV (see Figure 44a-b). The gradual change in the surface iron oxidation state is also confirmed by the much smaller shift of the iron peak positions relative to non-redox active elements upon polarization. Cathodic bias increases the amount of  $\text{Fe}^{2+}$  and even leads to the formation of  $\text{Fe}^0$ . The amounts of oxidic and metallic Fe were quantified with a simplified peak model of the

Fe 2p<sub>3/2</sub> peak consisting of one oxidic (Fe<sup>2+/3+</sup>) and one metallic (Fe<sup>0</sup>) Fe component<sup>84</sup>. This model is a simplification, but robust in the quantification of the relative amounts of both components.

The formation of metallic iron is accompanied by a strong decrease of the total iron signal intensity (Figure 44a-b and 10b), the formation of a Fermi-edge feature in the valence band spectra (Figure 44c-d) and a distinct increase of the water splitting activity, as seen by the strongly asymmetric current-voltage characteristics (Figure 44e) and the decrease of the electrode polarization resistance (Figure 45a). On LSF, these effects were more pronounced, which is discussed in detail in ref <sup>84</sup>. There the formation and re-oxidation of metallic iron is highly reversible. It occurs already at an overpotential of -20 mV and the Fe<sup>0</sup> peak vanishes at open circuit potential. Also lowering the chemical potential of oxygen in the atmosphere by increasing the hydrogen content leads to formation of Fe<sup>0</sup> (lowest spectra in Figure 44b and d).

On STF some hysteresis in the evolution and re-oxidation of Fe<sup>0</sup> is observed. Also polarization resistance changes by Fe<sup>0</sup> are less pronounced on STF (Figure 45a). An overpotential of -150 mV is required for the formation of Fe<sup>0</sup>, while full re-oxidation of Fe occurs close to 0V (Figure 45b). This hysteresis is also reflected in the electrochemical characteristics: Without the presence of metallic Fe (open circles in Figure 44e, inset) the electrode current is smaller, despite equal polarization. This can be interpreted as additional evidence that the strong non-linearity of the current-voltage characteristics is indeed related to the presence of Fe<sup>0</sup> on the surface.

The almost step-like change of metallic Fe content with overpotential (which is proportional to the chemical potential of oxygen) is characteristic for a phase change. A very recently conducted surface XRD study on similar LSF thin films, however, showed that the evolution of a second metallic Fe phase does not lead to a decomposition of the perovskite. Rather only a small fraction of the total Fe content is exsolved - and the perovskite lattice stays intact. The total decomposition of the perovskite is most likely hindered kinetically in thin films, because coulometric titration<sup>47</sup> and XRD measurements<sup>27</sup> on LSF powder revealed total decomposition at oxygen partial pressures < 10<sup>-27</sup> bar, corresponding to  $\eta < -0.13V$  in 1:1 H<sub>2</sub>+H<sub>2</sub>O atmosphere, which was fulfilled in this study.

Exsolution of highly dispersed transition metal nanoparticles from a perovskite-type host material has already been observed on copper, nickel or palladium-doped perovskites and vanadates by SEM and XRD studies<sup>51, 85, 121</sup> and could be correlated to enhanced hydrogen electrode kinetics. Also in our study, Fe<sup>0</sup> is most likely present in nanosize form with a diameter larger than the photoelectron mean free path. Hence, most of the Fe<sup>0</sup> is not

detected by XPS and the total Fe intensity decreases (Figure 45c). Also depth-profiling (not shown) shows no significant surface enrichment or depletion of Fe<sup>0</sup>, which rules out a metallic surface or subsurface layer.

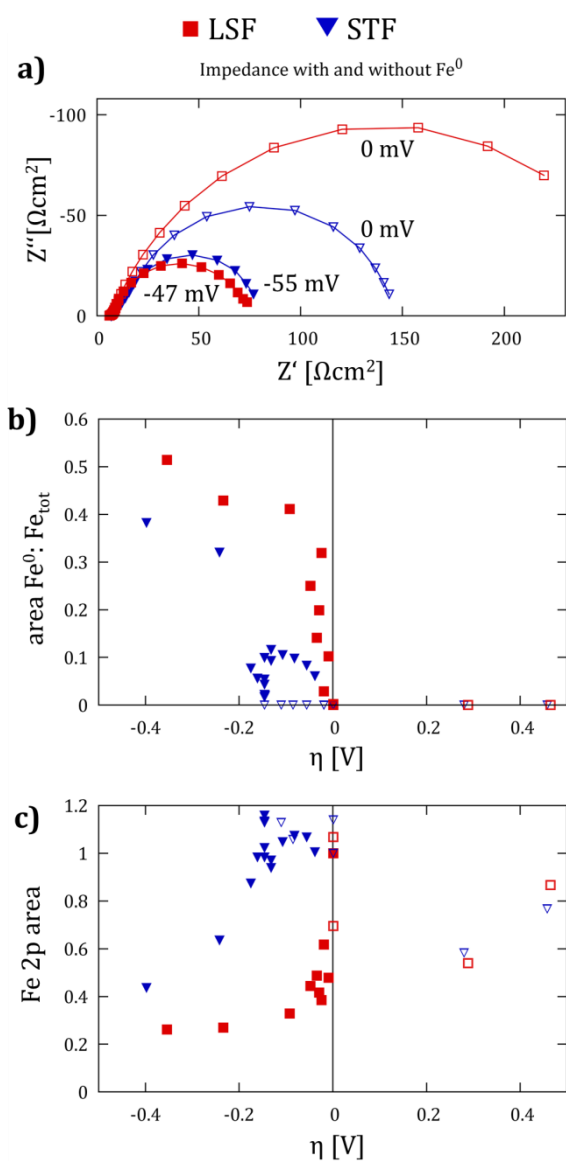


Figure 45. a) Impedance spectra measured on LSF and STF electrodes in H<sub>2</sub>/H<sub>2</sub>O with (solid symbols,  $\eta \approx -50$  mV) and without (open symbols,  $\eta = 0$  mV) the presence of Fe<sup>0</sup>. A strong decrease of the electrode resistance is observed already at very low  $\eta$ , especially for LSF. b) Total Fe 2p<sub>3/2</sub> signal intensity (normalized to the initial area) showing a drastic decrease when Fe<sup>0</sup> is formed. c) Ratio of metallic to total Fe signal intensity. The reduction and oxidation of Fe is reversible on LSF and shows a slight hysteresis on STF.

### 7.3.5 Oxygen partial pressure ( $pO_2^{eff}$ ) dependent chemical capacitance as an indicator for the defect chemical regime

Impedance spectroscopic measurements were carried out simultaneously to the XPS investigation. The determination of the electrolyte resistance allowed for a separation of electrode and electrolyte overpotential. Furthermore the spectra were fitted with a simple equivalent circuit, consisting of a resistor representing the electrolyte resistance and a parallel connection of resistor and constant phase element, representing the electrode impedance. Using this circuit model, the chemical capacitance was estimated by equation (9). This capacitance can be plotted as a function of the effective oxygen partial pressure ( $pO_2^{eff}$ ), which depends on the atmospheric  $pO_2$  and the electrode overpotential, according to equation (11). In addition to the measured chemical capacitance, the defect models elaborated in chapter 2.3 were used to calculate the expected chemical capacitance of STF and LSF bulk. Oxygen nonstoichiometry data from<sup>32</sup> was used to determine the equilibrium constants  $K_{red}$  and  $K_i$  in equations (2) and (4).

These results are shown in Figure 46 and Figure 47. Blue symbols indicate data points recorded in reducing atmosphere (1:1  $H_2:H_2O$ ), red points indicate data recorded in oxidizing conditions (0.5 mbar  $O_2$ ). The solid black lines represent the theoretical defect model.

The oxygen partial pressure dependence of the measured chemical capacitance qualitatively follows the relation expected from bulk defect chemical data. Quantitatively, however, the measured slopes of  $\log(C_{chem})$  vs  $\log(pO_2^{eff})$  are often shallower than the defect chemical model. An extensive study on the relation of chemical capacitance and bulk defect chemistry is currently carried out by Ghislain Rupp and Alexander Schmidt. It is also important to note, that metallic Fe evolves on the surface of the surface of these highly Fe containing perovskites when the effective  $pO_2$  becomes smaller than  $10^{-22}$  mbar, suggesting in line with literature that the 1:1  $H_2:H_2O$  atmosphere is close to the thermodynamical stability limit of the single phase perovskite.

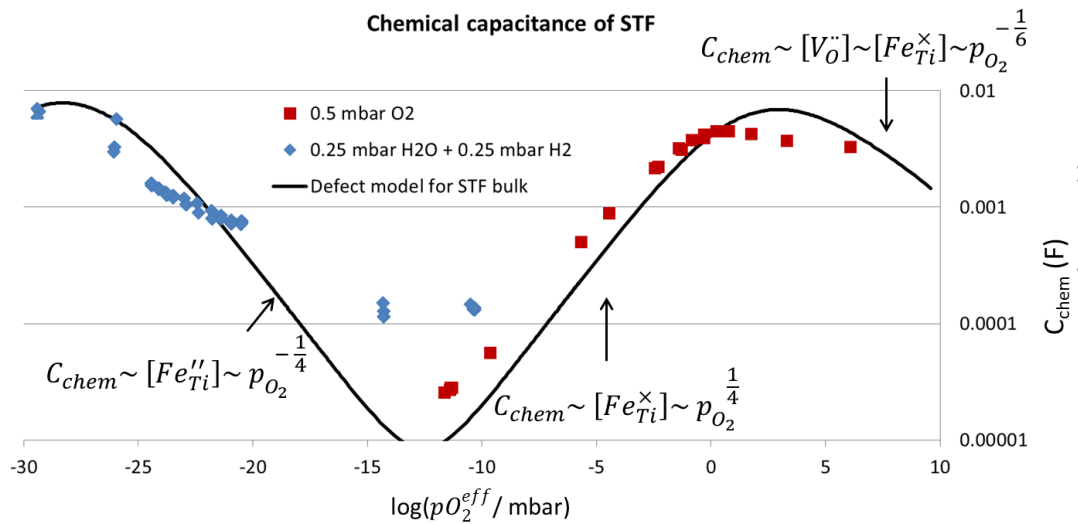


Figure 46. Measured chemical capacitance of the LSF electrode as function of the effective oxygen partial pressure at 600°C. The open circuit  $p_{O_2}$  is 0.5 mbar in oxidizing and  $3 \cdot 10^{-21}$  mbar in reducing conditions. Solid line: calculated chemical capacitance of idealized STF bulk (volume: 300 nm thickness,  $11 \text{ mm}^2$  area), using oxygen nonstoichiometry data from<sup>32</sup>. The different defect regimes correspond well with the measured chemical capacitance.

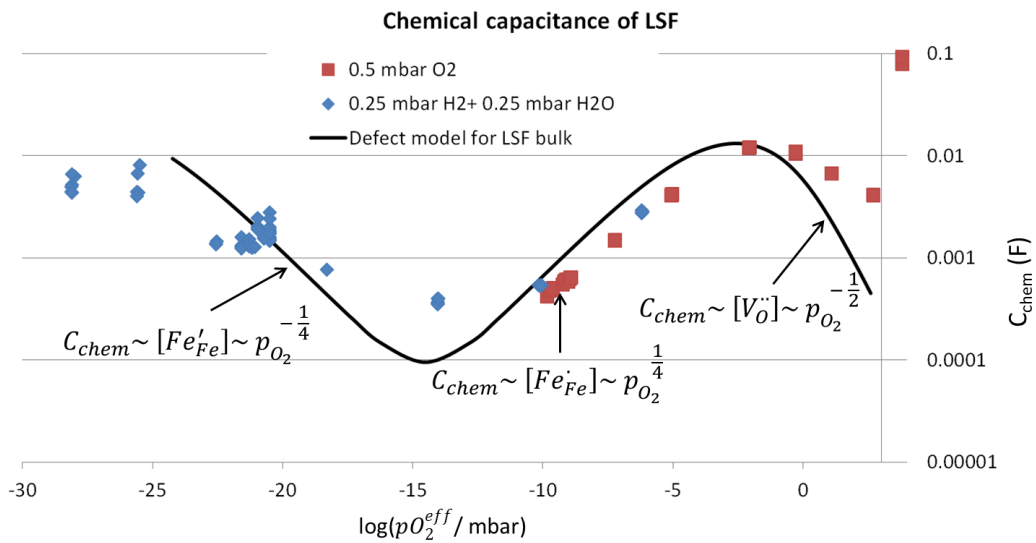


Figure 47. Measured chemical capacitance of the LSF electrode as function of the effective oxygen partial pressure at 600°C. The open circuit  $p_{O_2}$  is 0.5 mbar in oxidizing and  $3 \cdot 10^{-21}$  mbar in reducing conditions. The increased scatter under reducing conditions is probably connected with the segregation of  $Fe^0$ . Solid line: calculated chemical capacitance of idealized LSF bulk (volume: 300 nm thickness,  $11 \text{ mm}^2$  area), using a defect chemical model from Ref.<sup>47</sup>. The different defect regimes correspond well with the measured chemical capacitance.

## 7.4 Conclusions

Near-ambient XPS studies revealed numerous details of the surface chemistry of  $\text{SrTi}_{0.7}\text{Fe}_{0.3}\text{O}_{3-\delta}$  (STF),  $\text{La}_{0.6}\text{Sr}_{0.4}\text{FeO}_{3-\delta}$  (LSF) and  $\text{La}_{0.6}\text{Sr}_{0.4}\text{CoO}_{3-\delta}$  (LSC) thin films in different atmospheres and upon electrochemical polarization. Simultaneous electrochemical impedance spectroscopy measurements allowed determination of the actual working electrode overpotential and oxygen exchange activity.

In oxidizing atmosphere, the valence band edges of LSF and STF are slightly below the Fermi level, which indicates localized electronic defects, while the valence band edge spectra of LSC reveal a metal-like electronic structure. The temperature dependence of the electronic conductivity supports this interpretation: The electronic conductivity is thermally activated for LSF and STF but almost temperature independent in LSC.

Binding energies of non-redox active elements (Sr, La, O, Ti) in LSF and STF showed a pronounced dependence on the atmosphere and the electrochemical polarization. The binding energy shift corresponds to the Fermi level shift expected from defect chemical models for changing the chemical potential of oxygen. This accordance is a strong indication of well-defined and homogeneous electrode polarization and rate-limiting surface kinetics.

High binding energy components located at the surface were found for strontium and oxygen on all three samples in oxidizing atmosphere. In good agreement with other studies, the surface is presumably enriched in SrO and/or  $\text{Sr}(\text{OH})_2$ . A separate surface oxygen component could not be identified in reducing atmosphere. The energy separation and relative amount of these surface components did not change significantly during electrochemical polarization.

Only the transition metals iron and cobalt appear to undergo valence changes. In oxidizing atmosphere near-surface iron is present as  $\text{Fe}^{3+}$ , irrespective of the polarization. In reducing atmosphere, iron is present in the oxidation states as  $\text{Fe}^{3+}$ ,  $\text{Fe}^{2+}$  and  $\text{Fe}^0$ . The relative amounts of these oxidation states strongly depend on the polarization. The evolution of a  $\text{Fe}^0$  phase under cathodic polarization can drastically increase the water splitting activity, particularly on LSF.

## 8 XPS investigation of polarized SOFC anodes at operation temperature in UHV

### 8.1 Introduction

Typically, UHV-based photoelectron spectroscopy of SOFC electrode materials is used *ex-situ* to detect compositional changes after various types of surface treatment or after cell operation<sup>114, 122-123</sup> and subsequent quenching. However, the very different temperature and atmospheric conditions of electrode operation and analysis only allow limited information on oxidation states of the elements and no information at all about adsorbed species during operation. These problems can be partly overcome in ambient pressure XPS experiments, which are typically carried out at synchrotron facilities, see chapter 7.

Still, identification of reacting or catalysing surface species in ambient pressure XPS is not straightforward. This is partly caused by the broken symmetry at the surface. This changes (typically lowers) the enthalpy and entropy for oxygen vacancy formation at the surface, which was already shown for ceria<sup>22</sup>. Also, segregation of certain cations, such as Sr<sup>87, 114-115, 122</sup> is a common phenomenon. These effects may additionally cause a surface potential and compositional gradient, and it is conceivable that such surface effects cause surface species identifiable by XPS but need not be related to the electrochemical surface reaction. The existence of non-reacting surface species also complicates the identification of atmospheric adsorbates and reaction intermediates. Hence, a method of differentiating between effects caused by adsorbed or catalysing surface species and by the mere broken symmetry at the oxide surface is of high relevance for a more insightful interpretation of ambient pressure XPS measurements.

One promising strategy to gain complementary information to ambient pressure XPS measurements is to perform similar measurements without the presence of a gas phase. This provides a reference surface state without the presence of adsorbed species. For a meaningful reference, temperature and chemical potential of oxygen in the material (effective  $pO_2$ ) should equal to the APXPS conditions, which can be achieved by usage of a properly designed electrochemical model cell with thin film working electrode, and a thicker, porous counter electrode. During the measurements, this cell is then heated and electrochemically polarized.

Unfortunately, an effective bulk  $pO_2$  close to 1 atmosphere in UHV at elevated temperature inevitably causes oxygen loss and therefore varying oxygen content in the electrode and high background pressure. Therefore, such investigations of SOFC cathode materials are impossible in UHV. However, for the investigation of fuel side electrode materials, the effective oxygen partial pressure can be varied between  $\sim 10^{-3}$  mbar (roughly the limit where significant oxygen release becomes critical) and the decomposition  $pO_2$  of either electrode or electrolyte, simply by applying a voltage to an electrochemical model cell. This pressure range covers the operation conditions of fuel cell as well as electrolysis cell electrodes.

In this chapter, details about the design and annealing procedure of the electrochemical model cell, the adaption of the commercial XPS sample holder for high sample temperature, as well as the experimental procedure of the XPS measurements are elaborated. Additionally, preliminary results on the oxidation states of Fe in LSF and STF, as well of Ni and Cr in  $La_{0.7}Sr_{0.2}Cr_{0.9}Ni_{0.1}O_{3-\delta}$  are presented as a function of information depth (by variation of the photoelectron emission angle) and effective  $pO_2$ .

## 8.2 Experimental

### 8.2.1 Adaption of the 1" type sample holder for steady state high temperature experiments

The commercially available 1" type sample holders by SPECS consist of a 1.5 mm thick rectangular sheet of molybdenum, which has a bayonet joint attached – see Figure 48. These sample holders can be heated by an electron bombardment heater, capable of a filament voltage up to 1000 V and emission current up to 100 mA.

However, operation at the maximum power is only possible for short-term heating (sample flashing). For steady state experiments, thermal decoupling between heated zone and sample stage is crucial to achieve high sample temperature without heating the stage above 300°C. Furthermore, proper electric insulation of sample and sample stage is required for application of a sample bias, which is sketched in Figure 48. The modifications to the commercial sample holder were as follows:

A 10 mm hole was drilled into the electron bombardment heated centre of the sample holder, and covered by a 1.5 mm thick, 15 mm diameter quartz disk. For proper function of the electron bombardment heater and electrical contacting, Pt paste was applied to both sides of the quartz disk (without electrical connection) and sintered at 1200°C for 5 hours.

Quartz is known for low linear thermal expansion ( $\sim 10^{-6} K^{-1}$ ). This is essential as it prevents the risk of cracking due to temperature gradients or rapid heating and cooling.

Also the low thermal conductivity of quartz ( $\sim 2 \text{ Wm}^{-2}\text{K}^{-1}$ ) is beneficial for thermal decoupling. When the electron-heated centre of the disk has a surface temperature of  $600^\circ\text{C}$ , the perimeter of the disk is expected to be several hundred  $^\circ\text{C}$  colder due to thermal radiation losses. The temperature difference between top and bottom of the quartz disk is expected to be no larger than  $25^\circ\text{C}$ . Further thermal decoupling was achieved by reducing the mechanical contact area between quartz disk and sample holder by sintering small pieces of  $0.1 \text{ mm}$  Pt wire to the bottom of the disk, which reduces the actual mechanical contact area to a small fraction of a square millimetre.

In addition to thermal decoupling, the top of the quartz disk is also electrically decoupled from the grounded sample holder, which is heated by electron bombardment. This is a prerequisite for meaningful impedance spectroscopic measurements and application of a cell voltage.

The electrical contacts of working and counter electrodes were established via Kanthalum wires, which also served as mechanical fixation of sample and quartz disk. Kanthalum is mechanically sufficiently strong to penetrate the typically weakly electron conducting MIEC layer and directly contact the embedded Pt current collector which was used in the investigated model cells.

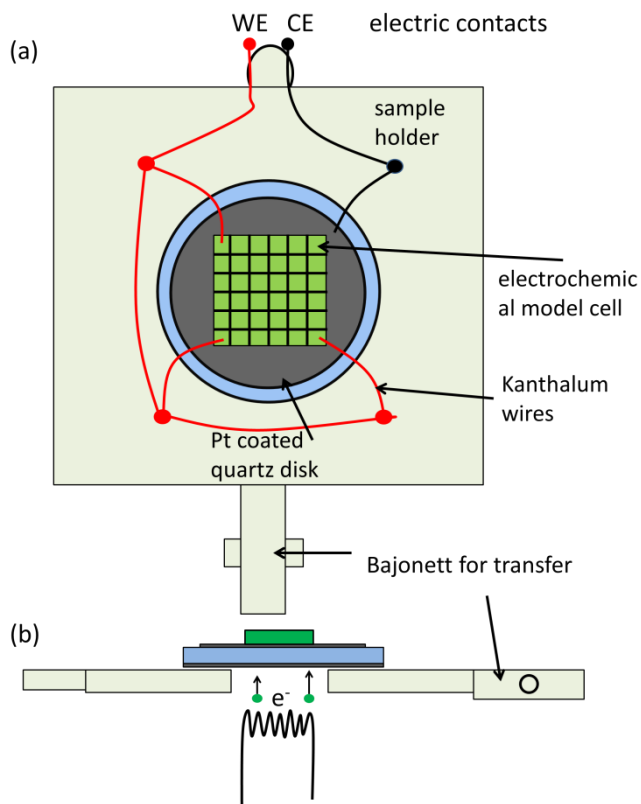


Figure 48. Top-view (a) and cross-section (b) sketch of a model cell mounted on the modified sample holder. For a better overview, the electrical wires are not shown in the cross section.

## 8.2.2 Fabrication of a model cell for UHV based experiments

Classical electrochemical model cells with a thin film working electrode typically have a kinetically fast counter electrode. This ensures that overpotential losses occur primarily in the electrolyte and working electrode and therefore the oxygen partial pressure in the working electrode can be calculated simply from the applied voltage minus electrolyte losses. In UHV, however, there is no atmospheric oxygen, and a counter electrode with fast surface kinetics is not possible. Application of a voltage in UHV does not lead to a steady state current, but a significant amount of oxygen ions is exchanged between the electrodes via the chemical capacitance. The model cell is therefore best described as a solid oxide battery. Still, a counter electrode with known and constant effective oxygen partial pressure is required for establishing a defined effective oxygen partial pressure in the working electrode when a potential is applied to the cell. In such a case, the chemical capacitance of the counter electrode has to be much larger than the working electrode capacitance. When a voltage is applied to such a cell, the effective oxygen partial pressure in the counter electrode stays constant, and the oxygen partial pressure in the working electrode can be varied according to Nernst's equation.

### Preparation of the counter electrodes

For the fabrication of such a counter electrode with high chemical capacitance,  $\text{Ce}_{0.8}\text{Gd}_{0.2}\text{O}_{1.9-\delta}$  (Treibacher AG, Austria) was mixed with ethyl-cellulose in a weight ratio of 1:0.2 and ground in a mortar for  $\sim 30$  minutes. The resulting powder was mixed with 50 weight % Terpineole (with respect to the ceria mass) and generously brushed on the rough side of one side polished  $10 \times 10 \times 0.5 \text{ mm}^3$  YSZ single crystals, and a thin current collecting Pt paste layer was brushed on top. After drying and sintering for 5 hours at  $1200^\circ\text{C}$  in air, a porous GDC layer of  $\sim 20 \mu\text{m}$  was achieved. Brushing of thicker GDC layers led to delamination due to shrinking during the sintering process. GDC is an electrolyte with very small chemical capacitance in oxidizing conditions. In hydrogen containing atmospheres, however Ce gets partly reduced to  $\text{Ce}^{3+}$ , resulting in a sufficiently large chemical capacitance<sup>75</sup>. The resulting counter electrodes exhibited a chemical capacitance of almost  $1 \text{ F/cm}^2$  in 1:1  $\text{H}_2+\text{H}_2\text{O}$  atmosphere at  $600^\circ\text{C}$ , which is 20-1000 times larger than the chemical capacitance of typical thin film electrodes.

### 8.2.3 Deposition of the working electrode and current collector

After fabrication of the counter electrode electrode, a  $\sim 70 \text{ nm}$  thick mesh-type Ti-Pt current collector (5  $\mu\text{m}$  stripes with 25  $\mu\text{m}$  square holes) was sputter deposited and structured via photolithography and argon ion beam etching. On top of the current collector, different SOFC anode materials were deposited via PLD. The materials and

sputter conditions are summarized in Table 6. In case of the LSCrNi7291 electrode, a GDC buffer layer was used to avoid the comparatively large resistance at the electrode-electrolyte interface.

After deposition, the 10\*10 mm<sup>2</sup> samples were fractured into pieces of ~5-10 mm<sup>2</sup> area to increase the number of usable samples. Also the temperature estimation by the electrolyte resistance becomes more accurate on small model cells, since the resistance of the electrical wiring (ca. 25 Ω inside the XPS chamber) becomes smaller compared to the electrolyte resistance, which is about 80 Ohms in a 10 mm<sup>2</sup> sample at 600°C.

Material	Temperature	Pressure	Laser rate	Time	Laser Energy	Film thickness
SrTi <sub>0.3</sub> Fe <sub>0.7</sub> O <sub>3</sub>	650°C	0.02 mbar	5 Hz	20'	400 mJ	100 nm
La <sub>0.6</sub> Sr <sub>0.4</sub> FeO <sub>3-δ</sub>	650°C	0.04 mbar	5 Hz	30'	400 mJ	100 nm
GDC +	650°C +	0.04 mbar +	5 Hz +	16' +		175 nm +
La <sub>0.7</sub> Sr <sub>0.2</sub> Cr <sub>0.2</sub> Ni <sub>0.1</sub> O <sub>3-δ</sub>	700°C	0.015 mbar	10 Hz	9'	400 mJ	100 nm

Table 6: Deposition parameters of the thin films electrodes used for the electrochemical XPS measurements.

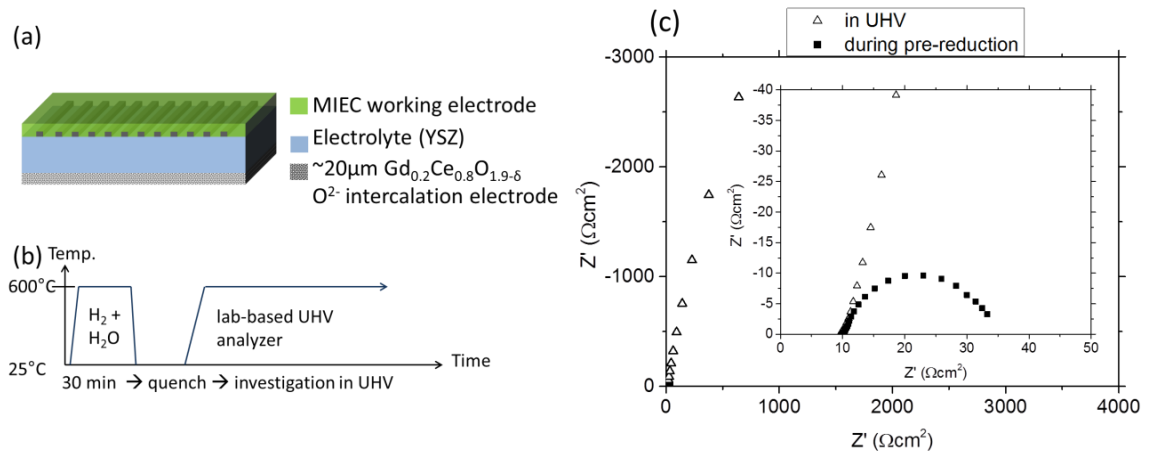


Figure 49: Sketch of the prepared model cell (a), temperature profile of the pre-reduction procedure (b) and impedance spectra measured on LSF during pre-reduction and in UHV at 600°C (c).

### 8.2.4 Pre-reduction procedure

After deposition of the working electrode, the effective oxygen partial pressure in the electrodes corresponds to the mildly oxidizing PLD conditions. Heating of such a cell in UHV would lead to significant oxygen loss and hence bad vacuum in the chamber and a drifting chemical potential of oxygen in the electrodes.

In order to avoid oxygen loss in the UHV chamber, the samples were reduced at 600°C in H<sub>2</sub>+H<sub>2</sub>O atmosphere in the sample quenching tracer exchange setup<sup>124</sup>, which was improved by reducing the thermal mass of the sample holder, and by the addition of two

electrical contacts, see Figure 50. Electrochemical impedance spectroscopy was employed to measure the ASR and chemical capacitance of the working electrode, as shown in Figure 49b.

After a reduction time of 30 minutes, the sample was quenched within a few seconds, which ensured conservation of the equilibrium oxygen nonstoichiometry at 600°C.

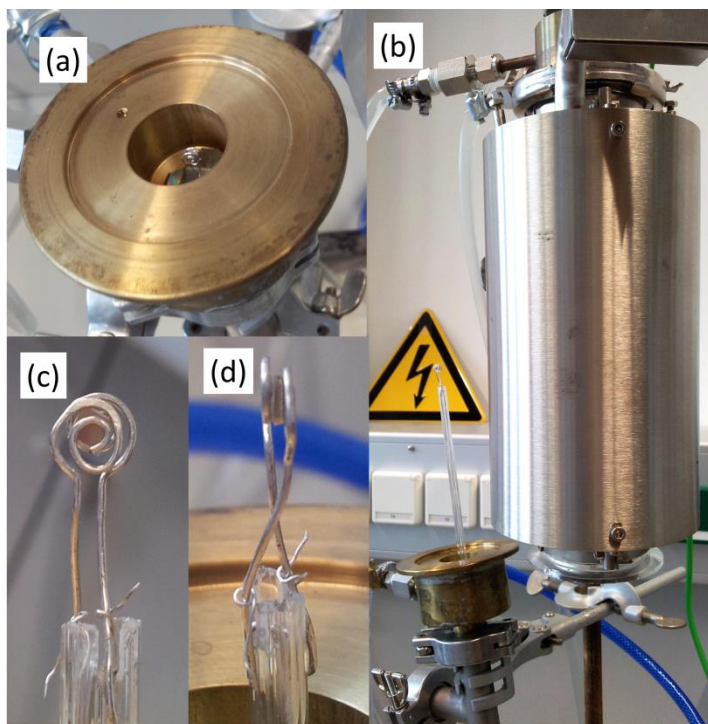


Figure 50: Photographs of the modified tracer exchange setup. The sample (ca.  $2.5 \times 2.5 \text{ mm}^2$ ) is clamped between two Pt-Ir wires that act as electrical contacts (c-d) and can be moved between the heating position (b) and the quenching position inside the water-cooled flange (a). Fast heating and cooling rates are achieved due to the small thermal mass of the sample and heating wires.

### 8.2.5 Measurements inside the UHV chamber

After the reduction procedure, the samples were mounted and contacted on the modified sample holder and transferred into the photoelectron spectrometer. There, the samples were heated again to operating temperature (600°C, determined by EIS, using the resistance of the electrolyte). When collecting photoelectrons from the heated sample, the voltage of the electron bombardment heater has to be smaller than the slowest detected photoelectrons, otherwise a tremendous background of  $\sim 10^5$  CPS is caused by elastically and inelastically scattered electrons from the heater. A maximum heater voltage of 700 V is therefore reasonable when Fe2p spectra are acquired.

The oxygen nonstoichiometry in working and counter electrode is conserved during heating in UHV, since the effective oxygen partial pressure in the sample ( $10^{-21}$  mbar,

or -1030 mV vs 1 bar O<sub>2</sub>) is too low for evolution of O<sub>2</sub>, and reactions with H<sub>2</sub> or H<sub>2</sub>O are not possible due to the absence of a gas phase.

Electrochemical impedance spectroscopy measurements in UHV confirmed this assumption. The two impedance spectra shown in Figure 49b exhibit very different ASR values, but similar capacitances when fitted with a parallel connection of resistor and capacitor. The chemical capacitance is a fingerprint of the oxygen nonstoichiometry in oxides<sup>58, 69, 75</sup>. The chemical capacitance of the working electrode measured during the pre-reduction and in the UHV chamber deviated by less than 10% and therefore confirms the conservation of the oxygen nonstoichiometry.

In order to stay consistent with the treatment of the cell as a solid oxide battery, the overpotential is always indicated relative to 1 bar O<sub>2</sub>, e.g. a hypothetical standard oxygen electrode. When samples were pre-reduced as described, the open circuit conditions at 600°C correspond to -1030 mV Vs O<sub>2</sub>. This allows for a consistent comparison of data collected with different pre-reduction conditions.

## 8.3 Results and discussion

### 8.3.1 Evolution of metallic Fe from LSF and STF

The evolution of metallic Fe from LSF and STF thin film electrodes was already reported by ambient-pressure XPS, surface XRD, SEM and electrochemical impedance spectroscopy. Complementary photoelectron spectroscopy measurements in UHV were performed to check whether the presence or absence of a gas phase changes the characteristics of Fe exsolution. In both materials the onset of Fe<sup>0</sup> precipitation was observed at overpotentials slightly larger than -1030 mV vs. O<sub>2</sub>, which was also found in the ambient pressure XPS study (chapter 7). This further confirms the excellent conservation of the oxygen chemical potential during quenching and reheating of the sample, as sketched in Figure 49. SEM images in Figure 52. also support the evolution of metallic nanoparticles. Particle sizes of 5-20 nm were observed on STF37, whereas on LSF64, the particles were in the range of 20-50 nm. Overall, the evolution of Fe<sup>0</sup> showed did not reveal significant differences when compared to the ambient pressure XPS study in chapter 7.

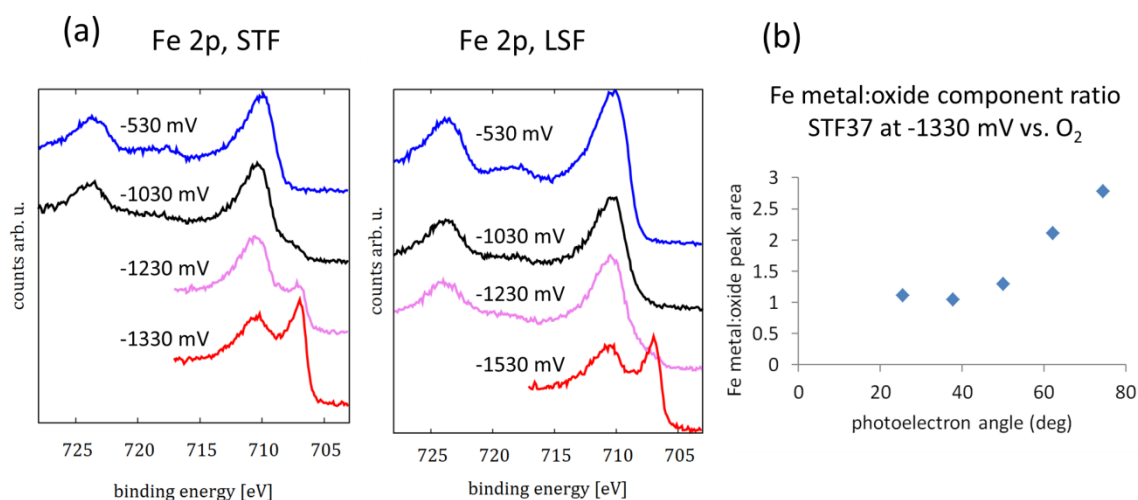


Figure 51: (a) XPS spectra acquired on pre-reduced LSF and STF electrodes during various levels of electrochemical polarization vs. 1 bar O<sub>2</sub> at 600°C. (b) Angle-resolved metal: oxide peak area ratio. At a larger angle against the surface normal the intensity of the metallic peak increases, supporting the interpretation of surface particles.

In the near-ambient pressure measurements, the total Fe content determined by the Fe2p<sub>3/2</sub> peak area strongly decreased during the evolution of Fe<sup>0</sup>, whereas in the UHV-based experiments a slight increase of Fe content during Fe exsolution can be observed. This difference can be understood from the size of the Fe particles (5-50 nm), which is larger than the XPS information depth of ~2 nm on the perovskite surface.

The ambient pressure analyser detects photoelectrons at normal emission angle, and the information depth is varied by changing the photon and photoelectron energy. In this geometry a large fraction of the signal arises from the remaining Fe depleted oxide surface, and no significant change in the metal to oxide ratio is expected by depth profiling through variation of the photon energy. In contrast, the lab-based UHV spectrometer uses an angle-resolved analyser, with a mean photoelectron collection angle of 50° relative to the sample normal. Therefore, it is more sensitive to the metallic Fe segregations which point out of the surface, leading to a higher Fe signal intensity. This is shown in Figure 51b, where an increase in Fe<sup>0</sup> fraction can be observed at shallower photoelectron angle.

In the UHV-based experiments at open circuit voltage, surface Fe ions are found in oxidation states Fe<sup>2+</sup> and Fe<sup>3+</sup> in similar amount, whereas in the bulk mainly Fe<sup>3+</sup> is present, as shown in section 2.3. A strong anodic bias can oxidize the surface Fe ions to mainly Fe<sup>3+</sup>, which can be detected from the satellite structure at ~719 eV in Figure 51a. This result perfectly matches the ambient-pressure XPS measurements.

Although the effective oxygen partial pressure during polarization with -1530 mV vs O<sub>2</sub> is as low as 10<sup>-33</sup> mbar, total decomposition of the LSF perovskite structure did not occur. Thermogravimetric analysis of LSF64 powder predicts bulk decomposition when the

oxygen partial pressure is  $<10^{-24}$  mbar at 600°C, corresponding to an overpotential of only -1130 mV vs O<sub>2</sub>. Total decomposition of the LSF films might be hindered kinetically, but also contributions due to differences of bulk and thin film thermodynamics are possible.

However, decomposition of a STF37 thin film becomes visible after reduction at 790°C, see Figure 52d. This film was cycled between water-rich and hydrogen-rich atmospheres, which led to volume decomposition and massive coarsening of the thin film structure. Note the different length scale bar in Figure 52d.

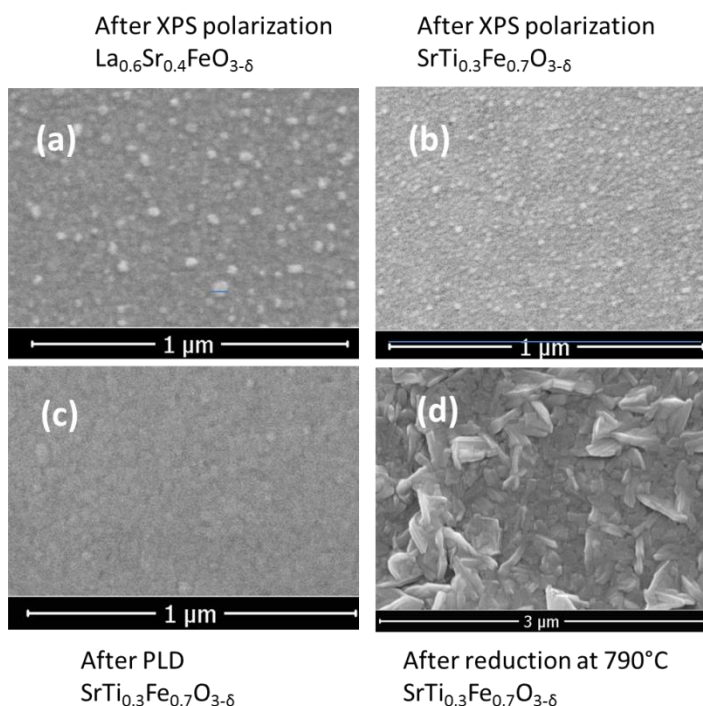


Figure 52. Comparison of the metal exsolution regimes in LSF64 and STF 37. (a-b) After polarization experiments in UHV XPS, under conditions very similar to those in ambient pressure XPS, small Fe particles segregate to the surface. (c) STF surface after PLD, showing no particles. (d) Surface image of STF37 after reduction in 32:1 H<sub>2</sub>:H<sub>2</sub>O atmosphere at 790°C. The strong roughening indicates decomposition and re-crystallization.

### 8.3.2 Evolution of metallic Ni from La<sub>0.7</sub>Sr<sub>0.2</sub>Cr<sub>0.9</sub>Ni<sub>0.1</sub>O<sub>3-δ</sub>

In addition to the LSF64 and STF37 samples, also A-site deficient, Ni doped La<sub>0.7</sub>Sr<sub>0.2</sub>Cr<sub>0.9</sub>Ni<sub>0.1</sub>O<sub>3-δ</sub> (LSCr-Ni) was investigated. It was already shown that this class of materials can form morphologically stable nano-sized Ni exsolutions<sup>50-51,67</sup>. As done with STF37 and LSF64, the samples were pre-reduced according to the scheme shown in Figure 49, and heated to ~600°C in the analyser.

The spectroscopic observation of Ni in lanthanum chromites is difficult, because the most prominent Ni 2p peak overlaps with the (much stronger) La 3d<sub>3/2</sub> peaks. Still, some information could be extracted from the Ni 3p peak at ~66.3 eV<sup>125</sup> (for Ni metal), which is much weaker than Ni 2p, but at least sufficiently separated from the neighbouring Cr 3s peak, shown in Figure 53.

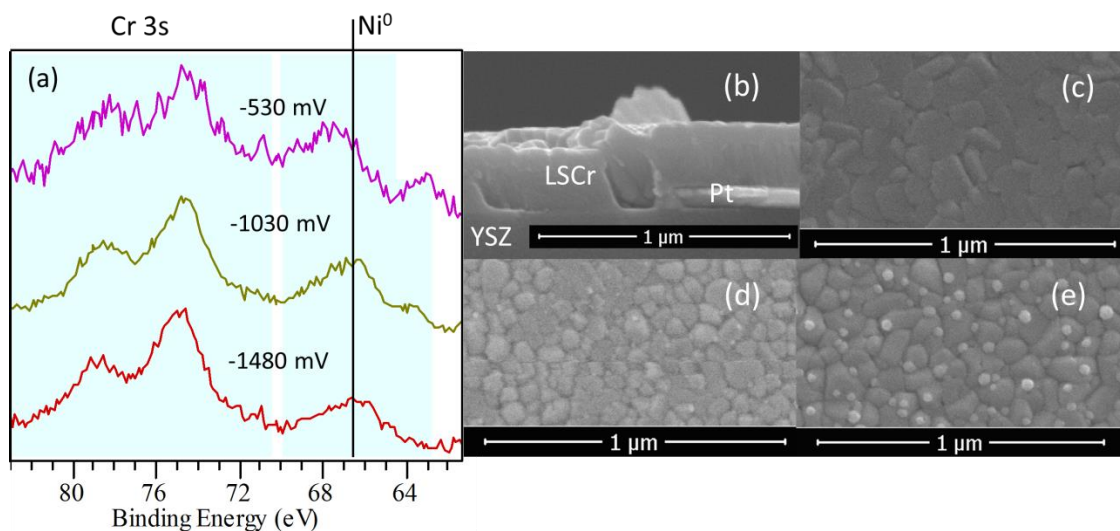


Figure 53: (a) Ni3p (and Cr3s) XPS spectra of A-site deficient LSCr-Ni films, showing an increase of Ni3p binding energy by approx. 1 eV at a polarization of -530 mV vs. O<sub>2</sub>, indicating a valence change from Ni metal to Ni oxide. (b) SEM cross section of the thin film, showing a smooth crack-free film also at the interface between LSCr-Ni on YSZ and LSCr-Ni on the current collector. (c) A-site stoichiometric LSCr-Ni film after reduction at 800°C for 5 hours, showing no exsolutions. (d) A-site deficient LSCr-Ni film after the presented polarization experiments in the XPS chamber, showing few very small Ni particles and (e) A-site deficient LSCr-Ni film after reduction at 800°C, showing a significant amount of Ni exsolutions.

Additional SEM imaging confirmed the Ni exsolution, and particles ranging from few nm to ~20 nm were found in the SEM images shown in Figure 53b-e. Interestingly, no Ni particles were observed on the A-site stoichiometric LSCr film. This result is in accordance with the theory proposed by Irvine et al, which renders A-site deficiency crucial for the exsolution of B-site dopants<sup>51</sup>.

### 8.3.3 Near-surface oxidation states of Cr

The surfaces of transition metal oxides are in most cases easier reducible than the bulk. This was already shown on ceria<sup>22</sup> and on LSF64 and STF73 in section 7.3.3. In the case of Sr-doped lanthanum chromites, the surface chemistry is more complex. The Cr2p spectra depicted in Figure 54 exhibit, apart from the spin-orbit splitting of ~9.5 eV, two components at 576 and 579 eV. In accordance with literature, these peaks can be attributed to Cr<sup>3+</sup> and Cr<sup>6+</sup>, respectively. By variation of the photoelectron angle, the information depth is varied, which reveals that the Cr<sup>6+</sup> fraction has a maximum in the vicinity of the surface. Although this observation may suggest a perovskite surface that is more oxidized than the bulk, the more likely explanation is more complex. In compounds investigated in literature, Cr<sup>6+</sup> occurs in tetrahedral coordination and it is hence unlikely to be present in a perovskite-type lattice. A conceivable interpretation of the assignment is possible when the phase stability of (La,Sr)CrO<sub>3</sub> is taken into account. This was extensively investigated in ref.<sup>126</sup> as a function of Sr concentration (10-30%), oxygen partial pressure

and temperature. It was shown that segregation of SrCrO<sub>4</sub> occurs under certain conditions. It is promoted by low temperature (<900°C), high oxygen partial pressure and high Sr concentration. Although macroscopic segregation of different phases in is both thermodynamically and kinetically unlikely, due to the low effective oxygen partial pressure and temperature, the observed Cr<sup>6+</sup> fraction can be explained by a coverage of roughly 1 layer of SrCrO<sub>4</sub> with tetrahedral coordinated Cr<sup>6+</sup>. In this surface layer also O and Sr most likely have slightly different binding energies. However, the effect convolutes with the surface segregation of Sr and surface oxygen species, which prevailed a clear assignment of the corresponding O1s and Sr3d peak components. Additionally, surface Sr segregation and SrCrO<sub>4</sub> formation can hardly be distinguished in terms of elemental composition. Hence, the assumption of a SrCrO<sub>4</sub> termination remains speculative, but conceivable. The intense Cr<sup>6+</sup> component also disqualifies the detection of possible Cr<sup>4+</sup> species, that are expected from the classical defect chemical model.

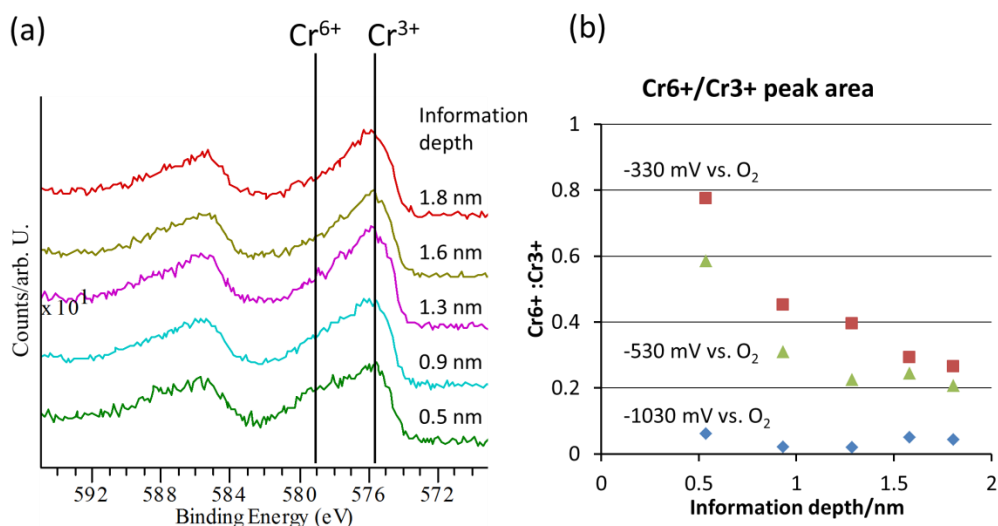


Figure 54: (a) Angle-resolved photoelectron spectra, with effective information depth indicated, measured on A-site deficient LSCr-Ni films at a sample temperature of 600°C at a pO<sub>2</sub> corresponding to -530 mV vs. O<sub>2</sub>. (b) Cr<sup>6+</sup>:Cr<sup>3+</sup> component ratio plotted as a function of information depth.

### 8.3.4 Binding energies

As already elaborated in section 7.3.3 application of overpotential to the electrochemical cells causes a shift of the observed binding energies, due to a shift of the electrochemical potential of electrons, which corresponds to the Fermi level. Upon application of a voltage the chemical potential of oxygen in the WE is changed, which in turn changes the chemical potentials of electrons and oxygen ions. For STF73 and LSF64, ambient pressure XPS measurements showed that the binding energies follow the simple relation of  $d\mu_{e_{on}} = dE_f \approx -e * d\eta$ .<sup>43</sup> However, in the most general case the extent of the Fermi level shift depends also on the relative change of the individual chemical potentials of electrons

and oxygen ions during reduction or oxidation of the material. In a grounded electrode where  $\mu = \tilde{\mu}$ , and  $\phi = 0$ , the relation of chemical potential of oxygen and chemical potential of electrons (or  $E_f$ ) can be written as

$$\frac{d\mu_{e_{on}}}{d\mu_o} = \frac{\frac{\partial\mu_{e_{on}}}{\partial c_{e_{on}}} dc_{e_{on}}}{\frac{d\mu_{O^{2-}}}{dc_{O^{2-}}} dc_{O^{2-}} - 2 \frac{d\mu_{e_{on}}}{dc_{e_{on}}} dc_{e_{on}}}. \quad (89)$$

The concentrations of oxygen ions and electrons are coupled via electroneutrality ( $dc_{e_{on}} = -2dc_{O^{2-}}$ ), which simplifies equation (89) to

$$\frac{d\mu_{e_{on}}}{d\mu_o} = \frac{-2 \frac{\partial\mu_{e_{on}}}{\partial c_{e_{on}}}}{\frac{d\mu_{O^{2-}}}{dc_{O^{2-}}} + 4 \frac{d\mu_{e_{on}}}{dc_{e_{on}}}}. \quad (90)$$

The change in the oxygen chemical potential is proportional to the overpotential via Nernst's equation ( $d\mu_o = e * 2\eta$ ) and in the case of non-interacting point defects, the derivative of chemical potential by concentration is  $k_b T/c$ . Using these relations, equation (90) simplifies to

$$\frac{d\mu_{e_{on}}}{d\eta} = \frac{dE_f}{d\eta} = \frac{dE_b}{d\eta} = -e \frac{\frac{4}{c_{e_{on}}}}{\frac{4}{c_{e_{on}}} + \frac{1}{c_{V_o}}}. \quad (91)$$

In the cases of LSF64 and STF73, it was shown in section 7.3.4 that the concentrations of electronic defects is much smaller than the concentration of ionic defects in the investigated  $pO_2$  range ( $c_{e_{on}} \ll c_{ion}$ ), which further simplifies equation (91) to  $d\mu_{e_{on}} = dE_f \approx -e * d\eta$ . Slopes between -0.9 and -1 eV/V were measured in the lab-XPS system when applying -330 to -1330 mV vs  $O_2$  to STF37 and -530 to -1530 mV vs  $O_2$  to LSF64. This confirmed both the defect chemical theory and the comparatively large chemical capacitance of the porous GDC counter electrode, see Figure 56a-b.

In Sr-doped lanthanum chromites the reduction enthalpy is much larger and hence the transition between electronic and ionic compensation of the dopant charge occurs at a significantly lower pressure/larger overpotential<sup>48, 127</sup>. In the regime of mainly electronic charge compensation, the chemical potential of electrons changes only marginally upon application of a bias, and the Fermi level remains constant during reduction upon the onset of ionic charge compensation. This effect was calculated, using the defect model of a 10% acceptor doped mixed conductor from section 2.1. The redox enthalpy was chosen such, that the onset of ionic charge compensation is at a partial pressure which corresponds to an overpotential of  $\sim 1V$  vs. 1bar  $O_2$ . The results of this simulation are shown in Figure 55.

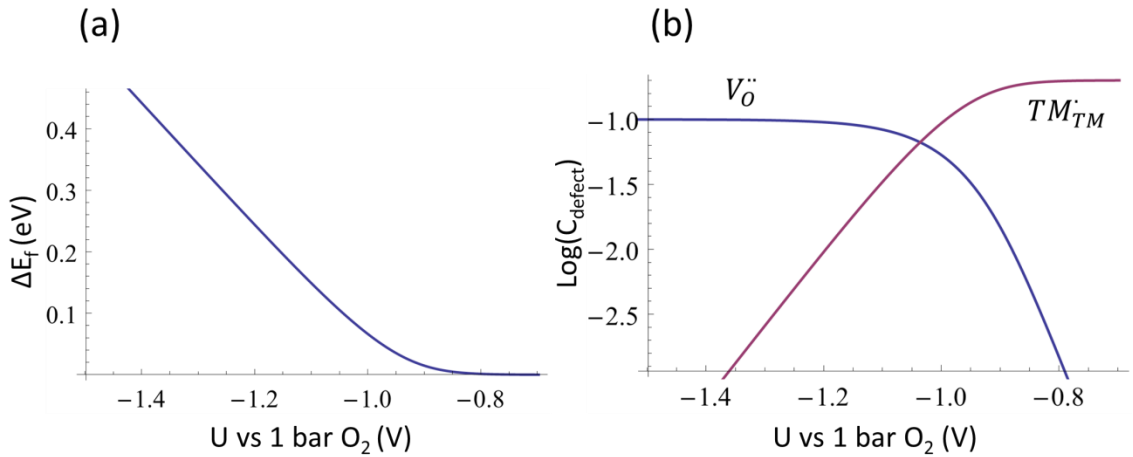


Figure 55: Defect chemical modelling of an acceptor-doped mixed conductor, showing the shift of the binding energy (a) as well as main electronic and ionic defect concentrations (b) as a function of overpotential vs. 1 bar  $O_2$ . The calculations show constant Fermi level in the regime of mainly electronic charge compensation, and shifting Fermi level in the regime of mainly ionic charge compensation. Defect concentrations are normalized to 1  $ABO_3$  formula unit.

In Figure 56, the measured binding energy shift vs. overpotential is plotted for all investigated materials. Most obviously, the Ni 3p peak does not follow the general trend at all. Here, the decrease in binding energy with overpotential is most likely caused by its reduction to the metallic state, as shown in the previous section. All of the other elements shift with slopes of approx.  $-0.5$  eV/V over a wide overpotential range, which is exactly the mean value between electronic and ionic charge compensation. However, the defect chemical calculation assumes non-interacting point defects and neglects surface effects, such as differing redox enthalpies and the conceivable formation of a  $SrCrO_6$  termination. Hence, this model is insufficient to describe the actual defect chemistry of the surface, although it is in good agreement with thermogravimetric data in literature.<sup>48</sup>

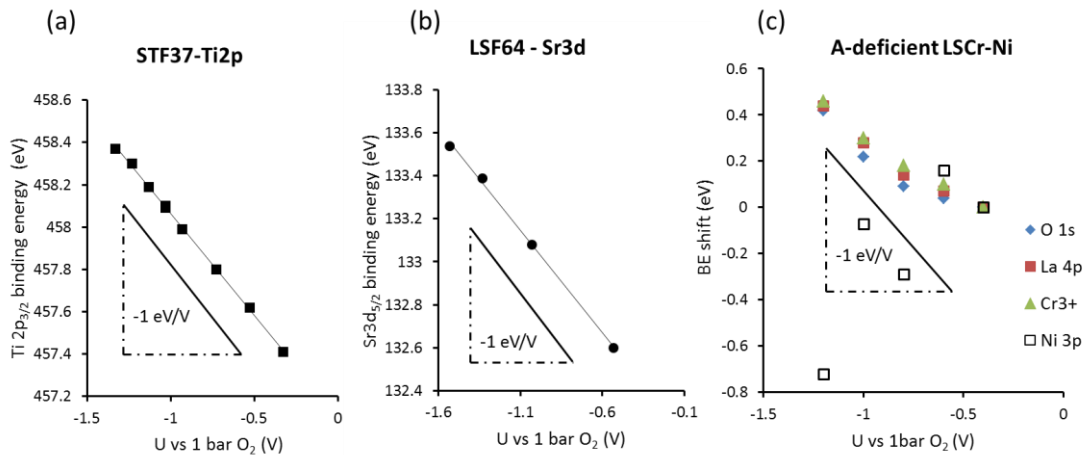


Figure 56: observed relation of binding energy shift vs. overpotential on STF37 (a), LSC64 (b) and  $La_{0.7}Sr_{0.2}Cr_{0.9}Ni_{0.1}O_{3.6}$  (c). At the lowest overpotential vs.  $O_2$  the shift was defined as 0.

## 8.4 Conclusions

A method of investigating SOFC electrode materials in a lab-based UHV XPS analyser was developed, in which the temperature and chemical potential of oxygen are tuneable in a range that is typical for the fuel side electrodes in solid oxide cells. The modifications of the commercially available sample holders, as well as the sample design and pre-reduction procedure were elaborated. Preliminary measurements on model cells revealed several interesting characteristics.

On the electrode materials STF37 and LSF64, the key results obtained in section 7.3.4 were reproduced, including the formation of metallic Fe on the sample surface. Despite the fundamentally different atmospheric environments of ambient pressure and UHV-based XPS, the characteristics of Fe<sup>0</sup> exsolution and near-surface Fe oxidation states were in excellent agreement. This confirms the interpretation that the reduction of Fe is driven by the effective oxygen partial pressure in the electrode, and not by the atmosphere. Furthermore the nanoparticle size and morphology of the Fe<sup>0</sup> phase could be confirmed by angle-resolved measurements as well as SEM analysis.

On A-site deficient, Ni-doped  $\text{La}_{0.7}\text{Sr}_{0.2}\text{Cr}_{0.9}\text{Ni}_{0.1}\text{O}_{3-\delta}$  several important preliminary observations could be made:

Cr is found in the oxidation states Cr<sup>3+</sup> and Cr<sup>6+</sup>, with varying concentrations, depending on the overpotential. Cr<sup>6+</sup> is located at the sample surface. In combination with investigations of the phase stability of (La,Sr)CrO<sub>3</sub> perovskite, the evolution of a SrCrO<sub>4</sub> layer on the surface with tetrahedral coordinated Cr<sup>6+</sup> is conceivable at higher oxygen partial pressures. Cr<sup>6+</sup> is not observable at an overpotential of -1V vs O<sub>2</sub> or lower.

Metallic Ni particles evolve at the sample surface during reduction in H<sub>2</sub>+H<sub>2</sub>O atmosphere. These particles can be reversibly oxidized by polarization of the cell in UHV. Doping of a reduction-stable chromite-based perovskite with Ni thus leads to the formation of metallic particles that are stable in an effective oxygen partial pressure window that covers the realistic working conditions of fuel side electrodes in SOFCs and SOECs. Interestingly, reduction of A-site stoichiometric  $\text{La}_{0.8}\text{Sr}_{0.2}\text{Cr}_{0.9}\text{Ni}_{0.1}\text{O}_{3-\delta}$  at 800°C does not lead to evolution of metallic Ni particles that can be observed by SEM.

The dependence of the binding energies on the overpotential shows a slope of approx. -0.5 eV/V, which corresponds neither to a mixed conductor with mainly electronic acceptor charge compensation (-1 eV/V) nor to mainly ionic charge compensation (no BE shift). This result suggests that the surface defect chemistry of this material significantly deviates from a perfect bulk defect model, which is probably linked to the reversible formation of a SrCrO<sub>4</sub> termination at the surface.

## 9 The electrolyte spreading resistance of microelectrodes - more than a resistive offset

### 9.1 Introduction

Thin film microelectrodes are frequently employed to investigate fundamental properties of mixed conducting or metallic SOFC electrode materials<sup>7, 28, 30, 33-34, 52, 89, 110, 128</sup>. When a comparatively large counter electrode is used, the measured impedance is given by the sum of electrolyte and working electrode resistance, and the counter electrode is negligible. This geometry helps in avoiding the complications of the reference electrode placement, which is very nontrivial on thin solid electrolytes<sup>112</sup>. In this chapter, a detailed finite-element study of the electrolyte spreading resistance of microelectrodes and its implication on impedance measurement is given.

Usually, the electrolyte spreading resistance is regarded as a resistive offset in the impedance spectra of surface active or triple phase boundary active electrodes. On microelectrodes that are small compared to the electrolyte substrate thickness, the electrolyte resistance can be calculated via the spreading resistance formula<sup>129</sup>.

$$R_{spreading} = \frac{1}{2\sigma d_{WE}} \quad (92)$$

$\sigma$  and  $d_{WE}$  are the electrolyte conductivity and working electrode diameter, respectively.

Finite electrolyte dimensions increase or decrease the electrolyte resistance, depending on the location of the counter electrode and correction factors are given in section 9.3. Apart from this, also the measurement frequency and the electrochemical properties of working and counter electrodes influence the resistive losses in the electrolyte. The electrolyte resistances in the high frequency range and under DC conditions may significantly differ from each other, which may lead to artefacts in the impedance spectra.

Highly electron conducting electrodes have an area-related capacitance, which may be caused by a double layer at the electrode-electrolyte interface of metallic electrodes, or a chemical capacitance in mixed conducting electrodes. Due to this capacitance, the electrode impedance is short circuited in the high frequency regime and the current density along the electrode is governed by the electrolyte and inhomogeneous.

In DC conditions, on the other hand, the current density along the electrodes is (in most cases) governed by the electrochemical properties of working and counter electrodes.

In sections 9.4 and 9.5 it is shown how these frequency dependent current density distributions influence the impedance spectra. The electrolyte spreading resistance varies with the frequency. This causes features in a frequency range typically assigned to electrode processes. These may vary from weakly pronounced shoulders to even well-separated, distorted semicircular features. When the electrode arc is significantly larger than the electrolyte resistance, then these contributions have a minor impact on the DC polarization resistance.

## 9.2 Numerical model

Finite element simulations using Comsol 5.0 and the electric currents module are the basis of this chapter. A very simple geometry with a circular microelectrode and a circular substrate was used for most simulations, see Figure 57. This allowed computation in cylindrical coordinates and thus an increase of the mesh density (ca 1000 mesh points along the electrode).

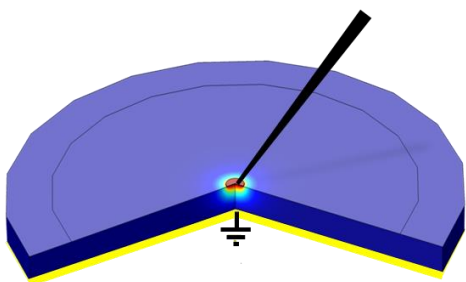


Figure 57. Sketch of the numerical model for simulation of impedance spectra.

All simulated impedance spectra shown here assume an electrolyte conductivity of 0.001 S/cm (YSZ at 512°C)<sup>130</sup> and a total electrochemical electrode resistance of 100 kΩ.

In the numerical model the resistive contributions of the electrolyte are calculated by the electric energy dissipation within the electrolyte, which is in accordance to Ohm's law  $P = I_{WE}^2 R_{YSZ}$ . The electrical power (P) was calculated by integrating the resistive losses within the electrolyte, resulting in

$$R_{YSZ} = \frac{\int \frac{j^2}{\sigma_{YSZ}} dV_{YSZ}}{I_{WE}^2}. \quad (93)$$

Using this model, the dimensions of electrode and electrolyte (section 9.3) are varied to find a good correction of the spreading resistance formula to fit finite substrate dimensions. In sections 9.4 and 9.5 the electrochemical properties of the working and

counter electrode are varied by introducing surface impedances at the respective terminals.

### 9.3 Effect of finite substrate dimensions.

The spreading resistance formula (equation (92)) is only exactly valid when the substrate is very (or infinitely) large compared to the electrode diameter. When the size of the sample is finite, or the microelectrode size is even similar to the substrate thickness ( $d_{WE} \approx$  thickness), the high-frequency resistance ( $R_{HF}$ ) deviates from the spreading resistance formula. A simple dimensionless correction factor ( $F$ ) is sufficient to compensate the deviation from the spreading resistance formula for finite sample thickness. The computed high frequency resistance ( $R_{HF}$ ) then reads

$$R_{HF} = R_{spreading} * F . \quad (94)$$

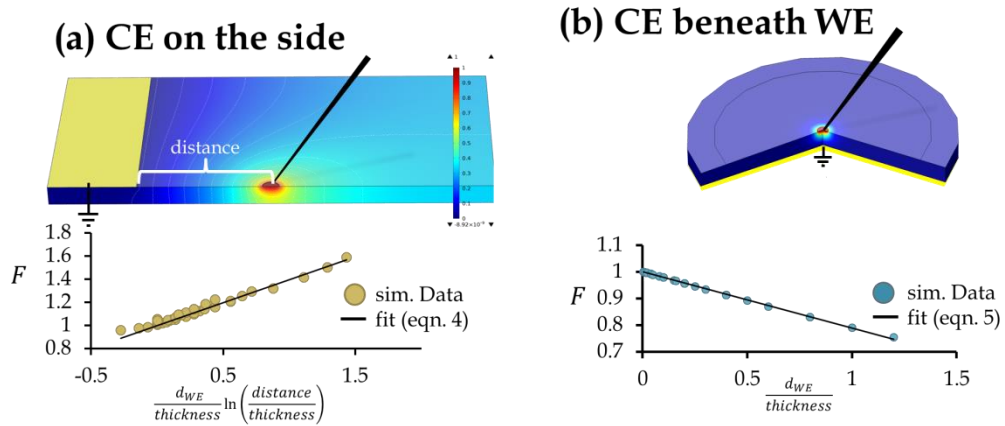


Figure 58. Correction factors of the spreading resistance formula for finite electrolyte dimensions, assuming (a) a counter electrode on the top side and (b) a counter electrode on the bottom of the electrolyte.

As seen in Figure 58, a simple one-parameter fit using a heuristic dimension-less correction factor can sufficiently accurately correct the spreading resistance formula to calculate the high-frequency resistance. For **counter electrodes on the side of the substrate**, it reads

$$F = 1 + \frac{0.39d_{WE}}{thickness} \ln\left(\frac{distance}{thickness}\right) . \quad (95)$$

“Thickness” is the thickness of the electrolyte substrate and “distance” is the distance between microelectrode center and counter electrode edge (see Figure 58a).

When the **counter electrode is placed beneath the working electrode**, the correction factor reads

$$F = 1 - \frac{0.212d_{WE}}{thickness} \quad (96)$$

## 9.4 Electrolyte resistance of surface and TPB active electrodes

Apart from the electrolyte dimensions, also the type of the working electrode (TPB-active vs. surface active) and the frequency play a crucial role on the current-path (and the losses) in the electrolyte. The spectra simulated here use the model sketched in Figure 57 with a reversible counter electrode and a 200  $\mu\text{m}$  working electrode. Also, the impedance model of the working electrode is a simple parallel connection of an area-related resistance and capacitance. In case of triple phase boundary (TPB) active electrodes a finite TPB width between 1 and 100 nm is assumed. For such simple electrode kinetics the intuitive equivalent circuit model would be the one given in Figure 59.

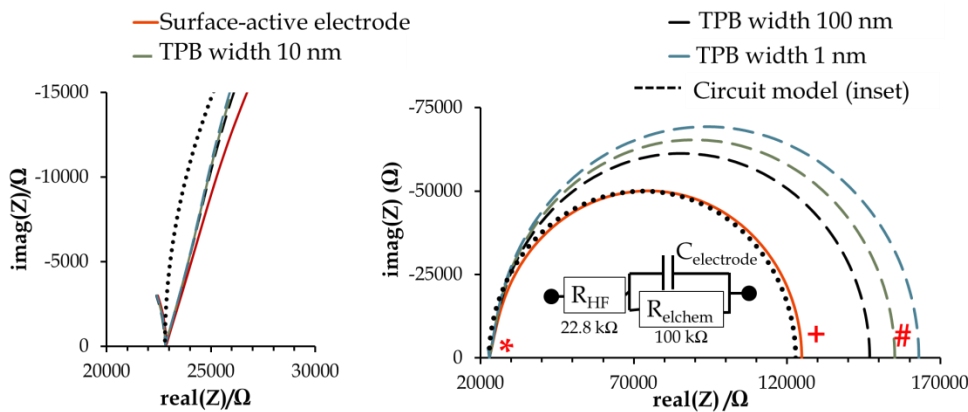


Figure 59. Simulated impedance spectra of a 200  $\mu\text{m}$  diameter electrode, assuming triple phase or surface activity. All simulated electrodes have an electrochemical resistance of 100 k $\Omega$ . Deviations from the intuitive equivalent circuit model (black dots) are only caused by the electrolyte spreading resistance.

As visible in Figure 59, simulated impedance spectra of microelectrodes slightly deviate from the perfect resistor-capacitor model when the electrolyte spreading resistance is not negligible. Moreover the electrode arc is significantly larger in case of TPB active electrodes.

Three different regimes can be found in these simulations:

### High frequency regime (\*)

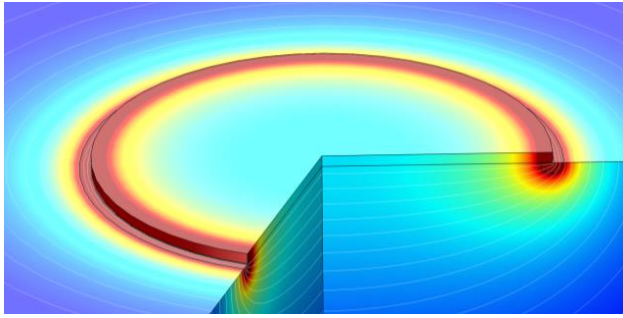


Figure 60. Electrolyte current density (color) and equipotential lines in the electrolyte dominated high-frequency regime.

In the high-frequency regime the electrode impedance is short-circuited on the entire area via its area-related capacitance (primary current distribution). This may be a chemical capacitance or electrode-electrolyte double layer capacitance. The electrolyte resistance can be calculated using the spreading resistance formula with the correction factor in equation (96). The current density has a maximum at the electrode border – see Figure 60.

### DC-case, surface active electrode (+)

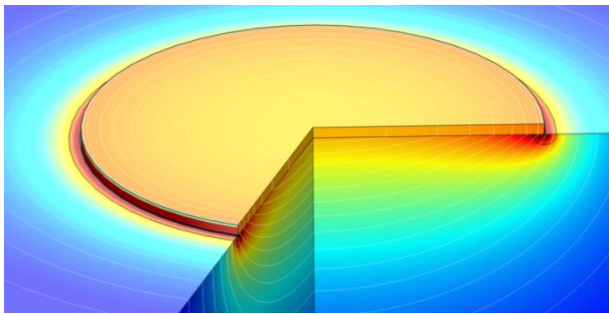


Figure 61. DC current density (color) and equipotential lines of a surface active electrode. The current density is rather homogeneous along the electrode surface.

In DC conditions the current density at the electrode is determined by the electrochemical activity of the electrode (secondary current distribution). Surface active electrodes have a homogeneous current density, as sketched in Figure 61. The electrolyte resistance calculated via equation (93) is roughly 10% larger than the corresponding high-frequency resistance. This causes the difference between the simulated impedance spectrum (red) and the analytical model (black dots) in Figure 59.

## DC case, triple phase active electrode(#)

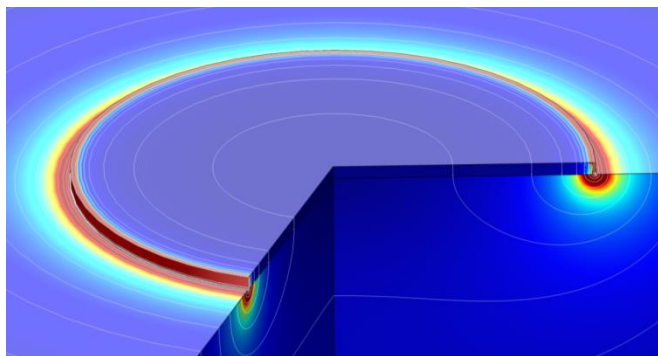


Figure 62. Electrolyte current density (color) and equipotential lines of a TPB active electrode in DC conditions.

On a TPB active electrode the oxygen ion current enters the electrolyte only on the electrode border (Figure 62). Due to this strong current constriction, the electrolyte resistance is much larger than the high-frequency spreading resistance. A TPB width of zero would even lead to infinite electrolyte resistance. Any TPB width below the oxygen anion diameter is of course absurd. Assuming a reasonable finite TPB width range (1-100 nm)<sup>128</sup>, the electrolyte resistance is roughly 2-3 times larger than the spreading resistance for a 200  $\mu\text{m}$  microelectrode (see Figure 58). For a TPB width of 1 nm, 70% of the entire electrolyte losses (including the ‘normal’ spreading resistance) are dissipated in a radius only  $< 10 \mu\text{m}$  from the TPB.

## 9.5 Effects of non-ideal counter electrodes

The location of the counter electrode on a finite substrate changes the electrolyte resistance, see Figure 58. As long as the counter electrode is reversible, this only affects the ohmic offset in the impedance spectra. However, also well-separated artefacts in the electrode impedance may occur when the working electrode has a high capacitance, which is typical for a mixed conductor, and a counter electrode on the bottom of the substrate is not reversible and has a much lower (area-specific) capacitance (typical for a porous metal electrode).

Impedance spectra exhibiting the mentioned pronounced artifacts and the corresponding current distribution in the electrolyte are shown in Figure 63 and their origin is discussed in the following. For the simulations, a cylindrical electrolyte with 10 mm diameter and 0.5mm thickness, having a conductivity of 0.001 S/cm, corresponding to YSZ at 512°C, was chosen (Figure 58b). A surface active 200  $\mu\text{m}$  working electrode in the center and two different counter electrodes were considered. One counter electrode was placed on the bottom and the other (having the same properties as the working electrode) was ringshaped and on top of the sample near the perimeter. This situation is sketched in

Figure 63b. The electrodes were modelled by a simple parallel connection of an area specific resistance and capacitance and values are given in Table 7.

Bottom electrode capacitance	bottom electrode ASR	WE diameter	WE chemical capacitance	WE ASR	CE side capacitance	CE side ASR
Figure 63: 10-100 $\mu\text{F}/\text{cm}^2$	1000 $\Omega\text{cm}^2$	(a-b): 200 $\mu\text{m}$	20 $\text{mF}/\text{cm}^2$	31.4 $\Omega\text{cm}^2$	20 $\text{mF}/\text{cm}^2$	31.4 $\Omega\text{cm}^2$
Figure 64: 30 $\mu\text{F}/\text{cm}^2$	none	(c): 100-300 $\mu\text{m}$				

Table 7. Properties of the simulations in Figure 63 and Figure 64.

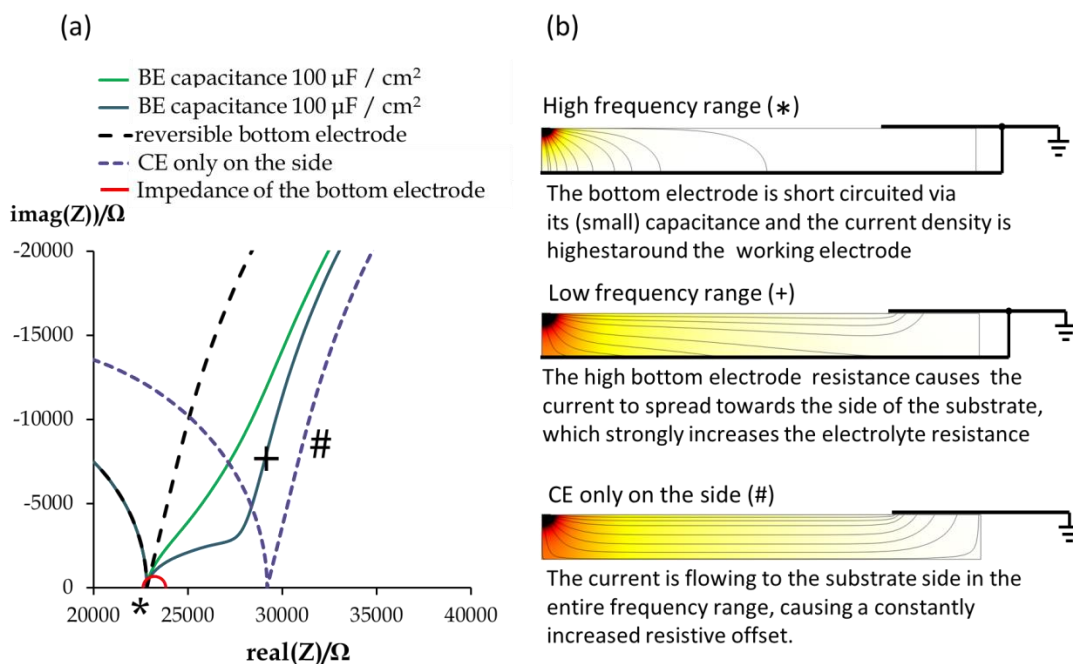


Figure 63. Simulated impedance spectra (a) and current distributions (b) in the electrolyte, assuming different electrochemical properties of the bottom counter electrode.

In Figure 63a simulated impedance spectra with varying counter electrode properties and constant working electrode are shown. For better visibility of the features, only the onset of the electrode arc is shown. In the case of a reversible bottom electrode or a counter electrode only on the substrate side (dashed lines) only minor deviations from the ideal semi-circular shape are found. Those were already discussed in section 9.4. If a non-reversible bottom electrode is modelled (solid blue and green curves), well-separated high frequency features occur. The resistive contribution of these features is significantly larger than the impedance of the counter electrode (tiny red semicircle). In Figure 63b, the origin of these features is sketched: In the high frequency range, the current in the electrolyte is capacitively coupled between working and bottom electrode, and the electrolyte resistance corresponds to the case sketched in Figure 58b. At lower frequencies only a small fraction of the measured current flows into the bottom electrode and most of the current is flowing to the side of the substrate. In this regime the electrolyte resistance is

larger and corresponds to the case sketched in Figure 58a. Such features are more separated when the ratio of WE capacitance to bottom electrode capacitance becomes larger.

Such artefacts do not only occur in computational models, but also in measured impedance spectra. This is shown in Figure 64. The impedance spectra in Figure 64b were measured on microelectrodes of  $\text{Ce}_{0.8}\text{Gd}_{0.2}\text{O}_{2-\delta}$ , containing a thin film Pt grid as current collector, in  $\text{H}_2+\text{H}_2\text{O}$  atmosphere at  $\sim 505^\circ\text{C}$ . Under these conditions, GDC becomes a mixed ionic-electronic conductor with a relatively high chemical capacitance. Also in this case two counter electrodes were employed: An extended counter electrode of the same material was placed on the side of the electrolyte and a porous Pt counter electrode was applied to the bottom to avoid 'inductive loops'<sup>131</sup>. The impedance spectra in Figure 64b for different working electrode sizes show a size dependent electrolyte bulk offset, a medium frequency feature and the onset of the (comparatively large) electrode semicircle. The resistive magnitude of the medium frequency feature does not change with the diameter of the working electrode, but the degree of separation between low and medium frequency arc varies due to the changing total chemical capacitance of the working electrode. The same characteristics were also found in the finite element simulation shown in Figure 64a.

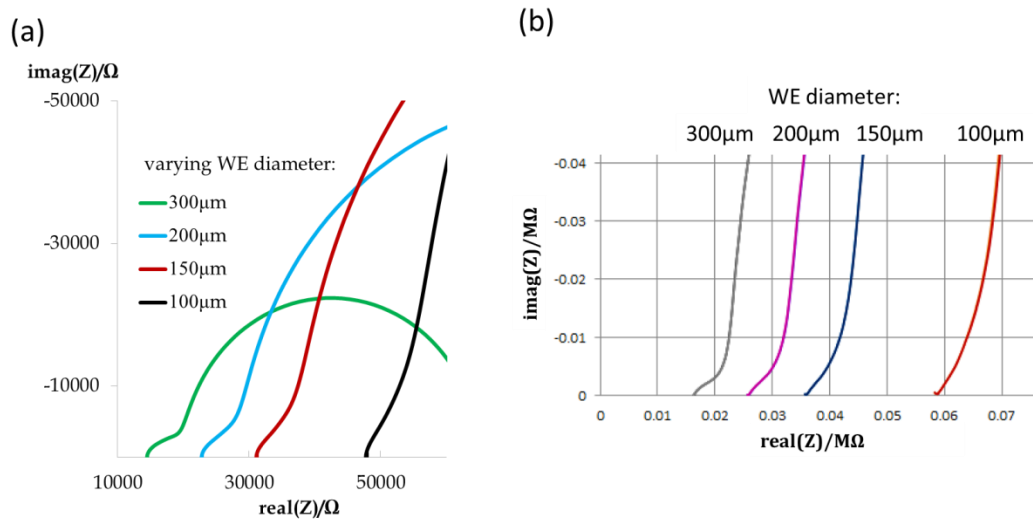


Figure 64. Simulated (a) and measured (b) impedance spectra of GDC microelectrodes at  $\sim 505^\circ\text{C}$  on a 0.5 mm thick YSZ substrate with a porous Pt bottom electrode and an additional counter electrode on the side.

## 9.6 Conclusions

The electrolyte resistance in microelectrode measurements is typically regarded as a simple resistive offset. This is, however, often not the case due to different primary (electrolyte dominated) and secondary (electrode dominated) current distributions within the electrolyte. These cause artefacts in the high frequency range of simulated impedance spectra and on TPB active electrodes the DC electrolyte resistance may easily become 2-3 times higher than the high frequency spreading resistance.

Pronounced artefacts can also occur when a non-reversible counter electrode with small capacitance (e.g. a metal paste) is used on the bottom of the electrolyte substrate. It is therefore recommended to place the counter electrode remote from the working electrode – e.g. on the side of the electrolyte substrate, and to avoid a porous metal counter electrode on the bottom of the sample.



## Summary

The mechanism of electrochemical water splitting and hydrogen oxidation was investigated on reduction stable mixed conducting materials by using model electrodes deposited on yttria-stabilized zirconia (YSZ) substrates.

In particular, the perovskite-type materials  $\text{Sr}(\text{Ti,Fe})\text{O}_{3-\delta}$  (STF) and  $\text{La}_{0.6}\text{Sr}_{0.4}\text{O}_{3-\delta}$  (LSF) were investigated in detail. Their electronic conductivities were found to be in the range of  $10^{-2}$  to  $10^{-1}$  S/cm in  $\text{H}_2+\text{H}_2\text{O}$  atmosphere at  $650^\circ\text{C}$ , which is several orders of magnitude lower than conductivities reported for air. Due to this low conductivity, meaningful electrochemical impedance measurements required application of platinum thin film current collectors to the thin film electrodes under investigation. Even with current collectors applied, in-plane charge transport may have a significant impact on the polarization resistance.

A novel electrode design with two interdigitating current collectors in a single microelectrode was therefore developed to enable a detailed understanding of the electrochemical properties of such electrodes. Equivalent circuit models for this special electrode design were established, using the equations of charge transport and electrochemical reactions for small applied potentials. The two current collectors per microelectrode allow measurements in in-plane contact configuration where the potential is applied between the two current collectors, and electrochemical contact configuration where the entire microelectrode is polarized against an extended counter electrode. Simultaneous fitting of both impedance spectra using only one parameter set allowed the determination of several important materials parameters, such as the area-specific resistance of the surface reaction, electronic conductivity and ionic conductivity. This method, together with in-plane measurements with electrodes deposited on MgO substrates, was employed to investigate the electrochemical properties of  $\text{Sr}(\text{Ti,Fe})\text{O}_{3-\delta}$ , containing 30 and 70 mol % Fe. Oxygen partial pressure independent ionic conductivity was found together with an increase of electronic conductivity and chemical capacitance, with decreasing  $p\text{O}_2$ . This is in qualitative agreement with the bulk defect model. Higher Fe content increased electronic and ionic conductivity and the oxygen exchange rate. Variation of the current collector placement (on top or beneath the MIEC film) and current collector geometry revealed a strong catalytic activity of the Pt-STF-atmosphere triple phase boundary.

The circuit model of a weakly electron conducting electrode predicts that the MIEC is polarized only in an electrochemically active region that extends to a distance of several micrometres from the current collectors.  $^{18}\text{O}$  isotope exchange was performed to visualize this electrochemically active region. Thin films of STF and GDC on YSZ, containing electrically polarized current collectors, were heated in reducing  $\text{H}_2+\text{H}_2^{18}\text{O}$  atmosphere. Subsequent imaging of the tracer distribution by secondary ion mass spectroscopy (SIMS) could visualize the electrochemically active zones. Increased or decreased tracer fraction was found near cathodically or anodically polarized current collectors, respectively. Although qualitative agreement was found, the tracer exchange coefficient in equilibrium ( $k^*$ ) was much faster compared to expectations from the electrochemical surface ASR and the effect of electrical polarization on the  $^{18}\text{O}$  incorporation rate was much weaker than expected from typical kinetic models that suggest an exponential dependence.

This quantitative mismatch was more closely investigated by impedance spectroscopic measurements on LSF and STF model electrodes performed during  $^{18}\text{O}$  tracer exchange, allowing for simultaneous determination of electrical ( $k^{\text{el}}$ ) and the tracer ( $k^*$ ) exchange coefficients of oxygen. Three different atmospheres were used: dry  $^{18}\text{O}_2$ ,  $^{16}\text{O}_2$  humidified with  $\text{H}_2^{18}\text{O}$ , and reducing  $\text{H}_2+\text{H}_2^{18}\text{O}$ . In dry oxidizing atmosphere, reasonable agreement of  $k^*$  and  $k^{\text{el}}$  was found, which indicated that  $^{18}\text{O}_2$  isotope exchange occurs via a redox reaction, mediated by a bulk electron transfer. In humid oxidizing and humid reducing atmospheres, however, very high tracer exchange coefficients ( $k^* > 100 k^{\text{el}}$ ) were observed. This huge difference indicates different mechanisms of electrical and tracer oxygen exchange. A fast equilibrium rate of water dissociation on a surface oxygen vacancy into two surface OH groups was identified as the dominating tracer exchange mechanism. In this reaction, no electron transfer is required because the contributing O and H atoms remain in oxidation states -2 and +1, respectively. Such a reaction without an electron transfer cannot be driven electrically, so it does not contribute to  $k^{\text{el}}$ , while increasing  $k^*$  by more than two orders of magnitude. Due to this mechanism it is crucial to avoid even traces of humidity when tracer exchange coefficients are related to the electrochemical activity of electrode materials. In the case of  $\text{H}_2+\text{H}_2\text{O}$  atmosphere these results prove that water dissociation and desorption is fast and that the electron transfer to a surface OH group or the subsequent evolution of  $\text{H}_2$  is rate limiting.

Also ambient pressure XPS was employed to investigate the chemistry of electrode surfaces during well-defined polarization. Working electrode materials were  $\text{La}_{0.6}\text{Sr}_{0.4}\text{CoO}_{3-\delta}$ , (LSC), LSF and STF. The surface properties were investigated in oxidizing (0.5 mbar  $\text{O}_2$ ) and reducing conditions (0.25 mbar  $\text{H}_2$  + 0.25 mbar  $\text{H}_2\text{O}$ ). Chemically distinct surface species of Sr and O were found on all materials in oxidizing atmosphere

(0.5 mbar O<sub>2</sub>), indicating that the surface termination is not a perovskite bulk-plane. Also the binding energies of all peaks of fixed valent elements shifted as a function of the electrode bulk pO<sub>2</sub>, which was varied by electrochemical polarization and atmospheric composition. This binding energy shift could be correlated to a Fermi level shift and the quantitative relation  $\Delta E_b = -e * \eta$  confirmed that the overall oxygen exchange rates limited by the surface reaction of the working electrode.

In reducing H<sub>2</sub>+H<sub>2</sub>O atmosphere, near surface Fe on LSF and STF was observed in oxidation states +3, +2 and 0, depending on the electrochemical polarization. Fe<sup>0</sup> evolves under cathodic polarization and is forming nanoparticles that strongly increase the water splitting activity of LSF and STF. However, the evolution of Fe<sup>0</sup> particles occurs only in conditions that are close to bulk decomposition of the perovskite lattice.

Also in a lab-based XPS analyser model cells with a thin film working electrode could be successfully heated and electrochemically polarized. With a proper cell design and pre-reduction procedure the chemical potential of oxygen in the electrode bulk could be precisely controlled, and the evolution of a metallic phase could be confirmed on LSF, STF and La<sub>0.7</sub>Sr<sub>0.2</sub>Cr<sub>0.9</sub>Ni<sub>0.1</sub>O<sub>3-δ</sub>. The characteristics of Fe<sup>0</sup> evolution in the ambient pressure and UHV XPS analyser were very similar, indicating that the electrode bulk pO<sub>2</sub> is much more decisive for the evolution of Fe<sup>0</sup> than the atmospheric conditions. Furthermore, it shows that the electrode bulk pO<sub>2</sub> can be precisely controlled also in a UHV analyser by using a model cell with a counter electrode that has a large chemical capacitance.

In a numerical study of the impedance of thin film microelectrodes, it was shown that the electrolyte spreading resistance of a microelectrode not only depends on the dimensions of the electrolyte, but also on the applied frequency and the electrochemical properties of working and counter electrodes. As a consequence all impedance spectra of microelectrodes slightly deviate from the perfect semicircular shape. Pronounced artefacts could be simulated and observed on measured impedance spectra when a counter electrode with low chemical capacitance – e.g. a porous metal electrode was used on the bottom of the electrolyte substrate. Such a counter electrode is therefore not recommended.



## References

1. Ge, X. M.; Chan, S. H.; Liu, Q. L.; Sun, Q., Solid oxide fuel cell anode materials for direct hydrocarbon utilization. *Advanced Energy Materials* **2012**, *2* (10), 1156-1181.
2. Park, S.; Vohs, J. M.; Gorte, R. J., Direct oxidation of hydrocarbons in a solid-oxide fuel cell. *Nature* **2000**, *404* (6775), 265-267.
3. Minh, N. Q.; Singhal, C.; Williams, M., Solid Oxide Fuel Cells: Development Activities, Trends and Technological Challenges. *ECS Transactions* **2009**, *17* (1), 211-219.
4. Brisse, A.; Schefold, J.; Zahid, M., High temperature water electrolysis in solid oxide cells. *International Journal of Hydrogen Energy* **2008**, *33* (20), 5375-5382.
5. Ebbesen, S. D.; Mogensen, M., Electrolysis of carbon dioxide in solid oxide electrolysis cells. *Journal of Power Sources* **2009**, *193* (1), 349-358.
6. Zhan, Z.; Kobsiriphat, W.; Wilson, J. R.; Pillai, M.; Kim, I.; Barnett, S. A., Syngas production by coelectrolysis of CO<sub>2</sub>/H<sub>2</sub>O: the basis for a renewable energy cycle. *Energy & Fuels* **2009**, *23* (6), 3089-3096.
7. Nanning, A. Electrochemical reactions and transport paths of SrTi<sub>0.7</sub>Fe<sub>0.3</sub>O<sub>3-δ</sub> thin film model electrodes in H<sub>2</sub>-H<sub>2</sub>O atmosphere. Diploma Thesis, TU Vienna, Vienna, **2013**.
8. Singhal, S. C.; Kendall, K., *High-temperature solid oxide fuel cells: fundamentals, design and applications: fundamentals, design and applications*. Elsevier, **2003**.
9. Adler, S. B., Factors governing oxygen reduction in solid oxide fuel cell cathodes. *Chemical Reviews* **2004**, *104* (10), 4791-4844.
10. Merkle, R.; Maier, J., How Is Oxygen Incorporated into Oxides? A Comprehensive Kinetic Study of a Simple Solid-State Reaction with SrTiO<sub>3</sub> as a Model Material. *Angewandte Chemie International Edition* **2008**, *47* (21), 3874-3894.
11. Matsuzaki, Y.; Yasuda, I., The poisoning effect of sulfur-containing impurity gas on a SOFC anode: Part I. Dependence on temperature, time, and impurity concentration. *Solid State Ionics* **2000**, *132* (3), 261-269.
12. Atkinson, A.; Barnett, S.; Gorte, R. J.; Irvine, J.; McEvoy, A. J.; Mogensen, M.; Singhal, S. C.; Vohs, J., Advanced anodes for high-temperature fuel cells. *Nature materials* **2004**, *3* (1), 17-27.
13. Cho, S.; Fowler, D. E.; Miller, E. C.; Cronin, J. S.; Poepelmeier, K. R.; Barnett, S. A., Fe-substituted SrTiO<sub>3-δ</sub>-Ce<sub>0.9</sub>Gd<sub>0.1</sub>O<sub>2</sub> composite anodes for solid oxide fuel cells. *Energy & Environmental Science* **2013**, *6* (6), 1850-1857.
14. Fowler, D. E.; Haag, J.; Boland, C.; Bierschenk, D. M.; Barnett, S. A.; Poepelmeier, K. R., Stable, Low Polarization Resistance Solid Oxide Fuel Cell Anodes: La<sub>1-x</sub>Sr<sub>x</sub>Cr<sub>1-x</sub>Fe<sub>x</sub>O<sub>3-δ</sub> (x= 0.2-0.67). *Chemistry of Materials* **2014**, *26* (10), 3113-3120
15. Tao, S.; Irvine, J. T., A redox-stable efficient anode for solid-oxide fuel cells. *Nature Materials* **2003**, *2* (5), 320-323.
16. Tao, S.; Irvine, J. T. S., Synthesis and Characterization of (La<sub>0.75</sub>Sr<sub>0.25</sub>)Cr<sub>0.5</sub>Mn<sub>0.5</sub>O<sub>3-δ</sub>, a Redox-Stable, Efficient Perovskite Anode for SOFCs. *Journal of The Electrochemical Society* **2004**, *151* (2), A252-A259.
17. Yue, X.; Irvine, J. T. S., Impedance Studies on LSCM/GDC Cathode for High Temperature CO<sub>2</sub> Electrolysis. *Electrochemical and Solid-State Letters* **2012**, *15* (3), B31-B34.

18. Jiang, S. P.; Zhang, L.; Zhang, Y., Lanthanum strontium manganese chromite cathode and anode synthesized by gel-casting for solid oxide fuel cells. *Journal of Materials Chemistry* **2007**, *17* (25), 2627-2635.
19. Lay, E.; Gauthier, G.; Rosini, S.; Savaniu, C.; Irvine, J. T., Ce-substituted LSCM as new anode material for SOFC operating in dry methane. *Solid State Ionics* **2008**, *179* (27), 1562-1566.
20. Chen, X. J.; Liu, Q. L.; Chan, S. H.; Brandon, N. P.; Khor, K. A., High-performance cathode-supported SOFC with perovskite anode operating in weakly humidified hydrogen and methane. *Fuel Cells Bulletin* **2007**, *2007* (6), 12-16.
21. Cowin, P. I.; Petit, C. T.; Lan, R.; Irvine, J. T.; Tao, S., Recent progress in the development of anode materials for solid oxide fuel cells. *Advanced Energy Materials* **2011**, *1* (3), 314-332.
22. Chueh, W. C.; McDaniel, A. H.; Grass, M. E.; Hao, Y.; Jabeen, N.; Liu, Z.; Haile, S. M.; McCarty, K. F.; Bluhm, H.; El Gabaly, F., Highly enhanced concentration and stability of reactive  $\text{Ce}^{3+}$  on doped  $\text{CeO}_2$  surface revealed in operando. *Chemistry of Materials* **2012**, *24* (10), 1876-1882.
23. Feng, Z. A.; El Gabaly, F.; Ye, X.; Shen, Z.-X.; Chueh, W. C., Fast vacancy-mediated oxygen ion incorporation across the ceria-gas electrochemical interface. *Nature Communications* **2014**, *5*.
24. Chueh, W. C.; Hao, Y.; Jung, W.; Haile, S. M., High electrochemical activity of the oxide phase in model ceria-Pt and ceria-Ni composite anodes. *Nature Materials* **2012**, *11* (2), 155-161.
25. Zhang, C.; Grass, M. E.; Yu, Y.; Gaskell, K. J.; DeCaluwe, S. C.; Chang, R.; Jackson, G. S.; Hussain, Z.; Bluhm, H.; Eichhorn, B. W., Multielement activity mapping and potential mapping in solid oxide electrochemical cells through the use of operando XPS. *ACS Catalysis* **2012**, *2* (11), 2297-2304.
26. Zhang, C.; Yu, Y.; Grass, M. E.; Dejoie, C.; Ding, W.; Gaskell, K.; Jabeen, N.; Hong, Y. P.; Shavorskiy, A.; Bluhm, H., Mechanistic Studies of Water Electrolysis and Hydrogen Electro-Oxidation on High Temperature Ceria-Based Solid Oxide Electrochemical Cells. *Journal of the American Chemical Society* **2013**, *135* (31), 11572-11579.
27. Kogler, S.; Nenning, A.; Rupp, G. M.; Opitz, A. K.; Fleig, J., Comparison of Electrochemical Properties of  $\text{La}_{0.6}\text{Sr}_{0.4}\text{FeO}_{3-\delta}$  Thin Film Electrodes: Oxidizing vs. Reducing Conditions. *Journal of The Electrochemical Society* **2015**, *162* (3), F317-F326.
28. Fleig, J.; Baumann, F. S.; Brichzin, V.; Kim, H. R.; Jamnik, J.; Cristiani, G.; Habermeier, H. U.; Maier, J., Thin film microelectrodes in SOFC electrode research. *Fuel Cells* **2006**, *6* (3-4), 284-292.
29. Baumann, F. S.; Fleig, J.; Konuma, M.; Starke, U.; Habermeier, H. U.; Maier, J., Strong performance improvement of  $\text{La}_{0.6}\text{Sr}_{0.4}\text{Co}_{0.8}\text{Fe}_{0.2}\text{O}_{3-\delta}$  SOFC cathodes by electrochemical activation. *Journal of The Electrochemical Society* **2005**, *152* (10), A2074-A2079.
30. Baumann, F.; Fleig, J.; Cristiani, G.; Stuhlhofer, B.; Habermeier, H.-U.; Maier, J., Quantitative comparison of mixed conducting SOFC cathode materials by means of thin film model electrodes. *Journal of The Electrochemical Society* **2007**, *154* (9), B931-B941.
31. Wedig, A.; Merkle, R.; Stuhlhofer, B.; Habermeier, H.-U.; Maier, J.; Heifets, E., Fast oxygen exchange kinetics of pore-free  $\text{Bi}_{1-x}\text{Sr}_x\text{FeO}_{3-\delta}$  thin films. *Physical Chemistry Chemical Physics* **2011**, *13* (37), 16530-16533.
32. Kim, J. J.; Kuhn, M.; Bishop, S. R.; Tuller, H. L., Cathodic and defect properties of  $\text{Ba}_x\text{Sr}_{1-x}\text{Ti}_{1-y}\text{Fe}_y\text{O}_{3-\delta}$  mixed conducting oxides. *Solid State Ionics* **2013**, *230* (0), 2-6.
33. Baumann, F. S.; Fleig, J.; Habermeier, H.-U.; Maier, J., Impedance spectroscopic study on well-defined  $(\text{La,Sr})(\text{Co,Fe})\text{O}_{3-\delta}$  model electrodes. *Solid State Ionics* **2006**, *177* (11), 1071-1081.

34. Baumann, F.; Maier, J.; Fleig, J., The polarization resistance of mixed conducting SOFC cathodes: A comparative study using thin film model electrodes. *Solid State Ionics* **2008**, *179* (21), 1198-1204.
35. Huber, T.; Kubicek, M.; Opitz, A.; Fleig, J., The Relevance of Different Oxygen Reduction Pathways of  $\text{La}_{0.8}\text{Sr}_{0.2}\text{MnO}_3$  (LSM) Thin Film Model Electrodes. *Journal of The Electrochemical Society* **2015**, *162* (3), F229-F242.
36. Opitz, A. K.; Fleig, J., Investigation of  $\text{O}_2$  reduction on Pt/YSZ by means of thin film microelectrodes: The geometry dependence of the electrode impedance. *Solid State Ionics* **2010**, *181* (15-16), 684-693.
37. Opitz, A. K.; Lutz, A.; Kubicek, M.; Kubel, F.; Hutter, H.; Fleig, J., Investigation of the oxygen exchange mechanism on Pt-yttria stabilized zirconia at intermediate temperatures: Surface path versus bulk path. *Electrochimica Acta* **2011**, *56* (27), 9727-9740.
38. Navickas, E.; Huber, T. M.; Chen, Y.; Hetaba, W.; Holzlechner, G.; Rupp, G.; Stöger-Pollach, M.; Friedbacher, G.; Hutter, H.; Yildiz, B., Fast oxygen exchange and diffusion kinetics of grain boundaries in Sr-doped  $\text{LaMnO}_3$  thin films. *Physical Chemistry Chemical Physics* **2015**, *17* (12), 7659-7669.
39. Balachandran, U.; Eror, N., Electrical conductivity in lanthanum-doped strontium titanate. *Journal of The Electrochemical Society* **1982**, *129* (5), 1021-1026.
40. Marina, O. A.; Canfield, N. L.; Stevenson, J. W., Thermal, electrical, and electrocatalytical properties of lanthanum-doped strontium titanate. *Solid State Ionics* **2002**, *149* (1), 21-28.
41. Søgaaard, M.; Hendriksen, P. V.; Mogensen, M., Oxygen nonstoichiometry and transport properties of strontium substituted lanthanum ferrite. *Journal of Solid State Chemistry* **2007**, *180* (4), 1489-1503.
42. Kuhn, M.; Kim, J. J.; Bishop, S. R.; Tuller, H. L., Oxygen Nonstoichiometry and Defect Chemistry of Perovskite-Structured  $\text{Ba}_x\text{Sr}_{1-x}\text{Ti}_{1-y}\text{Fe}_y\text{O}_{3-y/2+\delta}$  Solid Solutions. *Chemistry of Materials* **2013**, *25* (15), 2970-2975.
43. Nenning, A.; Opitz, A.; Rameshan, C.; Rameshan, R.; Blume, R.; Hävecker, M.; Knop-Gericke, A.; Rupprechter, G.; Klötzer, B.; Fleig, J., Ambient Pressure XPS Study of Mixed Conducting Perovskite-type SOFC Cathode and Anode Materials under Well-Defined Electrochemical Polarization. *The Journal of Physical Chemistry C* **2016**, *120* (3), 1461-1471.
44. Mueller, D. N.; Machala, M. L.; Bluhm, H.; Chueh, W. C., Redox activity of surface oxygen anions in oxygen-deficient perovskite oxides during electrochemical reactions. *Nature Communications* **2015**, *6*.
45. Suntivich, J.; Hong, W. T.; Lee, Y.-L.; Rondinelli, J. M.; Yang, W.; Goodenough, J. B.; Dabrowski, B.; Freeland, J. W.; Shao-Horn, Y., Estimating Hybridization of Transition Metal and Oxygen States in Perovskites from OK-edge X-ray Absorption Spectroscopy. *The Journal of Physical Chemistry C* **2014**, *118* (4), 1856-1863.
46. Fleig, J., The grain boundary impedance of random microstructures: numerical simulations and implications for the analysis of experimental data. *Solid State Ionics* **2002**, *150* (1), 181-193.
47. Kuhn, M.; Hashimoto, S.; Sato, K.; Yashiro, K.; Mizusaki, J., Oxygen nonstoichiometry, thermo-chemical stability and lattice expansion of  $\text{La}_{0.6}\text{Sr}_{0.4}\text{FeO}_{3-\delta}$ . *Solid State Ionics* **2011**, *195* (1), 7-15.
48. Onuma, S.; Yashiro, K.; Miyoshi, S.; Kaimai, A.; Matsumoto, H.; Nigara, Y.; Kawada, T.; Mizusaki, J.; Kawamura, K.; Sakai, N., Oxygen nonstoichiometry of the perovskite-type oxide  $\text{La}_{1-x}\text{Ca}_x\text{CrO}_{3-\delta}$  ( $x = 0.1, 0.2, 0.3$ ). *Solid State Ionics* **2004**, *174* (1), 287-293.
49. Mizusaki, J.; Yamauchi, S.; Fueki, K.; Ishikawa, A., Nonstoichiometry of the perovskite-type oxide  $\text{La}_{1-x}\text{Sr}_x\text{CrO}_{3-\delta}$ . *Solid State Ionics* **1984**, *12*, 119-124.

50. Neagu, D.; Oh, T.-S.; Miller, D. N.; Ménard, H.; Bukhari, S. M.; Gamble, S. R.; Gorte, R. J.; Vohs, J. M.; Irvine, J. T., Nano-socketed nickel particles with enhanced coking resistance grown in situ by redox exsolution. *Nature Communications* **2015**, *6*.
51. Neagu, D.; Tsekouras, G.; Miller, D. N.; Ménard, H.; Irvine, J. T. S., In situ growth of nanoparticles through control of non-stoichiometry. *Nature Chemistry* **2013**, *5* (11), 916-923.
52. Nenning, A.; Opitz, A. K.; Huber, T. M.; Fleig, J., A novel approach for analyzing electrochemical properties of mixed conducting solid oxide fuel cell anode materials by impedance spectroscopy. *Physical Chemistry Chemical Physics* **2014**, *16* (40), 22321-22336.
53. DeCaluwe, S. C.; Grass, M. E.; Zhang, C.; Gabaly, F. E.; Bluhm, H.; Liu, Z.; Jackson, G. S.; McDaniel, A. H.; McCarty, K. F.; Farrow, R. L., In situ characterization of ceria oxidation states in high-temperature electrochemical cells with ambient pressure XPS. *The Journal of Physical Chemistry C* **2010**, *114* (46), 19853-19861.
54. Wedig, A.; Lynch, M. E.; Merkle, R.; Maier, J.; Liu, M., Sheet Resistance in Thin Film Solid Oxide Fuel Cell Model Cathodes: A Case Study on Circular  $\text{Bi}_{1-x}\text{Sr}_x\text{FeO}_{3-\delta}$  Microelectrodes. *ECS Transactions* **2012**, *45* (1), 213-224.
55. Ciucci, F.; Hao, Y.; Goodwin, D. G., Impedance spectra of mixed conductors: a 2D study of ceria. *Physical Chemistry Chemical Physics* **2009**, *11* (47), 11243-11257.
56. Ciucci, F.; Chueh, W. C.; Goodwin, D. G.; Haile, S. M., Surface reaction and transport in mixed conductors with electrochemically-active surfaces: a 2-D numerical study of ceria. *Physical Chemistry Chemical Physics* **2011**, *13* (6), 2121-2135.
57. Huber, T.; Opitz, A.; Kubicek, M.; Hutter, H.; Fleig, J., Temperature gradients in microelectrode measurements: Relevance and solutions for studies of SOFC electrode materials. *Solid State Ionics* **2014**, *268*, 82-93.
58. Jamnik, J.; Maier, J., Generalised equivalent circuits for mass and charge transport: chemical capacitance and its implications. *Physical Chemistry Chemical Physics* **2001**, *3* (9), 1668-1678.
59. Hendriks, M.; Ten Elshof, J.; Bouwmeester, H.; Verweij, H., The electrochemical double-layer capacitance of yttria-stabilised zirconia. *Solid State Ionics* **2002**, *146* (3), 211-217.
60. Rothschild, A.; Menesklou, W.; Tuller, H. L.; Ivers-Tiffée, E., Electronic structure, defect chemistry, and transport properties of  $\text{SrTi}_{1-x}\text{Fe}_x\text{O}_{3-y}$  solid solutions. *Chemistry of Materials* **2006**, *18* (16), 3651-3659.
61. Steinsvik, S.; Bugge, R.; Gjønnnes, J.; Taftø, J.; Norby, T., The Defect Structure of  $\text{SrTi}_{1-x}\text{Fe}_x\text{O}_{3-y}$  ( $x=0-0.8$ ) Investigated by Electrical Conductivity Measurements and Electron Energy Loss Spectroscopy (EELS). *The Journal of Physics and Chemistry of Solids* **1997**, *58* (6), 969-976.
62. Burriel, M.; Garcia, G.; Santiso, J.; Kilner, J. A.; Chater, R. J.; Skinner, S. J., Anisotropic oxygen diffusion properties in epitaxial thin films of  $\text{La}_2\text{NiO}_{4+\delta}$ . *Journal of Materials Chemistry* **2008**, *18* (4), 416-422.
63. Gerstl, M.; Frömling, T.; Schintlmeister, A.; Hutter, H.; Fleig, J., Measurement of  $^{18}\text{O}$  tracer diffusion coefficients in thin yttria stabilized zirconia films. *Solid State Ionics* **2011**, *184* (1), 23-26.
64. Wang, L.; Merkle, R.; Maier, J.; Acartürk, T.; Starke, U., Oxygen tracer diffusion in dense  $\text{Ba}_{0.5}\text{Sr}_{0.5}\text{Co}_{0.8}\text{Fe}_{0.2}\text{O}_{3-\delta}$  films. *Applied Physics Letters* **2009**, *94* (7), 071908.
65. Van der Pauw, L., A method of measuring the resistivity and Hall coefficient on lamellae of arbitrary shape. *Philips Technical Review* **1958**, *20* (8), 220-224.
66. Maier, J., *Physical Chemistry of Ionic Materials: Ions and Electrons in Solids*. Wiley: **2004**.
67. Arrivé, C.; Delahaye, T.; Joubert, O.; Gauthier, G., Exsolution of nickel nanoparticles at the surface of a conducting titanate as potential hydrogen electrode material for solid oxide electrochemical cells. *Journal of Power Sources* **2013**, *223*, 341-348.

68. Chueh, W. C.; Lai, W.; Haile, S. M., Electrochemical behavior of ceria with selected metal electrodes. *Solid State Ionics* **2008**, *179* (21), 1036-1041.
69. Lai, W.; Haile, S. M., Impedance spectroscopy as a tool for chemical and electrochemical analysis of mixed conductors: a case study of ceria. *Journal of the American Ceramic Society* **2005**, *88* (11), 2979-2997.
70. Jung, W. C.; Tuller, H. L., A New Model Describing Solid Oxide Fuel Cell Cathode Kinetics: Model Thin Film  $\text{SrTi}_{1-x}\text{Fe}_x\text{O}_{3-\delta}$  Mixed Conducting Oxides—a Case Study. *Advanced Energy Materials* **2011**, *1* (6), 1184-1191.
71. Jung, W. C.; Tuller, H. L., Impedance study of  $\text{SrTi}_{1-x}\text{Fe}_x\text{O}_{3-\delta}$  ( $x=0.05$  to  $0.80$ ) mixed ionic-electronic conducting model cathode. *Solid State Ionics* **2009**, *180* (11), 843-847.
72. Jung, W. C.; Tuller, H. L., Investigation of Cathode Behavior of Model Thin-Film  $\text{SrTi}_{1-x}\text{Fe}_x\text{O}_{3-\delta}$  ( $x=0.35$  and  $0.5$ ) Mixed Ionic-Electronic Conducting Electrodes. *Journal of The Electrochemical Society* **2008**, *155* (11), B1194-B1201.
73. Merkle, R.; Maier, J., Oxygen incorporation into Fe-doped  $\text{SrTiO}_3$ : Mechanistic interpretation of the surface reaction. *Physical Chemistry Chemical Physics* **2002**, *4* (17), 4140-4148.
74. Rothschild, A.; Litzelman, S. J.; Tuller, H. L.; Menesklou, W.; Schneider, T.; Ivers-Tiffée, E., Temperature-independent resistive oxygen sensors based on  $\text{SrTi}_{1-x}\text{Fe}_x\text{O}_{3-\delta}$  solid solutions. *Sensors and Actuators B: Chemical* **2005**, *108* (1), 223-230.
75. Chueh, W. C.; Haile, S. M., Electrochemical studies of capacitance in cerium oxide thin films and its relationship to anionic and electronic defect densities. *Physical Chemistry Chemical Physics* **2009**, *11* (37), 8144-8148.
76. Yao, Y.; Xie, T.; Gao, Y., *Handbook of Physical Chemistry*. Science and Technology Press, Shanghai: **1985**.
77. Filal, M.; Petot, C.; Mokchah, M.; Chateau, C.; Carpentier, J., Ionic conductivity of yttrium-doped zirconia and the “composite effect”. *Solid State Ionics* **1995**, *80* (1), 27-35.
78. Dudek, M.; Mosiałek, M.; Mordarski, G.; Socha, R.; Rapacz-Kmita, A., Ionic conductivity of the  $\text{CeO}_2\text{-Gd}_2\text{O}_3\text{-SrO}$  system. *Archives of Metallurgy and Materials* **2011**, *56* (4), 1249-1255.
79. Nenning, A.; Navickas, E.; Velicsanyi, P.; Opitz, A. K.; Hutter, H.; Fleig, J., Mapping electrochemically driven gas exchange of mixed conducting  $\text{SrTi}_{0.7}\text{Fe}_{0.3}\text{O}_{3-\delta}$  and  $\text{Ce}_{0.8}\text{Gd}_{0.2}\text{O}_{1.9}$  thin films by  $^{18}\text{O}$  tracer incorporation under reducing atmosphere. *Solid State Ionics* **2015**, *273*, 25-29.
80. Bessler, W. G.; Vogler, M.; Störmer, H.; Gerthsen, D.; Utz, A.; Weber, A.; Ivers-Tiffée, E., Model anodes and anode models for understanding the mechanism of hydrogen oxidation in solid oxide fuel cells. *Physical Chemistry Chemical Physics* **2010**, *12* (42), 13888-13903.
81. Velicsanyi, P.; Gerstl, M.; Nenning, A.; Hutter, H.; Fleig, J.; Opitz, A., The Effect of Mn Co-doping on the Electrochemical Properties of  $\text{Gd}_{0.2}\text{Ce}_{0.8}\text{O}_{1.9-\delta}/\text{Pt}$  Model-composite Electrodes. *ECS Transactions* **2015**, *68* (1), 1509-1516.
82. Jung, W.; Dereux, J. O.; Chueh, W. C.; Hao, Y.; Haile, S. M., High electrode activity of nanostructured, columnar ceria films for solid oxide fuel cells. *Energy & Environmental Science* **2012**, *5* (9), 8682-8689.
83. Oh, T.-S.; Rahani, E. K.; Neagu, D.; Irvine, J. T.; Shenoy, V. B.; Gorte, R. J.; Vohs, J. M., Evidence and Model for Strain-Driven Release of Metal Nanocatalysts from Perovskites during Exsolution. *The Journal of Physical Chemistry Letters* **2015**, *6*, 5106-5110.
84. Opitz, A. K.; Nenning, A.; Rameshan, C.; Rameshan, R.; Blume, R.; Hävecker, M.; Knop-Gericke, A.; Rupprechter, G.; Fleig, J.; Klötzer, B., Enhancing Electrochemical Water-Splitting Kinetics by Polarization-Driven Formation of Near-Surface Iron(0): An In Situ XPS

- Study on Perovskite-Type Electrodes. *Angewandte Chemie International Edition* **2015**, 54 (6), 2628-2632.
85. Adjianto, L.; Padmanabhan, V. B.; Gorte, R. J.; Vohs, J. M., Polarization-Induced Hysteresis in CuCo-Doped Rare Earth Vanadates SOFC Anodes. *Journal of The Electrochemical Society* **2012**, 159 (11), F751-F756.
  86. Swaroop, S.; Kilo, M.; Kossoy, A. E.; Lubomirsky, I.; Riess, I., Fast ion transport in nanoscaled thin film cerium oxide. *Solid State Ionics* **2008**, 179 (21), 1205-1208.
  87. Kubicek, M.; Rupp, G. M.; Huber, S.; Penn, A.; Opitz, A. K.; Bernardi, J.; Stöger-Pollach, M.; Hutter, H.; Fleig, J., Cation diffusion in  $\text{La}_{0.6}\text{Sr}_{0.4}\text{CoO}_{3-\delta}$  below 800°C and its relevance for Sr segregation. *Physical Chemistry Chemical Physics* **2014**, 16 (6), 2715-2726.
  88. Horita, T.; Yamaji, K.; Sakai, N.; Yokokawa, H.; Kawada, T.; Kato, T., Oxygen reduction sites and diffusion paths at  $\text{La}_{0.9}\text{Sr}_{0.1}\text{MnO}_{3-x}$ /yttria-stabilized zirconia interface for different cathodic overvoltages by secondary-ion mass spectrometry. *Solid State Ionics* **2000**, 127 (1), 55-65.
  89. Opitz, A. K.; Kubicek, M.; Huber, S.; Huber, T.; Holzlechner, G.; Hutter, H.; Fleig, J., Thin film cathodes in SOFC research: How to identify oxygen reduction pathways? *Journal of Materials Research* **2013**, 28 (16), 2085-2105.
  90. Nenning, A.; Navickas, E.; Hutter, H.; Fleig, J., Water-Induced Decoupling of Tracer and Electrochemical Oxygen Exchange Kinetics on Mixed Conducting Electrodes. *Submitted to The Journal of Physical Chemistry Letters*, **2016**.
  91. Maier, J., On the correlation of macroscopic and microscopic rate constants in solid state chemistry. *Solid State Ionics* **1998**, 112 (3), 197-228.
  92. Fleig, J.; Maier, J., The polarization of mixed conducting SOFC cathodes: Effects of surface reaction coefficient, ionic conductivity and geometry. *Journal of the European Ceramic Society* **2004**, 24 (6), 1343-1347.
  93. Kubicek, M.; Huber, T. M.; Welzl, A.; Penn, A.; Rupp, G. M.; Bernardi, J.; Stöger-Pollach, M.; Hutter, H.; Fleig, J., Electrochemical properties of  $\text{La}_{0.6}\text{Sr}_{0.4}\text{CoO}_{3-\delta}$  thin films investigated by complementary impedance spectroscopy and isotope exchange depth profiling. *Solid State Ionics* **2014**, 256, 38-44.
  94. Georges, S.; Skinner, S. J.; Lacorre, P.; Steil, M. C., Oxide ion diffusion in optimised LAMOX materials. *Dalton Transactions* **2004**, (19), 3101-3105.
  95. Liu, J.; Chater, R.; Morris, R. J.; Skinner, S., Oxygen surface exchange and diffusion studies of  $\text{La}_2\text{Mo}_2\text{O}_9$  in different exchange atmospheres. *Solid State Ionics* **2011**, 189 (1), 39-44.
  96. Sakai, N.; Yamaji, K.; Horita, T.; Xiong, Y. P.; Kishimoto, H.; Brito, M. E.; Yokokawa, H., Effect of water on electrochemical oxygen reduction at the interface between fluorite-type oxide-ion conductors and various types of electrodes. *Solid State Ionics* **2004**, 174 (1), 103-109.
  97. Sakai, N.; Yamaji, K.; Horita, T.; Xiong, Y. P.; Kishimoto, H.; Yokokawa, H., Effect of Water on Oxygen Transport Properties on Electrolyte Surface in SOFCs I. Surface Reaction Mechanism of Oxygen Isotope Exchange on Solid Oxide Electrolytes. *Journal of the Electrochemical Society* **2003**, 150 (6), A689-A694.
  98. Sakai, N.; Yamaji, K.; Horita, T.; Kishimoto, H.; Xiong, Y.; Yokokawa, H., Significant effect of water on surface reaction and related electrochemical properties of mixed conducting oxides. *Solid State Ionics* **2004**, 175 (1), 387-391.
  99. Huang, Y.-L.; Pellegrinelli, C.; Wachsmann, E. D., Fundamental Impact of Humidity on SOFC Cathode Degradation. *ECS Transactions* **2015**, 68 (1), 699-712.
  100. Huang, Y. L.; Pellegrinelli, C.; Wachsmann, E. D., Fundamental Impact of Humidity on SOFC Cathode ORR. *Journal of The Electrochemical Society* **2016**, 163 (3), F171-F182.

101. Holzlechner, G.; Kubicek, M.; Hutter, H.; Fleig, J., A novel ToF-SIMS operation mode for improved accuracy and lateral resolution of oxygen isotope measurements on oxides. *Journal of Analytical Atomic Spectrometry* **2013**, *28* (7), 1080-1089.
102. Nanning, A.; Opitz, A. K.; Rameshan, C.; Rameshan, R.; Blume, R.; Hävecker, M.; Knop-Gericke, A.; Rupprechter, G.; Klötzer, B.; Fleig, J., Ambient Pressure XPS Study of Mixed Conducting Perovskite-Type SOFC Cathode and Anode Materials under Well-Defined Electrochemical Polarization. *The Journal of Physical Chemistry C* **2016**, *120* (3), 1461-1471.
103. Starr, D.; Liu, Z.; Hävecker, M.; Knop-Gericke, A.; Bluhm, H., Investigation of solid/vapor interfaces using ambient pressure X-ray photoelectron spectroscopy. *Chemical Society Reviews* **2013**, *42* (13), 5833-5857.
104. Knop-Gericke, A.; Kleimenov, E.; Hävecker, M.; Blume, R.; Teschner, D.; Zafeiratos, S.; Schlögl, R.; Bukhtiyarov, V. I.; Kaichev, V. V.; Prosvirin, I. P., X-Ray Photoelectron Spectroscopy for Investigation of Heterogeneous Catalytic Processes. *Advances in Catalysis* **2009**, *52*, 213-272.
105. Liu, X.; Yang, W.; Liu, Z., Recent Progress on Synchrotron-Based In-Situ Soft X-ray Spectroscopy for Energy Materials. *Advanced Materials* **2014**, *26* (46), 7710-7729.
106. McDaniel, A. H.; Chueh, W. C.; Shavorskiy, A.; Tyliszczak, T.; Bluhm, H.; McCarty, K. F.; El Gabaly, F., (Invited) Probing Surface and Bulk States of Cathode Materials with Synchrotron-Based Soft X-Rays in a Functioning Solid Oxide Fuel Cell. *ECS Transactions* **2013**, *58* (3), 47-53.
107. Crumlin, E. J.; Bluhm, H.; Liu, Z., In situ investigation of electrochemical devices using ambient pressure photoelectron spectroscopy. *Journal of Electron Spectroscopy and Related Phenomena* **2013**, *190*, 84-92.
108. Crumlin, E. J.; Mutoro, E.; Hong, W. T.; Biegalski, M. D.; Christen, H. M.; Liu, Z.; Bluhm, H.; Shao-Horn, Y., In Situ Ambient Pressure X-ray Photoelectron Spectroscopy of Cobalt Perovskite Surfaces under Cathodic Polarization at High Temperatures. *The Journal of Physical Chemistry C* **2013**, *117* (31), 16087-16094.
109. Pechini, M. Method of preparing lead and alkaline earth titanates and niobates and coating method using the same to form a capacitor. *Patent US 3330697 A*, **1967**.
110. Rupp, G.; Limbeck, A.; Kubicek, M.; Penn, A.; Stöger-Pollach, M.; Friedbacher, G.; Fleig, J., Correlating surface cation composition and thin film microstructure with the electrochemical performance of lanthanum strontium cobaltite (LSC) electrodes. *Journal of Materials Chemistry A* **2014**, *2* (19), 7099-7108.
111. Hävecker, M. Innovative Station for In Situ Spectroscopy. [https://www.helmholtz-berlin.de/pubbin/igama\\_output?modus=einzel&sprache=en&gid=1671](https://www.helmholtz-berlin.de/pubbin/igama_output?modus=einzel&sprache=en&gid=1671) (accessed 2015-02-27).
112. Adler, S., Reference electrode placement in thin solid electrolytes. *Journal of The Electrochemical Society* **2002**, *149* (5), E166-E172.
113. Cai, Z.; Kubicek, M.; Fleig, J. r.; Yildiz, B., Chemical Heterogeneities on  $\text{La}_{0.6}\text{Sr}_{0.4}\text{CoO}_{3-\delta}$  Thin Films - Correlations to Cathode Surface Activity and Stability. *Chemistry of Materials* **2012**, *24* (6), 1116-1127.
114. Jung, W.; Tuller, H. L., Investigation of surface Sr segregation in model thin film solid oxide fuel cell perovskite electrodes. *Energy & Environmental Science* **2012**, *5* (1), 5370-5378.
115. Kubicek, M.; Limbeck, A.; Frömling, T.; Hutter, H.; Fleig, J., Relationship between cation segregation and the electrochemical oxygen reduction kinetics of  $\text{La}_{0.6}\text{Sr}_{0.4}\text{CoO}_{3-\delta}$  thin film electrodes. *Journal of The Electrochemical Society* **2011**, *158* (6), B727-B734.
116. Petrov, A.; Kononchuk, O.; Andreev, A.; Cherepanov, V.; Kofstad, P., Crystal structure, electrical and magnetic properties of  $\text{La}_{1-x}\text{Sr}_x\text{CoO}_{3-y}$ . *Solid State Ionics* **1995**, *80* (3), 189-199.
117. Bucher, E.; Sitte, W., Defect chemical analysis of the electronic conductivity of strontium-substituted lanthanum ferrite. *Solid State Ionics* **2004**, *173* (1), 23-28.

118. Kuhn, M.; Fukuda, Y.; Hashimoto, S.; Sato, K.; Yashiro, K.; Mizusaki, J., Oxygen Nonstoichiometry and Thermo-Chemical Stability of Perovskite-Type  $\text{La}_{0.6}\text{Sr}_{0.4}\text{Co}_{1-y}\text{Fe}_y\text{O}_{3-\delta}$  ( $y = 0, 0.2, 0.4, 0.5, 0.6, 0.8, 1$ ) Materials. *Journal of The Electrochemical Society* **2013**, *160* (1), F34-F42.
119. Descostes, M.; Mercier, F.; Thromat, N.; Beaucaire, C.; Gautier-Soyer, M., Use of XPS in the determination of chemical environment and oxidation state of iron and sulfur samples: constitution of a data basis in binding energies for Fe and S reference compounds and applications to the evidence of surface species of an oxidized pyrite in a carbonate medium. *Applied Surface Science* **2000**, *165* (4), 288-302.
120. Fleig, J., On the current–voltage characteristics of charge transfer reactions at mixed conducting electrodes on solid electrolytes. *Physical Chemistry Chemical Physics* **2005**, *7* (9), 2027-2037.
121. Katz, M. B.; Graham, G. W.; Duan, Y.; Liu, H.; Adamo, C.; Schlom, D. G.; Pan, X., Self-Regeneration of Pd– $\text{LaFeO}_3$  Catalysts: New Insight from Atomic-Resolution Electron Microscopy. *Journal of the American Chemical Society* **2011**, *133* (45), 18090-18093.
122. Chen, Y.; Jung, W.; Cai, Z.; Kim, J. J.; Tuller, H. L.; Yildiz, B., Impact of Sr segregation on the electronic structure and oxygen reduction activity of  $\text{SrTi}_{1-x}\text{Fe}_x\text{O}_3$  surfaces. *Energy & Environmental Science* **2012**, *5* (7), 7979-7988.
123. Tsvetkov, N.; Lu, Q.; Yildiz, B., Improved electrochemical stability at the surface of  $\text{La}_{0.8}\text{Sr}_{0.2}\text{CoO}_3$  achieved by surface chemical modification. *Faraday Discussions* **2015**, *182*, 257-269.
124. Kogler, S. Electrochemical properties of  $\text{La}_{0.6}\text{Sr}_{0.4}\text{FeO}_{3-\delta}$  in reducing and oxidizing conditions. PhD Thesis, TU Vienna, **2014**.
125. McIntyre, N.; Cook, M., X-ray photoelectron studies on some oxides and hydroxides of cobalt, nickel, and copper. *Analytical Chemistry* **1975**, *47* (13), 2208-2213.
126. Miyoshi, S.; Onuma, S.; Kaimai, A.; Matsumoto, H.; Yashiro, K.; Kawada, T.; Mizusaki, J.; Yokokawa, H., Chemical stability of  $\text{La}_{1-x}\text{Sr}_x\text{CrO}_3$  in oxidizing atmospheres. *Journal of Solid State Chemistry* **2004**, *177* (11), 4112-4118.
127. Fergus, J. W., Lanthanum chromite-based materials for solid oxide fuel cell interconnects. *Solid State Ionics* **2004**, *171* (1), 1-15.
128. Fleig, J.; Schintlmeister, A.; Opitz, A.; Hutter, H., The determination of the three-phase boundary width of solid oxide fuel cell cathodes by current-driven  $^{18}\text{O}$  tracer incorporation. *Scripta Materialia* **2011**, *65* (2), 78-83.
129. Llewellyn-Jones, F., *The physics of electrical contacts*. Clarendon Press: **1957**.
130. Huber, T. M. Konstruktion einer Vakuum-Mikrokontaktapparatur und Impedanzmessungen an mikrostrukturierten Platin- und Nickelelektroden auf Yttrium stabilisiertem Zirconiumoxid in Wasserstoff Atmosphäre. MSC Thesis, TU Vienna, **2010**.
131. Fleig, J.; Jamnik, J.; Maier, J.; Ludvig, J., Inductive loops in impedance spectroscopy caused by electrical shielding. *Journal of The Electrochemical Society* **1996**, *143* (11), 3636-3641.

# List of Abbreviations and Acronyms

## Materials:

- STF73:  $\text{SrTi}_{0.7}\text{Fe}_{0.3}\text{O}_{3-\delta}$
- STF37:  $\text{SrTi}_{0.3}\text{Fe}_{0.7}\text{O}_{3-\delta}$
- LSF64:  $\text{La}_{0.6}\text{Sr}_{0.4}\text{FeO}_{3-\delta}$
- LSC64:  $\text{La}_{0.6}\text{Sr}_{0.4}\text{CoO}_{3-\delta}$
- LSM:  $\text{La}_x\text{Sr}_{1-x}\text{MnO}_{3-\delta}$
- GDC:  $-\text{Ce}_{1-x}\text{Gd}_x\text{O}_{2-\delta}$ .
- A-deficient LSCr-Ni:  $\text{La}_{0.7}\text{Sr}_{0.2}\text{Cr}_{0.9}\text{Ni}_{0.1}\text{O}_{3-\delta}$
- A-stoichiometric LSCr-Ni:  $\text{La}_{0.8}\text{Sr}_{0.2}\text{Cr}_{0.9}\text{Ni}_{0.1}\text{O}_{3-\delta}$
- YSZ:  $\text{ZrO}_2$  doped with 9.5 mol%  $\text{Y}_2\text{O}_3$

## Mathematical symbols:

- $\Delta_{\text{R}}\text{H}^0$  standard reaction enthalpy
- $\Delta_{\text{R}}\text{S}^0$  standard reaction entropy
- $\mu^0$  chemical potential under standard conditions
- $\mu_i$  chemical potential of species i
- $\tilde{\mu}_i = \mu_i + z_i e \varphi$  electrochemical potential of species i
- $\varphi$  electric potential
- $\eta^*$  polarization potential
- $c_0$  concentration of oxygen sites (per  $\text{cm}^3$ )
- $c_i$  concentration of particle i (per  $\text{cm}^3$ )
- d distance between atomic layers in the crystal
- $D^*$  tracer diffusion coefficient ( $\text{cm}^2\text{s}^{-1}$ )
- $D^\delta$  chemical diffusion coefficient ( $\text{cm}^2\text{s}^{-1}$ )
- $D^a$  conductivity based diffusion coefficient ( $\text{cm}^2\text{s}^{-1}$ )
- e elementary charge (or euler's number)
- $E_f$  Fermi energy, equivalent for  $\tilde{\mu}_{\text{electron}}$
- $E_b$  binding energy in XPS
- $E_{\text{kin}}$  kinetic energy
- I current

- $j$  imaginary unit  $\sqrt{-1}$
- $J_i$  particle current
- $j_i$  current density of particle  $i$
- $k^*$  tracer surface exchange coefficient ( $\text{cm s}^{-1}$ )
- $k^q$  conductivity based surface exchange coefficient ( $\text{cm s}^{-1}$ )
- $k_B$  Boltzmann's constant
- $a$  specific length
- $q$  charge (Coulomb)
- $q_i$  charge of the particle ( $z_i e = q_i$ )
- $T$  temperature
- $U_{\text{set}}$  applied potential (between two electrodes)
- oxygen vacancy
- $Z$  impedance
- $z_i$  charge number

#### Acronyms

- ASR area specific resistance
- $C$  capacitance
- CPE constant phase element
- EIS Electrochemical Impedance Spectroscopy
- $K$  equilibrium constant
- MIEC mixed ionic electronic conductivity
- PLD pulsed laser deposition
- SOC solid oxide cell
- SOEC solid oxide electrolysis cell
- SOFC solid oxide fuel cell
- TEC thermal expansion coefficient
- TOF-SIMS time of flight - secondary ion mass spectrometry
- TPB three phase boundary
- XPS X-ray photoelectron spectroscopy
- NAP-XPS near-ambient pressure XPS
- XRD X-ray diffraction

## List of Figures

Figure 1. Sketch of the electrochemically active zones on mixed conducting (left) and metallic (right) SOFC anodes. ....	6
Figure 2. Computed defect diagram of LSF64 at 615°C, using oxygen nonstoichiometry data from Ref. <sup>47</sup> and the defect model from section 2.1. Defect concentrations are normalized to the number of ABO <sub>3</sub> formula units. ....	15
Figure 3. Computed defect diagram of STF73 at 615°C, using oxygen nonstoichiometry data from Ref. <sup>42</sup> and the defect model from section 2.1. Defect concentrations are normalized to the number of ABO <sub>3</sub> formula units. ....	15
Figure 4. Computed defect diagram of La <sub>0.8</sub> Sr <sub>0.2</sub> CrO <sub>3-δ</sub> at 615°C, using defect chemical data from Ref. <sup>49</sup> , extrapolated from 1000°C to 615°C and the defect chemical model from section 2.1. Defect concentrations are normalized to the number of ABO <sub>3</sub> formula units.....	16
Figure 5. Sketched cross-section of a microelectrode with (a) embedded current collectors, or (b) current collectors on top of the MIEC film. (c): optical micrograph of a produced electrode in transmitted light mode. ....	18
Figure 6. (a) SEM image of a 300 nm thick STFO film on YSZ and sputtered Pt. (b) Diffraction pattern of the thin film. ....	19
Figure 7. Top view (a, c) and cross-section (b, d) of the two measurement modes. In the in-plane mode (a, b) the voltage is applied between the two metal finger structures. In the electrochemical mode (c, d), both current collectors are treated as one electrical terminal and measured against a macroscopic counter-electrode.....	20
Figure 8. Processes relevant for the impedance of a MIEC anode with metal fingers below the anode (left) and on top (right). Arrows indicate anodic current, although impedance spectroscopy probes both directions. ....	21
Figure 9 Equivalent circuit for MIEC electrodes with high electronic and ionic conductivity, according to <sup>58</sup> . ....	22
Figure 10. Generalized transmission line circuit describing a MIEC thin film on an electrolyte (a). Generalized transmission line circuit describing a MIEC film on an electronic conductor (e.g. current collector) (b) .....	25
Figure 11. Terminals of the transmission line circuit which are set to the metal finger edges (a). For the electrochemical measurement mode (b), two circuits with different given boundary conditions result in the same impedance function. The same is true for the in-plane measurement mode (c). ....	28
Figure 12. Calculated normalized polarization potential ( $\eta^*/U_0$ ) in the DC case for in-plane and electrochemical measurement modes.....	28

Figure 13. (a-b) Full equivalent circuits for electrodes with current collectors deposited on top of the current collectors: (a) electrochemical mode, (b) in-plane mode. (c-d) Full equivalent circuits for electrodes with embedded current collectors, also in (c) electrochemical and (d) in-plane mode. The elements $R_{int}$ , $C_{int}$ , $C_{chem}$ and $R_{surface}$ reflect area-specific resistances and capacitances, $R_{eon}$ and $R_{ion}$ are electronic and ionic sheet resistance, respectively.....	28
Figure 14 Simulated spectra for current collectors on top (dashed lines) and beneath the electrode (solid lines). The inset shows a magnification of the in-plane spectra.....	30
Figure 15. (a) Measured (symbols) and fitted (lines) impedance spectra of an electrode with 103 nm thickness and 11.6 mm finger distance at 660°C. (b-d) The calculated lateral distribution of the polarization potential is plotted for three different frequencies.....	32
Figure 16. (a): Impedance spectra (symbols) including fit (lines) for a 103 nm thick STF0 microelectrode with different finger distances at 660°C. The insets show magnifications emphasising the in-plane measurements. (b): Materials parameters of different electrodes at 660°C with a film thickness of 103 nm, deduced by fitting of the impedance spectra. The parameters are independent of the metal finger distance (ASR = area specific resistance).....	35
Figure 17. Arrhenius plot of the relevant resistive parameters and plot of the chemical capacitance between 490 and 760°C.....	36
Figure 18. Types of investigated samples: (a) Microelectrode with current collectors on YSZ in electrochemical contacting mode. (b) Continuous STF thin film with embedded current collectors on MgO for in-plane conductivity measurements. (c) Symmetrical 5x5mm cell used for temperature-dependent measurements. (d) Sketch thin films with top and embedded current collectors. (f) Micrograph of microelectrodes with the 9 investigated current collector geometries.....	48
Figure 19. (a) Equivalent circuit used to fit the in-plane measurements on MgO substrates. (b) Impedance spectrum (circles) and fit (solid line) of an in-plane measurement of STF37 at 650°C.....	50
Figure 20. Electronic conductivity (a), ionic conductivity (b) and chemical capacitance (c) of STF37 and STF73 at 650°C in varying $H_2:H_2O$ mixing ratio, plotted as a function of $pO_2$ .....	52
Figure 21. Impedance spectra of STF37 microelectrodes measured in the electrochemical mode with current collectors embedded and on top at 650°C, normalized to the atmosphere exposed STF surface area.....	54
Figure 22. Inverse ASR of STF microelectrodes as function of the triple-phase boundary density (normalized to the atmosphere-exposed STF surface) measured in electrochemical mode at 650°C. The grey bar on the bottom represents the typical range of ASR measured on electrodes with embedded current collectors and thus without triple-phase boundary.....	55
Figure 23. (a) Impedance spectra of macroscopic symmetrical cells with STF37 and STF73 electrodes (b) Arrhenius plot of the area specific resistance of the electrodes°C.....	56
Figure 24. SEM images of STF37 and STF73 before and after reduction at 650°C and 800°C for 5h in 25mbar $H_2+0.8mbar H_2O$ .....	57

Figure 25. Area specific resistance and chemical capacitance as function of $pO_2$ (a) and DC characteristics (b) of STF37 at 650°C.....	58
Figure 26. (a) Noble metal electrodes, which provide an electrical contact and block oxygen diffusion, were prepared below (EB geometry) and on top (ET geometry) of the GDC or STFO layer. The oxygen diffusion pathways under equilibrium conditions are sketched for ET and EB current collectors. Working and counter electrodes were contacted and polarized in the tracer exchange chamber. b) Increased oxygen incorporation rate caused by cathodic bias near an EB current collector; in some distance from the current collector edge only thermally driven tracer exchange remains due to limited electronic conductivity within the MIEC thin film.....	63
Figure 27. Isotope distribution images measured by ToF-SIMS and (b) lateral tracer fraction profiles of an STFO thin film near to the edge of an electrode with EB geometry for thermally and bias driven $^{18}O$ incorporation. ....	65
Figure 28. Isotope distribution image with lateral tracer fraction profiles in a GDC thin film near to an EB current collector and the corresponding profiles for three different bias values (c and d). Cathodic bias (-200 mV: blue curve; -500 mV: green curve) locally increases the electronic conductivity and thus the width of the electrochemically active zone. (b) The depth profiles of isotope concentration were checked in the MIEC film on top of the EB current collector (red triangles) and on top of YSZ (green circles). ....	67
Figure 29. Isotope distribution images and lateral tracer fraction profiles of cathodically (-500 mV) and anodically (+500 mV) polarized noble metal electrodes with (a) EB and (b) ET geometry on the STFO layer.....	68
Figure 30. $k^q$ as a function of time while switching between dry and humid oxidizing atmospheres at 420°C.....	74
Figure 31. a) Sketch of sample geometry and tracer exchange routine during EIS. For measurements in reducing atmosphere the MIEC films were micropatterned to circular microelectrodes. b) Impedance measurements on $La_{0.6}Sr_{0.4}FeO_{3-\delta}$ (LSF) and $SrTi_{0.3}Fe_{0.7}O_{3-\delta}$ (STF) thin film electrodes during tracer exchange in dry and humid oxidizing atmosphere at 418°C, normalized to the active electrode area. c) and d) $^{18}O$ tracer depth profiles in LSF and STF measured after the exchange, including a simulation assuming $k^* = k^q_{dry} (^{18}O_2(dry) \text{ theoretical})$ . ....	75
Figure 32. a) Impedance measurements on LSF and STF thin films microelectrodes during isotope exchange in humid reducing atmosphere at 396°C. b) Measured $^{18}O$ depth profiles, including a simulation assuming $k^* = k^q$ (theoretical).....	75
Figure 33. In order to highlight the difference between dry and humid atmospheres, the ratios of $k^q/k^*$ from Table 1 are shown in the bar graph. The sketches show different oxygen incorporation mechanisms in $^{18}O_2$ and $H_2^{18}O$ atmospheres. Reaction (1) shows the $^{18}O_2$ incorporation (only in dry atmosphere) into surface vacancies, requiring an electron transfer. Proposed mechanism of the $H_2^{18}O$ tracer exchange reaction: (2) Tracer-marked water adsorbs on a surface vacancy and dissociates into two $OH^-$ groups. The tracer marked $^{18}OH^-$ can then be transformed to tracer $^{18}O^{2-}$ via two parallel processes: (3) Fast desorption of water, using a neighbouring oxide ion. (4) Slow electron transfer to two surface hydroxyls and formation of $H_2$ .....	78

- Figure 34. Sketch of the entire working electrode surface (a) and photograph of a part (b). The Pt current collectors ( $5\ \mu\text{m}$  width,  $25\ \mu\text{m}$  distance) were placed beneath the LSF and STF layer to provide good electric contact. (c) Sketched cross section of the sample and mount in the ambient XPS chamber..... 84
- Figure 35. Impedance spectra of LSF (red squares), STF (blue circles) and LSC (black triangles) in 0.5 mbar  $\text{O}_2$  at  $615\pm 15^\circ\text{C}$ . Fitting with a simplified impedance model (green line) enables a reasonable estimation of electrolyte losses and electrode polarization resistance..... 86
- Figure 36.(a) O 1s and (b) Sr 3d spectra of STF, LSC and LSF in 0.5 mbar  $\text{O}_2$ ,  $615^\circ\text{C}$ ,  $U_{\text{set}} = 0\ \text{V}$ . In addition to the fixed doublet separation of Sr 3d<sub>3/2</sub> and Sr 3d<sub>5/2</sub> states, two chemically different components (green and brown) can be fitted to the spectra of Sr and O. c) Plot of the area ratio of the high and low binding energy components as function of the analysis depth (IMFP) by photon energy variation shows strong surface enrichment of the high binding energy components. Both low binding energy O 1s components were summarized as “bulk” oxygen. .... 87
- Figure 37. O 1s spectra of LSC (a) and STF (b) in 0.5 mbar  $\text{O}_2$  as a function of beam irradiation time. After 6-7 hours of irradiation the high binding energy component – probably OH groups – has decreased in intensity. After moving to a new position, the previous intensity is almost restored. This effect is stronger on STF. (c) Subsequently recorded (top to bottom) XPS spectra of the O 1s region in LSF. The high binding energy (surface) component irreversibly disappears during an initial cathodic polarization, the effect of beam damage could therefore not be explicitly studied – the indicated potential is the set voltage, not  $\eta$ . .... 89
- Figure 38. : a) Arrhenius plot of the electronic conductivity of LSC (black squares), LSF (red circles) and STF (blue triangles) thin films in air. b) Valence band spectra at  $615^\circ\text{C}$  in 0.5 mbar  $\text{O}_2$ . The conductivity of LSC is virtually temperature independent and a metal-like Fermi edge structure is visible in the valence band spectra. The conductivities of STF and LSF are thermally activated and their valence band structures are semiconductor-like..... 89
- Figure 39. Fe 2p, O 1s and Sr 3d XPS spectra of STF (blue) and LSF (red) in  $\text{O}_2$  (thick lines) and  $\text{H}_2$ - $\text{H}_2\text{O}$  (thin lines + symbols) atmospheres: the binding energy of O and Sr increases by roughly 0.9 eV in reducing atmosphere, due to a Fermi level shift. The oxidation states of O and Sr remain unaffected. The well-separated oxygen component of STF at 532 eV disappears in reducing atmosphere. Satellite features in the Fe 2p spectra appear at 718 eV (indicating  $\text{Fe}^{3+}$ ) in oxidizing and 715+718 eV (indicating mixed  $\text{Fe}^{2+/3+}$ ) in reducing conditions. Intensities of the spectra were rescaled to compensate different gas-phase absorption and cation composition. .... 91
- Figure 40 XPS spectra of the Ti 2p (a) and La 3d peaks (b). The Ti 2p<sub>1/2</sub> peak is strongly broadened, which is typical for this component. Also the La 3d region shows doublet splitting and in addition strong satellite features (at 838 and 856 eV). These are caused by a charge transfer to a neighbouring atom. When the atmosphere is changed from oxidizing to reducing, the binding energy increases by roughly 0.9V, due to a Fermi level shift..... 91

- Figure 41. Changes of the defect chemistry under varying  $pO_2$  cause a shift of the Fermi level within the band gap. Accordingly the measured binding energy shifts – also for elements that do not undergo chemical changes. .... 94
- Figure 42. O 1s, Fe 2p, Co 2p and Sr 3d core level XPS spectra of LSC (black), STF (blue) and LSF (red) thin films under polarization (indicated voltage). No significant changes in surface and bulk states or transition metal satellite features are observed upon bias. Spectra were measured at photoelectron energies of 120-140 eV and scaled to compensate for different Sr and Fe contents. .... 96
- Figure 43. Peak positions as a function of overpotential in 0.5 mbar  $O_2$ . On LSF and STF, all peaks shift with slopes of -0.7 to -1.0 eV/V, which is largely caused by a Fermi level shift. On LSC the slopes are significantly smaller (-0.5 to -0.7 eV/V) and the Co 2p peak does not shift at all. Most likely, the metallic electronic structure of LSC and the higher reducibility of Co ions cause the differences. .... 96
- Figure 44. : Valence band and Fe 2p XPS spectra of STF (a,c) and LSF (b,d) polarized by different overpotentials in  $H_2/H_2O$  atmosphere. Each spectrum is plotted with the same scale. Near-surface Fe gets gradually reduced from  $Fe^{3+}$  to  $Fe^{2+}$  with decreasing anodic bias. Upon cathodic polarization, an additional  $Fe^0$  species evolves, visible by the evolution of a Fermi edge feature in the valence band ( $\times$ ) and an additional Fe 2p<sub>3/2</sub> peak at 706.5 eV ( $\times$ ). Simultaneously, a strong decrease in the total Fe signal is observed. The applied overpotentials are indicated for each spectrum. e) DC-characteristics of LSF (red squares) and STF (blue circles). When  $Fe^0$  is present during cathodic polarization (filled symbols), the current increases strongly nonlinear already for very small bias (inset). .... 99
- Figure 45. a) Impedance spectra measured on LSF and STF electrodes in  $H_2/H_2O$  with (solid symbols,  $\eta \approx -50$  mV) and without (open symbols,  $\eta = 0$  mV) the presence of  $Fe^0$ . A strong decrease of the electrode resistance is observed already at very low  $\eta$ , especially for LSF. b) Total Fe 2p<sub>3/2</sub> signal intensity (normalized to the initial area) showing a drastic decrease when  $Fe^0$  is formed. c) Ratio of metallic to total Fe signal intensity. The reduction and oxidation of Fe is reversible on LSF and shows a slight hysteresis on STF. .... 101
- Figure 46. Measured chemical capacitance of the LSF electrode as function of the effective oxygen partial pressure at 600°C. The open circuit  $pO_2$  is 0.5 mbar in oxidizing and  $3 \cdot 10^{-21}$  mbar in reducing conditions. Solid line: calculated chemical capacitance of idealized STF bulk (volume: 300 nm thickness, 11 mm<sup>2</sup> area), using oxygen nonstoichiometry data from<sup>32</sup>. The different defect regimes correspond well with the measured chemical capacitance. .... 103
- Figure 47. Measured chemical capacitance of the LSF electrode as function of the effective oxygen partial pressure at 600°C. The open circuit  $pO_2$  is 0.5 mbar in oxidizing and  $3 \cdot 10^{-21}$  mbar in reducing conditions. The increased scatter under reducing conditions is probably connected with the segregation of  $Fe^0$ . Solid line: calculated chemical capacitance of idealized LSF bulk (volume: 300 nm thickness, 11 mm<sup>2</sup> area), using a defect chemical model from Ref.<sup>47</sup> The different defect regimes correspond well with the measured chemical capacitance. .... 103

- Figure 48. Top-view (a) and cross-section (b) sketch of a model cell mounted on the modified sample holder. For a better overview, the electrical wires are not shown in the cross section.....107
- Figure 49: Sketch of the prepared model cell (a), temperature profile of the pre-reduction procedure (b) and impedance spectra measured on LSF during pre-reduction and in UHV at 600°C (c).....109
- Figure 50: Photographs of the modified tracer exchange setup. The sample (ca. 2.5x2.5 mm<sup>2</sup>) is clamped between two Pt-Ir wires that act as electrical contacts (c-d) and can be moved between the heating position (b) and the quenching position inside the water-cooled flange (a). Fast heating and cooling rates are achieved due to the small thermal mass of the sample and heating wires.....110
- Figure 51: (a) XPS spectra acquired on pre-reduced LSF and STF electrodes during various levels of electrochemical polarization vs. 1 bar O<sub>2</sub> at 600°C. (b) Angle-resolved metal: oxide peak area ratio. At a larger angle against the surface normal the intensity of the metallic peak increases, supporting the interpretation of surface particles. ....112
- Figure 52. Comparison of the metal exsolution regimes in LSF64 and STF 37. (a-b) After polarization experiments in UHV XPS, under conditions very similar to those in ambient pressure XPS, small Fe particles segregate to the surface. (c) STF surface after PLD, showing no particles. (d) Surface image of STF37 after reduction in 32:1 H<sub>2</sub>:H<sub>2</sub>O atmosphere at 790°C. The strong roughening indicates decomposition and recrystallization.....113
- Figure 53: (a) Ni3p (and Cr3s) XPS spectra of A-site deficient LSCr-Ni films, showing an increase of Ni3p binding energy by approx. 1 eV at a polarization of -530 mV vs. O<sub>2</sub>, indicating a valence change from Ni metal to Ni oxide. (b) SEM cross section of the thin film, showing a smooth crack-free film also at the interface between LSCr-Ni on YSZ and LSCr-Ni on the current collector. (c) A-site stoichiometric LSCr-Ni film after reduction at 800°C for 5 hours, showing no exsolutions. (d) A-site deficient LSCr-Ni film after the presented polarization experiments in the XPS chamber, showing few very small Ni particles and (e) A-site deficient LSCr-Ni film after reduction at 800°C, showing a significant amount of Ni exsolutions. ....114
- Figure 54: (a) Angle-resolved photoelectron spectra, with effective information depth indicated, measured on A-site deficient LSCr-Ni films at a sample temperature of 600°C at a pO<sub>2</sub> corresponding to -530 mV vs. O<sub>2</sub>. (b) Cr<sup>6+</sup>:Cr<sup>3+</sup> component ratio plotted as a function of information depth. ....115
- Figure 55: Defect chemical modelling of an acceptor-doped mixed conductor, showing the shift of the binding energy (a) as well as main electronic and ionic defect concentrations (b) as a function of overpotential vs. 1 bar O<sub>2</sub>. The calculations show constant Fermi level in the regime of mainly electronic charge compensation, and shifting Fermi level in the regime of mainly ionic charge compensation. Defect concentrations are normalized to 1 ABO<sub>3</sub> formula unit.....117
- Figure 56: observed relation of binding energy shift vs. overpotential on STF37 (a), LSC64 (b) and La<sub>0.7</sub>Sr<sub>0.2</sub>Cr<sub>0.9</sub>Ni<sub>0.1</sub>O<sub>3-δ</sub> (c). At the lowest overpotential vs. O<sub>2</sub> the shift was defined as 0. ....117
- Figure 57. Sketch of the numerical model for simulation of impedance spectra. ....120

Figure 58. Correction factors of the spreading resistance formula for finite electrolyte dimensions, assuming (a) a counter electrode on the top side and (b) a counter electrode on the bottom of the electrolyte.....	121
Figure 59. Simulated impedance spectra of a 200 $\mu\text{m}$ diameter electrode, assuming triple phase or surface activity. All simulated electrodes have an electrochemical resistance of 100 k $\Omega$ . Deviations from the intuitive equivalent circuit model (black dots) are only caused by the electrolyte spreading resistance.....	122
Figure 60. Electrolyte current density (color) and equipotential lines in the electrolyte dominated high-frequency regime.....	123
Figure 61. DC current density (color) and equipotential lines of a surface active electrode. The current density is rather homogeneous along the electrode surface. ....	123
Figure 62. Electrolyte current density (color) and equipotential lines of a TPB active electrode in DC conditions.....	124
Figure 63. Simulated impedance spectra (a) and current distributions (b) in the electrolyte, assuming different electrochemical properties of the bottom counter electrode.....	125
Figure 64. Simulated (a) and measured (b) impedance spectra of GDC microelectrodes at $\sim 505^\circ\text{C}$ on a 0.5 mm thick YSZ substrate with a porous Pt bottom electrode and an additional counter electrode on the side.....	126

## List of Tables

Table 1. Dimensions of the electrodes and current collectors. The meander length and effective circumference are according to Figure 7a. ....	20
Table 2. Mean values of the fitting parameters and their standard deviation for two different thin film samples at 660°C. ....	35
Table 3. Activation energies of the resistive parameters, 310 nm film. ....	36
Table 4. Summary of tracer ( $k^*$ ) and electrical ( $k^q$ ) exchange coefficients of $\text{La}_{0.6}\text{Sr}_{0.4}\text{FeO}_{3-\delta}$ and $\text{SrTi}_{0.3}\text{Fe}_{0.7}\text{O}_{3-\delta}$ in various atmospheres. ....	76
Table 5. Parameters for the thin film working electrode deposition via PLD. ....	83
Table 6: Deposition parameters of the thin films electrodes used for the electrochemical XPS measurements. ....	109
Table 7. Properties of the simulations in Figure 63 and Figure 64. ....	125

## Acknowledgements

After three joyful and (mostly) productive years of my life it is time to thank the many people that supported me during this time. Without the help and input of them, I would have never accomplished my scientific goals.

I thank Prof. Jürgen Fleig not only sharing a lot of his time for scientific discussions and thorough optimization of my publications but also for his trust and encouragement for my work.

I also thank my colleague Edvinas for his vital contributions to my work by extensive SIMS analysis and contributing substantial parts of the submitted manuscripts.

Many parts of my thesis are the result of joint experiments and collaborations with Christoph Rameshan from Günther Rupprechter's Sergey Volkov with Vedran Vonk from Prof. Andreas Stierle's Group Group at the DESY and Bernhard Klötzer's group at the University of Innsbruck. Thank you for the great collaboration and hard work during the beam times.

Acknowledgements also go to the FWF and the project "*Solids4Fun*" for financial support and my colleagues in the doctoral college for fruitful discussions and long evenings of playing Werewolves. I thank André Vogel for organizing the seminars and the Summer School each year.

Some of my experiments were done on the XPS analyser at the Analytical Instrumentation Center, which was brought to its now reliably operating state by the constant maintenance of Kurt Piplitz, Johannes Frank, Wolfgang Werner, Roland Leber, Annette Foelske-Schmitz and Markus Sauer, as well as Jens Sauter and Dieter Funnemann from SPECS. Thank you for your enduring efforts.

Special thanks also go to Alexander Opitz who gave me an excellent introduction into the theory and practical usage of our lab equipment and the diploma students that I supervised during my thesis: Peter for investigating Mn doped GDC, Lukas for his thorough characterization of STF electrodes, and David for his pioneering work on the water uptake of LSF.

My office colleagues Gregor, Sandra, Alex and Christoph deserve a special mention for being supportive whenever I had a question and also for bringing chocolate and occasional fun into the dry office work. Special thanks go to Christoph for cheering me up with his outbursts of fury whenever there was a software problem.

Finally I want to thank all of my current and former group members (so I don't risk forgetting anyone) for contributing to many interesting or simply enjoyable discussions, joining the billiard and bowling games in the evenings and being part a friendly and cooperative workgroup.